

CENTRAL LIBRARY



SCHOLARLY PUBLICATIONS

*A CURRENT AWARENESS BULLETIN
OF RESEARCH OUTPUT BY*

FACULTY, STUDENT AND ALUMNI

~ JANUARY 2014 ~

DELHI TECHNOLOGICAL UNIVERSITY

(FORMERLY DELHI COLLEGE OF ENGINEERING)

GOVT. OF N.C.T. OF DELHI

SHAHBAD DAULATPUR, MAIN BAWANA ROAD

DELHI 110042

PREFACE

This is the Eleventh Issue of Current Awareness Bulletin started by Delhi Technological University, Central Library. The aim of the bulletin is to compile, preserve and disseminate information published by the faculty, students and alumni for mutual benefits. The bulletin also aims to propagate the intellectual contribution of Delhi Technological University (DTU) as a whole to the academia.

The bulletin contains information resources available in the internet in the form of articles, reports, presentations published in international journals, websites, etc. by the faculty and students of DTU. The publications of faculty and student which are not covered in this bulletin may be because of the reason that the full text either was not accessible or could not be searched by the search engine used by the library for this purpose.

The learned faculty and students are requested to provide their uncovered publications to the library either through email or in CD, etc to make the bulletin more comprehensive.

This issue contains the information published during January 2014. The arrangement of the contents is alphabetical. The full text of the article which is either subscribed by the university or available in the web is provided in this bulletin.

CONTENTS

1. A futuristic approach towards interface layer modifications for improved efficiency in inverted organic solar cells, J. P. Tiwari, **Sriraj Pillai*, **Sonal Parakh*, (Department of Physics), Farman Ali, Abhishek Sharma, and Suresh Chand
2. A Modified Droop Control Method for Parallel Operation of VSI's in Microgrid, **Ashutosh Trivedi*, D.K.Jain and **Mukhtiar Singh*
3. A Review on Feasibility of Conventional Fluoride Removal Techniques in Urban Areas **Tarundeep Gill*, **Shashi Tiwari* and **P. Albino Kumar*, Department of Environmental Engineering
4. A Simple Approach for Image Enhancement using New Power-Law Transformation Operators, **Om Prakash Verma* (Department of Information Technology), Nitesh Gi, Pooja Gupta and Megha
5. An Adaptive Single Seed Based Region Growing Algorithm for Color Image Segmentation, Puneet Kumar Jain and **Seba Susan* (Department of Information Technology)
6. An Experimental Investigation of Jatropha Biodiesel Blends in a Multi Cylinder CI Engine: Performance and Emissions Study **Amit Pal* (Department of Mechanical Engineering)
7. Black Hole Attack Mitigation Method based on Route Discovery Mechanism in AODV Protocol **Anishi Gupta* (Department of Computer of Engineering)
8. Content based Image Retrieval: A Quantitative Comparison between Query by Color and Query by Texture *#Sunkari Madhu*

9. Day Ahead Hourly Load and Price Forecast in ISO New England Market using ANN, ***Kishan Bhushan Sahay** and ***M. M Tripathi** (Department of Electrical Engineering)
10. Depth and Scale Modeling of Object for 3D Motion Analysis in Video, Gurjit Singh Walia ***Prof Rajiv Kapoor** and ***Satbir Singh**, (Department of Electronics and Communication)
11. Design of Unity Power Factor Controller for Three-phase Induction Motor Drive Fed from Single Phase Supply ***Rachana Garg**, ***Priya Mahajan**, Parmod Kumar, and ***Rohit Goyal**
12. Edge Strength based Fuzzification of Colour Demosaicking Algorithms ***Seba Susan** and ***Deepak Aneja**
13. Field Characteristics in Dielectric Rectangular Wave Guide with harmonics Deepender Dabas and ***N S Raghava** (ECE Deptt)
14. Glowworm Swarm Optimization Technique for Optimal Power Flow, Rahul Dogra and ***Nikita Gupta**, M.Tech Power Systems
15. Kinetics Studies on the Catalytic Thermal Degradation of High Density Polyethylene, Vandana, Pratibha Chaudhary and ***Ramesh Chander Sharma** (Department of Applied Chemistry and Polymer Technology)
16. LOSS MINIMIZATION POLICY FOR A PRODUCTION LINE WITH IMMEDIATE FEEDBACK AND MULTI SERVER FACILITY AT ALL PROCESSING UNITS Abhimanu Singh, ***Datta, C. K.** (Production Engineering)
17. Membrane Technique for Leachate Treatment-A Literature Review ***Arpita Anand** and ***Shashank Shekhar Singh**, (Department of Environmental Engineering)

18. PERFORMANCE AND EMISSION CHARACTERISTICS OF CASTOR SEED OIL BIODIESEL ON MEDIUM CAPACITY DIESEL ENGINE @*Harveer Singh Pali*, , \$*Vipul Vibhanshu*, and **Naveen Kumar*, Department of Mechanical Engineering
19. PERFORMANCE COMPARIS ON OF FILTER CIRCUITS BASED ON TWO DIFFERENT CURRENT CONVEYOR TOPOLOGIES, **Garima Varshney*, **Neeta Pandey*, **Raj eshwari Pandey* and **Asok Bhattacharyya*, (Department of Electronics and Communication Engg)
20. Phase control of nanostructured iron oxide for application to biosensor, **Rachna Sharma*, (Department of Applied Physics) Ved Varun Agrawal, A. K. Srivastava, Govind, Lata Nain, Mohd Imran, Soumya Ranjan Kabi, **R. K. Sinha*, (Department of Applied Physics) and **Bansi D. Malhotra*, (Department of Biotechnology)
21. Planning, Designing, Monitoring and Inspection of Wastewater Treatment Systems of Industries, £*Sameer Kumar* and £*Gaurav Singh* (Environmental Engineering)
22. Pr3p doped lead tungstentellurite glasses for visible red lasers\$ Q7 M. Venkateswarlua, M.V.V.K.S. Prasad, K. Swapna, Sk. Mahamuda, **A. Srinivasa Rao*, (Department of Applied Physics) A. Mohan Babu and D. Haranath
23. Sensitivity Analysis of Characteristic Parameters of Railway Electric Traction System, **Rachana Garg*, **Priya Mahajan*, (Deptt. of Electrical Engg.) and Parmod Kumar
24. Solid Waste Management: Its Sources, Collection, Transportation and Recycling, **Gaurav K. Singh*, *Kunal Gupta*, and **Shashank Chaudhary* (Environmental Engineering)
25. Speed Control of Hybrid Electric Vehicle Using Artificial Intelligence Techniques Japjeet Kaur, ~<*Prerna Gaur*, <*Piyush Saxena* and Vikas Kumar

- 26.** Tertiary recycling of poly(ethylene terephthalate) wastes for production of polyurethane–polyisocyanurate foams, P.K. Roy, **R. Mathur, *D. Kumar* (Department of Applied Chemistry and Polymer Technology) and C. Rajagopal
- 27.** Thermodynamic Analysis of Linde System for Liquefaction of Gases, **Devender Kumar*, and **R.S Mishra*, (Department of Mechanical Engineering)
- 28.** VIBRATION INDUCED DUE TO ACOUSTIC EXCITATION IN DIFFUSE FIELD CONDITIONS Naveen Garg and **Sagar Maji* (Department of Mechanical, Production & Industrial Engineering)

* Faculty
@ Research Scholar
\$ PG Scholar
£ Undergraduate Student
Alumni
~ Ex Faculty
< Ex Research Scholar



A futuristic approach towards interface layer modifications for improved efficiency in inverted organic solar cells

J. P. Tiwari, Sriraj Pillai, Sonal Parakh, Farman Ali, Abhishek Sharma, and Suresh Chand

Citation: [Applied Physics Letters](#) **104**, 041114 (2014); doi: 10.1063/1.4863434

View online: <http://dx.doi.org/10.1063/1.4863434>

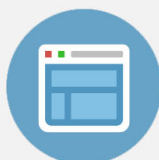
View Table of Contents: <http://scitation.aip.org/content/aip/journal/apl/104/4?ver=pdfcov>

Published by the [AIP Publishing](#)



Re-register for Table of Content Alerts

Create a profile.



Sign up today!





A futuristic approach towards interface layer modifications for improved efficiency in inverted organic solar cells

J. P. Tiwari,^{1,a)} Sriraj Pillai,^{1,2} Sonal Parakh,^{1,2} Farman Ali,¹ Abhishek Sharma,¹ and Suresh Chand¹

¹Physics of Energy Harvesting Division (Organic and Hybrid Solar Cell Group), CSIR-National Physical Laboratory, CSIR-Network of Institutes for Solar Energy (NISE), Dr. K. S. Krishnan Marg, New Delhi 110012, India

²Department of Physics, Delhi Technological University, Bawana Road, Delhi 110042, India

(Received 13 November 2013; accepted 7 January 2014; published online 30 January 2014)

Inverted polymer Solar Cells of the classical poly (3-hexylthiophene) (P3HT):(6,6)-phenyl-C₆₁butyric acid methyl ester (PC₆₁BM) blend on indium tin oxide substrates were fabricated, which shows improved device performance, by using a facile solution-processed ZnO-polyelectrolytes [poly (diallyldimethylammonium chloride) (PDADMAC), Poly (acrylic acid sodium salt) (PAS), poly (4-styrenesulfonic acid) (PSS), and Polyvinylpyrrolidone (PVP)] nanocomposite as a cathode interface layer compared to devices using pristine ZnO as cathode buffer layer in ambient conditions. The devices with different combinations of polyelectrolyte with ZnO show different improvements in the device efficiency. The combinations of ZnO with PVP and PDADMAC show highest amount of improvements in the efficiency by a factor of ~ 17 – 19 . The improvement of the efficiency may be due to various phenomena, such as the passivation of ZnO surface as well as bulk traps, work function modification, improved energy level alignment, improved electronic coupling of the inorganic/organic interface, improved light harvesting, and decrease of surface as well as bulk charge recombination in the device. The introduction of polyelectrolyte into ZnO inhibits the aggregation of ZnO nanoparticles yielding the large area ZnO nanoclusters; and hence, forming the uniform film of ZnO resulting in the modifications of morphology as well as electronic structure of ZnO-polyelectrolyte nano-composite favouring better electronic coupling between cathode and active layer and hence enhancing the current and, consequently, the efficiency. This simple low temperature ZnO-polyelectrolyte nanocomposite based protocol proposed for cathode interface layer modification may be very much useful for roll to roll industrial manufacturing of organic solar cells. © 2014 AIP Publishing LLC. [<http://dx.doi.org/10.1063/1.4863434>]

Organic Solar Cells (OSCs) are expected to be alternative energy resource for future generation and are likely to be commercializing very soon.^{1–3} Hence, much attention has been given to OSCs in past few years in view of improvements of their power conversion efficiency (PCE) and life time. The PCE of OSCs has reached in the range of 7–9 in literature;^{4–6} however, still improvements are needed in PCE.⁷ The factors,⁸ which determine the PCE of OSCs, are open circuit voltage (V_{oc}), short circuit current (J_{sc}), and fill factor (FF). The V_{oc} depends on the active layer materials where as J_{sc} depends on the absorption spectrum as well as on the transport of charge carriers through the film. Further, the FF which represents how difficultly or easily the charge carriers can be extracted out of the device, depends on many factors such as series resistance, shunt resistance, and on the quality of diode.

Besides PCE, the stability of OSCs is a major factor which is playing a role against commercialization of OSCs. In general, conventional OSCs comprise an active layer sandwiched between two electrodes, namely, Indium Tin Oxide (ITO) on bottom and metal electrode on the top. The diffusion of air into the active layer through pinholes and grain boundaries causes degradation of the device in air.

Moreover, the hygroscopic nature^{9,10} of the hole transporting poly (3, 4 ethylene dioxythiophene) doped with polystyrene sulfonate (PEDOT:PSS) layer aids towards degradation of the device.

One approach to resolve the issue of degradation is to adopt the inverted geometry where the charge separation and collection is reversed. In the inverted structure the interface of ITO/PEDOT:PSS can be avoided by using various high band gap n-type of oxides^{11,12} such as ZnO, TiO_x, V₂O₅, and NiO instead of PEDOT:PSS. Moreover, the environmental friendly nature, high optical transparency, relatively higher electron mobility, blocking capability for the UV-light induced photodegradation of organic materials, and availability of various techniques of wet synthesis of ZnO makes it most suitable material to be used as an electron transport layer (ETL) in the inverted OSCs.^{13–18} However, the major problems in using ZnO nanoparticle films are (i) the presence of defects due to adsorption of oxygen, (ii) back charge transfer from ZnO to electron donating conjugated polymer, and (iii) the spatial distribution of ZnO nanoparticles is also not uniform, which renders large series resistance leading to poor electronic coupling with the active layer. Hence, alternative approaches are needed in view of creating low defect, smooth, and uniform films of the ETL which can create better electronic coupling with the active layer. Self assembled monolayers,^{19,20} polyelectrolyte applied on the top^{21–25} of ZnO film can eliminate the surface traps up to some extent

^{a)}Author to whom correspondence should be addressed. Electronic addresses: jai_tiwari@yahoo.com and tiwarijp@mail.nplindia.org. Tel.: 91-11-4560-8620 (O) and 91-11-28741285 (R).

and can improve the electronic coupling of ZnO/active layer for improved device parameters. However, these strategies can only remove traps on the surface of the film and bulk defects remain intact which significantly affect the device parameters. Further, the strategies of monolayer and a thin layer of polyelectrolyte on the surface of ZnO have challenges on industrial scale as it complicates the film forming process. Recently, it is suggested that one can passivate bulk traps by using TiO_x -ZnO nano-composite.^{26,27} Further, there are reports of using polyelectrolyte as an electron transporting or injecting/collecting layers in the OSCs as well as for polymer based light emitting diodes.^{28–35} Hence, the use of ZnO/polyelectrolyte hybrid nano-composite may be an alternative approach which can address the issues of series resistance, distribution of nanoparticles, unbalanced charge injection, and bulk/surface defects in ZnO films in view of improving different device parameters for high efficient and durable organic solar cells. Herein, we had chosen the well known polymers, namely, poly (diallyldimethylammonium chloride) (PDADMAC), Poly (acrylic acid sodium salt) (PAS), poly (4-styrenesulfonic acid) (PSS), and Polyvinylpyrrolidone (PVP) (Fig. 1) for the synthesis of ZnO-polyelectrolyte nano composite used as an ETL in inverted device configuration. These polyelectrolytes are very much soluble in polar solvents, such as water or water/alcohol mixture, hence; offer the option of mixing it with ZnO to be used as interface layer in the inverted organic solar cells. The combination of polyelectrolyte with ZnO may change electronic configuration as well as morphology and hence, device efficiency.

We have fabricated a high efficiency inverted organic solar cell, viz., ITO/ZnO-polyelectrolyte (~ 25 nm)/poly (3-hexylthiophene) (P3HT):(6,6)-phenyl- C_{61} butyric acid methyl ester (PC_{61}BM) (~ 90 nm)/ MoO_3 (~ 8 nm)/Al (~ 125 nm), using a solution processed ZnO-polyelectrolyte nano composite as the cathode interfacial layer. The inverted cells based on the

blend of P3HT and PC_{61}BM using ZnO-PDADMAC as interface layer demonstrated a J_{sc} of 10.86 mA/cm^2 and PCE of ~ 1.86 , which is ~ 18.6 times higher than the PCE value of inverted solar cell based on sole ZnO inter face layer fabricated under same ambient conditions keeping all the parameters unchanged. Further, similar enhancement (~ 17.1 times) of device efficiency is observed for ZnO-PVP nano-composite system. So, we can say that in the ZnO-polyelectrolyte nano-composite, the surface as well as bulk traps of ZnO may have smoothened/filled up by polyelectrolyte, and may be favouring the restraining interfacial charge recombination, enhancing the photovoltaic performance of OSCs.

Herein, we used four different polyelectrolytes, viz., PDADMAC, PAS, PVP, and PSS. The entire chemical used here was purchased from the sigma Aldrich. The ZnO-polyelectrolyte nanocomposite was synthesized from a precursor, in which zinc acetate dihydrate (Sigma Aldrich, 99.99%) and poly electrolyte solutions were mixed in 2:1 ratio. Exactly speaking 0.235 g of zinc acetate dihydrate was added in 5 ml propanol and allowed to stir for 5 min. A white cloudy solution was obtained and then few drops of stabilizer diethanolamine were added to this solution. Slowly, we observe that the cloudiness disappears and a colourless, transparent solution is obtained. Now, this solution is stirred at 60°C for 2 h and kept untouched and undisturbed for 24 h. To make PSS, PAS, PDADMAC, and PVP solution, we added 0.5 ml of this polymer in 0.5 ml of water and stirred it for 30 min. Now to prepare the nanocomposite solution, we added 1 ml of polyelectrolyte solution to 2 ml of zinc oxide solution and the resultant solution was stirred for 30 min. For the device fabrication, first of all patterned ITO were wiped using a tissue paper dipped in acetone. Here, all the dust and other particles are removed from the ITO. Following this, the ITOs are ultra-sonicated for 20 min in a beaker filled with soap water. Here, further other micro-sized impurities are removed. Once the ultrasonic cleaning is complete, the ITOs were further rubbed using cotton. This process of rubbing with soap is carried out until a proper thin layer of water stays on the ITO. Then ITO is boiled in acetone for 20 min, in trichloroethylene (TCE) for 15 min, and in isopropanol for 15 min. These cleaned ITOs are dried in oven at 150°C for 30 min. Before using these ITOs for fabricating a device we did UV-ozone treatment of all the ITOs. Subsequently, the ITOs were spin coated with ZnO, ZnO-PAS, ZnO-PSS, ZnO-PDADMAC, and ZnO-PVP solutions at 3500 rpm. These films are heated at 200°C for 30 min. The morphology of the film was investigated using ZEISS EVO MA10 model of SEM, Atomic Force Microscopy (NTMDT), and photoluminescence (PL) using Fluorolog. Further, a blend of P3HT: PC_{61}BM in the ratio 1:0.6 was prepared in total 30 mg/ml in dichlorobenzene and spin coated on the top of ZnO and zinc oxide based nanocomposite film at 900 rpm at room temperature and annealed at 120°C for 10 min. Then the films were transferred to thermal evaporator for deposition of MoO_3 and Al layer, in which case a mask of size $\sim 2 \text{ mm} \times 3 \text{ mm}$ is used in vacuum of $\sim 10^{-6}$ Torr. Once the device is fabricated, J-V characterization of the device is carried out with cell illuminated under simulated AM1.5G illumination at 100 mW/cm^2 using Keithley 2420 Source Meter interfaced with a computer. The measurements were done

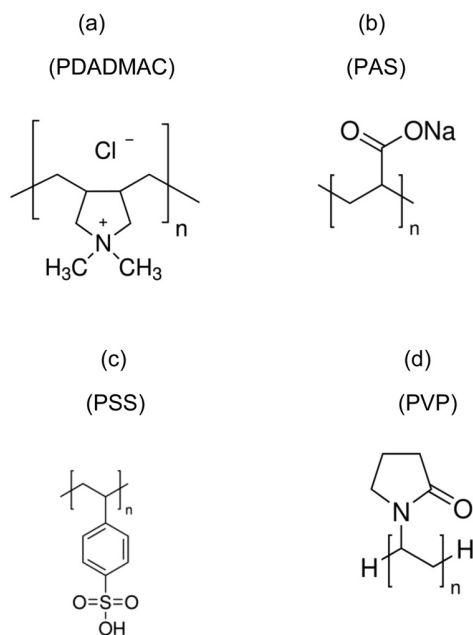


FIG. 1. Schematic drawing of (a) PDADMAC, (b) PAS, (c) PSS, and (d) PVP.

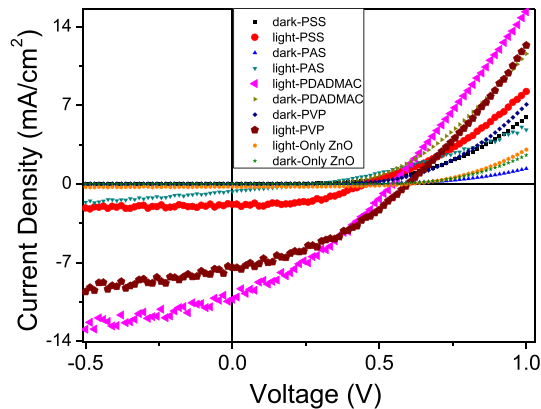


FIG. 2. J-V plot for devices- ITO/ZnOIP3HT:PC₆₁BMiMoO₃/Al, ITO/ZnO-PASIP3HT:PC₆₁BMiMoO₃/Al, ITO/ZnO-PSSIP3HT:PC₆₁BMiMoO₃/Al, ITO/ZnO-PVPIP3HT:PC₆₁BMiMoO₃/Al, and ITO/ZnO-PDADMACIP3HT:PC₆₁BMiMoO₃/Al.

both in illuminated and dark conditions. All the J-V characteristics of devices are presented in Fig. 2 both in dark as well as in illuminated conditions. In the ZnO-only devices a typical open circuit voltage (V_{oc}) of 0.59 V, short circuit current (J_{sc}) of 0.25, and fill factor of 58.2 achieved giving a PCE of 0.10. When PAS, PSS, PVP, and PDADMAC was added to ZnO to obtain the nanocomposite layer, then the device exhibited improved performance with nano composites of ZnO-PSS, ZnO-PVP, and ZnO-PDADMAC (Table I). A close observation of Table I reveals that the nanocomposite of ZnO with polymer gives better performance in terms of device parameter, viz., J_{sc} . The device with the ZnO-PAS as an interface layer shows inferior device characteristics in terms of J_{sc} , V_{oc} , and FF, which can be explained with the help of SEM shown in Figs. 3(a)–3(d), as we can observe that the film of ZnO-PAS is not smooth one and it have agglomerated nanoparticles of ZnO distributed

TABLE I. Inverted devices parameters whose J-V plots are shown in Fig. 2.

Interface layer	FF (%)	V_{oc} (V)	J_{sc} (mA/cm ²)	PCE (%)
ZnO	58.20	0.59	0.25	0.10
ZnO-PAS	31.60	0.36	0.07	0.01
ZnO-PSS	54.00	0.45	1.77	0.42
ZnO-PVP	40.00	0.59	9.62	1.71
ZnO-PDADMAC	33.00	0.54	10.82	1.86

over all the area and even more it is having voids (Fig. 3(d)) on the surface of the ZnO-PAS film. Hence, its poor coupling with active layer may be responsible for its inferior performance as it happens with the pristine ZnO based devices (Figs. 4(c) and 4(d)). The Figs. 4(c) and 4(d) clearly show the agglomerated ZnO nanoparticles when its spin coated on ITO from the solution. Herein, we want to make it clear that most of the devices with pristine ZnO as interface layer are highly susceptible for shorts in our experimental conditions. We tried to make the device using pristine ZnO by varying composition from 0.035 to 0.535 g/5 ml. However, we came to an end of shorting of the devices, and only a few worked with lower values of efficiency. The devices with the composite layers produced good device as shown in Table I. We know that device efficiency using pristine ZnO as an interface layer is small. Further, optimization of solution concentration/thickness may give better performance as reported in literature for pristine ZnO based inverted devices. However, here our motive is the demonstration of effect of ZnO-polyelectrolyte nanocomposite on the device performance. These values (Table I) of device parameters showed superior interface properties of the ZnO-PSS, ZnO-PVP, and ZnO-PDADMAC nanocomposite. The Figs. 4(a), 4(b), 5(a), and 5(b) show a representative SEM/AFM image of the spin coated nanocomposite of ZnO-PDADMAC on the ITO,

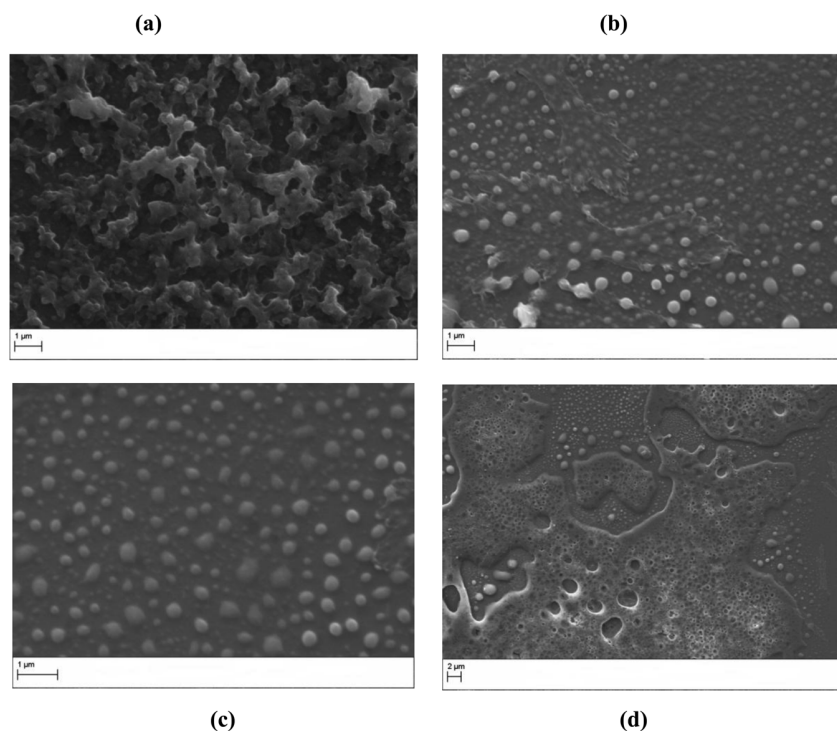


FIG. 3. SEM of a film of ZnO-PAS nanocomposite, (a)–(c) showing agglomerated nanoparticles of ZnO in PAS matrix and (d) voids on the surface of the film.

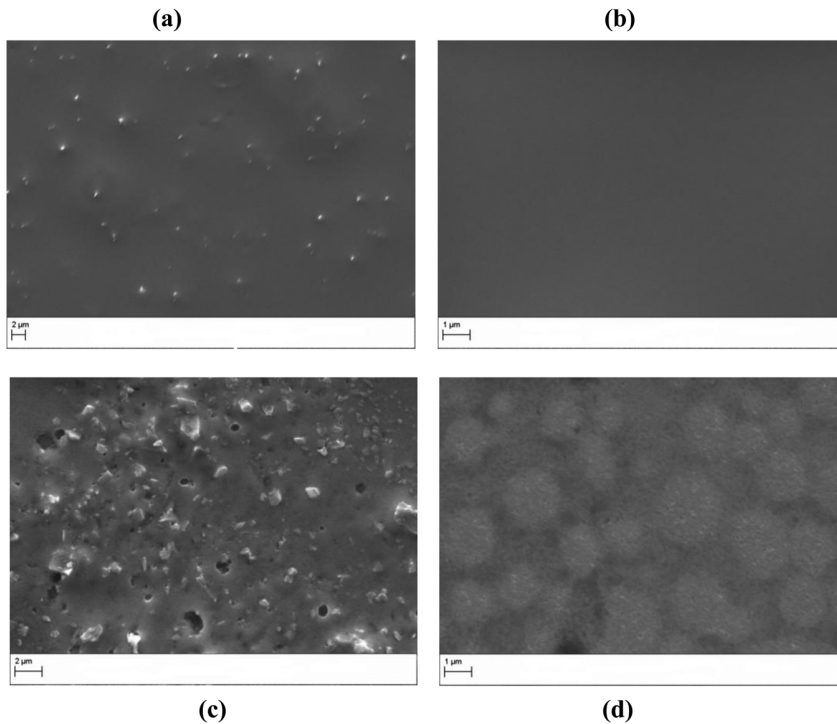


FIG. 4. SEM of a film of (a) and (b) ZnO-PDADMAC, (c) and (d) pristine zinc oxide, showing agglomerated zinc oxide nanoparticles in (c) and (d), and finely distributed and planarized ZnO-PDADMAC nanocomposite film.

which clearly demonstrates that the ZnO nanoparticles are finely distributed over the entire surface and the surface is very smooth (Fig. 5). In addition, we have observed that the ZnO-PSS and ZnO-PVP also shows (figure is not shown here) the fine distribution of ZnO nanoparticles in the matrix of PSS and PVP. Hence, the improved electron collection capability (Table I) is expected from the ZnO-PDADMAC, ZnO-PVP, and ZnO-PSS nanocomposite morphology which have resulted in better device parameters (Table I).

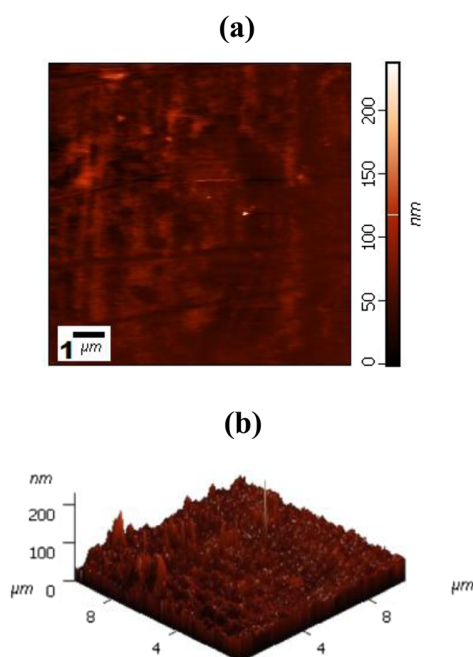


FIG. 5. AFM images of (a) ZnO-PDADMAC topography (b) height images, spin coated on the ITO surface taken in tapping mode. Both of images were obtained for $10\ \mu\text{m} \times 10\ \mu\text{m}$ surface area. The root mean square (RMS) roughness of the ZnO-PDADMAC film is $\sim 5\ \text{nm}$.

In order to explain the improved current collection (Table I) in devices with composite layer, we tried to investigate the effect of PDADMAC, PVP, and PSS modification on the surface defects of Zn nanoparticles through PL under 330 nm photoexcitation as shown in Fig. 6. The emission band at $\sim 370\ \text{nm}$ may be due to exciton emission. The two shoulders at ~ 420 and $\sim 439\ \text{nm}$ may be originating from the Zn interstitial defects. Further, the broad emission at $\sim 475\ \text{nm}$ may be attributed to transition among photoexcited carriers, oxygen vacancies, surface defects, etc. As obvious from Fig. 6 the emission intensity decreases for composite layer with respect to the pristine zinc oxide layer, which may be indication of passivation of surface traps in composite layers. Moreover, we have investigated the electron transporting property of the pristine ZnO as well as of ZnO-PDADMAC nano composite using electron only devices of the structure ITO/ZnO/Al and ITO/ZnO-PDADMAC/Al respectively. We measured the space charge limited current

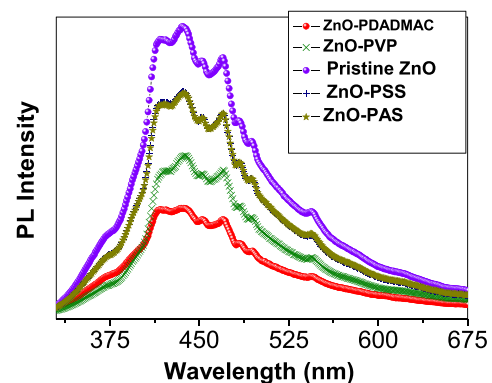


FIG. 6. PL spectra of ZnO, ZnO-PSS, ZnO-PAS, ZnO-PVP, and ZnO-PDADMAC films prepared through spin coating at 3500 rpm.

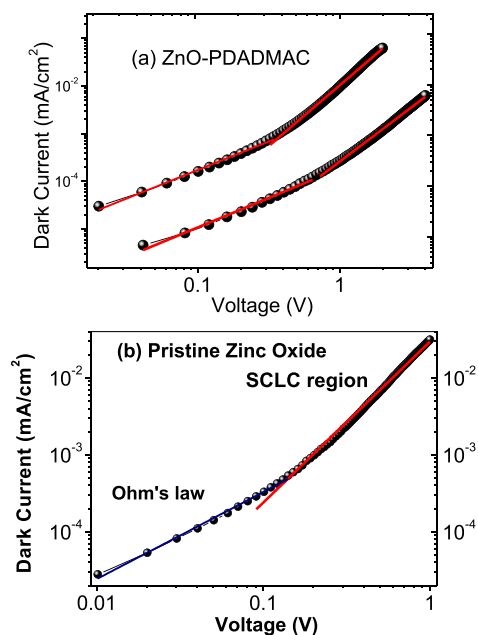


FIG. 7. Log J vs. Log V plots for (a) ZnO-PDADMAC (b) pristine ZnO film based electron only devices for mobility measurements using Mott-Gurney SCLC relation.

(Fig. 7) (SCLC) of these device and calculated the effective charge carrier mobility with the help of well known Mott-Gurney SCLC relation.²¹ We found that the effective electron mobility ($\sim 6.1 \times 10^{-4} \text{ cm}^2 \text{V}^{-1} \text{s}^{-1}$) is higher for composite layers with respect to pristine zinc oxide ($\sim 4.2 \times 10^{-4} \text{ cm}^2 \text{V}^{-1} \text{s}^{-1}$) layers. Thus, the passivation of surface traps as well as mobility improvements will lower the trap assisted recombination at the interface, increasing the charge collection, and hence the efficiency in composite layers devices. Further, a closure observation of Table I shows the decrease of fill factor of the devices with composite layer with respect to the pristine zinc oxide based devices. The observed decrease in the device FF may be attributed to the excess polyelectrolyte layer on the ZnO surface as suggested by Small *et al.*³³

In summary, we synthesized ZnO-PAS, ZnO-PVP, ZnO-PDADMAC, and ZnO-PSS nano-composite through solution route and demonstrated OSC devices by incorporating them in the inverted structure. The PVP, PSS, and PDADMAC not only improved the electron collection (Table I) efficiency of the inverted devices but also smoothened the ZnO-surfaces (Figs. 3–5), thereby reducing the leakage current and improving the device efficiency. The power conversion efficiency value of ~ 1.86 (Table I) of a ZnO-PDADMAC nano-composite based inverted device is ~ 18.6 times higher to the efficiency of ZnO as an inter layer for P3HT:PC₆₁BM based system. Hence, this study represents an alternative approach to modify interfacial layer for developing devices with improved efficiency.

We acknowledge the technical support of G. D. Sharma, Ramil Bharadwaj, Neeraj Chaudhary, and Reema Ganotra (M. Tech. student) for film preparation for SEM/AFM/PL/Electron only device studies. Further, the financial support from the

Project NWP-54 funded by CSIR is acknowledged. Moreover, we acknowledge our director (Professor R.C. Budhani) for his critical evaluation of our work during group meetings.

- ¹F. C. Krebs, *Sol. Energy Mater. Sol. Cells* **93**, 394 (2009).
- ²F. C. Krebs, N. Espinosa, M. Hösel, R. R. Søndergaard, and M. Jørgensen, *Adv. Mater.* **26**, 29–39 (2014).
- ³K. D. G. I. Jayawardena, L. J. Rozanski, C. A. Mills, M. J. Beliatas, N. A. Nismy, and S. R. P. Silva, *Nanoscale* **5**, 8411 (2013).
- ⁴Z. He, C. Zhong, S. Su, M. Xu, H. Wu, and Y. Cao, *Nat. Photon.* **6**, 591 (2012).
- ⁵Z. He, C. Zhong, X. Huang, W. Y. Wong, H. Wu, L. Chen, S. Su, and Y. Cao, *Adv. Mater.* **23**, 4636 (2011).
- ⁶M. A. Green, K. Emery, Y. Hishikawa, W. Warta, and E. D. Dunlop, *Prog. Photovoltaics* **20**, 12 (2012).
- ⁷L. Dou, J. You, Z. Hong, Z. Xu, G. Li, R. A. Street, and Y. Yang, *Adv. Mater.* **25**, 6642 (2013).
- ⁸R. A. J. Janssen and J. Nelson, *Adv. Mater.* **25**, 1847 (2013).
- ⁹K. Kawano, R. Pacios, D. Poplavskyy, J. Nelson, D. D. C. Bradley, and J. R. Durrant, *Sol. Energy Mater. Sol. Cells* **90**, 3520 (2006).
- ¹⁰Y. Sun, J. H. Seo, C. J. Takacs, J. Seifert, and A. J. Heeger, *Adv. Mater.* **23**, 1679 (2011).
- ¹¹J. Meyer, S. Hamwi, M. Kröger, W. Kowalsky, T. Riedl, and A. Kahn, *Adv. Mater.* **24**, 5408 (2012).
- ¹²R. Lampande, G. W. Kim, J. Boizot, Y. J. Kim, R. Podes, and J. H. Kwon, *J. Mater. Chem. A* **1**, 6895 (2013).
- ¹³A. K. K. Kyaw, X. W. Sun, C. Y. Jiang, G. Q. Lo, D. W. Zhao, and D. L. Kwong, *Appl. Phys. Lett.* **93**, 221107 (2008).
- ¹⁴S. Bai, Z. Wu, X. Xu, Y. Jin, B. Sun, X. Guo, S. He, X. Wang, Z. Ye, H. Wei, X. Han, and W. Ma, *Appl. Phys. Lett.* **100**, 203906 (2012).
- ¹⁵Z. Ma, Z. Tang, E. Wang, M. R. Andersson, O. Inganäs, and F. Zhang, *J. Phys. Chem. C* **116**, 24462 (2012).
- ¹⁶Z. Liang, Q. Zhang, O. Wiranwetchayan, J. Xi, Z. Yang, K. Park, C. Li, and G. Cao, *Adv. Funct. Mater.* **22**, 2194 (2012).
- ¹⁷P. P. Boix, J. Ajuria, I. Etxebarria, R. Pacios, G. G. Belmonte, and J. Bisquert, *J. Phys. Chem. Lett.* **2**, 407 (2011).
- ¹⁸A. K. K. Kyaw, D. H. Wang, D. Wynnands, J. Zhang, T. Q. Nguyen, G. C. Bazan, and A. J. Heeger, *Nano Lett.* **13**, 3796 (2013).
- ¹⁹M. Song, J. W. Kang, D. H. Kim, J. D. Kwon, S. G. Park, S. Nam, S. Jo, S. Y. Ryu, and C. S. Kim, *Appl. Phys. Lett.* **102**, 143303 (2013).
- ²⁰S. K. Hau, H. L. Yip, H. Ma, and A. K. Y. Jen, *Appl. Phys. Lett.* **93**, 233304 (2008).
- ²¹H. Y. Park, D. Lim, K. D. Kim, and S. Y. Jang, *J. Mater. Chem. A* **1**, 6327 (2013).
- ²²T. Yang, M. Wang, C. Duan, X. Hu, L. Huang, J. Peng, F. Huang, and X. Gong, *Energy Environ. Sci.* **5**, 8208 (2012).
- ²³C. Xie, L. Chen, and Y. Chen, *J. Phys. Chem. C* **117**, 24804 (2013).
- ²⁴J. Subbiah, C. M. Amb, I. Irfan, Y. Gao, J. R. Reynolds, and F. So, *ACS Appl. Mater. Interfaces* **4**, 866 (2012).
- ²⁵Y. M. Chang and C. Y. Leu, *J. Mater. Chem. A* **1**, 6446 (2013).
- ²⁶J. Liu, S. Shao, B. Meng, G. Fang, Z. Xie, L. Wang, and X. Li, *Appl. Phys. Lett.* **100**, 213906 (2012).
- ²⁷A. Gadisa, T. Hairfield, L. Alibabaei, C. L. Donley, E. T. Samulski, and R. Lopez, *ACS Appl. Mater. Interfaces* **5**, 8440 (2013).
- ²⁸S. B. Jo, J. H. Lee, M. Sim, M. Kim, J. H. Park, Y. S. Choi, Y. Kim, S. G. Ibn, and K. Cho, *Adv. Energy Mater.* **1**, 690 (2011).
- ²⁹H. Ting, L. Fan, K. Yuan, and Y. Chen, *ACS Appl. Mater. Interfaces* **5**, 5763 (2013).
- ³⁰G. E. Lim, Y. E. Ha, M. Y. Jo, J. Park, Y. C. Kang, and J. H. Kim, *ACS Appl. Mater. Interfaces* **5**, 6508 (2013).
- ³¹H. Choi, J. S. Park, E. Jeong, G. H. Kim, B. M. Lee, S. O. Kim, M. H. Song, H. Y. Woo, and J. Y. Kim, *Adv. Mater.* **23**, 2759 (2011).
- ³²Y. Zhou, C. F. Hernandez, J. Shim, J. Meyer, A. J. Giordano, H. Li, P. Winget, T. Papadopoulos, H. Cheun, J. Kim, M. Fenoll, A. Dindar, W. Haske, E. Najafabadi, T. M. Khan, H. Sojoudi, S. Barlow, S. Graham, J. L. Brédas, S. R. Marder, A. Kahn, and B. Kippelen, *Science* **336**, 327 (2012).
- ³³C. E. Small, S. Chen, J. Subbiah, C. M. Amb, S. W. Tsang, T. H. Lai, J. R. Reynolds, and F. So, *Nat. Photonics* **6**, 115 (2012).
- ³⁴Y. J. Lee, J. Wang, S. R. Cheng, and J. W. P. Hsu, *ACS Appl. Mater. Interfaces* **5**, 9128 (2013).
- ³⁵X. Bulliard, S. G. Ihn, S. Yun, Y. Kim, D. Choi, J. Y. Choi, M. Kim, M. Sim, J. H. Park, W. Choi, and K. Cho, *Adv. Funct. Mater.* **20**, 4381 (2010).

A Modified Droop Control Method for Parallel Operation of VSI's in Microgrid

Ashutosh Trivedi¹, D.K.Jain² and Mukhtiar Singh¹

¹Delhi Technological University, Delhi

²Deen Bandhu Chhotu Ram University of Science and Technology, Murthal, Haryana

Abstract—The methods based on the droop characteristics have inherent advantages in parallel operation of voltage source inverters (VSI's). The droop control method requires information of voltage and current only at point of common coupling without any communication link between individual inverters. In conventional droop method, the active and reactive power are shared in linear relation to frequency and voltage, hence, the performance of the controller is imprecise under different loading conditions. In this paper, a modified droop characteristics has been proposed for sharing power among the VSI's in order to achieve better frequency and voltage regulation. This modified method has the ability to regulate the frequency even at low power outputs while preventing overloading during peak power demand. The modelling and simulation of the proposed method has been performed in MATLAB/SIMULINK to validate the approach.

Index Terms—Droop method, Micro-grid, Parallel Operation of Inverters.

I. INTRODUCTION

Now a days, use of power electronics based distributed resources (DR) have increased in the main electricity power system (EPS). The concept of micro-grid has emerged in view of the requirement of the small local power system which have their own load, and can supply power even in failure of the main grid. In micro-grid, the integration of these inverters is one of the key requirement. Due to short overloading capacity of the inverters, several parameters especially output filter parameters have to be taken care of while designing the system [2,3].

The X/R ratio of tie lines between inverters plays a vital role in inverter's control. Theoretically, active and reactive powers are function of both voltage and frequency, however, if X/R ratio is high, then active power depends more on frequency and similarly reactive power have more impact on voltages. With low X/R ratio, the above relation gets reversed [6].

There are two main control modes in micro-grid. First one is grid connected mode while another is islanded mode. In grid connected mode, the VSI's operates in current control mode to supply active and reactive power at grid frequency and line voltages [7]. In grid connected mode the main role of VSI's is to only inject the generated power into the grid and any power mismatch is supplied/absorbed by the grid to meet the load demand. In islanding mode, the grid is absent, VSI's have to balance the power mismatch with defined sharing of power among them. The constant frequency and constant voltage type VSI's need communication link for power sharing, so reliability of the system depends upon

the reliability of communication channel. Master slave based system requires minimum communication bandwidth but can be utilized only for small area system. The failure of the master will cause the whole system to collapse in large distributed system [4].

A truly redundant VSI's based micro-grid should not require any communication between VSI's to operate in parallel. The droop control method needs no communication medium for parallel operation as its control algorithm uses those line quantity which are locally available at point of common coupling (PCC). As droop is a natural characteristics of governor action in conventional EPS, similar $P-\omega$ and $E-Q$ droop for active and reactive power sharing in parallel operation of inverters has been suggested in many papers [5]. With conventional droop, different inverters share power linearly according to their droop coefficients. Such system suffers from reduced voltage and frequency for long duration which may affect the power quality. Further, A few papers have described the state of charge (SoC) based droop method, but implementation of this method requires measurement for DC link voltage and stored energy which is complicated [10].

In this paper, the conventional droop control characteristics has been modified so as to meet the requirement of the inverters operating in parallel in all inverter based micro-grid. The paper is divided into six sections. Section-1 gives the general introduction. Section-2 describes the concept of conventional droop method. Proposed droop method is described in Section-3. Sections 4-6 give simulation results and discussion.

II. THE CONCEPT OF DROOP CONTROL

The concept of droop control used in parallel operation of VSI's is taken from conventional power system control, where due to the system inertia, the system frequency decreases with increase in load. It is important to mention that the conventional power system has large rotating mass, so large amount of energy is stored in the form of inertia. The micro-grid, where sources are predominantly connected via power electronics interface, has almost negligible inertia. Introducing droop in power controller can emulate inertia in VSI's as in the conventional turbine-synchronous generator system.

The basic $P-\omega$ and $E-Q$ droop characteristic are shown in figure-1.

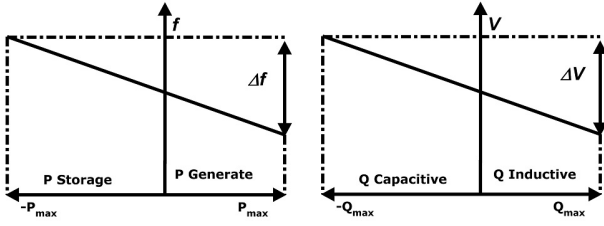


Figure 1. Conventional P/Q Droop Curves.

The active and reactive power flow from an inverter to the grid through an impedance can be expressed as [5]:

$$P = \left(\frac{EV}{Z} \cos(\delta) - \frac{V^2}{Z} \right) \cos(\theta) + \frac{EV}{Z} \sin(\delta) \sin(\theta) \quad (1)$$

$$Q = \left(\frac{EV}{Z} \cos(\delta) - \frac{V^2}{Z} \right) \sin(\theta) - \frac{EV}{Z} \sin(\delta) \cos(\theta) \quad (2)$$

where Z and θ are the magnitude and the phase of the output impedance respectively; V is the common bus voltage; δ is the phase angle between the inverter output voltage and the micro-grid voltage. There is no decoupling between P - E and Q - ω

So as to decouple the above relations, the output impedance is taken as purely inductive. $Z = X$ and $\theta = 90^\circ$.

$$P = \frac{EV}{X} \sin(\delta) \quad (3)$$

$$Q = \frac{EV}{X} \cos(\delta) - \frac{V^2}{X} \quad (4)$$

Usually the angle δ is very small. The values of $\sin \delta \approx \delta$ and $\cos \delta \approx 1$, consequently,

$$P = \frac{EV}{X} \cdot \delta \quad (5)$$

$$Q = \left(\frac{EV}{X} - \frac{V^2}{X} \right) \quad (6)$$

For small perturbations,

$$\Delta \delta \propto \Delta P$$

and similarly,

$$\Delta E \propto \Delta Q$$

from above deductions, a linear relation can be established between $\omega - P$ and $E - Q$, i.e.

$$\omega = \omega^* - m_f \cdot P \quad (7)$$

$$E = E^* - m_e \cdot Q \quad (8)$$

The equations (7-8) represent conventional droop method, where E is the amplitude of the inverter output voltage; ω is the frequency of the inverter; ω^* and E^* are the frequency and amplitude of inverter voltage at no-load respectively; m_f and

m_e are the proportional droop coefficients of frequency and voltage.

It is observed that droop coefficients largely affect the stability of the system. The increasing value of Q -droop coefficient of the system results into shifting of the real poles (zero frequency) to the right side of the imaginary axis in complex plane while increase in ω -droop coefficient causes low frequency poles to travel into unstable region[9]. Therefore, the higher coefficient values is avoided for stability reason. But the value of coefficient within the permissible limits may have following effects:

- 1) High value of droop coefficient, means low inertia and hence contribution to the stability for the whole system is low. However, the power sharing is very precise with long settling time.
- 2) Lower value of droop, can be treated as high inertia system, with almost isochronous behaviour. It provides faster to balance the power demand-supply. However, at the same time the power sharing among the inverter may not be precise.

III. PROPOSED DROOP CONTROL

To achieve better dynamic response, additional derivative terms in linear droop has been reported [6].

With the derivative term, the droop equations can written as :

$$\omega = \omega^* - m_f \cdot P - n_f \cdot \frac{dP}{dt} \quad (9)$$

$$E = E^* - m_e \cdot Q - n_e \cdot \frac{dQ}{dt} \quad (10)$$

Integration of equation (9) leads to,

$$\int \omega dt = \int \omega^* dt - m_f \int P dt - n_f \int \frac{dP}{dt} dt$$

or

$$\theta = \omega^* t - m_f \int P dt - n_f P$$

the above equation can be bifurcated as constant frequency and instantaneous phase ($\theta = \omega^* t + \phi$), where

$$\phi = -m_f \int P dt - n_f P \quad (11)$$

The coefficients m_f and n_f represents the proportional and derivative terms of PD regulator respectively.

To achieve improved performance from droop coefficient m_f , one must take care of the following points:

- 1) It must be modified in such a way that overloading of inverter can be prevented in peak load. This will avoid the frequent tripping of inverters due to its protection scheme. At the same time the contribution of other sources to deliver demanded power should increase.
- 2) Below the rated load, the value of m_f must be low in order to achieve maximum contribution in stabilizing the overall system, Whereas the inverter can be utilized up

to its rated valve rating to share instantaneous power and meeting out load demand rapidly.

Thus, from above reasoning, It is clear that the coefficient must be proportional to power, therefore

$$m_f \propto P$$

$$m_f = m_{fp}P \quad (12)$$

Where m_{fp} represents the a new proportionality coefficient, and accordingly the equation (7) can be modified as,

$$\omega = \omega^* - m_{fp}P^2 \quad (13)$$

The plots between ω and P based on conventional and modified droop characteristics have been shown in figure-2, for 5kW, 50 Hz with droop in frequency of 1 Hz. For better understanding of the proposed method, the new droop characteristics has been divided into three zone; Isochronous, linear and steep droop zone. In isochronous zone, the frequency do not vary too much w.r.t output power, and hence in this region inverter can share more power than with conventional method. Moreover, in this zone the inverter is always expected to be loaded upto the most served power. This may be beneficial in the case of renewable energy sources (RES), where this power is generally available. During steep zone, frequency drop will be very rapid (while normal loading is although higher than conventional) so the overloading of the inverter could be avoided.

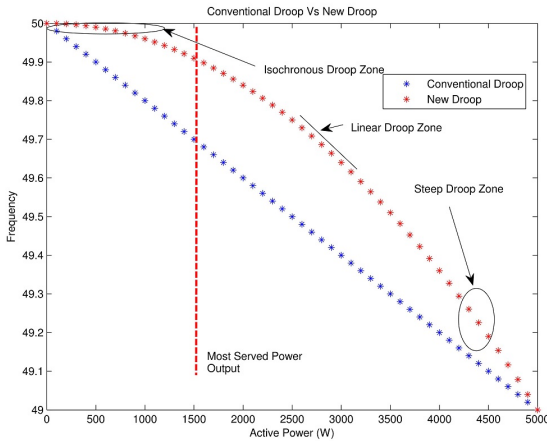


Figure 2. Conventional and Proposed Droop Method

a) Calculation of the new droop coefficient, m_{fp} : The m_{fp} coefficient can be taken as,

$$m_{fp} = m_f / P_{max}$$

rewriting equation (10)

$$\omega = \omega^* - m_{fp}.P^2 - n_f \frac{dP}{dt} \quad (14)$$

Now, the derivative term in equation (14) will help in settling down the response rapidly. The constant coefficient n_f also can be improved by making it proportional to power P , doing

this will provides variable coefficient, which increases linearly when power output increase. Therefore, at maximum power output it provides faster response during rapid power changes. It will cause better tracking of steep droop.

Now replacing n_f with $n_{fp}.P$ and integrating equation (15),

$$\phi = -m_{fp} \int P^2 dt - n_{fp} \frac{P^2}{2} \quad (15)$$

The value of n_{fp} must be such that the phase shift caused by square term should not become too high.

In this work, it has been taken as $\frac{n_f}{2 \cdot P_{max}^2}$ so that at higher output power, the maximum phase drift remains within limit.

Similarly, Q droop can be written as,

$$E = E^* - m_{eq}.Q^2 - n_{eq}.Q \cdot \frac{dQ}{dt} \quad (16)$$

where,

m_e and n_e is replaced by $m_{eq}.Q$ and $n_{eq}.Q$

$m_{eq}, n_{eq} = \text{Constant}$, can be taken equal to $\frac{m_e}{Q_{max}}$ and $\frac{n_e}{2 \cdot Q_{max}^2}$ respectively.
 $P_{max}/Q_{max} = \text{Rated active / reactive power.}$

The dynamic coefficients of droop controller will provide different effective droop gradient upon loading conditions. In simulation, the proposed method has been applied to frequency droop only.

IV. SIMULATION

Simulation of the proposed scheme is performed in MATLAB/SIMULINK. The block diagram of the system is shown in figure-3

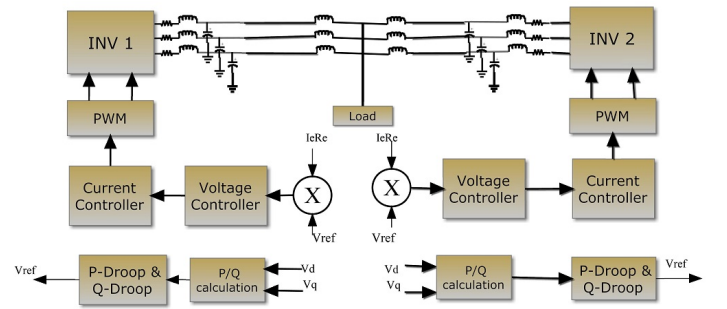


Figure 3. Block Diagram of Controller's of Parallel Operating Inverters

The measured value of three phase voltages and currents are converted into DC quantity by $dq0$ transformation. Proportional plus Integral control type voltage and current controller has been implemented for inner loops [8]. The virtual resistor has been used for passive damping by considering equivalent drop in reference voltage proportional to filter capacitor current. This proportional value is termed as a constant K_c in ohm. All measured quantity are essentially local and are taken from PCC and the inverter output. Both the inverters are 3-phase 3-level VSI, having LC filter at output. System has been designed for 50 Hz, 230 V_{l-l}. All other system parameters are given in table-1.

The tie line has been taken as three phase series inductance (no coupling effect) with very low value of inductance. There

are few local loads attached to each inverter so that inverters must be loaded to some value before sharing any power. A three phase circuit breaker is used in simulation to connect them instantaneously when required.

Parameter	Inverter 1 and 2
Switching Frequency	5kHz
Filter series Inductance(L_f)	3.2mH
Filter shunt capacitance(C_f)	35 μ F
Filter series Inductor's ESR	0.2 Ω
Filter shunt capacitor ESR	0
Cornor frequency filter (ω_c)	2990 rad/s
Voltage controller Proportional gain(K_{pv})	0.5
Voltage controller Integral gain(K_{iv})	336
Current controller Proportional gain(K_{pc})	8.7
Current controller Integral gain(K_{ic})	1609
Virtual Resistance(K_c)	0.8 Ω
DC link Voltage(V_d)	500V
F-Droop Proportional gain (m_p)	$1e^{-4}$
V-droop Proportional gain(n_p)	$0.8e^{-3}$
m_{fp}	$1e^{-4}/5000$
n_{fp}	$1e^{-4}/2*25e^6$
m_{ep}	—
n_{ep}	—

Table I
SYSTEM PARAMETERS

V. RESULTS AND DISCUSSION

A. Power Sharing with Same Droop Characteristics

To show power sharing capability of the proposed method, inverter-2 is connected to inverter-1 at 0.12 sec of simulation time. Initially, as inverters are not synchronized there would be a phase and amplitude difference between both the inverter voltages which causes high power swing between them as is observed in figures-4 and 5.

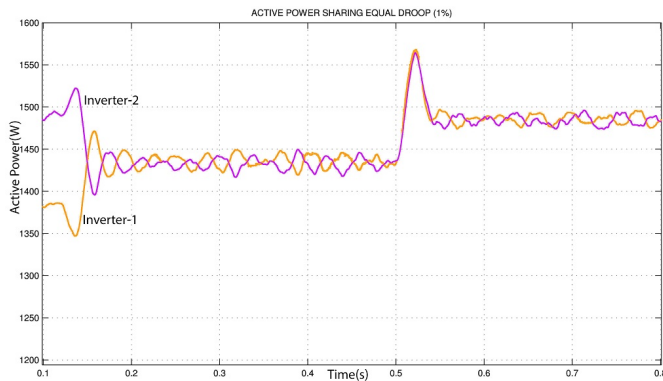


Figure 4. Active Power Sharing Between both Inverter by Proposed Method

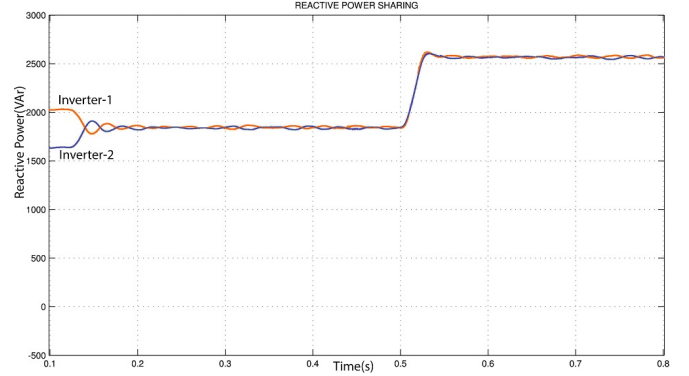


Figure 5. Reactive Power Sharing Between both Inverter by Proposed Method

Again with the increase in load at 0.5 sec, the power is equally shared by both the inverters with good precision as shown in figure-5.

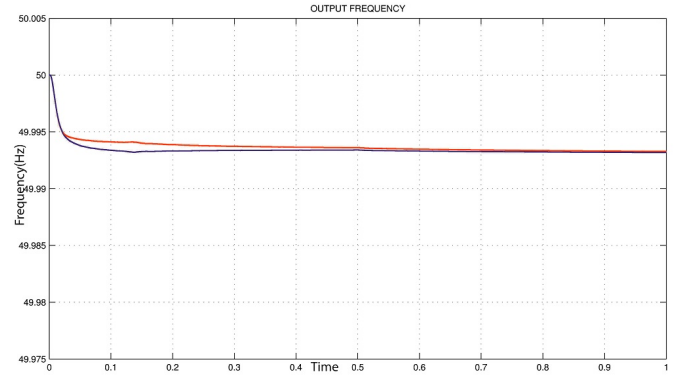


Figure 6. Inverter Frequencies in Proposed Method

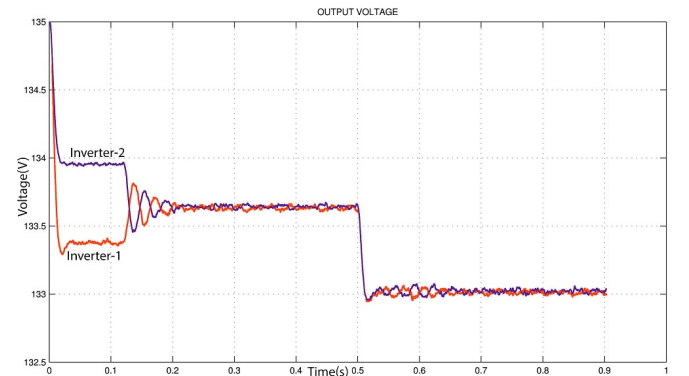


Figure 7. Inverter Voltages in Proposed Method

From figures-6 and 7, it is clear that the frequency and voltage has been controlled upto rated value. The deviation in system voltage and frequency are the main power quality issues which can be improved by the proposed method.

B. Power Sharing with Different Droop Characteristics

To show the effectiveness of the proposed method, the inverter-1 is controlled using proposed droop controller while

Inverter-2 by conventional droop controller. The main purpose of the proposed control approach is to load the inverter upto its maximum capacity during light load conditions and also to prevent the inverter from overloading during peak load conditions. It can be easily made out from figures-8 and 9, at low power demand inverter -1 shares more power than the inverter-2, while, during peak load the inverter with conventional droop control shares power beyond its rated capacity and inverter -1 with the proposed method is restricted to the rated capacity. Further, the system with proposed droop control technique settles down quickly during load perturbations.

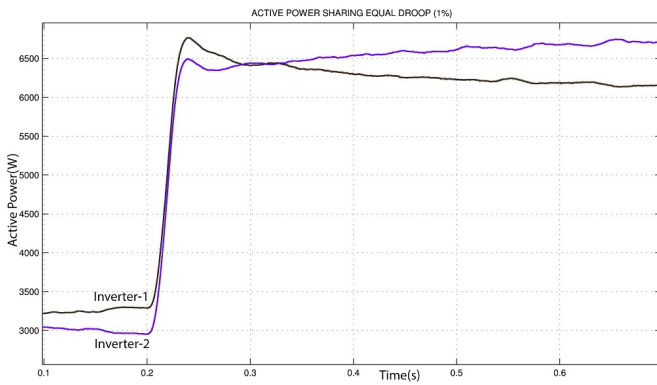


Figure 8. Active Power Sharing of the Inverters

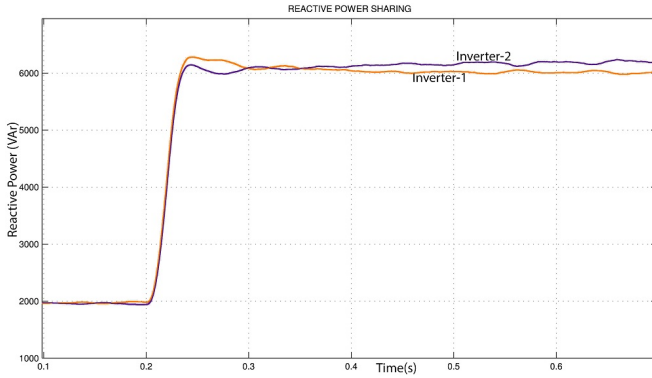


Figure 9. Reactive Power Sharing of the Inverters

VI. CONCLUSION

The proposed droop controller has various advantages over conventional droop method. The modification in droop characteristics shows its ability to provide better regulation of frequency and voltage with fast and precise dynamic response. With low output power, the frequency regulation is almost isochronous in nature, providing fast transient sharing of power while at high output power, reduction of overloading has been observed. The proposed droop characteristic can be applied to PV type sources which can normally produce power below their rated capacity. Hence, in design one can choose this output as operating point accordingly and assign droop coefficients in such a way that the inverter provides desired regulation of frequency at this operating point.

REFERENCES

- [1] Chris Marnay et al, "Polymaking of Microgrids, Economic and Regulatory Issue of Microgrid Implementation", IEEE Power and Energy Magazine, May/June 2008.
- [2] Takao Kawabata, et.al, "Parallel Operation of Voltage Source Inverters", IEEE Transactions on Industry Applications, vol. 24. no. 2, pp 281-287, March/April 1988.
- [3] M.C. Chandorkar, et.al, "Novel Architectures and Control for Distributed UPS Systems", IEEE Applied Power Electronics Conference and Exposition, pp 683-689, 1994.
- [4] Joachim Holtz, et.al "Multi-Inverter UPS System with Redundant Load Sharing Control", IEEE Transactions on Industrial Electronics, vol.31, no.6, pp 506-513, December 1990.
- [5] Mukul C. Chandorkar, et.al, "Control of Parallel Connected Inverters in Standalone AC Supply Systems", IEEE Transactions on Industry Applications, vol.29, no.1, pp 136-143, January/February 1993.
- [6] Anil Tuladhar, et.al, "Control of Parallel Inverters in Distributed AC Power Systems with Consideration of Line Impedance Effect", IEEE Transactions on Industrial Applications, vol.36, no.1, pp 131-138, January/February 2000.
- [7] Josep M. Guerrero, et.al, "A Wireless Controller to Enhance Dynamic Performance of Parallel Inverters in Distributed Generation Systems", IEEE Transactions on Power Electronics, vol. 19, no.5, September 2004.
- [8] Wei Yao, et.al, "An Improved Multiple-loop Controller for Parallel Operation of Single-phase Inverters with no Control Interconnections", IEEE Power Electronics Specialists Conference, pp 448-452, 2007.
- [9] Nagaraju Pogaku, et.al, "Modeling, Analysis and Testing of Autonomous Operation of an Inverter-Based Microgrid", IEEE Transactions on Power Electronics, vol. 22, no. 2, 2007.
- [10] Josep M. Guerrero, et.al, "Control Strategy for Flexible Micro grid Based on Parallel Line-Interactive UPS Systems", IEEE Transactions on Industrial Electronics, vol.56, no. 3, pp 726-736, March 2009.
- [11] Xiaonan Lu, et.al, "SoC-Based Droop Method for Distributed Energy Storage in DC Microgrid Applications", IEEE International Symposium on Industrial Electronics (ISIE), pp 1640-1645, 2012.

A Review on Feasibility of Conventional Fluoride Removal Techniques in Urban Areas

Tarundeep Gill, Shashi Tiwari and P. Albino Kumar

*Department of Environmental Engineering,
Delhi Technological University, Delhi 110042.*

Abstract

Present study was carried out to evaluate the feasibility of conventional rural based defluoridation technique - Nalgonda technique, Activated alumina in urban areas. Nalgonda technique is being used extensively due to ease in construction of the reactor, operation & maintenance. This technique is very effective even when the fluoride concentration is above 20 mg/L. However, generation of acid or alkali water, residual aluminum, soluble aluminum fluoride complexes and fluoride contaminated sludge limits its practical applications. Above this, leakage of sulphate as aluminium sulphate with concentration as high as 400 mg/L in treated water, makes it un-potable and caused pitting effect on RCC reservoir/reactor or container. Cement paste is also employed for effective removal of F^- due to high concentration of Ca^{2+} and additional adsorption of the remaining F^- into amorphous calcium phosphate. However lime creates the problem of hardness of effluent water and co-precipitation particle of CaF_2 are too fine to be sedimented without coagulation. Limitation of CaF_2 precipitation also includes its inability to reduce F^- concentration of less than 10- 20 mg/L against permissible limit of 1.5 mg/L. Activated Alumina though showed effective removal of fluoride, slow rate of adsorption, pH adjustment, accumulation of bacteria in the long run inhibits its commercial application. Also sludge generation is one of its main drawbacks. Application of these conventional techniques in urban areas will lead to generation of large amount of fluoride sludge which creates another issue of solid waste management. It will be advisable to set up decentralized locality based fluoride removal treatment unlike high capacity water treatment in urban areas.

Keywords: Defluoridation, Nalgonda technique, Activated alumina, Co-Precipitation.

1. Introduction

Fluorine is the most highly reactive element and exists in water mainly as fluoride ion. Fluoride is highly toxic and is considered as an accumulative toxin (Pillai and Stanley 2002). It is present in ground water coming either from natural sources like weathering and volcanic processes or from wastewater of industries like fertilizer, glass, ceramics, brick, iron works and electroplating (Nigussei et al., 2007). Fluoride has both beneficial and harmful effects on the human health depending upon its level. Among the beneficial effects of fluoride in human body, strengthening of bones and prevention from tooth decay are significant (Fawell et al., 2006). W.H.O has stated that it should be in the range of 0.1 to 0.5ppm. The Indian Standard for fluoride contents is 1 ppm. This shows that the requirement of fluoride content changes and it depends on the geographical condition and the age of human beings. Excess fluorides in drinking water cause dental fluorosis and/or skeletal fluorosis. Removal of fluoride from drinking water, defluoridation, is normally accomplished by adsorptive (including ion exchange) and precipitation processes. Nalgonda Technique was developed by National Environmental Engineering Research Institute (NEERI), Nagpur, India (Bulusu et al., 1979), which involves, the addition in sequence, of an alkali, chlorine and aluminium sulphate or aluminium chloride or both; followed by settling and filtration. Adsorption is also a method used for removal of fluoride in which materials like activated carbon, activated alumina, bone char, or ion-exchange resins are used as adsorbents (McKee and Johnston, 1934). Presently several methods have been practised to remove fluoride from drinking water, however in urban, the application of these techniques has certain drawbacks at the time of implementation.

2. Materials and Method

In the process of Nalgonda Technique, alum (aluminium sulphate) and lime (calcium oxide) are added to and rapidly mixed with the fluoride contaminated water. Induced by a subsequent gentle stirring, “cotton wool”-like flocs develops (aluminium hydroxides) and is subject to removal by simple settling. The main contents of the fluoride are removed along with the flocs through combination of sorption and ion exchange with some of the produced hydroxide groups (Dahi et al., 2006). Activated alumina for defluoridization through adsorption involves preparation at low temperature dehydration. The fluoride uptake capacity of activated alumina depends on the specific grade of activated alumina, the particle size and the water chemistry (pH, alkalinity and fluoride concentrations) (Ganesh et al., 2006; Kumar and Gopal 2000). Bone char used for defluoridation involve sieving of bone char to the average particle diameters of 0.65, 0.79 and 1.29 mm, then washing it with deionized water, drying in a furnace at 100° C for 24 h and stored in plastic containers. The concentration of fluoride in an aqueous solution was determined by a potentiometric method.

3. Results and Discussion

Nalgonda techniques, activated carbon, bone char methods used for defluoridation of water are used basically in rural areas, which is community based. Nalgonda process did not achieve a great degree of success in field application as it removes only a smaller portion of fluoride (18–33%) in the form of precipitates and converts a greater portion of ionic fluoride (67–82%) into soluble aluminium fluoride complex ion, and therefore this technology is erroneous. Adoption of Nalgonda technique for defluoridation of water is not desirable due to use of aluminium sulfate as coagulant, the sulfate ion concentration increases tremendously and in few cases, it crosses the maximum permissible limit of 400 mg/L, which causes cathartic effect in human beings. The residual aluminium in excess of 0.2 mg/L in treated water causes dangerous dementia disease as well as pathophysiological, neurobehavioural, structural and biochemical changes. It also affects musculoskeletal, respiratory, cardiovascular, endocrine and reproductive systems. On household scale it is introduced in buckets or drums and at community. For larger communities a waterworks-like flow system is developed, where the various processes of mixing, flocculation and sedimentation are separated indifferent compartments.

Defluoridation using Activated Alumina (AA) has been one of the widely used adsorption/ ion exchange methods water and many reports are available on large-scale installations for townships, requiring supervision and skilled personnel. The quality of treated water from such facilities was assured. However, this approach was not immediately feasible because of increase hardness and surface loading (the ratio of total fluoride concentration to activated alumina dosage). The process is highly selective and is pH specific with low adsorption capacity, poor physical integrity, requires acidification and pretreatment and its effectiveness for fluoride removal reduces after each regeneration.

Bone char, though cost effective with a defluoridation percentage of 62 to 66%, still poses limitations such as harbors of bacteria and hence unhygienic conditions. Without a regular fluoride analysis, nothing indicates when the material is exhausted and the fluoride uptake is ceased. Moreover, the use of bone-char will have psychological effects on consumers. In urban areas, peoples generally use R.O techniques to maintain the fluoride from groundwater source but it proves costly. Thus, these conventional techniques are not that much suitable for the urban areas, we need such a technique having economical cost and easily accessible.

4. Conclusion

The literature survey has indicated that each of the discussed techniques can remove fluoride under specified conditions. The fluoride removal efficiency varies according to many site-specific chemical, geographical and economic conditions, so actual applications may vary from the generalizations made. Any particular process, which is suitable at a particular region, may not meet the requirements at some other place. Nalgonda technique, Activated Alumina, Bone Char is suitable technique for Indian

rural communities. Thus we have to look for urban areas accessible methods for defluoridation which are economical and effective.

References

- [1] Pillai, K. S., & Stanley, V. A. (2002). Implications of fluoride-an endless uncertainty. *Journal of Environmental Biology*, 23, 81-87.
- [2] W. Nigussie, F. Zewge, and B.S. Chandravanshi, "Removal of excess fluoride from water using waste residue from alum manufacturing process", *Journal of Hazardous Materials*, vol. 147, no. 3, pp. 6954-963, 2007
- [3] J. Fawell, K. Bailey, J. Chilton, E. Dahi, L. Fewtrell, and Y. Magara, *Fluoride in drinking water*, WHO IWA Publishing, 2006
- [4] Bulusu, K.R., Sundaresan, B.B., Pathak, B.N., Nawlakhe, W.G., Kulkarni, D.N., Thergaonkar, V.P., 1979. Fluorides in water, defluoridation methods and their limitations. *J. Institute Engineers (India)- Environmental Engineering Division* 60, 1-25.
- [5] McKee, R.H., Jhonston, W.S., 1934. Removal of fluorides from drinking water. *Industrial Engineering Chemistry* 26 (8), 849-850.
- [6] Eli Dahi, Felix Mtalo, Balthazar Njau and Henrik Bregnhj. Reaching the unreached: Challenges for the 21st century. Defluoridation using the Nalgonda Technique in Tanzania. From the proceedings of 22nd WEDC Conference, New Delhi, India, 1996.
- [7] Muthu Ganesh.I, Vinodhtn.V, Padmapriya.G, Dr.K.Sathiyarayanan, Mr. P. C. Sabumon. An improved method for defluoridation. *Indian J. Environ Health*. January 2003; 45(1): 65-72.
- [8] S. Kumar and K. Gopal.A Review on Fluorosis and its Preventive Strategies. *Indian J. Environmental Protection*. June 2000;20(6):430-6.

A Simple Approach for Image Enhancement using New Power-Law Transformation Operators

Om Prakash Verma¹, Nitesh Gill², Pooja Gupta² and Megha²

¹Department of Information Technology, Delhi Technological University, Delhi, India.

²Department of Computer Science Engineering, Maharaja Agrasen Institute of Technology, Delhi, India.

opverma.dce@gmail.com, niteshgill1251@gmail.com, poojagupta.may91@gmail.com, megha.jul91@gmail.com.

Abstract— In this paper, we present a new approach for the enhancement of a highly underexposed color image using a power-law transformation operator. A function called exposure [1] is used to measure the intensity exposition of the image. This function facilitates the estimation of highly underexposed region of the given image. The chromatic information of the color space is decoupled from the achromatic information using HSV (Hue, Saturation and Intensity) model. The hue component, in the model is preserved to keep the original color composition of the image intact. The other two components of the model are saturation and intensity. These two components play a significant role in enhancement of highly underexposed images by recovering the lost information in the image. New power-law transformation operators are defined for the two components, i.e. saturation and intensity, to improve the tone of the image. The values of these two components are varied to get the enhanced image.

Index Terms— Exposure, Image Enhancement, Power-Law Operator, Highly Underexposed Image.

I. INTRODUCTION

An important consideration in image processing is the measurement of light in order quantity to describe an image. The effect of inadequate lighting, the aperture size, the shutter speed, and the nonlinear mapping of the image intensity may lead to the most common defects, found in recorded images, of poor contrast. Such type of defects in recorded images is reflected in the gray level histogram of the images. Several image enhancement algorithms exist in the spatial domain. One of these kinds is reported in [2], where the image enhancement is based on the human perception (retinex). Tao and Asari [3] extended the approach in [2], where the color saturation adjustment for producing more natural colors is implemented.

Image enhancement approaches may introduce color artifacts if directly applied to the R, G and B components of a degraded color image which is inappropriate for the human visual system. Velde [4] attempts to enhance the color image in the LUV color space. The HSV [5] color space was developed to be more “intuitive” in manipulating color and were designed to approximate the way human perceive and interpret color. In the HSV model, hue describes the shade of

color and where that color is found in the color spectrum. Saturation plays an important role in the enhancement of highly underexposed images as it describes how pure the hue is with respect to a white reference. Finally, intensity is a relative description of how much light is coming from the color. In the process of color image enhancement, the original color (hue) of the image is generally not disturbed. Hue-preserved color image enhancement is presented in [6]. Deepak and Joonwhoam [7] proposed a similar approach by working only on the luminance component of HSV color space. Gorai and Ghosh [8] also presented a hue-preserved color image enhancement in which the quality of the intensity is improved by a parameterized transformation function, in which parameters are optimized by PSO based on an objective function.

In this paper, we present an approach for enhancement of highly underexposed images. The intensity and the saturation component, in HSV model, are made variable while keeping the hue of the image fixed. A function called exposure [1] is used to provide an estimation of the intensity level of an image. This function considers the shape of the histogram of the intensity component for calculating the exposure value of the given image. Based on the exposure value, the level of underexposed region of an image can be estimated. Highly underexposed images then can be modified by power-law transformation operator. The parameters of the function are adjusted to make them applicable to a particular type of degradation in the image. Eschbach and Webster [9] proposed a method for altering the exposure of an image, by iteratively comparing the intensity with a pair of preset thresholds T_{light} and T_{dark} , which indicate the satisfactory brightness and darkness, respectively, while processing the image until the threshold conditions are satisfied. Shyu and Leoua [10] present a better approach based on Genetic Algorithms (GAs) for the color image enhancement. In the context of image processing, only a few papers address the issue of highly underexposed images. Hanmandlu and Jha [11,12] used a global contrast intensification (GINT) operator, which is an extended NINT operator for the enhancement of the luminance part in the fuzzy domain, and also propose the quality factors. The parameters of this operator are found by

optimizing the image entropy. This approach works well for underexposed images but fails for highly underexposed images. A novel approach for the enhancement of mixed exposed color images using an optimal fuzzy system and Bacterial Foraging Optimization (BFO) is presented in [1]. Another approach is proposed using modified Artificial Ant Colony System (AACS) in [13]. In comparison, the proposed approach is found to be simple and better than the above approaches. The major drawback of both the above approaches is that they work well for mixed exposed images but fails to enhance highly underexposed images. Thus we define a simple technique for color image enhancement. The proposed new function is used for the enhancement of highly underexposed images and it gives very good results even before applying any optimization operations.

The organization of the paper is given as follows. Section II introduces the image categorization based on the intensity exposition of the image. This helps in identifying the (highly) underexposed images. Section III presents the proposed enhancement technique using the power-law transformation operator. The power-law transformation operator works in the underexposed region of the image histogram and improves the visual quality of the image. The results are discussed in section IV and conclusions are drawn in section V.

II. IMAGE CATEGORIZATION BASED ON INTENSITY EXPOSITION OF IMAGE

The histogram is used to graphically characterize the images. When an image is exposed correctly the histogram of its pixel intensity values will seem fairly centered in the mid-range and expanded at all intensity levels. Badly exposed images, on the other hand, will have a histogram skewed to one side and its mean can be centered in the limits of the pixel range.

Here, we use a function called exposure proposed in [1] for enhancement of highly underexposed images. This function denotes what amount of the image gray levels are highly underexposed. The parameter “Exposure” is used to identify highly underexposed images and is given by

$$Exposure = \frac{1}{L} \frac{\sum_{x=1}^L h(x).x}{\sum_{x=1}^L h(x)} \quad (1)$$

where, x indicates the gray level values of the image, $h(x)$ represents the histogram of the whole image, and L represents the total number of gray levels. This parameter is normalized in the range $[0, 1]$. If the exposure value is in the range of 0.1-0.3 then the image has more of underexposed region. Further if exposure value is less than 0.2 then it is a highly underexposed image. It has been found that for a pleasing image, the exposure should be as close to 0.5.

III. PROPOSED ENHANCEMENT TECHNIQUE

The HSV color space (Hue, Saturation, Value) is often used because it corresponds better than the RGB color space in how people experience color.

In the proposed approach the intensity value of the pixel is changed through the power-law transformation operator. For each pixel in the given image the modified pixels are obtained from the mappings performed by the power law transformation operator.

A. POWER LAW TRANSFORMATION

The histogram equalization method for image enhancement suffers from the fact that it may sometimes decrease the contrast. In the power law transformation one has to choose the exponent appearing in the transformation function such that it does not degrade the quality of image.

The power-law transformation is defined as

$$Y = cX^\gamma \quad (2)$$

where, X and Y are the gray level of the pixels in the output and input images, respectively and c is a constant. For various values of γ different levels of enhancements can be obtained. Figure 1 shows the plot of power law transformation with the input gray level X along the x axis and the output gray level Y on the y axis for various values of γ and constant $c = 1$.

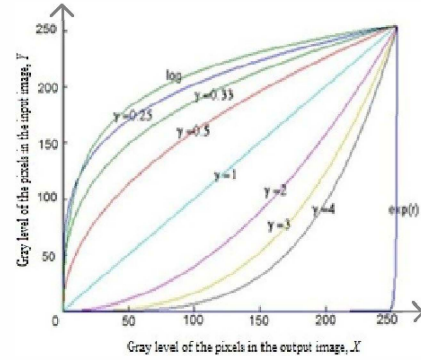


Figure 1: The plot of power law transformation

A family of possible transformation curves can be obtained just by varying the γ .

B. PROPOSED POWER-LAW TRANSFORMATION OPERATOR

In our experimentation, we propose two separate power-law transformation operators one for saturation component and other for intensity component.

The Intensity component is given as:-

$$V' = \lambda V^\beta \quad (3)$$

For the intensity component, the value of β is kept less than 1. Here V is the original intensity and V' is the transformed intensity. λ is the intensity constant.

And the Saturation component is given as:-

$$S' = \sigma S^\alpha \quad (4)$$

The value of α for this component is kept slightly more than 1 to obtain an improved quality image. S is the original saturation and S' is the transformed saturation. σ is the saturation constant.

C. ALGORITHM FOR PROPOSED TECHNIQUE

- Step 1) Input the given image and convert the image from RGB to HSV color space.
- Step 2) Compute the histogram $h(x)$ where $x \in \{V\}$. Here V is gray-level component.
- Step 3) Calculate the value of exposure using (1).
- Step 4) Based on the value of exposure identify underexposed and highly underexposed images.
- Step 5) Compute the values of intensity and saturation component using (3) and (4). Verify the values of β , λ , α , and σ respectively.
- Step 6) Now re-calculate the value of exposure for the enhanced image using (1).
- Step 7) Convert back the HSV color space image to corresponding RGB color space image.

The proposed approach has been implemented using MATLAB. Around 60 images of highly underexposed type are considered as test images. Some of the images are presented here.

The power law transformation operator provides a simple approach for the enhancement of the highly underexposed images. It is noticed from the experimentation that the value of the exposure approaches 0.5 by varying α, β, λ , and σ but pleasantness of the image is maintained when value of λ is kept 1.5 and $\beta = 0.5$ for intensity component and value of $\sigma = 1$ and $\alpha = 1.5$ for the saturation component. Thus the two power-law operators are:

$$\text{Saturation component} \quad S' = S^{1.5} \quad (5)$$

$$\text{Intensity component} \quad V' = 1.5 \times V^{0.5} \quad (6)$$

IV. RESULTS AND DISCUSSIONS

Table-1: The Exposure for different values of α/β , $\sigma = \lambda = 1$

Image	α/β Original Exposure	Enhanced exposure							
		1.5/0.6	1.5/0.5	1.5/0.4	1.5/0.3	2/0.6	2/0.5	2/0.4	2/0.3
Stage	0.0806	0.1976	0.2481	0.3139	0.4002	0.2046	0.2567	0.3248	0.4141
Bridge	0.1703	0.3148	0.3709	0.4399	0.5259	0.3152	0.3716	0.4408	0.5269
Girl	0.0184	0.0657	0.0932	0.1337	0.1951	0.0688	0.0973	0.1394	0.2028
Mall	0.0613	0.1460	0.1814	0.2268	0.2854	0.1510	0.1877	0.2346	0.2951
Sidewalk	0.1758	0.3163	0.3685	0.4330	0.5136	0.3265	0.3801	0.4465	0.5293
Board	0.0960	0.2087	0.2543	0.3114	0.3840	0.2127	0.2591	0.3176	0.3917
Snail	0.0469	0.1253	0.1619	0.2109	0.2771	0.1284	0.1660	0.2161	0.2838
Ambience	0.1638	0.2720	0.3116	0.3613	0.4246	0.2810	0.3220	0.3734	0.4389
Hills	0.1938	0.3168	0.3605	0.4154	0.4867	0.3268	0.3717	0.4280	0.5011

Table-2: The Exposure for different values of α/β , $\sigma = 1$ and $\lambda = 1.5$

Image	α/β Original Exposure	Enhanced exposure							
		1.5/0.6	1.5/0.5	1.5/0.4	1.5/0.3	2/0.6	2/0.5	2/0.4	2/0.3
Airport	0.0537	0.2027	0.2634	0.3475	0.4651	0.2142	0.2785	0.3678	0.4925
Stage	0.0806	0.2946	0.3702	0.4689	0.5980	0.3049	0.3832	0.4852	0.6182
Bridge	0.1703	0.4707	0.5544	0.6579	0.7729	0.4715	0.5555	0.6592	0.7744
Girl	0.0184	0.0970	0.1378	0.1989	0.2909	0.1013	0.1440	0.2072	0.3027
Mall	0.0613	0.2167	0.2699	0.3381	0.4264	0.2243	0.2794	0.3498	0.4409
Sidewalk	0.1758	0.4507	0.5272	0.6219	0.7380	0.4589	0.5375	0.6348	0.7538
Board	0.0960	0.3112	0.3794	0.4652	0.5738	0.3170	0.3867	0.4744	0.5852
Snail	0.0469	0.1860	0.2408	0.3144	0.4138	0.1907	0.2469	0.3222	0.4239
Ambience	0.1638	0.3941	0.4496	0.5173	0.6004	0.4061	0.4629	0.5317	0.6159
Hills	0.1938	0.4670	0.5288	0.6030	0.6906	0.4815	0.5447	0.6186	0.7023

Table-1 shows the value of exposure when α and β are varied and $\lambda = \sigma = 1$. Table-2 shows the value of exposure when α and β are varied and value of $\lambda = 1.5$ and $\sigma = 1$. For the subjective evaluation of the appearance, a few of the test images are shown in figures 2(c) to 11(c)

The proposed approach is compared with the existing BFO[1]. Table-3 shows the comparison between the

exposure obtained by using the BFO approach[1] and the proposed technique. From the table it can be seen that the exposure value for the images “Bridge”, “Girl”, “Hill” with the proposed approach is more than the BFO approach. Figures(2) to (11) shows that the proposed approach carries out the enhancement to a more pleasing level.

Table-3: Exposure comparison with BFO Approach [1]

Image	Original Exposure	Exposure using BFO[1]	Exposure using Proposed Technique
Airport	0.0537	0.2304	0.2634
Stage	0.0806	0.2612	0.3702
Bridge	0.1703	0.2644	0.5544
Girl	0.0184	0.0991	0.1378
Mall	0.0613	0.2243	0.2699
Sidewalk	0.1758	0.4513	0.5272
Board	0.0960	0.1565	0.3794
Snail	0.0469	0.1529	0.2408
Ambience	0.1638	0.3401	0.4496
Hills	0.1938	0.3977	0.5282



Figure 2: “Airport” (a) Original (b) Enhanced image using BFO (c) Enhanced Image using proposed technique

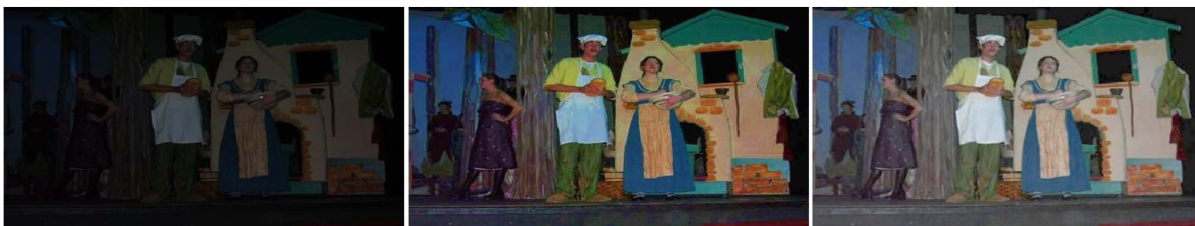


Figure 3: “Stage” (a) Original (b) Enhanced image using BFO (c) Enhanced Image using proposed technique



Figure 4: “Bridge” (a) Original (b) Enhanced image using BFO (c) Enhanced Image using proposed technique



Figure 5: “Girl” (a) Original (b) Enhanced image using BFO (c) Enhanced Image using proposed technique



Figure 6: “Mall” (a) Original (b) Enhanced image using BFO (c) Enhanced Image using proposed technique

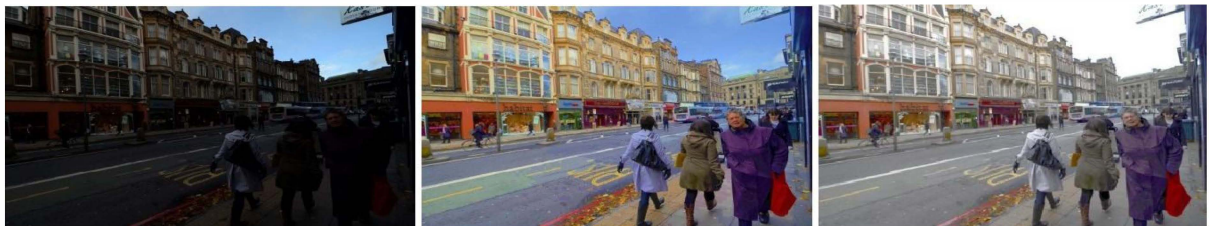


Figure 7: “Sidewalk” (a) Original (b) Enhanced image using BFO (c) Enhanced Image using proposed technique

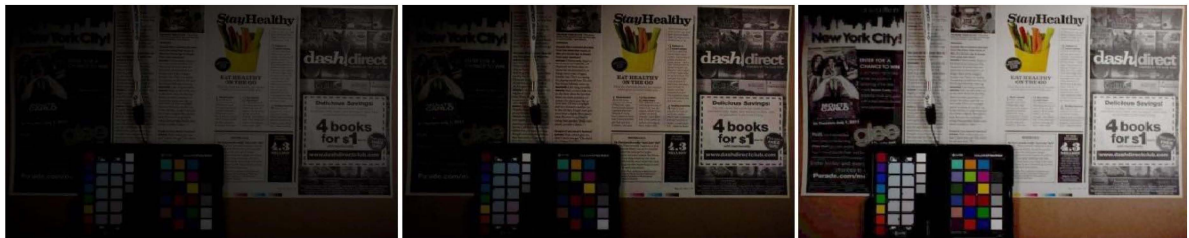


Figure 8: “Board” (a) Original (b) Enhanced image using BFO (c) Enhanced Image using proposed technique



Figure 9: “Snail” (a) Original (b) Enhanced image using BFO (c) Enhanced Image using proposed technique



Figure 10: “Ambience” (a) Original (b) Enhanced image using BFO (c) Enhanced Image using proposed technique

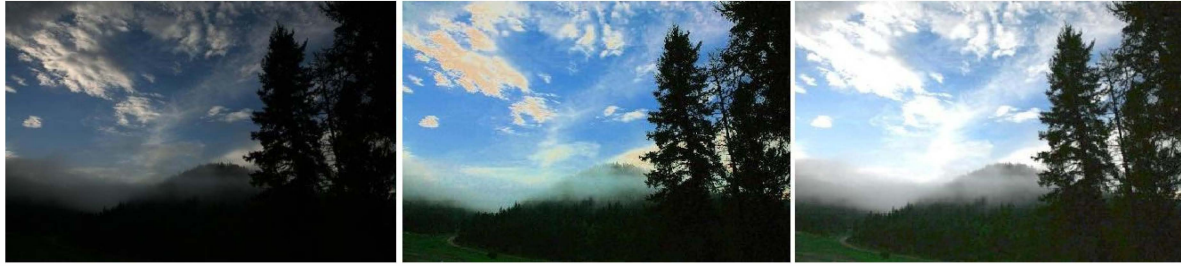


Figure 11: "Hills" (a) Original (b) Enhanced image using BFO (c) Enhanced Image using proposed technique

V. CONCLUSIONS

The objective of this paper is to come up with a new approach to enhance the highly underexposed image by using power-law transformation operator. An image may be identified as a highly underexposed image with the amount of exposure parameter. A visually pleasing image has been obtained by applying two power-law transformation operators. The result of the proposed technique has been compared with the BFO approach [1]. The proposed approach is simple and better results are obtained for highly underexposed images.

Several contributions made as part of this work include: 1) demarcation of highly underexposed image; 2) presentation of efficient operators for the enhancement of highly underexposed image, and 3) presentation and verification of effective operators to get visually appealing images.

REFERENCES

- [1] Madasu Hanmandlu, Senior Member, IEEE, Om Prakash Verma, Nukala Krishna Kumar, and Muralidhar Kulkarni, "A Novel Optimal Fuzzy System for Color Image Enhancement Using Bacterial Foraging" in *Instruments and Measurement*, IEEE Transactions, Aug 2009, vol. 58, issue: 8, pp. 2867-2879.
- [2] Z. Rahman, D. J. Jobson, and G. A. Woodell, "Multi-scale retinex for color image enhancement" in *Proc. IEEE Int. Conf. Image Process*, 1996, vol. 3, pp. 1003-1006.
- [3] L. Tao and . Asari, "Modified luminance based MSR for fast and efficient image enhancement" in *Proc. IEEE 32nd AIPR*, 2003, pp. 174-179.
- [4] K.V. Vekle, "Multi-scale color image enhancement," in *Proc. IEEE Int. Conf. Image Process*, 1999, vol. 3, pp. 584-587.
- [5] R.C. Gonzalez, R.E. Woods, *Digital Image Processing*, Addison-Wesley, Reading, MA, 1992.
- [6] S. K. Naik and C. A. Murthy, "Hue-preserving color image enhancement without gamut problem" in *IEEE Trans. Image Process*, Dec. 2003, vol. 12, no. 12 pp. 1591-1598.
- [7] G. Deepak, L. Joonwhoam, "Color image enhancement in HSV space using nonlinear transfer function and neighborhood dependent approach with preserving details" in *4th Pacific-Rim Symposium on Image and Video Technology*, 2010, pp. 422-426.
- [8] A. Gorai, A. Ghosh, "Hue-Preserving Color Image Enhancement Using Particle Swarm Optimization (PSO)" in *Recent Advances in Intelligent Computational Systems (RAICS)*, 2011 IEEE, Sep 2011, pp. 563-568.
- [9] R. Eschbach and N. Y. Webster, "Image-dependent exposure enhancement" Patent number 5414538, May 9, 1995. U.S. patent [19].
- [10] M. Shyu and J. Leoua, "A genetic algorithm approach to color image enhancement" *Pattern Recognit.*, Jul. 1998, vol. 31, no. 7, pp. 871-880.
- [11] M. Hanmandlu, D. Jha, R. Sharma, "Color image enhancement by fuzzy intensification" *Pattern Recognit. Lett.* 24 (2003), pp. 81-87.
- [12] M. Hanmandlu and D. Jha, "An optimal fuzzy system for color image enhancement," *IEEE Trans. Image Process*, Oct. 2006 vol. 15, no. 10, pp. 2956-2966.
- [13] Om Prakash Verma, Puneet Kumar, Madasu Hanmandlu, Sidharth Chhabra, "High dynamic range optimal fuzzy color image enhancement using Artificial Ant Colony System" *Applied Soft Computing* 12 (2012), pp. 394-404.

An Adaptive Single Seed Based Region Growing Algorithm for Color Image Segmentation

Puneet Kumar Jain

Center of Excellence in Information and Communication
Technology
Indian Institute of Technology Jodhpur
Jodhpur, India
puneetecb@gmail.com

Seba Susan

Department of Information Technology
Delhi Technological University
Delhi, India
Seba_406@yahoo.in

Abstract— In this paper an adaptive single seed based region growing algorithm (ASSRG) is proposed for color image segmentation. The proposed method starts with the center pixel of the image as the initial seed. The region growing formula uses three homogeneity criteria local, global and relative, in two steps to label the pixel to a region. It first checks for the color similarity of the pixel with respect to the connected labelled pixel and secondly with the mean value of a growing region. If the similarity criterion is fulfilled then this pixel is included in the growing region. Otherwise the similarity of the pixel with respect to its 8-neighbors is compared with respect to the mean value of a growing region. If the pixel is closer to the growing region as compared to its neighbors then it is included in the growing region, otherwise it is labelled as boundary pixel. After one region is completely grown, the next seed pixel is selected from the boundary pixel stack. Region merging is performed to reduce over segmentation in the results. We have applied our algorithm to Berkley images with successful results and the evaluation of the segmented images has been done using Liu's F-factor, total number of regions segmented and time taken by the algorithm. A fuzzy rule based modification of the algorithm is also proposed to further improve results. The proposed algorithm is also compared with SSRG algorithm using Otsu's threshold, SRGRM algorithm and MRG region growing techniques and is shown to outperform all methods.

Keywords— Color image segmentation, Single seeded region growing, Liu's F-factor, Fuzzy rule based region growing, region growing formula.

I. INTRODUCTION

Image segmentation is a technique to partition a given image into a finite number of non overlapping regions using some characteristics of the image, such as grey value distribution, texture distribution, etc. [1]. Automatic image segmentation and object extraction are critical issues in computer vision applications, which led to the proposal and development of a large number of segmentation techniques. Image segmentation techniques are classified into two main categories [2]. One is region based [3,4,5], which relies on the homogeneity of spatially localized features, whereas the other is non-region based which uses discontinuity measures [6,7,8,9] and do not consider local information such as regions similarity, boundaries and smoothness. Region growing was proposed by Adams and Bischof [10] in 1994. Due to efficient results for realistic images, it is used widely in different

applications [11,12,13]. In recent works edge extraction and seeded region growing was integrated to enhance segmentation accuracy [14,15,16]. Moigne and Tilton develop an Iterative Parallel Region Growing algorithm (IPRG) [17].

In Iterative region growing [17,22], pixels are merged to optimize an objective function in each iteration. The 3D relaxation labeling technique is used for region segmentation by Cheng [23]. Dehmeshki et al. [24] proposed adaptive sphericity oriented contrast region growing based on fuzzy connectivity map. Trémeau and Colantoni used a combination of two structures of graph, region adjacency graph and the line graph for color image segmentation methods [25]. The algorithm proposed by Hojjatoleslami and Kruggel [21] involves a gray level similarity criterion to expand the region and a size criterion to prevent from over-growing. Hojjatoleslami and Kittler [26] use average contrast and peripheral contrast to control the growing phase.

Most of the region growing methods result in over segmented images. Merging phase is used to overcome this problem in which small regions are merged to produce desired output. In most of the merging algorithms small regions are merged to the closest connected region based on some similarity criteria [12,27]. Chang and Li [11] adaptively assess region homogeneity from region feature distributions to decide merging of regions.

To enhance the capability of region growing algorithms, we propose a new adaptive single seed based region growing algorithm for color image segmentation, which starts with the center pixel of the image as the initial seed. Most of the region growing techniques do not produce efficient results because they only take into account local homogeneity relationship. As they do not integrate global relationships between region and pixel, they do not perform well. To incorporate both local and global relationships, the proposed algorithm uses three homogeneity criteria calculated with respect to connected labelled pixel, mean value of the growing region and similarity to its 8-neighbors. We also fuzzify the proposed algorithm to improve results. A single seed based region growing (SSRG) algorithm using the Otsu's threshold as the growing criteria was proposed by the authors in [30], and serves as a precursor to the work done in this paper.

The paper is organized as follow: Section II discusses the problems of existing region growing methods and the motivation for the proposed method. In Section III we present the proposed ASSRG algorithm. Section IV depicts fuzzy version of the proposed algorithm. In Section V segmentation results of the proposed algorithm and comparisons with SSRG algorithm using Otsu's threshold and two other methods are discussed. Section VI draws the conclusion from the overall results.

II. THEORETICAL BACKGROUND

The key factors which affect the region growing techniques are positions of the initial seeds, the region growing formula and the growing sequence of the seeds. Region growing methods typically start with the initialization of seeds which are grown by linking the neighboring pixels according to the growing formula, until all pixels are labelled. In [14] edge detection is performed first and then the centroid between two edges is selected as initial seed. Cui et al [18] adopt the Harris corner detector to calculate the initial seed. Watershed algorithm is used to select initial seeds by Tang [19]. Huang et al. [20] used edge and smoothness factors as criteria to determine initial seeds. But seed selection is affected by the limitations of the techniques used and increases the computation overhead.

Another factor, on which region growing methods depend, is growing formula. Initial seeds grow by integrating their neighborhoods which fulfil some similarity criteria [12, 21] which is either determined heuristically or from some simple algorithm like Otsu's adaptive threshold technique. The region growing formula should be capable of fulfilling the following homogeneity criteria:

- Pixels must be homogeneous with respect to some properties, inside one region.
- Pixels must have distinct properties with respect to pixels from other region.

Region growing formula should also be time efficient and able to segment a wide range of images.

Proposed algorithm uses three homogeneity criteria to segment an image efficiently with the above requirements. We consider that a pixel could be associated with a region R_i if

- 1) It is similar enough to connected pixel belonging to the region R_i .
- 2) It is similar enough to the mean value of the region R_i
- 3) It is more similar to the mean value of the region R_i than to its 8-neighbors.

These criteria have been applied in two steps in our algorithm. If the first two criteria are fulfilled by the pixel then it is labelled to growing region otherwise third one is analysed.

III. PROPOSED ADAPTIVE SINGLE SEED BASED REGION GROWING ALGORITHM

In the first step of the proposed ASSRG algorithm image I is read in RGB color space. Then center pixel of the image is selected as the initial seed to start the region growing phase. The region growing phase starts with analysing intensity values of neighbors of seed pixel in RGB space. $[I_{x,y}]_{R, G, B}$ represents

intensity value at coordinates (x,y) in image I in RGB color space. $MEAN_{RC}$ represent the mean intensity value of pixels labelled with RC region. RC is a counter used to label the pixels of a region which is growing. Region growing formula uses Euclidean distance between intensity values of pixels in RGB space to determine similarity index. It first checks for similarity of pixel (m, n) to be labelled with connected pixel (x, y) and with mean value of the growing region ($MEAN_{RC}$). If the similarity criterion is fulfilled then the pixel is included in the growing region and labelled with RC. Otherwise the similarity of the pixel with respect to its 8-neighbors is compared with respect to the mean value of the growing region. If it is closer to growing region as compared to its 8-neighbors then it is included in the growing region, otherwise this pixel (m, n) is labelled as boundary pixel. After one region is completely grown, the next seed is selected from the boundary pixel stack. We select intensity value 10 for similarity criterion between pixel and connected labelled pixel and intensity value 50 for similarity criterion between pixel and mean value of the growing region based on many experimental trials.

Algorithm: ASSRG

STEP 1: Read color image $I(R \times C)$.

STEP 2: Initialization step

- Select initial seed pixel (x, y) as :
 $x = R/2; y = C/2;$
- Initialize a counter to track the region number of the region which is growing.
 $RC=1;$

STEP3: Assign initial mean value of region RC as:

- $[MEAN_{RC}]_{R, G, B} = [I_{x,y}]_{R, G, B}$.
Where $I_{x,y}$ represent intensity value in the image I at coordinates (x, y) .

STEP 4: Examine the 8-neighbors of the seed pixel (x,y) one by one in a window $I_{MN}(3 \times 3)$ with center pixel (x,y) labelled with region number RC and let pixel (m,n) represent one of the 8-neighbors at a time:

If pixel (m, n) not labelled with any region number then

Calculate distance between center pixel and neighbor pixels for all three R, G and B color space as:

$$[DIST1_{m,n}]_{R,G,B} = [DIST(I_{m,n} - I_{x,y})]_{R,G,B}$$

$$[DIST2_{m,n}]_{R,G,B} = [DIST(I_{m,n} - MEAN_{RC})]_{R,G,B}$$

$$DIST(f(x+i, y+j), f(x, y)) = \sqrt{(f(x+i, y+j) - f(x, y))^2}$$

Where

STEP 5: if $[DIST1_{m,n}]_R < 10$ and $[DIST1_{m,n}]_G < 10$ and $[DIST1_{m,n}]_B < 10$ AND $[DIST2_{m,n}]_R < 50$ and $[DIST2_{m,n}]_G < 50$ and $[DIST2_{m,n}]_B < 50$, then

- Label pixel (m,n) with RC and update $[MEAN_{RC}]_{R,G,B}$.

- Store pixel (m, n) in PG(Pixel to Grow) stack.

Else

- Calculate minima as:

$$[MINIMA]_{R,G,B} = [\text{minimum}\{S\}]_{R,G,B}$$

where S is a set created by 8-neighbors from the Center pixel as:

$S = \{I_{m,n} - I_{m-1,n-1}, I_{m,n} - I_{m-1,n}, I_{m,n} - I_{m-1,n+1}, I_{m,n} - I_{m,n-1},$
 $I_{m,n} - I_{m,n+1}, I_{m,n} - I_{m+1,n-1}, I_{m,n} - I_{m+1,n}, I_{m,n} - I_{m+1,n+1}\}$
 If $[(I_{m,n} - \text{MEAN}_{RC}) < \text{MINIMA}]_R$ and
 $[(I_{m,n} - \text{MEAN}_{RC}) < \text{MINIMA}]_G$ and
 $[(I_{m,n} - \text{MEAN}_{RC}) < \text{MINIMA}]_B$ then

- Label pixel (m, n) with RC and update $[\text{MEAN}_{RC}]_{R,G,B}$
 - Store pixel (m,n) in PG stack.
- Else
- Label pixel (m, n) as the boundary pixel and store in BP (Boundary Pixel) stack.

STEP 6: Repeat step 3-6 until all pixels of PG can be grown.

STEP 7: if BP stack is not empty

- Pick a pixel from BP, if it is labelled with some region number remove it from BP otherwise assign it as next seed pixel (x, y).
 - Update region counter RC as:
 $\text{RC} = \text{RC} + 1;$
 - Go to step 2 to grow next region RC.
- Else if BP is empty
- Go to step 8.

STEP 8: Post processing: merge small regions (less than 154 pixels) with closest connected region with respect to the mean value as explained in the POSTPROCESS procedure.

EXIT

Procedure: POSTPROCESS

STEP 1: take the output of the proposed algorithm as input.

STEP 2: repeat for all small regions (sized less than 154 pixels)

Step 2(a): find out connected regions.

Step 2(b): find out closest connected region with respect to the mean value in all three R, G and B space.

Step 2(c): Label all the elements with same as closest region and update mean value of updated region.

Exit

IV. FUZZIFICATION OF PROPOSED REGION GROWING ALGORITHM

In Fuzzy rule based adaptive single seed based region growing algorithm, step 4 and 5 of the proposed ASSRG algorithm proposed in section III in which decision is made to label pixel with same region or boundary pixel, is solved by fuzzy rule. The basic flow of the algorithm is same as proposed algorithm. The fuzzy rule is formulated as follows:

If $I_{x,y}$ and $I_{m,n}$ is VERY SIMILAR

AND

If $I_{m,n}$ and MEAN_{RC} is SIMILAR

OR

if $I_{m,n}$ and MEAN_{RC} is RELATIVELY SIMILAR

THEN

Label pixel (m,n) with same region number as growing region (RC)

ELSE

Label Pixel (m,n) as boundary pixel.

Where $I_{x,y}$ represent intensity values at coordinate (x,y) and $I_{m,n}$ represent intensity values of the immediate 8-neighbors of (x,y). MEAN_{RC} is the mean intensity value of region labelled with RC. MINIMA is the lowest difference between pixel (m, n) and its all 8-neighbors.

The fuzzy sets SIMILAR, VERY SIMILAR and RELATIVELY SIMILAR are given by

VERY SIMILAR ($I_{m,n}$):

$$FMV(I_{m,n}, I_{x,y}, 10) = \exp\left(\frac{-(I_{m,n} - I_{x,y})^2}{2(10)^2}\right) \quad (1)$$

SIMILAR ($I_{m,n}$):

$$FMV(I_{m,n}, \text{MEAN}_{RC}, 50) = \exp\left(\frac{-(I_{m,n} - \text{MEAN}_{RC})^2}{2(50)^2}\right) \quad (2)$$

RELATIVELY SIMILAR ($I_{m,n}$):

$$FMV(I_{m,n}, \text{MEAN}_{RC}, \text{MINIMA}) = \exp\left(\frac{-(I_{m,n} - \text{MEAN}_{RC})^2}{2(\text{MINIMA})^2}\right) \quad (3)$$

Where $FMV(x, \mu, \sigma)$ is the Gaussian distribution function is given by:

$$FMV(x, \mu, \sigma) = \exp\left(\frac{-(x - \mu)^2}{2\sigma^2}\right) \quad (4)$$

The standard deviation for all the three Gaussian functions is determined from the algorithm given in section III.

V. RESULTS AND DISCUSSION

To examine the efficiency of the proposed ASSRG algorithm, we applied it to 12 color images from the Berkley segmentation database [28] as shown in Fig. 1. The images are of the size either 481×321 or 321×481 . We use a system configured with Intel processor 2.63 GHz and 1 Gigabyte of RAM and the matlab2009 tool for implementation purpose. To evaluate proposed algorithm's results, we calculate a segmentation evaluation index: Liu's F-factor [29] given by:

$$F(I) = \sqrt{R} \times \sum e_i / \sqrt{A_i} \quad (5)$$

where, I is the image to be segmented, R total number of regions in the segmented image, A_i the area or the number of pixels of the i^{th} region and e_i the color error of regions. e_i is defined as the sum of the Euclidean distance of the color vectors between the original image and the segmented image of each pixel in the region. The term \sqrt{R} is a local measure which penalizes small regions or regions with a large color error. e_i indicates whether or not a region is assigned an appropriate feature (color). A large value of e_i means that the feature of the region is not well captured. In this paper, F is normalized by the size of the image and is scaled down by the factor 1/1000. The smaller the value of F, the better is the segmentation result. We also calculate time consumption by algorithm and total number of regions to evaluate our results.

Comparison methods:

We compare our proposed algorithm results with SSRG algorithm using Otsu's threshold proposed by the authors in [30] and two adaptive region growing algorithms SRGRM [20] and MRG [31].

C. Huang improvises the concept of integration of edge information to select seed regions proposed by them [32]. In this paper [20], a seeded region growing and merging

(SRGRM) algorithm for color image segmentation by automatic seed selection and region growing is proposed in the HSV color model. The non-edge and smoothness at pixel's neighbors are used as a criterion to determine the initial seeds. According to the authors, the results from their segmentation results are more accurate especially at the image boundary comparable to the automatic seeded region growing (ASRG) method proposed by Shih [33].

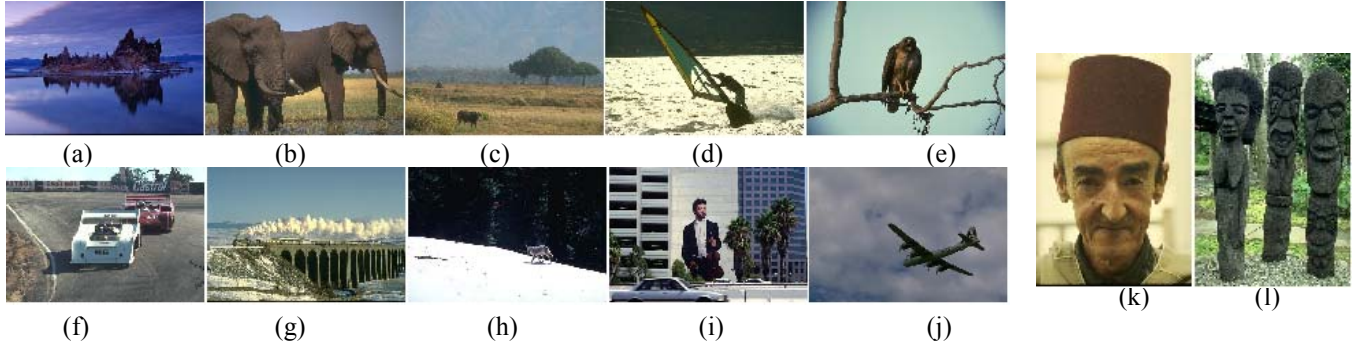


Fig. 1 Original images (a) Rock, (b) Elephant, (c) Tree and ox, (d) Man on boat, (e) Eagle, (f) F1 Race cars, (g) Bridge, (h) Fox on ice, (i) Man and building, (j) Airplane, (k) Old man, (l) statue

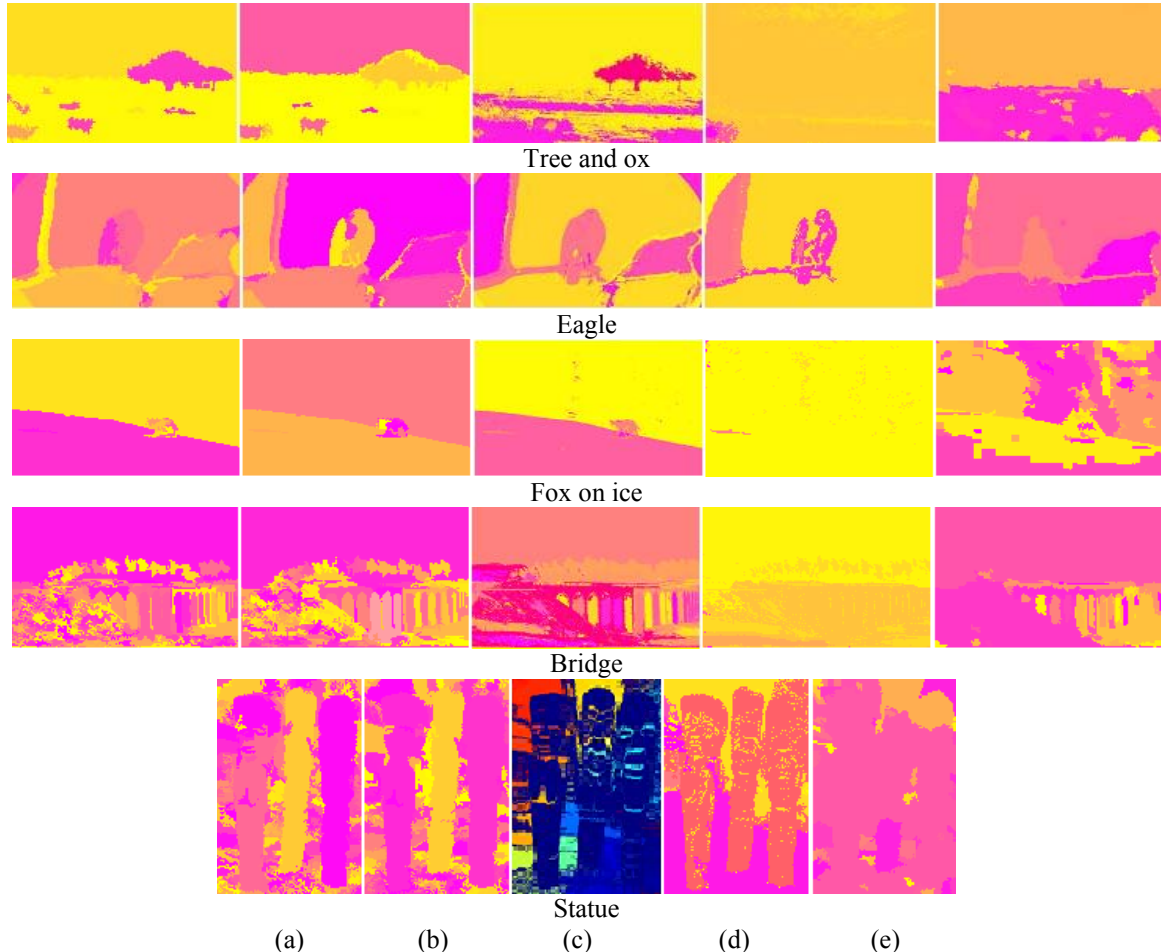


Fig. 2 Segmentation results (a) Proposed ASSRG algorithm, (b) Proposed fuzzy algorithm (c) SSRG algorithm using Otsu's threshold (d) MRG algorithm (e) SRGRM algorithm

Camapum proposed a new algorithm in [31] for automatic segmentation of images having clinical structures. The main contributions are the method of seed pixels selection and predicate of the Multi-Region Growing (MRG) [31] algorithm. The objective of this work is to help the clinical oncologist in this complex task by providing an accurate and a reliable automatic method. Their work follows the one started by Bueno [34]. In order to improve the results, they propose a new method of automatic markers detection through the image histogram. This improvement is very important and resulted in precise segmentation of images with poor contrast and acquired from different CT equipments. The statistic measures showed the high accuracy of segmentation, what makes it useful. The multi-region growing algorithm implemented in this work is quite independent of the input images. The seed selection and homogeneity criteria are robust leading to a successful segmentation. This justifies our selection of the region growing techniques used for comparison with proposed algorithm.

The results after applying region growing algorithms to the Berkley images are shown in Fig. 2. These results are obtained by converting the labelled image to a RGB image. As shown in Fig. 2(a) we obtain visually acceptable segmentation results for our proposed ASSRG algorithm. The results for ‘tree and ox’, ‘eagle’, ‘fox on ice’ showing good segmentation results for both proposed and fuzzy version of the proposed method. Slight over segmentation is observed in the case of images having large numbers of small regions like ‘bridge’ image and ‘statue’ image which contains several pieces of stones. Results of the fuzzy proposed algorithm show more continuous regions as compare to proposed method.

SSRG algorithm using Otsu’s threshold segments regions efficiently which have high intensity similarity between

connected pixels. The MRG is quite independent of the input image. It automatically finds out initial seeds and stopping criteria for growing formula that is a great advantage of the algorithm. Another advantage is that it does not require any post processing. MRG algorithm efficiently segments the images with varying contrast and dimension. It has limitation to segment those regions which have very low contrast in two connected regions. Our proposed method performs better for all images except images which have very small region like ‘man on boat’ image. SRGRM produce satisfactory results.

Evaluation factors shown in table 1 describe the efficiency of the proposed algorithm and the comparison algorithms. Numbers of regions segmented by proposed ASSRG algorithm are acceptable. The total time taken is low, which is about 11 to 22 seconds, except ‘statue’ image in which time taken is 57.90 seconds. It is also observed Liu’s F-factor is also low in the order of 10^{-5} - 10^{-6} , which describes the good segmentation results of our proposed method. The Liu’s F-factor is lower for the proposed and SSRG algorithms using Otsu’s threshold as compared to MRG and SRGRM algorithm however the number of regions produced by SSRG algorithm is very high, with $r = 2408$ for the ‘statue’ image. This defect is removed by the proposed method where the number of regions is significantly reduced with only a slight increase in Liu’s F-factor. The time taken is lower compare to the proposed method because of simple flow of the algorithm.

For proposed fuzzy algorithm total numbers of regions are lower and total time taken is slightly more with compare to proposed method. MRG algorithm has the advantage of no requirement of post processing which causes lower total time taken by algorithm compare to proposed method.

TABLE 1: EVALUATION FACTORS FOR PROPOSED ALGORITHM, PROPOSED FUZZY ALGORITHM, SSRG ALGORITHM USING OTSU’S THRESHOLD, MRG ALGORITHM, SRGRM ALGORITHM
R: total number of regions in segmented image
T: total time taken by algorithm (in seconds)
F: Liu’s F-factor

Image	Proposed ASSRG algorithm			Proposed fuzzy algorithm			SSRG algorithm using Otsu’s threshold			MRG algorithm			SRGRM algorithm		
	<i>R</i>	<i>T</i>	<i>F</i>	<i>R</i>	<i>T</i>	<i>F</i>	<i>R</i>	<i>T</i>	<i>F</i>	<i>R</i>	<i>T</i>	<i>F</i>	<i>R</i>	<i>T</i>	<i>F</i>
Rock	27	14.1	8.07e-6	19	21.0	1.59e-5	378	10.3	2.35e-6	31	7.3	3.58e-5	15	12.0	1.83e-5
Elephant	34	14.2	7.44e-6	28	21.5	2.38e-5	663	11.1	2.69e-6	21	7.6	1.59e-5	46	11.1	4.58e-5
Tree and Ox	10	13.3	2.39e-6	9	20.6	8.39e-6	778	10.6	3.35e-6	23	7.4	2.34e-5	33	13.9	2.16e-5
Man on boat	68	20.7	6.97e-5	48	25.3	1.68e-4	716	11.0	4.14e-6	24	8.1	4.57e-5	34	12.2	1.44e-4
Eagle	41	14.3	2.04e-5	33	21.2	4.17e-5	522	11.3	2.88e-6	32	3.9	2.52e-5	20	12.9	3.51e-5
F1 race cars	67	14.6	5.30e-5	62	23.4	1.00e-4	1000	12.0	5.81e-6	27	5.8	4.17e-5	87	12.8	1.06e-4
Bridge	144	22.7	1.61e-4	113	27.4	1.46e-4	1628	12.5	1.13e-5	32	7.1	3.47e-5	31	13.6	6.06e-5
Fox on ice	8	14.9	4.43e-6	9	20.8	5.05e-5	243	11.0	8.94e-7	23	8.0	1.90e-5	62	10.9	2.56e-4
Man and building	128	18.8	1.04e-4	113	25.2	2.41e-4	1103	12.0	9.76e-6	31	7.7	1.14e-4	89	10.7	1.65e-4
Airplane	4	10.2	9.21e-7	4	20.1	2.17e-6	25	9.8	1.62e-7	32	10.3	6.15e-6	13	21.7	2.87e-6
Old man	21	13.2	5.37e-6	15	20.2	2.01e-5	316	10.8	1.98e-6	33	7.5	4.99e-5	23	11.0	4.78e-5
statue	146	57.9	1.66e-4	132	49.0	2.04e-4	2408	13.2	1.58e-5	33	7.6	5.45e-5	45	10.9	7.43e-5

VI. CONCLUSION

In this paper an adaptive single seed based region growing algorithm (ASSRG) is proposed. The proposed algorithm solves the problem of initial seed selection in typical region growing algorithm and reduces computational overhead by growing on region at a time from a single seed in a hierarchical manner. Instead of selecting a threshold heuristically as in conventional region growing algorithms, a multi stage adaptive algorithm is proposed taking into account the relationship of a pixel with its 8-neighbors and the mean of the growing region. Based on segmentation results and the evaluation factor it is concluded that our proposed algorithm produces good segmentation results for a wide range of realistic images. A fuzzy rule based modification of the algorithm is also proposed in which decision making steps is solved by fuzzy rule and the results are compared with that of the proposed algorithm. The proposed algorithm is also compared with SSRG algorithm using Otsu's threshold, SRGRM algorithm and MRG algorithm and this shown to outperform all three methods.

REFERENCES

1. S.Sathish Kumar, M.Moorthi, M.Madhu, Dr.R.Amutha, "An improved method for image segmentation using fuzzy-neuro logic", International Conference on Computer Research and Development, DOI 10.1109/ICCRD.2010.155.
2. D. H. Ballard and C. Brown, Computer Vision. Berlin, Germany: Springer Verlag, 1982.
3. H. Jiang, J. Toriwaki, and H. Suzuki, "Comparative performance evaluation of segmentation methods based on region growing and division," Syst. Comput. Jpn., vol. 24, no. 13, pp. 28–42, 1993.
4. Kai-Tat Fung; Wan-Chi Siu; "DCT-based video downscaling transcoder using split and merge technique ", IEEE Transactions on Image Processing, Publication Year: 2006 , Page(s): 394 – 403.
5. Aneja, K.; Laguzet, F.; Lacassagne, L.; Merigot, A.," Video-rate image segmentation by means of region splitting and merging " IEEE International Conference on Signal and Image Processing Applications (ICSIPA), 2009, Page(s): 437 – 442.
6. A. J. Abrantes and J. S. Marques, "A class of constrained clustering algorithms for object boundary extraction," IEEE Trans. Image Processing, vol. 5, pp. 1507–1521, 1996.
7. L. Najman and M. Schmitt, "Geodesic saliency of watershed contours and hierarchical segmentation," IEEE Trans. Pattern Anal. Machine Intell., vol. 18, pp. 1163–1173, 1996.
8. Weihong Cui; Yi Zhang, "Graph Based Multi spectral High Resolution Image Segmentation", International Conference on Multimedia Technology (ICMT), 2010, Page(s): 1 – 5.
9. Tianhu Lei, Udupa, J.K., "Performance evaluation of finite normal mixture model-based image segmentation techniques" IEEE Transactions on image Processing, Volume: 12 , Issue: 10, Page(s): 1153 – 1169, 2009.
10. Adams, R., Bischof, L., "Seeded region growing", IEEE Transactions on Pattern Analysis and Machine Intelligence, vol. 16 , page 641-647, 1994.
11. Yian-Leng Chang and Xiaobo Li, "Adaptive Image Region-Growing", IEEE transactions on image processing, VOL. 3, NO. 6, November 1994.
12. Luis Garcia Ugariza, Eli Saber, Sreenath Rao Vantaram, Vincent Amuso, Mark Shaw, and Ranjit Bhaskar, "Automatic Image Segmentation by Dynamic Region Growth and Multiresolution Merging " IEEE transactions on image processing, VOL. 18, NO. 10, October 2009.
13. Shu-Yen Wan and William E. Higgins, "Symmetric Region Growing", IEEE transactions on image processing, Vol. 12, No. 9, September 2003.
14. Jianping Fan, David. K. Y. Yau, Ahmed. K. Elmagarmid, and Walid G. Aref, "Automatic Image Segmentation by Integrating Color-Edge Extraction and Seeded Region Growing ", transactions on image processing, Vol. 10, No. 10, October 2001.
15. T. Pavlidis and Y.-T. Liow, "Integrating region growing and edge detection," IEEE Trans. Pattern Anal. Machine Intell., vol. 12, pp. 225–233, 1990.
16. M. Tabb and N. Ahuja N, "Multiscale image segmentation by integrated edge and region detection," IEEE Trans. Image Processing, vol. 6, pp. 642–655, 1997.
17. Jacqueline Le Moigne and James C. Tilton, "Refining Image Segmentation by Integration of Edge and Region Data", IEEE transactions on geosciences and remote sensing, Vol. 33, No. 3, May 1995
18. Weihong Cui, Zequn Guan, Zhiyi Zhang, "An Improved Region Growing Algorithm for Image Segmentation", International conference on Computer Science and Software Engineering Vol. 6, Page(s):93 – 96.
19. Jun Tang, "Color Image Segmentation algorithm Based on Region Growing". International Conference on Computer Engineering and Technology. Vol 6 , Page(s): V6-634 - V6-637 2010.
20. Chaobing Huang, Quan Liu, Xiaopeng Li, "Color Image Segmentation by Seeded Region Growing and Region Merging ", International Conference on Fuzzy Systems and Knowledge Discovery ,FSKD 2010.
21. S. A. Hojjatoleslami and F. Kruggel, "Segmentation of Large Brain Lesions ", IEEE transactins on medical imaging, Vol. 20, No. 7, July 2001.
22. Qiyao Yu and David A. Clausi, "IRGS: Image Segmentation Using Edge Penalties and Region Growing ", IEEE transactions on pattern recognition and machine vision, VOL. 30, NO. 12, December 2008
23. S.-C. Cheng , "Region-growing approach to color segmentation using 3-D clustering and relaxation labeling", IEEW Proc.-Vis. Image Signal Process., Vol. 150, No. 4, August 2003.
24. Jamshid Dehmeshki, Hamdan Amin, Manlio Valdivieso, and Xujiong Ye, "Segmentation of Pulmonary Nodules in Thoracic CT Scans: A Region Growing Approach", IEEE transactions on medical imaging, VOL. 27, NO. 4, APRIL 2008 467.
25. Alain Trémeau and Philippe Colantoni, "Regions Adjacency Graph Applied to Color Image Segmentation", IEEE transactions on image processing, Vol. 9, No. 4, April 2000.
26. S. A. Hojjatoleslami and J. Kittler, "Region Growing: A New Approach", IEEE transactions on image processing, Vol. 7, No. 7, July 1998.
27. Jia-Nan Wang, Jun Kong, Ying-Hua Lu, Wen-Xiang Gu, Ming-Hao Yin, Yong-Peng Xiao, "A region-based SRG algorithm for color image segmentation ", International Conference on Machine Learning and Cybernetics, Hong Kong, 19-22 August 2007.
28. The Berkley Segmentation Database and Benchmark.
[online]http://www.eecs.berkeley.edu/-Research/Projects/CS/vision/bsds/.
29. Jianqing Liu , Yee-Hong Yang, " Multiresolution Color Image Segmentation " IEEE Transaction on pattern analysis and machine intelligence Vol no. 7, JULY 1994.
30. Verma, O.P.; Hanmandlu, M.; Susan, S.; Kulkarni, M.; Jain, P.K., "A Simple Single Seeded Region Growing Algorithm for Color Image Segmentation using Adaptive Thresholding, "Communication Systems and Network Technologies (CSNT), 2011 International Conference on , vol., no., pp.500,503, 3-5 June 2011 doi: 10.1109/CSNT.2011.107
31. Juliana Fernandes Camapum, Alzenir O. Silva, Alan N. Freitas, Hansencleaver de F. Bassani, Flávia Mendes O. Freitas" Segmentation of Clinical Structures from Images of the Human Pelvic Area" Symposium on Computer Graphics and Image Processing (SIBGRAPI'04).
32. Chaobing Huang, Quan Liu, "Color image retrieval using edge and edge-spatial features", Chinese Optics Letters, 2006, vol.4, no.8, pp.457-459
33. Frank Y. Shih, Shouxian Cheng. "Automatic seeded region growing for color image segmentation", Image and Vision Computing, 2005, vol.23, pp.877-886.
34. M. G. Bueno, *Computer Aided Segmentation of Anatomical Structures in computed Tomographic Images*, PhD Thesis, Coventry University, 1998.

Research Article

An Experimental Investigation of Jatropha Biodiesel Blends in a Multi Cylinder CI Engine: Performance and Emissions Study

Amit Pal^{A*}^ADepartment of Mechanical Engineering, Delhi Technological University, Formerly Delhi College of Engineering, Delhi-110042, IndiaAccepted 05 November 2013, Available online 01 December 2013, **Vol.3, No.5 (December 2013)**

Abstract

There is tremendous increase in transportation activities in recent times. Petroleum fuels are the key energy source in India and preferred as automotive fuel. Their use has been increasing continuously from 3.5 MMT (Million Metric Tons) in the year 1950-51 to 84.3 MMT in 1997-98 and about 113 MMT in 2001 and it were about 148 MMT in 2011-12. Petroleum based fuels are obtained from limited reserves which are highly intense in certain regions of the world. Therefore, those countries that do not have these resources and facing a foreign exchange crisis are looking for alternative fuels, which can be produced from materials available inside the country. Biodiesel is considered as clean fuel since it has almost no sulphur, no aromatics and has about 10 % built in oxygen, which helps it to burn fully. In present paper the engine performance and exhaust emissions of jatropha oil biodiesel blends, were investigated on a 39 kW multi cylinder engine, in B10 to B30 percent blends and compared with the petroleum diesel fuel. The experimental results show that the engine power and torque of the mixture of oil–diesel fuel are close to the values obtained from diesel fuel and the amounts of smoke, CO and HC exhaust emissions are lower than those of diesel fuel, except slight increase of NOx emissions at higher loads.

Keywords: Diesel Engine, Performance testing, Emissions, Smoke, jatropha, biodiesel

1. Introduction

The world is presently facing the twin problems of fossil fuel depletion and severe environmental degradation. Haphazard extraction and lavish consumption of fossil fuels resulted in reduction of underground carbon resources. The search for alternative fuels, which promise a melodious correlation with sustainable development, energy preservation, efficiency and environmental protection, has become highly prominent in the present context. In the last decade, several researchers have been examined that vegetable oils may be proved as one such alternative fuel and their potential. Vegetable oils are renewable and eco-friendly to the environment, and they are free of sulphur content in them. This makes vegetable fuel studies become current issue among the various popular investigations. Bio-diesel have many advantages over petroleum diesel fuel; produce less smoke and particulates, have high cetane number, produce lower carbon monoxide and hydrocarbon emissions, renewable, biodegradable and non-toxic. In India, with abundance of forest resources, there are a number of other non-edible tree borne oilseeds with an estimated annual production of more than 20 million tones, which have large potential for making biodiesel to supplement other conventional sources. Biodiesel is considered as clean fuel since it has

almost no sulphur, no aromatics and has about 10 % built in oxygen, which helps it to burn fully. Hebbal et al. (2006) have presented the investigation on deccan hemp, a non-edible vegetable oil in a diesel engine for its suitability as an alternate fuel.

Agarwal and Agarwal (2007) conducted experiments using various blends of Jatropha oil with mineral diesel to study the effect of reduced blend viscosity on emissions and performance of diesel engine. The acquired data were analyzed for various parameters such as thermal efficiency, brake specific fuel consumption (BSFC), smoke opacity, CO₂, CO and HC emissions. While operating the engine on Jatropha oil (preheated and blends), performance and emission parameters were found to be very close to mineral diesel for lower blend concentrations. Purushothaman and Nagarajan (2009) presented work on the performance, emission and combustion characteristics of a single cylinder, constant speed, direct injection diesel engine using orange oil as an alternate fuel and the results are compared with the standard diesel fuel operation. Results indicated that the brake thermal efficiency was higher compared to diesel throughout the load spectra. Carbon monoxide (CO) and hydrocarbon (HC) emissions were lower and oxides of nitrogen (NOx) were higher compared to diesel operation. Labeckas and Slavinskas (2006) reported the comparative bench testing results of a four stroke Diesel engine when operating on neat rapeseed oil methyl ester and it's 5 %,

*Corresponding author: **Amit Pal**

10 %, 20 % and 35 % blends with Diesel fuel. The brake specific fuel consumption at maximum torque and rated power found to be higher for rapeseed oil by 18.7 % and 23.2 % relative to Diesel fuel. The maximum brake thermal efficiency is higher for rapeseed oil at higher load. The maximum NO_x emissions increase proportionally with the mass percent of oxygen in the bio-fuel and engine speed. The carbon monoxide emissions and visible smoke emerging from the biodiesel over all load and speed ranges are lower by up to 51.6 % and 13.5 % to 60.3 %, respectively. The carbon dioxide (CO₂) is slightly higher in case of biodiesel. The emissions of unburned hydrocarbons for all bio-fuels are reported low.

In the study of Altuna et al. (2008) a blend of 50 % sesame oil and 50 % diesel fuel was used as an alternative fuel in a direct injection diesel engine. The experimental results show that the engine power and torque of the mixture of sesame oil–diesel fuel are close to the values obtained from diesel fuel and the amounts of exhaust emissions are lower than those of diesel fuel. Suresh kumar et al. (2008) presented the results of performance and emission analyses of an unmodified diesel engine fuelled with Pongamia Pinnata Methyl Ester (PPME) and its blends with diesel. Engine tests were conducted to get the comparative measures of brake specific fuel consumption (BSFC), brake specific energy consumption (BSEC) and emissions such as CO, CO₂, HC and NO_x to evaluate the behaviour of PPME and diesel in varying proportions. BSFC and BSEC for all the fuel blends and diesel tested decrease with increase in load. This is due to higher percentage increase in brake power with load as compared to increase in the fuel Consumption. For the blends B20 and B40, the BSFC is lower than and equal to that of diesel respectively and the BSEC is less than that of diesel at all loads. This could be due to the presence of dissolved oxygen in the PPME that enables complete combustion; engine emits more CO for diesel as compared to PPME blends under all loading conditions. The CO₂ emission increased with increase in load for all blends. The lower percentage of PPME blends emits less amount of CO₂ in comparison with diesel. Blends B40 and B60 emit very low emissions. This is due to the fact that biodiesel in general is a low carbon fuel and has a lower elemental carbon to hydrogen ratio than diesel fuel. HC emission decreases with increase in load for diesel and it is almost nil for all PPME blends except for B20 where some traces are seen at no load and full load. The NO_x emission for all the fuels tested followed an increasing trend with respect to load. The reason could be the higher average gas temperature, residence time at higher load conditions. In an experiment on a kirloskar single cylinder diesel engine with 10-20 % palm oil bio-diesel, Naveen and Dhuwe (2004) reported significant reduction in smoke level. Lapuerta et al. (2007) analyzed diesel engine emissions when using biodiesel fuels as opposed to conventional diesel fuels. The engine emissions from biodiesel and diesel fuels are compared, paying special attention to the most concerning emissions, nitric oxides and particulate matter. Some of the important outcomes are: at part load operation, no differences in power output,

since an increase in fuel consumption in the case of biodiesel would compensate its reduced heating value. There is slight increase of NO_x with biodiesel because of more oxygen content of biodiesel and at higher temperature it leads to increase NO_x. There is a sharp reduction in particulate emissions with biodiesel as compared to diesel fuel. CO is usually found to significantly decrease with biodiesel. A more complete combustion caused by the increased oxygen content in the flame coming from the biodiesel molecules has been pointed out as the main reason.

Some researchers worked to find the effect of viscosity on emissions and performance of diesel engine Agarwal et al. (2001), Gangwar et al. (2008) and Choudhary et al. (2008). Emission parameters such as smoke NO_x and CO₂ were found to have increased with increasing proportion of Jatropha oil in the blends compared to diesel. They found Jatropha oil to be a promising alternative fuel for compression ignition engines. Thermal efficiency was lower for unheated Jatropha oil compared to heated Jatropha oil and diesel. CO₂, CO, HC, and smoke opacity were slightly higher for neat Jatropha oil compared to that of diesel, but it were significantly less with Jatropha and other specie's bio-diesel. These emissions were found to be close to diesel for preheated Jatropha oil.

2. Experimental setup for performance testing

The setup consists of four cylinders, four stroke, Tata Indica diesel engine connected to eddy current type dynamometer for loading. The engine test setup specifications are given in Table 1, actual test setup is shown in Figure 1. The setup enables study of engine performance for various parameters such as torque, brake power, specific fuel consumption, brake thermal efficiency, opacity and p-θ diagram. The main aim of this experiment is to investigate the suitability and effect on performance of blending of biodiesel with gasoline diesel fuel.

Preparation of biodiesel blends

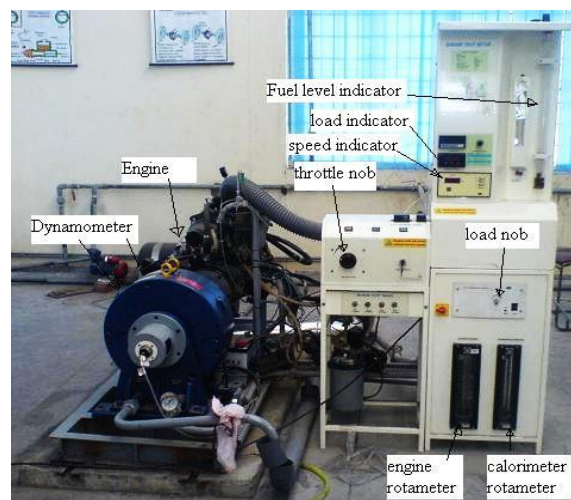


Figure 1: Actual Experimental setup.

Calorific value of petroleum diesel = 42000 kJ/kg.

Calorific value of biodiesel = 37000 kJ/kg.

Density of petroleum diesel = 800 kg/m³.

Density of biodiesel = 891 kg/m³.

Table 1: Specifications of the engine test setup

S.No.	Component	Specifications
1	Engine	Tata Indica, 4 Cylinder, 4 Stroke, water cooled, Power 39kW at 5000 rpm, Torque 85 NM at 2500 rpm, stroke 79.5mm, bore 75mm, 1405 cc, CR22
2	Dynamometer	eddy current, water cooled
3	Temperature	Input RTD PT100, Range 0–100 °C,
	transmitter	Output 20 mA and , Input Thermocouple, Range 0–1200 °C,
4	Piezo sensor	Range 5000 PSI,
5	Air box	M S fabricated with orifice meter and manometer
6	Load indicator	Digital, Range 0-50 Kg, Supply 230VAC
7	Engine	Input Piezo sensor, crank angle sensor,
	indicator	Input Piezo sensor, Communication RS 232, Crank angle sensor, No. No. of channel 2,
8	Software	Enginesoft
9	Temperature	Type RTD, PT100 and
	sensor	Thermocouple Type K
10	Fuel flow	DP transmitter, Range 0-500 mm
	transmitter	
11	Air flow	Pressure transmitter,
	transmitter	Range (-) 250 mm WC
12	Load sensor	Load cell, type strain gauge,
		Range 0-50 Kg

Table 2: Description of different blends of biodiesel

Blend	Amount of	Amount of	Calorific value	Resultant
	Diesel (ml)	Bio diesel (ml)	of blend (kJ/kg)	Density (kg/m ³)
Diesel	2000	0	42000	800
B-10	1800	200	41500	809
B-20	1600	400	41000	818
B-30	1400	600	40500	827

On this engine experiments are performed with different blends of biodiesel (pure diesel, B-10, B-20, and B-30). Jatropha biodiesel were prepared in our IC Engines laboratory. These blends are prepared in quantity of 2 liter each by mixing required quantity of biodiesel in petroleum diesel. There description of biodiesel blends is shown in Table 2.

3. Result and discussions on performance testing

Variation of Torque v/s Engine Speed

Figure 2 shows the variation of torque with speed for pure diesel and biodiesel blends of jatropha biodiesel. Variation of torque for different blends and pure diesel at a particular engine speed is within a very narrow range. In case of both

biodiesel blends and pure diesel, initially the torque rises sharply with increase in engine speed up to 2500 rpm. Between speed 2500 to 4000 rpm the variation or torque with speed remain almost constant. Further increase in speed causes decrease in torque. The pattern is almost same for all blends. At initial speed biodiesel have more torque especially jatropha biodiesel has more torque. Almost similar pattern has obtained for all percentage of blends.

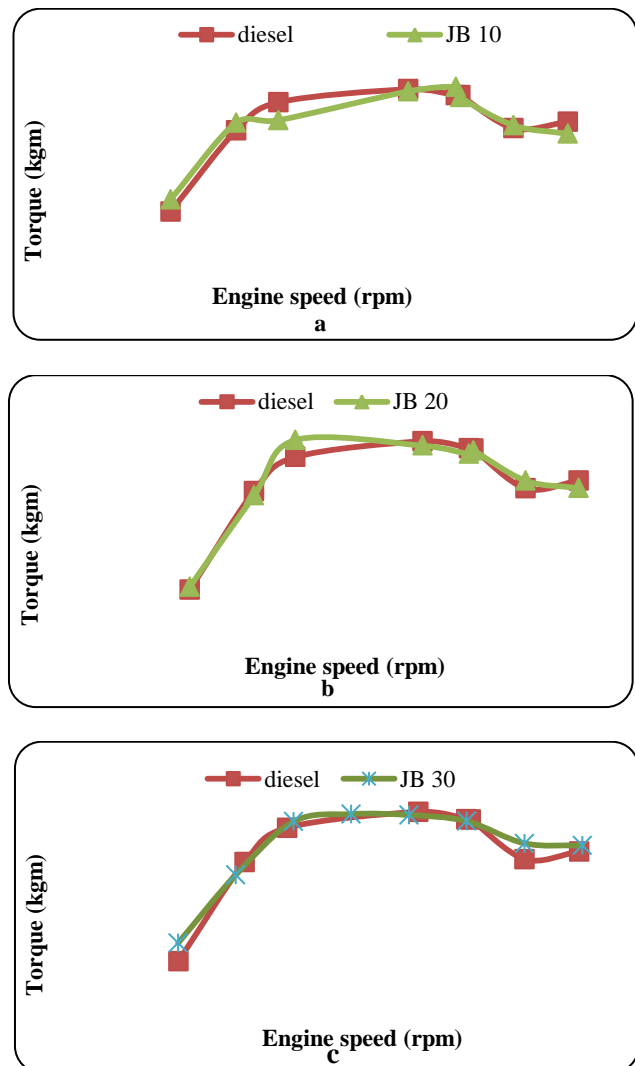


Figure 2: Comparison of Torque v/s Speed for different biodiesel blends of Jatropha oil

Variation of Brake Power v/s Speed

The variation of brake power vs. speed for both blends in comparison to pure diesel is shown in Figure 3. The Brake Power increases proportionally to engine speed in the range of 2000 to 4000 rpm. In this speed range variation of brake power is between 6-32 kW. For more than 4000 rpm there is fluctuating variation in brake power among the biodiesel blends. The variation of brake power is almost negligible for all types of blends and pure diesel for upto 4000 engine rpm. Between 4000 to 5000 rpm biodiesel

blends are having slightly higher brake power as compared to pure diesel. At initial speed brake power obtained is more in case of biodiesel. Except initial speed thumba biodiesel has more power compare to jatropha biodiesel.

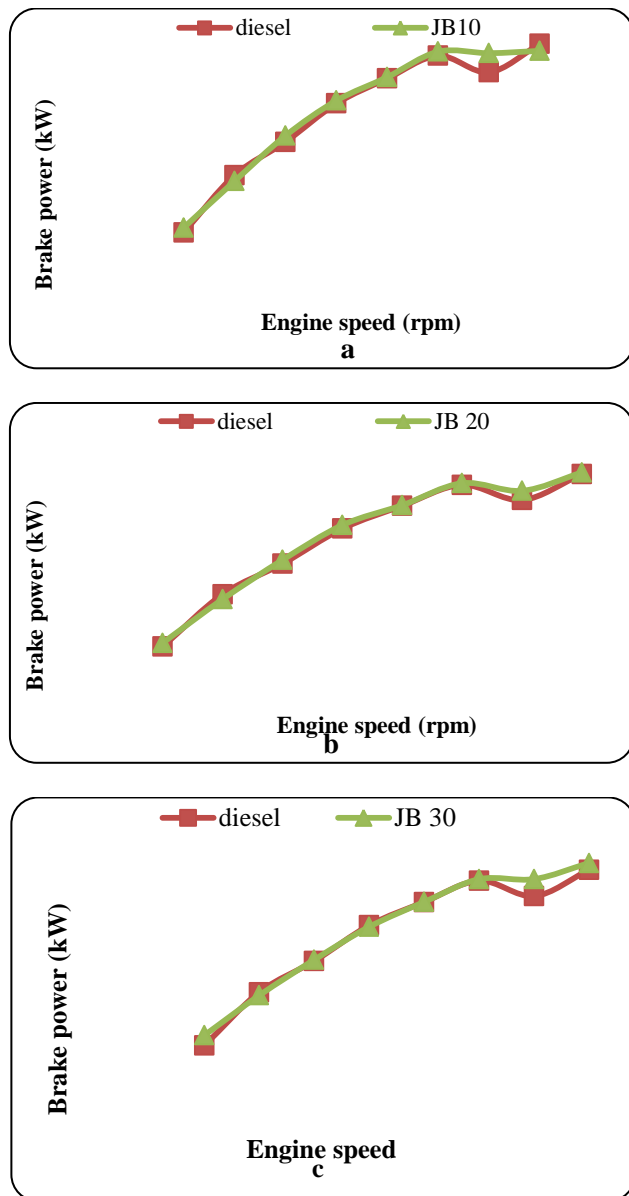


Figure 3: Comparison of Brake Power v/s Speed for different biodiesel blends of Jatropha oil

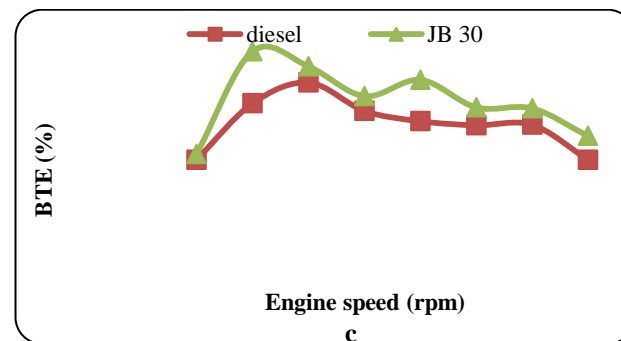
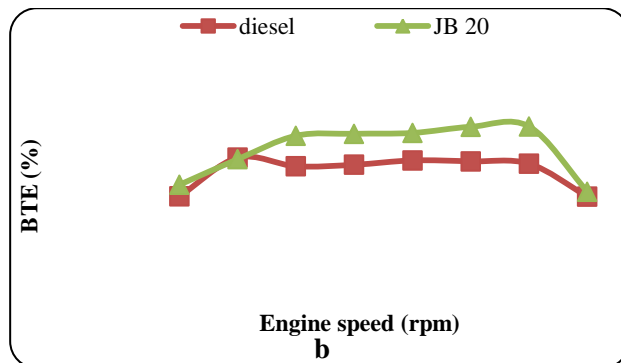
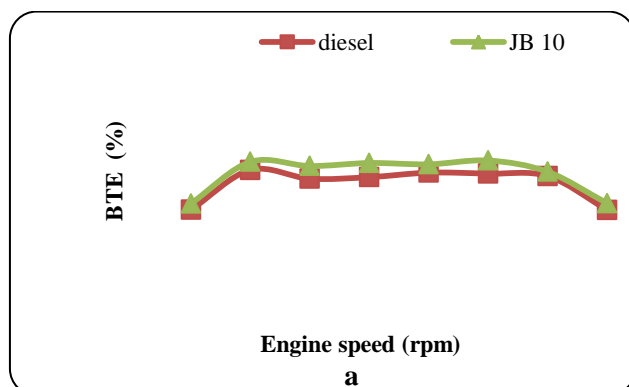
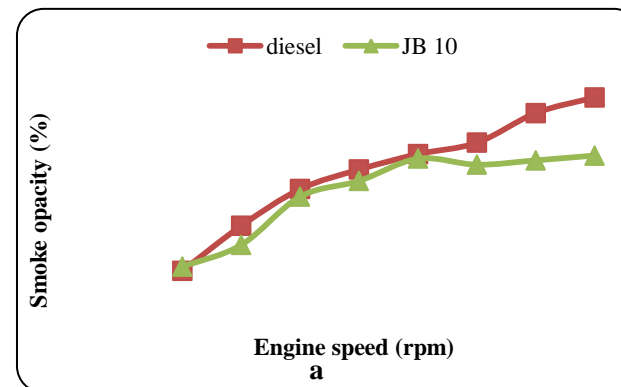


Figure 4: Brake Thermal Efficiency v/s Speed for different biodiesel blends of Jatropha oil

Brake Thermal Efficiency v/s Speed

Figure 4 shows comparison of Brake thermal efficiency vs. speed for different biodiesel blends of jatropha oil in comparison to diesel respectively. The maximum value of brake thermal efficiency for all blends & pure diesel is at 2000 rpm. For all blends of both oils variation of brake thermal efficiency is higher as compared to pure diesel for wide range of engine speed. The maximum thermal efficiency is achieved by using JB-30 blend is around 26.9 % at 2000 rpm which is 5 % higher as compared to pure diesel. The brake thermal efficiency is almost constant between rpm range of 2000 to 4000, and it decreases sharply with further increase in rpm and with increase in percentage of biodiesel blending the brake thermal efficiency increase for wide range of engine rpm. Jatropha oil exhibits comparatively higher efficiency for all speed range than pure diesel with all blends. Biodiesel blend of 30% shows much higher efficiency than diesel fuel.



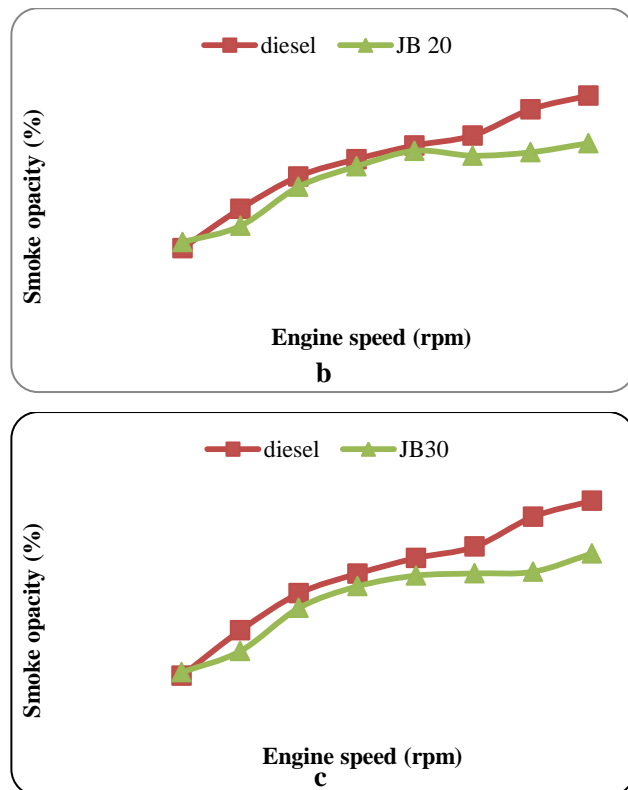


Figure 5: Comparison of Opacity v/s Speed for different biodiesel blends of Jatropha oil

Smoke Opacity v/s. Speed

To understand the pollution aspect of biodiesel the variation of opacity vs. speed are shown in Figure 5. The smoke opacity value for pure diesel is slightly higher as compared to all type of blends for wide range of engine rpm. For all biodiesel blends the opacity value increases from 10 to 60 % between the speed ranges of 2000 to 3500 rpm. There is no significant change in opacity value for above 4000 rpm engine speed. The trend regarding variation of opacity with respect to speed is almost similar for all type of blends and further the variation of opacity value of different blend at a particular rpm is almost negligible. Except initial speed opacity of biodiesel blends have less value than diesel oil. This is due to better combustion property of biodiesel.

4. Conclusions

From the engine performance testing it can be concluded that the performance parameters and emission characteristics for biodiesel (jatropha) are better results than the diesel oil. In this work performance of biodiesel is compared by the parameters like brake power, torque, brake thermal efficiency, specific fuel consumption and emission are characterized by opacity measurement. Some advantages obtained for biodiesel are:

At low speed more torque is obtained for biodiesel and torque almost constant for wide range of speed for both diesel and biodiesel blends. Maximum torque obtained for

jatropha oil is 7.5 kg-m at 2500 rpm and maximum percentage increase in torque is 30% more than the diesel oil which is obtained for 30% blend at 1500 rpm.

More brake power is obtained at initial speed and it is nearly constant for 2500 to 4000 rpm. The maximum brake power achieved is 35 kW at 5000 rpm for biodiesel a blend of 10%. Maximum percentage increase obtained for biodiesel of 30% blend is 3.5% at 1500 rpm.

Except at starting speed more brake thermal efficiency has obtained for higher speeds. For 10% blend of biodiesel there is not much difference in diesel and biodiesel. For higher blend biodiesel has much better efficiency than diesel oil. Maximum brake thermal efficiency increased is 1.98% for biodiesel at 2000 rpm.

Lower value of opacity has obtained for biodiesel than diesel oil at higher speeds. Maximum reduction in opacity obtained is about 35 % for biodiesel.

References

- Ministry of Petroleum and Natural Gas, Government of India, New Delhi, (Economic Division) report, Basic Statistics on Indian Petroleum & Natural Gas, 2011-12, Available at [www.http://petroleum.nic.in/petstat.pdf](http://petroleum.nic.in/petstat.pdf), Accessed on 04-11-2013 20:30 PM
- O. D., Hebbal, V. K., Reddy and K Rajagopal, 2006. Performance characteristics of a diesel engine deccan hemp oil. *Fuel* 85, 2187–2194.
- Deepak Agarwal and Avinash Kumar Agarwal, 2007, Performance and Emissions Characteristics of Jatropha Oil (Preheated And Blends) in A Direct Injection Compression Ignition Engine, *Applied Thermal Engineering*; 27: pp 2314–2323.
- K Purushothaman, and G Nagarajan, 2009, Performance, Emission and Combustion Characteristics of a Compression Ignition Engine Operating on Neat Orange Oil. *Renewable Energy*; 34 pp 242–245.
- Labeckas Gvidonas and Slavinskas Stasys, 2006, The Effect of Rapeseed Oil Methyl Ester on Direct Injection Diesel Engine Performance and Exhaust Emissions, *Energy Conversion and Management*; 47: pp1954–1967.
- Altuna Sehmus, Bulut Husamettin and Oner Cengiz, 2008, The Comparison of Engine Performance and Exhaust Emission Characteristics of Sesame Oil–Diesel Fuel Mixture with Diesel Fuel in A Direct Injection Diesel Engine, *Renewable Energy*; 33 pp 1791–1795.
- Suresh Kumar.R Velraj, R Ganeshan, 2008 Performance and Exhaust Emission Characteristics of a C I Engine Fuelled with Pongamia Pinnata Methyl Ester (PPME) and its Blends with Diesel. *Renewable Energy*; 33: pp 2294–2302.
- Naveen kumar and Abhay Dhuwe, (2004). Fuelling an Agricultural Diesel Engine with Derivatives of Palm Oil, *SAE International 2004, Paper no. 2004-28-0039*.
- Lapuerta Magin, Octavio Armas and Jose Rodriguez, Effect of Biodiesel Fuels on Diesel Engine Emissions. *Progress in Energy and Combustion Science* 2008; 34: pp198–223.
- Avinash Agarwal, and L M Das, 2001, Biodiesel Development and Characterization for Use as A Fuel in C. I. Engine, *Journal of Engineering for Gas Turbines and Power ASME transaction*; 123, number 2 pp 440-447.
- Harish Kumar Gangwar, and Avinash Kumar Agarwal, 2008, Emission and Combustion Characteristics of Vegetable Oil Blends in an Indirect Ignition Transportation Engine, *SAE International; Paper no. 2008-28-0034*
- S Choudhury, P K Bose., 2008 *Jatropha derived Biodiesel and its Suitability as C. I. Engine Fuel*, *SAE International*; paper no. 28-0040

Black Hole Attack Mitigation Method based on Route Discovery Mechanism in AODV Protocol

Anishi Gupta

Department of Computer of Engineering, Delhi Technological University, New Delhi, India

anishi.anishi@gmail.com

Abstract- Ad hoc On Demand Vector (AODV) is a reactive routing protocol in Mobile Ad hoc Network (MANET). There have been several past works done to mitigate black hole effect but most of the methods incur overhead to the existing protocols. For the aforesaid reason, in this paper, we propose a new method MEAODV (Modified Enhanced AODV), based on the previous work EAODV (Enhanced AODV). The MEAODV is based on route discovery process for mitigating black hole effect. It does not incur any overhead to the network. It has similar logic as in EAODV but has few different condition parameters for checking the RREP message for better route discovery mechanism. In simulation, MEAODV has outstanding results in terms of better Performance Delivery Ratio (PDR) and less End-to-End Delay as compare to EAODV method by varying malicious nodes whereas it offers better PDR than EAODV by varying number of nodes.

Keywords- AODV, Black hole, EAODV, End-to-End Delay, MANET, MEAODV, Packet Drop Ratio, Performance Delivery Ratio, RREP message, RREQ message.

I. INTRODUCTION

AODV, a reactive routing protocol uses a broadcast route discovery mechanism [1]. The protocol functions in two phases: route discovery and route maintenance. Initiation of a Route Discovery process is held whenever a source node wants to communicate with another node for which no routing information is present in its table. In Route Maintenance, symmetric links are being assured by Periodic hello messages. AODV protocol is vulnerable to many attacks such as black hole, warm hole and so on. Black hole effect on AODV protocol is more severe as compare to other protocols. In this paper, We have focus on black hole attack on a wireless network.

To carry out a Black hole attack, malicious node waits for neighbouring nodes to send RREQ messages [1]. When RREQ message is being received by the malicious node receives, it sends a false RREP message without checking the routing table, and quickly gives a route to destination over itself, before other nodes send a real one. It assigns high sequence number to in order to get down in the routing table of the victim node. Therefore route discovery process is assumed to be completed by requesting nodes and ignore RREP messages of other nodes and begin to send data packets to malicious node. All RREQ messages are being attacked by malicious node.

Review of past works mostly have disadvantage of network overhead. Since mobile devices have limited resources, thus give an adverse effect due to high processing overhead on an overall network performance including power usage. The main idea behind our proposed algorithm is to introduce a new method called MEAODV (Modified Enhanced AODV) which has more packet delivery ratio as compare to previous work EAODV method to mitigate the black hole attack. This method is an enhancement of previous work called EAODV [2].

MEAODV has given more control to routing updates in order to mitigate black hole effect. This paper is organized as follows. Section II discusses past works. Section III presents the MEAODV method. Section IV discusses simulation results and lastly, conclusion and future works are presented in Section V.

II. RELATED WORK

Many techniques have been proposed by researcher to prevent black hole attack. P. Raj and P. Swadas [3], proposed an adequate solution based on A DYNAMIC LEARNING SYSTEM. In this system they check RREP messages which comes from intermediate nodes. E.A Mary[4], proposed authentication based on certification in order to counter the black hole effect. Kamarularifin Abd. Jalil, Zaid Ahmad[5], proposed an Efficient Routing Discovery Algorithm (ERDA) whose aim was to reduce overhead and latency. Kamarularifin Abd. Jalil, Zaid Ahmad[2], proposed an Enhanced AODV(EAODV) algorithm based on process of route discovery. Main drawback of this algorithm is that, if multiple reply comes again from the same malicious node, then Reply is not discarded, moreover it is being accepted. This algorithm does not run if multiple reply comes from the same malicious node. Rajesh Yerneni, and Anil k. Sarje[6], proposed an Opinion AODV to mitigate black hole attack. Vrutik Shah, and Nilesh Modi[7], proposed a mitigation algorithm whose main drawback is that, if multiple reply messages come from the same malicious node which is already present in the malicious list, then every time we are using detection method(Packet drop ratio) to check for malicious reply. This increases end to end delay. Instead of detecting again, we should discard the packet.

III. MITIGATION METHOD FOR BLACK HOLE ATTACK

The MEAODV is an enhancement of EAODV routing protocol [2], which provides better Packet Delivery Ratio as compare to EAODV method against black hole attack. In MEAODV, there is a revision of logic as described in EAODV but with few different condition parameters for checking the RREP message for better route discovery mechanism.

The MEAODV method works similar to EAODV method except redundancy in the process of detecting malicious node is prevented. The MEAODV, by getting rt-modify parameter “false” exhibits a detection of malicious node only when malicious node has not previously send the RREP message(malicious node is not already present in intrud_list). If malicious node is already present in

intrud_list, there is no need to detect for malicious node, simply a packet of malicious node is dropped. Moreover, in the previous EAODV work, when rt-modify parameter is “false”, there is always a check on malicious node. This is done by detecting malicious node, even if it is already present on intrud_list. So this kind of redundancy is also prevented in the propose work named MEAODV.

This method also prevents RREP message of multiple malicious nodes from getting into the network and updating the routing table.

The code of MEAODV method is as follows:

Modified Enhance AODV

```

1. RecvReply(Packet P){
2. Save P.srcIPadd and P.ds_seqno to rreply_table
3. if(rt_modify is false){
4.     if(P.srcIPadd in intrud_list){
5.         Drop packet P
6.         flush rreply_table
7.         return}
8.     else{
9.         if(0<packet drop ratio<1){
10.            set rt_modify to true}
11.        else{
12.            save P.srcIPadd in intrud_list;
13.            Drop packet P
14.            flush rreply_table
15.            return}
16.        }
17.    }
18. if(P.dsIPadd not in RT routing table entry)
19. {
20.     Add P.dsIPadd to RT entry}
21. Select ds_seqno from RT
22. if(rt_modify and((P is from destination node)
23.    or (P.ds_seqno > RT.ds_seqno)
24.    or(P.ds_seqno= RT.ds_seqno and
25.    P.hopcount < RT.hopcount)))
26. {
27.     if (P is from destination node)
28.     { set rt_modify to false;
29.       update RT entry with P;
30.       send out data packets in buffer}
31. else if (intermediate node){forward packet}
32. else { discard packet}
33. }
```


The working of MEAODV is as follows:

1. At the beginning, `rt_modify` parameter is set to “false”.
 2. Since malicious node is the first node to reply, so it (M1) will send a RREP message to a sender node S.
 3. The `ip_address` and destination sequence number will be stored in reply table.
 4. Since `rt_modify` parameter is “false”, so detection for malicious node gets started.
 5. Since the node is the malicious one, its id is being saved in a intruder list, the RREP packet is dropped, reply table is flushed and `recvReply` function is returned.
 6. Again when a RREP packet is received from destination node D, then also a detection process for malicious node gets started.
 7. In the process of detection, Packet Drop Ratio comes out to be less than one, so `rt_modify` parameter is set to “true”.
 8. Now since `rt_modify` parameter is “true” and a node is destination, we make `rt_modify` “false”. RT Entry is updated with packet ‘P’ of destination node and packets are send out in buffer. Hence sender node S updates its routing table with new route information.
 9. Now, `rt_modify` becomes false, any reply message that comes after reply of destination node, will be ignored until the process of isolating malicious node is completed.
- Thus this method prevents malicious node from entering routing table.

The MEAODV method behaves differently from EAODV in the following ways:

1. In EAODV method, logic begins with `rt_modify` parameter initially set to “true”, where as in MEAODV method, `rt_modify` is initially set to “false”.
2. EAODV initially stored the value of “srcIPadd” and “DSN seq no.” of packet of malicious node which is being overwritten by packet information of destination node; where as, in MEAODV method, packet information of only destination node is stored as shown in fig.1[2] and fig.2.

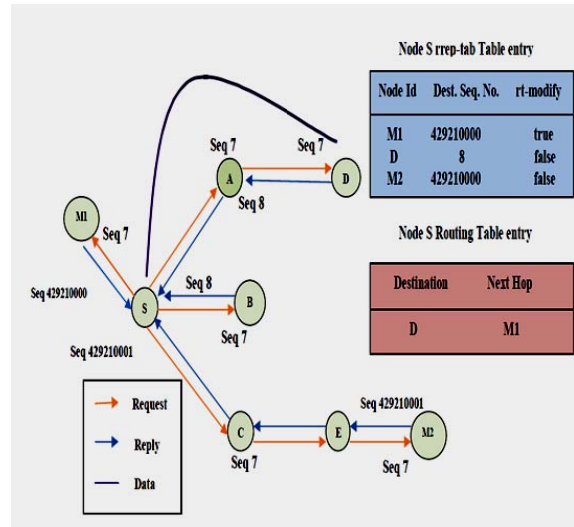


Fig. 1[2]. Route Discovery in the EAODV

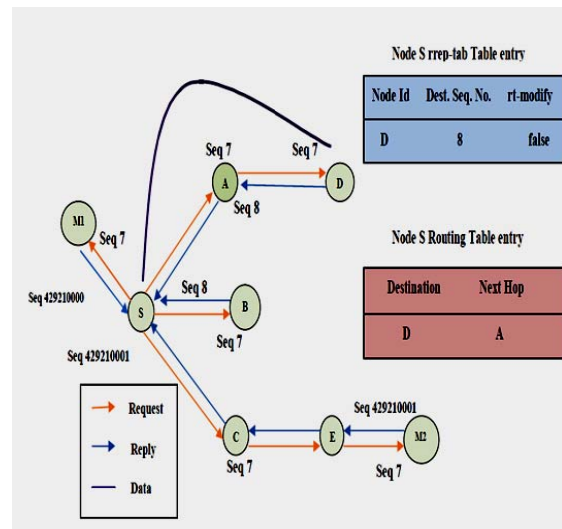


Fig. 2. Route Discovery in the MEAODV

IV. SIMULATION ENVIRONMENT

A simulation model was developed NS-2.35. AWK files are used to generate data after analyzing trace files. The results were analysed by using following three conditions:

- 1) Normal AODV protocol (without attack)
- 2) AODV protocol with EAODV method
- 3) AODV protocol with MEAODV method

Performance Delivery Ratio (PDR) and End-to-End Delay are used as an evaluation metric to measure the performance. The result of performance delivery ratio using normal AODV (without attack), AODV with EAODV method and AODV with MEAODV method are analysed. PDR of normal AODV is highest under absence of malicious node. When network is under attack, PDR of normal AODV drops drastically as compare to AODV with EAODV or MEAODV. By comparing EAODV and MEAODV method, MEAODV has slightly more PDR and less End to End Delay comparatively to EAODV method by varying malicious nodes as shown in figures. On increasing number of nodes, PDR of MEAODV increases comparatively to EAODV but end-to-end delay fluctuates. Overall simulation parameters are confined in Table 1.

TABLE 1
SIMULATION PARAMETERS

Parameters	Values
Simulator	NS 2.35
Protocol	AODV
Simulation Duration	600 seconds
Simulation Area	600*600
Movement Model	Manhattan Grid
Traffic Type	CBR
Data Payload	512 bytes/packet
Pause Time	0.2 seconds
Maximum Speed	55 m/s
Number of Nodes	30

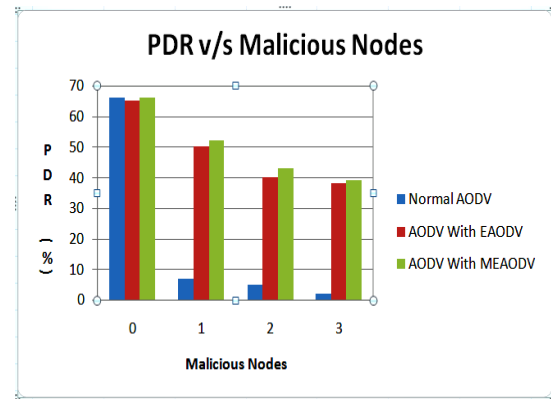


Fig. 3. Performance Delivery Ratio versus number of malicious nodes

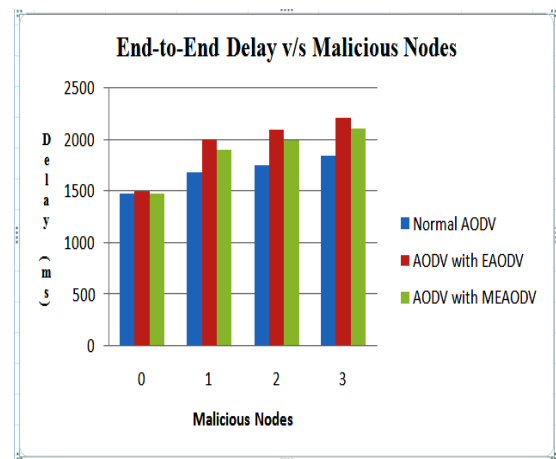


Fig. 4. End-to-End Delay versus number of malicious nodes

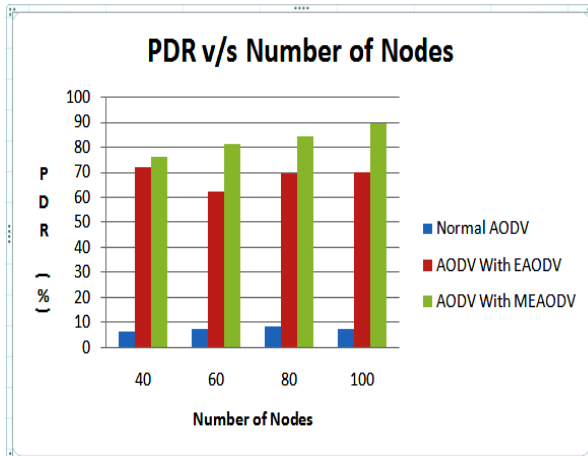


Fig. 5. Performance Delivery Ratio versus number of nodes

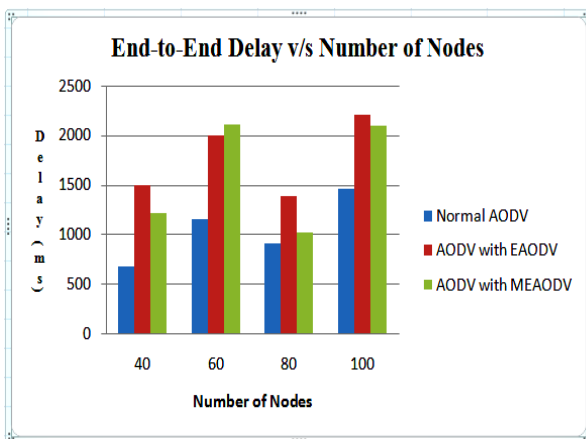


Fig.6 End-to-End Delay versus number of nodes

TABLE 2
COMPARISON OF MEAODV WITH EAODV (IN PRESENCE OF THIRTY NODES)

Parameter Metrices	Performance Delivery Ratio (%)		
	MEAODV	EAODV	Normal AODV
No. of Malicious Nodes			
Zero malicious node	66	65	66
One malicious node	59	50	7
Two malicious node	47	40	5
Three malicious node	43	38	2

TABLE 3
COMPARISON OF MEAODV WITH EAODV (IN PRESENCE OF ONE MALICIOUS NODE)

Parameter Metrices	Performance Delivery Ratio (%)		
	MEAODV	EAODV	Normal AODV
No. of Nodes			
40 nodes	76	72	6
60 nodes	81	62	7
80 nodes	84	69	8
100 nodes	89	70	7

TABLE 4
COMPARISON OF MEAODV WITH EAODV (IN PRESENCE OF THIRTY NODES)

Parameter Metrices	End-to-End Delay (msec)		
	MEAODV	EAODV	Normal AODV
No. of Malicious Nodes			
Zero malicious node	1471	1469	1467
One malicious node	1701	1993	1679
Two malicious node	1808	2090	1745
Three malicious node	2101	2203	1835

TABLE 5
COMPARISON OF MEAODV WITH EAODV (IN PRESENCE OF ONE MALICIOUS NODE)

Parameter Metrices	End-to-End Delay (msec)		
	MEAODV	EAODV	Normal AODV
No. of Nodes			
40 nodes	1209	1501	678
60 nodes	2103	2003	1156
80 nodes	1023	1386	908
100 nodes	2101	2203	1456

V. CONCLUSION

In this paper, we propose a black hole mitigating algorithm known as MEAODV whose performance delivery ratio is slightly greater and end to end delay is slightly less than EAODV method by varying malicious nodes. On increasing number of nodes, PDR increases comparatively to EAODV but end-to-end delay fluctuates. Our method provides a solution for mitigating black hole attack by controlling the routing update with new condition parameters and removing the redundancy in detecting malicious nodes. Results from above simulation shows that AODV with MEAODV method gives comparatively better performance as compare to AODV with EAODV method.

ACKNOWLEDGMENT

The author would like to thanks Dr. Daya Gupta for her guidance and support.

REFERENCES

- [1] Charles E. Perkins, and Elizabeth M. Royer, "Ad-Hoc On- Demand Distance Vector Routing", Proceedings of the Second IEEE Workshop on Mobile Computing Systems and Applications, Feb. 1999, pp. 90-100.
- [2] Zaid Ahmad, Kamarularifin Abd., and JalilJamalul-lail Ab Manan, "Black hole Effect Mitigation Method in AODV Routing Protocol", 2011 7th International Conference on Information Assurance and Security (IAS) IEEE 2011.
- [3] P. Raj and P. Swadas, *A dynamic learning system against black hole attack in AODV based MANET*, IJCSI International Journal of Computer Science, Vol.2, (2009).
- [4] E. A .Mary Anita, V. Vasudevan, Black Hole Attack Prevention in Multicast Routing Protocols for Mobile Ad hoc networks using Certificate Chaining, International Journal of Computer Applications (0975 – 8887) Volume 1 – No. 12 (2010).
- [5] Kamarularifin Abd. Jalil, Zaid Ahmad2, and Jamalul-Lail Ab Manan, "An Enhanced Route Discovery Mechanism for AODV Routing Protocol ", ICSECS 2011, Part III, CCIS 181, pp. 408–418, Springer- Verlag Berlin Heidelberg 2011.
- [6]Rajesh Yerneni, and Anil k. Sarje, "Secure AODV protocol to mitigate Black hole attack in Mobile Ad hoc Networks," ICCCNT' 2012 26th _28th July 2012, IEEE-20180, Coimbatore, India.
- [7]Vrutik Shah, and Nilesh Modi, " An inquisition based Detection and Mitigating Techniques of AODV Protocol in Existence of Packet Drop Attacks," International Journal of Computer Applications (0975 – 8887) Volume 69– No.7, May 2013.

Content based Image Retrieval: A Quantitative Comparison between Query by Color and Query by Texture

Sunkari Madhu

School of computing science & Engineering, Galgotias University, Greater Noida, Uttar Pradesh, India

Email: madhu.dtu@gmail.com

Abstract—Effective and efficient image retrieval techniques have become the fast and active research area because of explosive use of digital images. User interaction in CBIR system consists of a query formation. The user has problems in declaration of a query with different schemes which has been introduced in literature. In this paper, we analyze the two retrieval method, query by texture and query by color. Texture features involves the invariant histogram characteristics to retrieve the images and color features carry the color histogram in RGB color space to retrieve the images. It is observed from the experimental results, that the query by texture is more effective than the query by color for retrieving the general images.

Index Terms—invariant histogram, Image retrieval performance, query by Texture, query by color

I. INTRODUCTION

The term CBIR can be defined as to retrieve the image from low level features like color, texture, shape and spatial information [3], [10]. The most important challenge of CBIR system is to determine the exact/approximate matching image of database to the query image. Interaction of users in CBIR system is of vital worth [4], [24]. CBIR techniques extract content based features namely color, texture and shape from the image systematically and by comparison between query and database image determined by the corresponding difference between the features of images from distance function. Content based visual features are categorized into two domains; that is common visual content and Field Specific visual content like face recognition, task dependent applications we discuss only general visual contents here. This paper mainly focuses on the two features of CBIR i.e. Color and Texture. According to the features of these two, they both performed well in the retrieval process of general images, other features of CBIR Shape and spatial location performs well for example bio medical images, object oriented images such as buildings and tower [1]. From the comprehensive experimental results it is found that, Invariant Histogram perform well in many task dependent application, so it

can be recommended for every general image retrieval application.

Features of Color mainly color histogram and RGB color space have been addressed in detail in Section 2. Later on texture features have been discussed in section 3, experiment results and performance evaluation of CBIR system in Sections 4. In the end, in Section 5 we concluded the paper.

II. COLOR FEATURE

Color is a dominant and distinguishable feature for image retrieval. Mostly CBIR systems use color space, histogram, moments and color coherence vector to represent color [7]. Color feature is one of the most widely used features in low-level feature [18]. Compared with shape feature and spatial location feature, its results shows efficient stability and also have insensitive results to the rotation and zoom of image. Color histogram [19] is widely used to represent color feature. In this paper, histogram-based search method is investigated in RGB color spaces.

A. Color Spaces

Color space consists of three dimensional spaces and color is used as a vector in it. Color Spaces are required for description of color based retrieval of image [11]. Mostly RGB, LAB, LUV, HSV, YCrCb and opponent color space are used for color space. The selection of color space is done from *uniformity* characteristics [12], [23] and uniformity means to have colors points that have similar distance in color space as perceived by human eye.

B. Color Histogram

It is a standard demonstration of color characteristic in CBIR systems [13], [20]. It is very efficient in description of both local and global features of colors [14]. This computes the chromatic information and invariant of image along the view axes for translation and rotation, when the large scale image data base computes histogram, its efficiency is not satisfactory and to overcome this conflict joint histogram technique is introduced [15], [22]. Color histograms is a fundamental technique for retrieving images and extensively used in CBIR system [8], [25]. The color space has segmentation, for every segment the pixels of the color within its bandwidth are counted, which shows the relative

frequencies of the counted colors. We use the RGB color space for the histograms. Only minor differences have been observed with other color spaces for the histogram in [19]. Color Histogram $H(m)$ is a distant probability function of the image color [1]. This probability function is used for the determination of joint probability function for the intensities of the three color channels. Further informally, the color histogram is defined as [9], [21].

$$h_{a,b,c} = N \cdot \text{prob}(a,b,c)$$

where a, b, c represent the three color channel (RGB)

$$H(m) = [h_1, h_2, \dots, h_n]$$

$$H_k = n_k / N, k=1, 2, \dots, n;$$

where N is the number of pixel image M and n_k is the number of pixel with the image value k .

III. TEXTURE FEATURES

Texture is an essential feature for general images. But yet still not the comprehensive definition of it exist. Even though rough definition of it described in [2] as, A texture can be defined as gray level basic elements and spatial organization of these. The gray level elements may be single pixels and the Spatial location may be random, depend on one or more periodic primitives etc. based on corresponding matrices, autocorrelation, digital transformation techniques, textural edginess, morphological methods, A comprehensive detail of these techniques has been given in [4]. Texture feature definition for computer vision application is defined as a description of local shape and color feature or in a more comprehensive way it is defined as structure and randomness [16]. Structural methods consist of graphical method which tends to be more effective when applied to the texture [17].

A. Invariant Image Features

Invariant image feature have certain trans-formations that is translation, rotation and scaling. The characteristic of image features is, it does not change when the transformation are applied. In these work, invariant feature histograms is used as described in [5]. The proposed method is to compute the invariant features with transformation from the integration over all considered on transformation features and construction of image features technique for the gray scale image described in [6]. We will address image features which are invariant with respect to rotation and translation transformation. For a given an image M and complex valued function $f(M)$ it is possible to construct an invariant features $A[f](M)$ by integrating $f(gM)$ over the transformation group G :

$$A[f](M) = dg$$

This averaging technique for constructing the image feature is explained in detail [11] for general transformation group.

B. Invariant feature Histogram

Initially invariants mention above can be used for describing an image invariantly, although for texture

categorization we have stochastic texture. We therefore see an advantage of using invariant histogram of the local computations instead of the summation of these.

As the histogram is invariant with respect to the image translation, we may consider the histogram equation in [2] as

$$A(f)[M] = d$$

Which are the local computations within the two step integration. Note that $A(f)[M]$ is not a scalar anymore but of the same dimension as M i.e for each image point $M(i,j)$ a local invariant feature $[A(f)[M](i,j)]$ is calculated from circular neighborhood around (i,j) . The feature value of a pixel remain same as the one of its transformed pixel, which is generally located at another index. So $(A(f)[M](i,j))$ is itself not invariant but the histogram of $A(f)[M]$ is.

IV. EXPERIMENTS

The performance evaluation has been investigated to examine the behavior of Query by Color and Query by Texture. User were assigned to search for target image from mat lab application of CBIR system. Image queries have been conventionally presented using example image query image or the group of example image (query by group example) in CBIR systems. Mat lab application has been developed as prototypes of QBC and QBT.

A. Image Database

In the experiment, different image classification has been used for small image database. Comprehensive set of images having sub set of images like flowers, leaves, sky, faces, tiger, cone shapes, mountains etc.

Procedure:

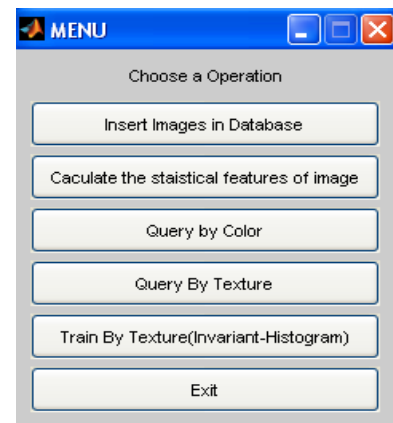


Figure 1. Feature dialog

CBIR system's job is to compute the most relevant images for given image query. User were given two jobs in mat lab application, retrieving the images by QBC and finding pre-selected target image from texture features. Subject were asked to select menu options using a feature dialog as shown in Fig. 1. Features of the images in the application were scheduled in a tree-structure foam. For example in the flower image database, No. of flowers and major color of the flower is listed. Subject have choice to carry on their image retrieving

process as much as they want to have relevant images .In the prototype of QBT, subjects were given a query images, and resubmit the queries unless they searched the exact image .The time taken to complete the task has been observed for both query features.

B. Graphical User Interface of QBC and QBT

The user was first given the GUI as shown in Fig. 1. The first and second menu option is used for inserting more images in database and calculating the statistical feature of database images.

Once the user done with the image inserting, then the user interface as shown in Fig. 2 appeared if QBC for Red is clicked. When the user started the searching process, an example image has been provided from the database. The best most similar images are retrieved from the database as a results as shown in Fig. 3. Upon receiving the results, user verify the result are relevant or not and resubmit another query image from the result to get the best results. The user may keep on doing the same process to refine the query for obtaining better results.

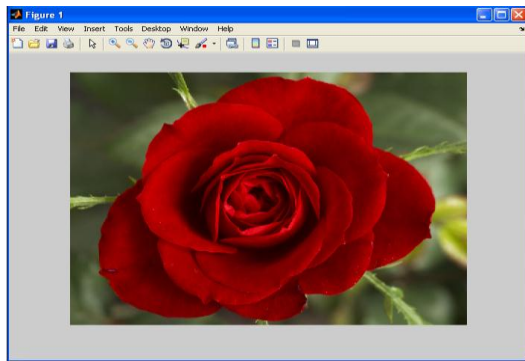


Figure 2. User interface of query image by color for Red

And next frame shown search result images. The order of ranking was top to bottom; left to right. The first rank was omitted because it was the example image for the query.

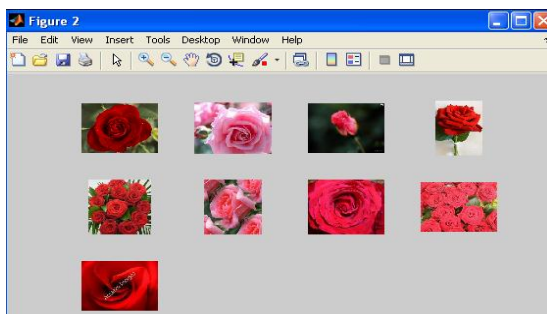


Figure 3. User interface of result panel of QBC for Red

The user interface as shown in Fig. 4 appeared if QBC is clicked. When the user started the searching process, an example image has been provided from the database. The best most similar images are retrieved from the database as a results as shown in Fig. 5. Upon receiving the results, user verify the result are relevant or not and resubmit another query image from the result to get the best results.

And next frame shown search result images. The order of ranking was top to bottom; left to right. The first rank

was omitted because it was the example image for the query.



Figure 4. User interface of query image by color for green



Figure 5. User interface of result panel of QBC for Green

The user interface as shown in Fig. 6 appeared if QBC is clicked. When the user started the searching process, an example image has been provided from the database. The best most similar images are retrieved from the database as a results as shown in Fig. 7. Upon receiving the results, user verify the result are relevant or not and resubmit another query image from the result to get the best results.



Figure 6. User interface of query image by color for Blue

And next frame shown search result images. The order of ranking was top to bottom; left to right. The first rank was omitted because it was the example image for the query.

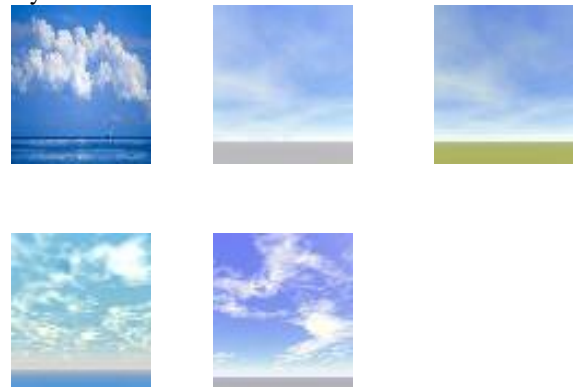


Figure 7. User interface of result panel of QBC for Blue

If the QBT prototype was clicked by the subject, the same dialog box was given to the subjects as appeared in Fig. 4 similar to that for query image by color. And the searching process is similar to the above mentioned task,

except it ended only when the subject found the target image. Subject carried out a searching process until the target was found and the time taken is recorded. The example query image and results of query by texture are shown as in Fig. 4 and 5.

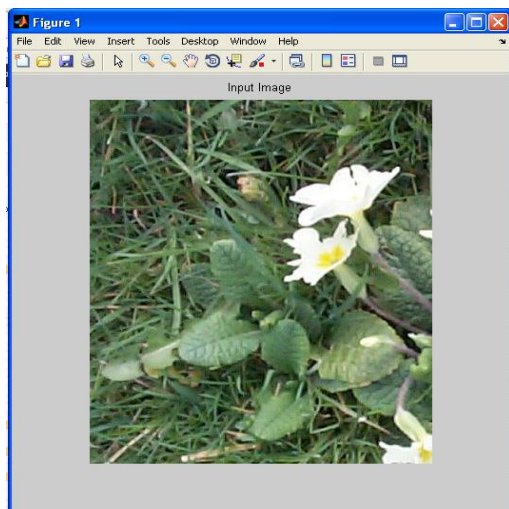


Figure 8. User interface of query image by texture

And next frame shown search target image.

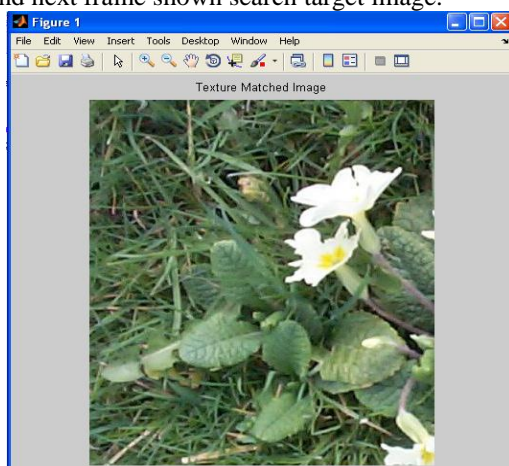


Figure 9. User interface of result panel of QBT

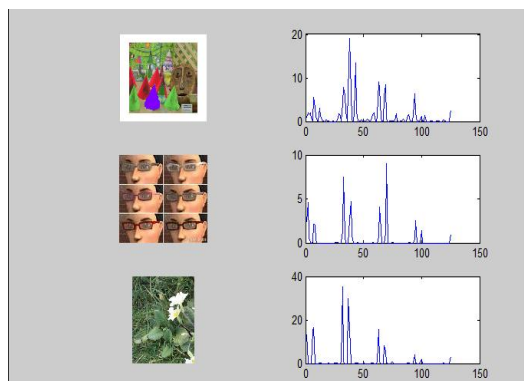


Figure 10. Graphical representation of images' invariant histogram

Subject might find the relevant image in the pop up window of result panel, and might continue to explore further results; until they decided to exit the system. The

texture feature has been extracted using invariant feature Histogram.

The Histogram of an image described the every pixel of image and its brightness level. The bottom of the graph represent the brightness level of each bin, corresponding to each brightness level, there is a vertical line which represent how many of pixel are there.

C. Experimental Results

The experimental result of both query interface are shown in Table I. Comparison are made between QBC and QBT using a small image database .T-test is conducted to determine if the difference is significant between these to query example. It is found that more relevant images are found using query by texture on every type of general images. The constraints of QBE is that the accomplishment of most similar image set is strongly depends on the initial set of image queries Experimental results shows that there is significant difference among the performance of both query method, and QBT is proven to produce better results in terms of identifying more relevant images and successfully retrieving a target image. The difference is found to be significant at p. 05 for the small image database. However, when the size of image database is large, the difference in total time taken and the average time taken per query between QBC and QBT are insignificant; it's mainly due to the more significant number of interactions with QBT prototype. The page zero problem in QBC avoids identifying more relevant images because they are not able to acquire better examples to submit as queries after a number of trails. It is understandable that user is more able to find a target image using QBT. In QBT the task is to find a target image instead of as many relevant images as possible. There are no significant difference between using QBT and QBC in other measurement except in the number of queries, at the p 0.01. We conclude that QBT provides more functionalities and capabilities to produce better performance in terms of identifying more relevant and approximately retrieving a target image successfully.

TABLE I

Prototype	Statistical features	QBT	QBC	p-value
No. of relevant images	Mean	118.34	104.28	.05*
	Std	78.68	84.10	.05
No .of queries	Mean	29.05	27.89	.05
	Std	24.20	17.43	.05
Total time taken	Mean	25.61	29.56	.05
	Std	22.11	26.78	.05

V. CONCLUSION

In this paper, we investigated two features for the query image of content based image retrieval, query by color and query by texture. These features have different characteristics to retrieved the more relevant images Retrieving process is done on the basis of Color

histogram in RGB space for query by color and Invariant histogram for query by texture. Invariant histogram has more functionalities and capabilities for the most relevant image to the representative labeled images on GUI. The results of a user evaluation shows that QBT out performs QBC. Considerably more most relevant images are recognized when the query image is taken QBT. A noticeable efficient rate in searching a most similar image is obtained.

REFERENCES

- [1] C. C. Yang, "Content-based image retrieval: A comparison between query by example and image browsing map approaches," *Journal of Information Science*, 2004.
- [2] S. Siggelkow and H. Burkhart, "Local invariant feature histogram for texture classification," 1997.
- [3] W. M. Arnold, M. W. Smeulders, S. Santini, A. Gupta, and R. Jain, "Content-based image retrieval at the end of the early years," *IEEE Transactions on Pattern Analysis and Machine Intelligence*, vol. 22, no. 12, December 2000.
- [4] N. Baaziz, O. Abahmane, and R. Missouri, "Texture feature extraction in the spatial-frequency domain for content-based image retrieval," *Computer Vision and Pattern Recognition*, Department of Computer Science and Engineering, University du Qu'bec en Outaouais 101 rue Saint Jean Bosco, C. P. 1250, Gatineau, Qu'bec, J8X 3X7 Canada, 2010.
- [5] S. Siggelkow, "Feature histograms for content-based image retrieval," Ph.D. thesis, University of Freiburg, Institute for Computer Science, Freiburg, Germany, 2002.
- [6] A. H. El-Kholy and A. M. Abdel-Haleim "Content-based image retrieval using combined features and weighted similarity," in *Proc. 2nd International Conference on Computer Technology and Development*, 2010.
- [7] G. Rafiee, S. S. Dlay, and W. L. Woo "A review of content based image retrieval database," *Science Citation Index Expanded (SCI-EXPANDED) and Conference Proceedings Citation Index-Science (CPCI-S)*.
- [8] T. Deselaers, D. Keysers, and H. Ney, "Features for image retrieval: An experimental comparison," *Image Understanding and Pattern Recognition*, 2008.
- [9] J. H. Wu, Z. R. Wei, and Y. L. Chang, "Color and texture feature for content based image retrieval," *International Journal of Digital Content Technology and Its Applications*, vol. 4, no. 3, June 2010.
- [10] T. Deselaers, D. Keysers, and H. Ney, "Features for image retrieval: A quantitative comparison," *Lehrstuhl F'ur Informatik VI*, 2004.
- [11] H. Schibulz-Mirbach, *Invariant Gray Scale Features*.
- [12] J. Puzicha, Y. Rubner, C. Tomasi, and J. Buhmann, "Empirical evaluation of dissimilarity measures for color and texture," in *Proc. Int. Conf on Computer Vision*, Sept. 1999, vol. 2, pp. 1165–1173.
- [13] A. B. Rao, R. K. Srihari, and Z. F. Zhang, "Spatial color histograms for content-based image retrieval," in *Proc. 11th IEEE International Conference on Tools with Artificial Intelligence*, 1999, pp. 183-186
- [14] P. Aigrain, H. Zhang, and D. Petkovic, "Content-based representation and retrieval of visual media: A state of the art review, multimedia tools and applications," *Multimedia Tools and Applications*, vol. 3, pp. 179-202, 1996.
- [15] Siggelkow, "Feature histograms for content-based image retrieval," Ph.D. thesis, University of Freiburg, Institute for Computer Science, Freiburg, Germany, 2000.
- [16] H. Tamura, S. Mori, and T. Yamawaki "Texture features corresponding to visual perception," *IEEE Trans. on Systems, Man, and Cybernetics*, vol. SMC-8, no. 6, June 1978.
- [17] H. Voorhees and T. Poggio, "Computing texture boundaries from images," *Nature*, vol. 333, pp. 364-367.
- [18] Th. Gevers, *Color Based Image Retrieval*, Springer Verlag GmbH, 2001, pp. 886-917.
- [19] H. B. Kekrel, P. Mukherjee, and S. Wadhwa, "Image retrieval with shape features extracted using gradient operators and slope magnitude technique with BTC," *International Journal of Computer Applications*, vol. 6, no. 8, September 2010.
- [20] H. B. Kekre and S. D. Thepade, "Image retrieval using augmented block truncation coding techniques," in *Proc. International Conference on Advances in Computing, Communication and Control*, 2009.
- [21] M. Mocofan, I. Ermalai, M. Bucos, M. Onita, and B. Dragulescu, "Supervised tree content based search algorithm for multimedia image databases," in *Proc. 6th IEEE International Symposium on Applied Computational Intelligence and Informatics*, Timioara, Romania, May 19-21, 2011.
- [22] G. J. Lu, "Techniques and data structures for efficient multimedia retrieval based on similarity," *IEEE Transactions on Multimedia*, vol. 4, no. 3, September 2002.
- [23] J. M. Kim, W. D. Cai, D. G. Feng, and H. Wu, "A new way for multidimensional medical data management: Volume of interest (VOI)-based retrieval of medical images with visual and functional features," *IEEE Transactions on Information Technology in Biomedicine*, vol. 10, no. 3, pp. 598-607, 2006.
- [24] T. Yeh, K. Tollmar, and T. Darrell, "Searching the Web with mobile images for location recognition," in *Proc. IEEE Computer Society Conference on Computer Vision and Pattern Recognition*, 2004.
- [25] L. Xavier, B. M. I. Thusnavis, and D. R. W. Newton, "Content based image retrieval using textural features based on pyramid-structure wavelet transform," in *Proc. 3rd International Conference on Electronics Computer Technology*, 8-10 April 2011, pp. 79-83

Sunkari Madhu, Nizamabad, Andhra Pradesh, India completed his Master of Technology (M.Tech) in Information Systems from Delhi Technological University, DELHI. Before that he completed his Master of computer applications (M.C.A) from University College of Engineering, Osmania University, Hyderabad, and Andhra Pradesh. His area of interest is Image processing. Madhu qualified National Eligibility Test(N.E.T) with Junior Research Fellowship(J.R.F) which was conducted by University Grants Commission(U.G.C),India. He has Qualified Andhra Pradesh State Eligibility Test(A.P.S.E.T) which was conducted by Osmania University,Hyderabad,Andhra Pradesh and also qualified Graduate Aptitude Test in Engineering (GATE) 2 times(2010,2012)Which was conducted by Indian Institute of Technologies(IITs).

Day Ahead Hourly Load and Price Forecast in ISO New England Market using ANN

Kishan Bhushan Sahay
Department of Electrical Engineering
Delhi Technological University
New Delhi, India
kishansahay16@gmail.com

M. M Tripathi
Department of Electrical Engineering
Delhi Technological University
New Delhi, India
mmtripathi@dce.ac.in

Abstract—In restructured daily power markets, forecasting electricity price and load are most essential tasks and basis for any decision making. Short-term load forecasting is an essential instrument in power system planning, operation, and control. Also, the accurate day ahead electricity price forecasting provides crucial information for power producers and consumers to develop accurate bidding strategies in order to maximize their profit. In this paper artificial intelligence (AI) has been applied in short-term load and price forecasting that is, the day-ahead hourly forecast of the electricity market parameters (load and price) over a week. Neural network fitting tool of MATLAB Software has been used to compute the forecasted load and price in ISO New England market. The data used in the forecasting are hourly historical data of the temperature, electricity load and natural gas price of ISO New England market. The ANN was trained on hourly data from the 2007 to 2011 and tested on out-of-sample data from 2012. The simulation results have shown highly accurate day-ahead forecasts with very small error in load and price forecasting.

Keywords—Day ahead electricity price forecast, locational marginal price (LMP), mean absolute percentage error, neural network, power system, short-term load forecasting.

I. INTRODUCTION

With the introduction of deregulation in power industry, many challenges have been faced by the participants in the emerging electricity market. Forecasting electricity parameters such as load and price have become a major issue in deregulated power systems [1]. The fundamental objective of electric power industry deregulation is efficient generation, consumption of electricity, and reduction in energy prices. To achieve these goals, accurate and efficient electricity load and price forecasting has become more important [2].

Accurate forecasting of electricity demand not only will help in optimizing the startup of generating units it also save the investment in the construction of required number of power facilities and help to check the risky operation and unmet demand, demand of spinning reserve, and vulnerability to failures [3]-[4].

Price forecasting provide crucial information for power producers and consumers to develop bidding strategies in order to maximize profit. It plays an important role in power system planning and operation, risk assessment and other decision making. Its main objective is to reduce the cost of electricity

through competition, and maximize efficient generation and consumption of electricity. Because of the non-storable nature of electricity, all generated electricity must be consumed. Therefore, both producers and consumers need accurate price forecasts in order to establish their own strategies for benefit or utility maximization [5].

In general, electricity demand and price in the wholesale markets are mutually intertwined activities. Short-term load forecasting is mainly affected by weather parameters. However, in short-term price forecasting, prices fluctuate cyclically in response to the variation of the demand. Many factors which influence the electricity price, such as hour of the day, day of the week, month, year, historical prices and demand, natural gas price etc. The ISO New England market is co-ordinated by an independent system operator (ISO). In the ISO New England market, it is observed that daily power demand curves having similar pattern, but the daily price curves are volatile. Therefore, forecasting of LMPs become more important as it helps market participants not only to determine the bidding strategies of their generators, but also in risk management [5].

Various AI techniques used in load and price forecasting problem are expert systems, fuzzy inference, fuzzy-neural models, artificial neural network (ANN). Among the different techniques of forecasting, application of ANN for forecasting in power system has received much attention in recent years [6]-[9]. The main reason of ANN becoming so popular lies in its ability to learn complex and nonlinear relationships that are difficult to model with conventional techniques [10].

In this paper, neural Network fitting tool of MATLAB has been used to compute the short-term load and price forecast in ISO New England market. Both the hourly temperature and hourly electricity load, historical data have been used in forecasting. The temperature variable is included because temperature has a high degree of correlation with electricity load. In price forecasting hourly natural gas data has been also considered as an input for forecast. The neural network models are trained on hourly data from the NEPOOL region (ISO New England), from 2007 to 2011 and tested on out-of-sample data from 2012. The simulation results obtained have shown that artificial neural network (ANN) is able to make very accurate short-term load and price forecast. Box plots [11] of the error distribution of forecasted load and price has been plotted as a

function of hour of the day, day of the week and month of the year.

The paper has been organized in five sections. Section II presents the overview of neural network used. Section III discusses the selection of various data and model of ANN for day-ahead load and price forecasting. Results of simulation are presented in Section IV. Section V discusses the conclusion and future work.

II. ARTIFICIAL NEURAL NETWORK FOR LOAD AND PRICE FORECASTING

Neural networks are composed of simple elements called neuron, operating in parallel. A neuron is an information processing unit that is fundamental to the operation of a neural network. The three basic elements of the neuron model are. A set of weights, an adder for summing the input signals and activation function for limiting the amplitude of the output of a neuron [12]. Artificial neural network is inspired by biological nervous systems. The Fig. 1 illustrates a situation. A neural network can be trained to perform a particular function by adjusting the values of the connections (weights) between elements. In load forecasting, typically, many input/target pairs are needed to train a neural network.

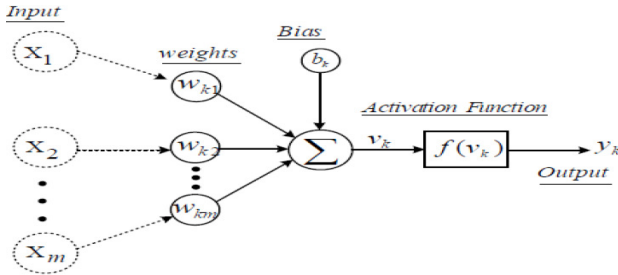


Fig. 1. Model of an artificial neural network (ANN).

In fitting problems, neural network is mapped between data set of numeric inputs and a set of numeric targets. The neural network fitting tool consists of two-layer feed-forward network with sigmoid hidden neurons and linear output neurons. It can fit multi-dimensional mapping problems arbitrarily well, given consistent data and enough neurons in its hidden layer. The neural network is trained with Levenberg-marquardt back propagation algorithm [13].

III. DATA INPUTS AND ANN MODEL

The models are trained on hourly data from the NEPOOL region (ISO New England) from 2007 to 2011 and tested on out-of-sample data from 2012. The data used in the ANN model are historical data of both the temperature and hourly electricity load. The relationship between demand and average temperature is shown in Fig. 2, where a close relationship between load and temperature can be observed. Hourly temperature data for location in high demand area of NEPOOL region has been considered in this paper. Relationship between LMP and system load for NEPOOL region in year 2012 is shown by Fig. 3. It shows that as the system load increases

with LMP and both are highly correlated. Fig. 4 shows the effect of natural gas price on LMP for ISO New England market and both are interdependent.

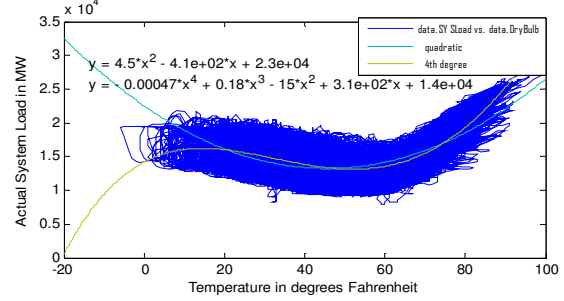


Fig. 2. Scatter plot of system load vs. temperature (degrees Fahrenheit) for NEPOOL region (ISO New England) for year 2007 to 2012 with fitting equation of quadratic and 4th degree.

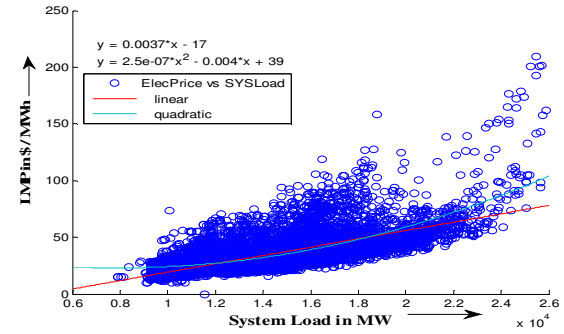


Fig. 3. Relationship between LMP and load in NEPOOL region for the year 2012 with linear and quadratic fitting equation.

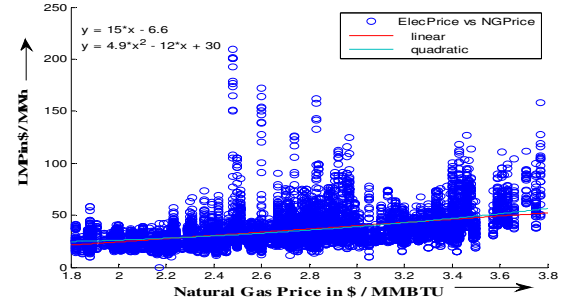


Fig. 4. Relationship between LMP and natural gas price by scatter plot for ISO New England market in year 2012 with fitting equations.

The ANN model includes creating a matrix of inputs from the historical data, selecting and calibrating the chosen model and then running the model. For the load forecast, the inputs include

- Dry bulb temperature
- Dew point temperature
- Hour of day
- Day of the week
- Holiday/weekend indicator (0 or 1)
- Previous 24-hr average load

- 24-hr lagged load
- 168-hr (previous week) lagged load

Similarly for price forecast, the inputs include

- Dry bulb temperature
- Dew point temperature
- Hour of day
- Day of the week
- Holiday/weekend indicator (0 or 1)
- System load
- Previous day's average load
- Load from the same hour the previous day
- Load from the same hour and same day from the previous week
- Previous day's average price
- Price from the same hour the previous day
- Price from the same hour and same day from the previous week
- Previous day's natural gas price
- Previous week's average natural gas price

IV. SIMULATION AND RESULTS

In this paper hourly day-ahead load and price forecasting has been done for sample of each week of data of year 2012 using neural network tool box of MATLAB R12a. The ANNs are trained with data from 2007 to 2011 of ISO New England market. The test sets are completely separate from the training sets and are not used for model estimation or variable selection. Various plots of the error distribution as a function of hour of the day, day of the week and month of the year are generated. Also, the various plots comparing the day ahead hourly actual and forecasted load and price for every weeks for the year 2012 are also generated. Simulation results of new ISO England market is discussed below.

A. Load Forecasting of New England Pool region (ISO New England)

In The ANN's accuracy on out-of-sample periods is computed with the Mean Absolute Percent Error (MAPE) metrics. The principal statistics used to evaluate the performance of these models, mean absolute percentage error (MAPE), is defined in eq. 1 below

$$MAPE [\%] = \frac{1}{N} \sum_{i=1}^N \frac{|L_A^i - L_F^i|}{L_A^i} \times 100 \quad (1)$$

where L_A is the actual load, L_F is the forecasted load, N is the number of data points.

The ANN model used in the forecasting has input, output and one hidden layers. Hidden layer has 48 neurons. Inputs to the neurons are listed above. After simulation the MAPE obtained is 1.59% for load forecasting for the year 2012, as shown in Fig. 5.

The box-plot of the error distribution of forecasted load as a function of hour of the day is presented in Fig. 6. It shows the

percentage error statistics of hour of the day in year 2012. It is also evident that the maximum error is for the 21st hour of the day and minimum error for 14th hour of the day in year 2012. The box-plot of the error distribution of forecasted load as a function of day of the week is evaluated in Fig. 7 which shows the percentage error statistics of day of the week in year 2012. The maximum error is for the Monday and minimum error for Saturday in year 2012. The box-plot of the error distribution of forecasted load as a function of month of the year 2012 is evaluated in Fig. 8. The figure indicates that the maximum error is for the October 2012 and minimum error is for May 2012.

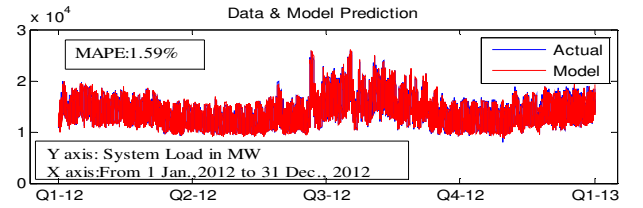


Fig. 5. Multiple series plot between actual load & forecasted load by using ANN in NEPOOL region (ISO New England) for year 2012.

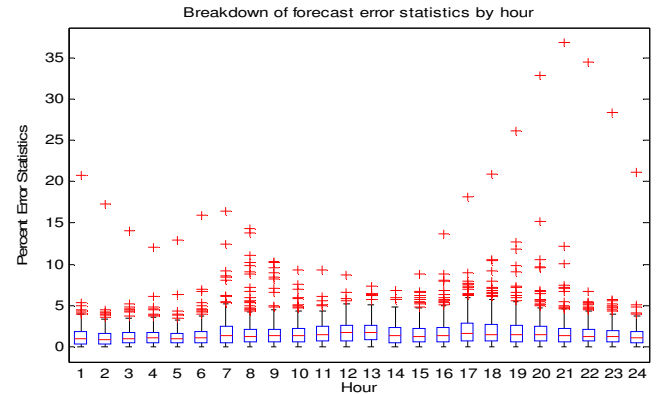


Fig. 6. Box-plot of the error distribution of forecasted load as a function of hour of the day for year 2012.

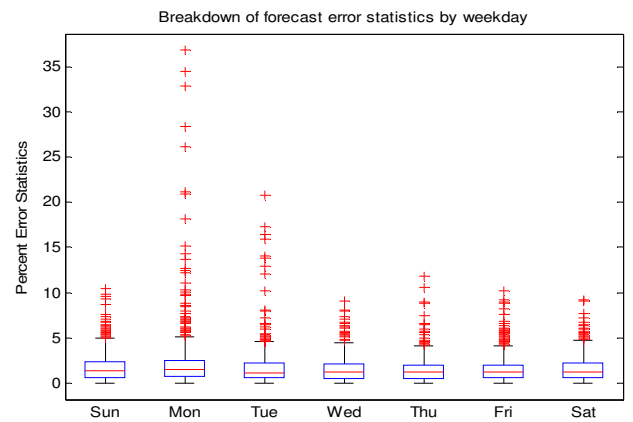


Fig. 7. Box-plot of the error distribution for the forecasted load as a function of day of the week in the year 2012.

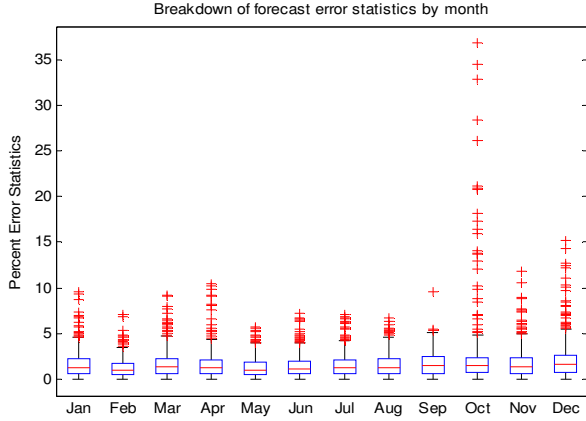


Fig. 8. Box-plot of the error distribution of forecasted load as a function of month of the year for the year 2012.

Multiple series plots between actual load & forecasted load from 29 January, 2012 to 04 February, 2012 & from 28 October, 2012 to 03 November, 2012 for NEPOOL region (ISO New England) and also plots of MAPE with maximum error (3.87%) and minimum error (0.90%) have been shown in Fig. 9 and Fig. 10.

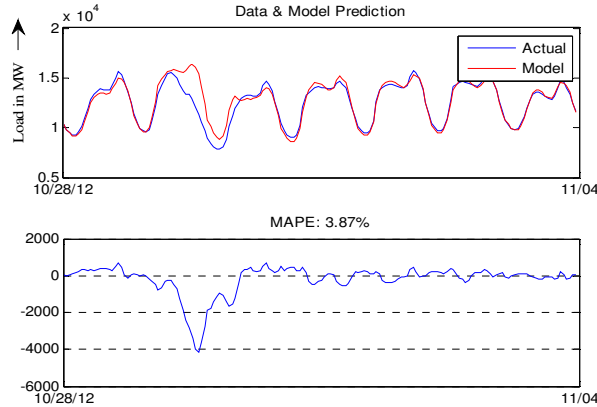


Fig. 9. Maximum MAPE is 3.87% for the load forecast of 28 October, 2012 to 03 November, 2012 NEPOOL region (ISO New England).

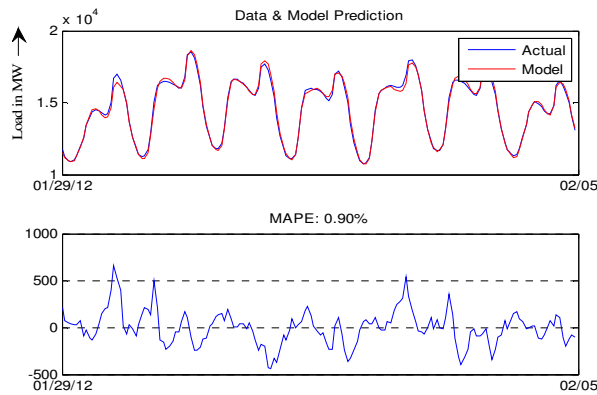


Fig. 10. Minimum MAPE is 0.90% for the load forecast of 29 January, 2012 to 04 February, 2012 NEPOOL region (ISO New England).

B. Price Forecasting of New England Pool region (ISO New England)

For price forecasting the accuracy of forecast is accomplished by MAPE, this is computed as in eq. 2 below

$$MAPE [\%] = \frac{1}{N} \sum_{i=1}^N \frac{|P_A^i - P_F^i|}{P_A^i} \times 100 \quad (2)$$

Where P_A and P_F are the actual and forecasted hourly prices, N is the number of hours, and i is the hour index.

The ANN model used in the forecasting has input, output and one hidden layers. Hidden layer has 22 neurons. The 14 different inputs to the input layer are same as specified above for price forecast. We were able to obtain an MAPE 9.25% for price forecasting in the year 2012, which is shown in Fig. 11.

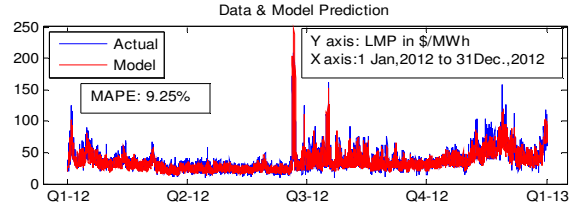


Fig. 11. Multiple series plot between actual & forecasted price by using ANN in NEPOOL region (ISO New England) for year 2012.

The box-plot of the error distribution of forecasted price as a function of hour of the day is evaluated in Fig. 12. It shows the percentage error statistics of hour of the day in year 2012. It is clear that the maximum error is for the 8th hour of the day and minimum error for 1st hour of the day in year 2012. The box-plot of the error distribution of forecasted price as a function of day of the week is evaluated in Fig. 13. It shows the percentage error statistics of day of the week in year 2012. The maximum error is for the Saturday and minimum error for Monday in year 2012. The box-plot of the error distribution of forecasted price as a function of month of the year is evaluated in Fig. 14 which shows the percentage error statistics of month of the year in year 2012. The maximum error is for the June month and minimum error for February.

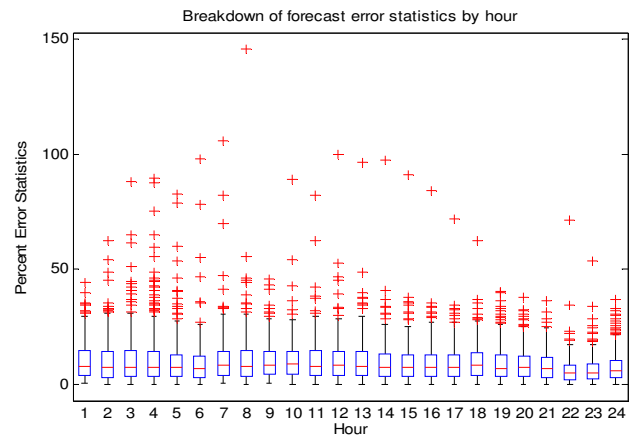


Fig. 12. Box-plot of the error distribution of forecasted price as a function of hour of the day for year 2012.

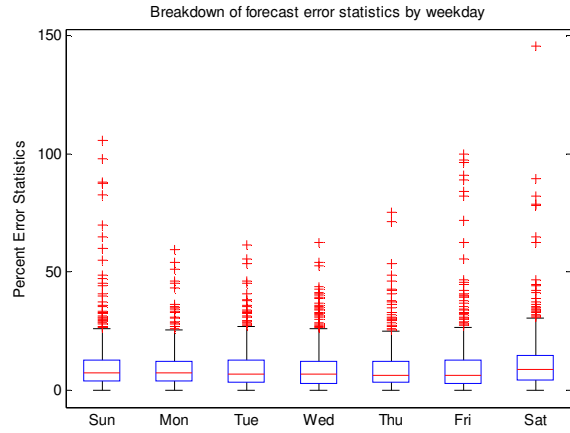


Fig. 13. Box-plot of the error distribution for the forecasted price as a function of day of the week in the year 2012.

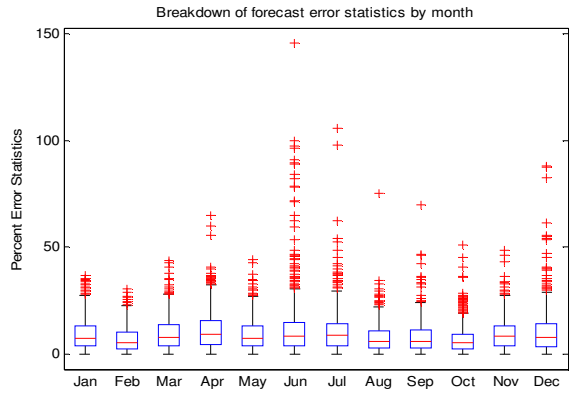


Fig. 14. Box-plot of the error distribution of forecasted price as a function of month of the year for the year 2012.

Multiple series plots between actual price & forecasted price from 17 June, 2012 to 23 June, 2012 & from 07 October, 2012 to 13 October, 2012 and also plots of MAPE with maximum error (19.87%) and minimum error (5.60%) have been shown in Fig. 15 and Fig. 16.

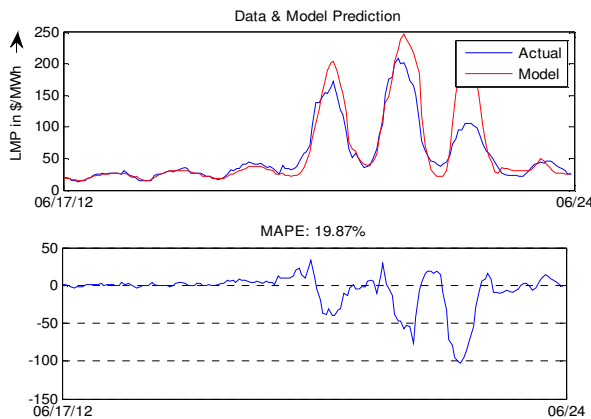


Fig. 15. Maximum MAPE is 19.87% for the price forecast of 17 June, 2012 to 23 June, 2012 in NEPOOL region (ISO New England).

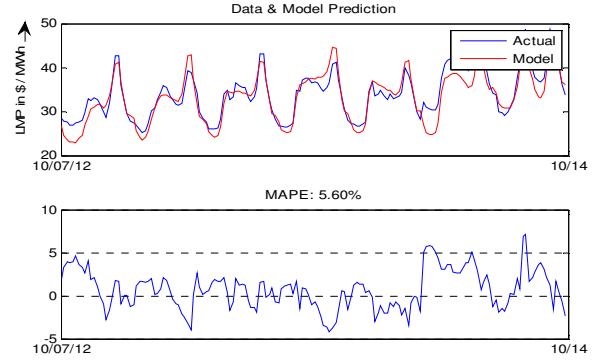


Fig. 16. Minimum MAPE is 5.60% for the price forecast of 7 October, 2012 to 13 October, 2012 in NEPOOL region (ISO New England).

The Mean Absolute Percentage Error (MAPE) between the forecasted and actual loads and prices for each week has been calculated and presented in the Table I for the year 2012. MAPE has been taken as a metric as a measure of error to show the effectiveness of the ANN over an average span of time. Most of time ANN is forecasting with minimum possible error and high absolute error at one or two instances may occur but effectiveness of ANN remains good most of the time. These errors may also be checked with more modifications in the ANN.

Comparison of MAPE (%) using different methods of load forecast has been shown in Table II with their maximum & minimum MAPE in their testing interval [1]-[10]. Also, from Table II it is clear that average MAPE is 1.59% for load forecast in the testing year 2012 by using ANN proposed in this paper. This is much better than the existing models of load forecast.

TABLE I
RESULTS FOR OUT-OF-SAMPLE TEST FOR YEAR 2012

S. N.	Duration mm/dd/yy -mm/dd/yy	MAPE (%)	
		Load	Price
1	01/01/12-01/07/12	2.03	11.23
2	01/08/12-01/14/12	1.24	8.72
3	01/15/12-01/21/12	1.39	10.61
4	01/22/12-01/28/12	1.79	6.46
5	01/29/12-02/04/12	0.90 (min)	7.25
6	02/05/12-02/11/12	1.22	6.57
7	02/12/12-02/18/12	1.13	6.88
8	02/19/12-02/25/12	1.36	6.49
9	02/26/12-03/03/12	1.49	9.13
10	03/04/12-03/10/12	1.59	8.19
11	03/11/12-03/17/12	1.96	7.71
12	03/18/12-03/24/12	1.73	9.64
13	03/25/12-03/31/12	1.32	11.64
14	04/01/12-04/07/12	1.61	8.70
15	04/08/12-04/14/12	1.34	11.37
16	04/15/12-04/21/12	1.80	12.58
17	04/22/12-04/28/12	1.53	12.15
18	04/29/12-05/05/12	1.45	9.79
19	05/06/12-05/12/12	0.93	8.78
20	05/13/12-05/19/12	1.01	7.68
21	05/20/12-05/26/12	1.15	9.08
22	05/27/12-06/02/12	1.76	8.92

23	06/03/12-06/09/12	1.29	7.61
24	06/10/12-06/16/12	0.94	8.39
25	06/17/12-06/23/12	1.58	19.87 (max)
26	06/24/12-06/30/12	1.68	14.73
27	07/01/12-07/07/12	1.78	11.59
28	07/08/12-07/14/12	1.43	9.64
29	07/15/12-07/21/12	1.43	10.44
30	07/22/12-07/28/12	1.47	12.07
31	07/29/12-08/04/12	1.23	7.40
32	08/05/12-08/11/12	1.70	5.98
33	08/12/12-08/18/12	1.60	6.59
34	08/19/12-08/25/12	1.25	8.79
35	08/26/12-09/01/12	1.64	10.73
36	09/02/12-09/08/12	1.53	9.70
37	09/09/12-09/15/12	2.08	7.87
38	09/16/12-09/22/12	1.70	6.99
39	09/23/12-09/29/12	1.28	6.49
40	09/30/12-10/06/12	1.37	6.63
41	10/07/12-10/13/12	1.56	5.60 (min)
42	10/14/12-10/20/12	1.80	7.08
43	10/21/12-10/27/12	1.35	6.37
44	10/28/12-11/03/12	3.87 (max)	11.01
45	11/04/12-11/10/12	1.86	11.41
46	11/11/12-11/17/12	1.59	7.31
47	11/18/12-11/24/12	2.27	8.81
48	11/25/12-12/01/12	1.28	11.11
49	12/02/12-12/08/12	1.74	13.72
50	12/09/12-12/15/12	1.76	8.47
51	12/16/12-12/22/12	1.84	6.16
52	12/23/12-12/29/12	2.57	10.95

TABLE II
COMPARISON OF MAPE (%) USING DIFFERENT
METHODS OF LOAD FORECASTING

S.N.	Methods	Max. MAPE	Min. MAPE	Avg. MAPE
1	GRNN	4.00	1.80	2.90
2	Back Propagation	3.27	1.73	2.53
3	SVM	6.10	1.50	2.71
4	Dual SVM Hybrid	3.62	1.21	2.10
5	ARMA	10.34	1.53	4.77
6	Recurrent ANN	4.10	1.39	2.08
7	Modified ANN	3.90	1.82	2.81
8	Hybrid ANN	2.79	1.58	2.14
9	Similar Day Approach	4.95	0.65	-----
10	Multi stage ANN STLF Engine	6.39	2.81	4.85
11	SOM-SVM Hybrid	2.68	1.34	2.06
12	ANN Used in this Paper	3.87	0.90	1.59

V. CONCLUSION AND FUTURE WORK

This paper presented day-ahead short-term electricity load and price forecast by using artificial neural network (ANN) approach in NEPOOL region (ISO New England). In ISO New England market, the main challenging issue is that the daily market price curves are highly volatile. The simulation result produced accurate predictions even in volatility cases. The test results also confirm that the power demand is the most important variable affecting the electricity price. The ANN model used has forecasted load and price for every week of the year 2012 and results indicates that it has performed well in every week even in the case of sudden weather changes. The forecasting reliabilities of the ANN model were evaluated by

computing the MAPE between the exact and predicted electricity load and price values. The MAPE for load forecasting varies from 0.9% to 3.87% and it varies from 5.6% to 19.87% in the case of price forecasting. The average MAPE obtained is 1.59% for load forecast and average MAPE for price forecast is 9.25% in the year 2012. The results suggest that present ANN model with the developed structure can perform good prediction with least error. In future effect of other weather parameters like humidity, precipitation, and wind velocity on short-term load and price forecasting may be worked out. A hybrid ANN model will also be worked out to take care of some high error weeks and refine the forecasting.

REFERENCES

- [1] Michael Negnevitsky, Paras Mandal and Anurag K. Srivastava, "An Overview of Forecasting Problems and Techniques in Power Systems," *IEEE PES Conference*, pp. 1-4, ISSN: 1944-9925, ISBN: 978-1-4244-4241-6, July 2009.
- [2] Paras Mandal, Tomonobu Senjyu, Katsumi Uezato, and Toshihisa Funabashi, "Several-Hours-Ahead Electricity Price and Load Forecasting Using Neural Networks," *IEEE PES Conference*, vol. 3, pp. 2146-2153, ISBN:0-7803-9157-8, June 2005.
- [3] Shu Fan and Rob J. Hyndman, "Short-Term Load Forecasting Based on a Semi-Parametric Additive Model," *IEEE Trans. Power Syst.*, vol. 27, Issue 1, pp. 134-141, Feb. 2012.
- [4] Paras Mandal, Tomonobu Senjyu, Katsumi Uezato, and Toshihisa Funabashi, "Forecasting Several-Hours-Ahead Electricity Demand Using Neural Network," *IEEE Conference on Power Syst.*, vol. 2, pp. 515-521, April 2004.
- [5] Paras Mandal, Tomonobu Senjyu, Atsushi Yona, Jung-Wook Park and Anurag K. Srivastava, "Sensitivity Analysis of Similar Days Parameters for Predicting Short-Term Electricity Price," *IEEE Trans. Power Syst.*, E-ISBN: 978-1-4244-1726-1, pp. 568-574, September 2007.
- [6] M. M. Tripathi, K. G. Upadhyay, S. N. Singh, "Short-Term Load Forecasting using Generalized Regression and Probabilistic Neural Networks in the Electricity Market", *The Electricity*, Volume 21, Issue 9, November 2008, pp 24-34
- [7] M. M. Tripathi, K. G. Upadhyay, S. N. Singh, "Electricity Price Forecasting using General Regression Neural network (GRNN) for PJM Electricity Market", *International Review of Modeling and Simulation (IREMOS)* ISSN: 1974-9821, Volume 1, No. 2, December 2008, pp 318-324
- [8] M. M. Tripathi, K. G. Upadhyay, S. N. Singh, "A novel method of Load forecasting using GRNN and PNN techniques in PJM and Australian Electricity Market using Market pricing signal as input", *International Journal of Computer Application in Engineering, Technology and Science (IJ-CA-ETS)* ISSN: 0974-3596, Vol. 2, Issue 2, June - December 2009, pp. 604-610.
- [9] M. M. Tripathi, S. N. Singh, K. G. Upadhyay, "Price Forecasting in Competitive Electricity Markets: an analysis", *Proceedings of International Conference on Energy Engineering (ICEE-2009)*, Puducherry, India, 7-9 January 2009, paper no. EEE4214.
- [10] K. G. Upadhyay, M. M. Tripathi, S. N. Singh, "An Approach to Short Term Load Forecasting using Market Price Signal", *International Conference on Distribution (CIRED 2007)*, Vienna, Austria, 21-24 May 2007, paper 0487.
- [11] http://www.mathworks.in/matlabcentral/fileexchange/file_infos/28684-electricity-load-and-price-forecasting-webinar-case-study.
- [12] Balwant singh Bisht and Rajesh M Holmukhe, "Electricity load forecasting by artificial neural network model using weather data," *IJEET Trans. Power Syst.*, vol. 4, no. 1, pp. 91-99, Jan. 2013
- [13] Neural Network overview from Neural Network toolbox.
- [14] From Matlab-2012a Neural Network(NN) fitting toolbox(nftool).
- [15] <http://www.iso-ne.com/>
- [16] <http://www.wsj.com>.

Depth and Scale Modeling of Object for 3D Motion Analysis in Video

Gurjit Singh Walia
Scientist , Scientific Analysis Group
DRDO , Ministry of Defence
Delhi , India
*Corresponding author

Prof Rajiv Kapoor*, Satbir Singh
Delhi Technological University (Formerly DCE)
Department of Electronics and Communication,
Bawana Road, Delhi, India
rajivkapoor.dtu@gmail.com

Abstract: The aim of this paper is to introduce the robust models for scaling and speed relations, with reference to the 3D distance from the camera, in order to enhance the target tracking and localization efficiency. The estimated distances of the object, using our model, from the camera is useful for handling both, self-occlusion and inter-object occlusion efficiently. Apart from the above, scaling factor estimation is useful for efficiently tracking the object under multi person tracking scenario. In order to establish our models, we have taken different sets of video sequence from standard video set captured under different environments. Curve fitting methods were applied in order to deduce the robust scaling and speed model for 3D motion analysis in single view video sequences.

Keywords—Regression , GMM, Scaling, 3D distance

I. INTRODUCTION

With the advent of digital image processing, different fields in computer vision were explored for their application in surveillance, unmanned vehicles, traffic control, video profiling, airport traffic monitoring and activity analysis etc. for both defense and civil applications [1]. The proliferation of high computing facility, high frame rate cameras and interdisciplinary application for video analysis has generated great deal of interest among the researchers. Image processing is complex due to the conversion from 3D world to 2D world, noise in the image, clutter in the environments, change in illumination, occlusion, etc. The effect of scaling of object when it moves away or towards the camera was recognized by different authors [17, 18, 19]. It was reported in literature, that a good representation model, of the object greatly cater for the scaling effect of the object. However, still exhaustive analysis of this effect has been studied only to a limited extent. The main reason for this is that a great amount of data needs to be analyzed for developing robust model for scaling effect with respect to the 3D distance from the camera. Similarly, actual speed of the object when it is away from the camera needs to be studied for handling occlusion while tracking the object in the video sequences. The objects which are away from the camera appear slower in the camera video as compared to the objects which are nearer to the camera. A number of geometric properties of the object get affected while we transfer from 3D world to 2D world. The compression of data makes the actual object in the video appear either larger or smaller, as it approaches closer or moves away from the

camera. Similar effect is observed in the speed of the object with its motion towards or away from the camera.

Our research problem is better illustrated in figure 1. The scaling and speed of the object with reference to the distance of the object from the camera clearly points towards the problem statement of our present research work.

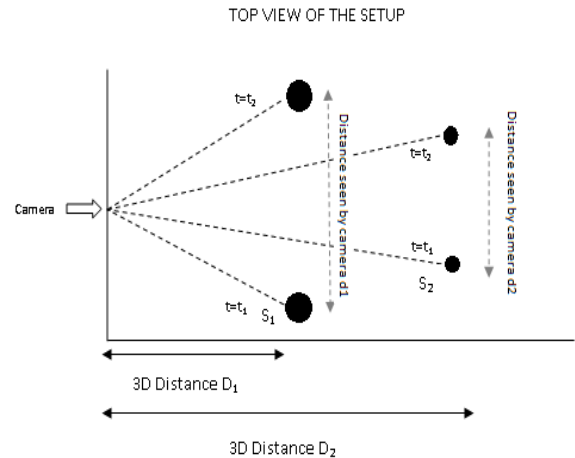


Figure 1: Scaling and Speed at different distance

Numbers of researcher are working towards the advancement of surveillance systems, but still most of the algorithms have prior assumptions which depend upon their application. Most of these algorithms have assumption such as small field of view, near/mid-field settings or top-down views [11, 12]. In general surveillance application needs wide area coverage as in traffic monitoring or scene-level activity modeling, thus the application of these algorithms where there is a pronounced effect of scaling and speed of the object, is questionable.

The scaling and speed problem was also catered through 3D reconstruction and camera calibration. Criminisi et al. [13] reconstructed 3D affine geometry by drawing parallel lines as a reference for the object, and further labeled the scene feature using hand labeling. Although, this algorithm is useful for architectural or forensic application, it could not be applied for automated surveillance application, where monitoring at real time is the foremost requirement. In [14], Jaynes proposed an algorithm with multiple cameras for surveillance application

which automatically aligned the image trajectories. Their algorithm also solved for the problem of relative posing of the cameras. However, multiple users need to be present for its application. The effect of scaling may still be present in the scenario where a single object is present in the video sequence. In another method for camera calibration, Lv et al. [15] assumed the objects to be perpendicular to ground plane and that their height remains the same. But, in actual scenario when object is moving, scaling comes into picture and needs to be catered with a robust model. The effect of scaling is tackled in tracking scenario by different methods. In [17] scale of fast changing object was estimated using the mean shift algorithm. However, iterative nature of the algorithm is more computationally expensive. In similar lien, Jiang in [18] used Scale Invariant Feature Transform (SIFT) for tackling the scaling effect of the object in a video sequence, but the algorithm is computationally expensive. Our proposed model could be useful for catering scaling and speed problem of the object in the video sequence and can be embedded in previously developed algorithms for enhanced video surveillance. With this, it is hoped that this manuscript will definitely give a seminal learning to academia, industry and defense establishments.

In this paper we follow a bottom-up approach in elaborating the issues that need to be handled when one aims for modeling object scale and speed in the video sequence. Entire paper has been divided into 5 sections. Mathematical model for curve fitting and the errors associated with it is explained in section 2. Section 3 gives the overview of our work along with some of the experiments setup with the details about the data sets used in our work. The results and analysis of the data is elaborated in section 4. Also, the best model which could be used for catering scaling and speed effect of the object is introduced. Finally, the concluding remarks and future direction in this field are sketched in Section 5.

II MATHEMATICAL MODELING AND CURVE FITTING

Regression analysis is used for finding relationship between one dependent variable and number of independent variables [3-4]. Regression modeling involves formation of relationship of the form $y = f(x_1, \dots, x_n, \alpha_1, \dots, \alpha_n) + \phi$ where α_1, α_2 are the weights and ϕ is the error variable which is estimated from the sample data. The proposed model is further tested for the goodness of the fit by different methods used for prediction of dependent variable form given independent variable.

There are a number of methods for finding regression modeling. The most commonly used for regression analysis are a) Method of moments b) least square and c) Graphic method. The principle of moment's method is based on the assumption that the moment of the observed value of the dependent variable is the same as the moment of the calculated value of the dependent variable. Based upon this all the weights and error variables are calculated. Similarly, graphical methods assume linear relation between dependent and independent variables. The complex expression is converted to linear relation before the start of modeling. The

method for curve fitting which is mostly used is least square method. In the present work, we have developed a model based upon the least square method. This method was proposed by German scientist Karl Gauss where the weight of the regression equations and the error variable are estimated by making sum of squares of vertical deviation, to minimum value. As shown in figure 2, x is the independent variable and y is the dependent variable. The aim of this method is to draw a regression line so that the vertical deviation of dependent variable is minimum. [5, 10].

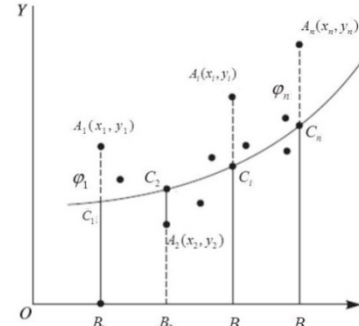


Figure 2: Regression line plot

For better illustration of method, let us take the curve as:

$$y = a + bx + cx^2 + \dots + kx^{m-1} \dots (1)$$

The sample points are taken from the experiments for finding the weight. As shown in the figure 2 above, sample points are taken as $(x_1, y_1), (x_2, y_2), (x_3, y_3), \dots, (x_m, y_m)$. Now, we draw a regression line for the best fit in the sample space. If the observed value of independent variable is $(x=x_i)$ then from this, the value of dependent variable is $=A_iB_i$. The regression line estimation from this is given by equation (2).

$$a + bx_i + cx_i^2 + \dots + kx_i^n = C_iB_i \dots (2)$$

Difference between the observed and the expected value is taken for each and every sample. Difference for sample x_i is given as $A_iB_i - C_iB_i = \phi_i$ (say). For different samples the error are found as $\phi_1, \phi_2, \phi_3, \dots, \phi_i, \dots, \phi_m$ where some of these errors are positive and some are negative valued. So square of these errors for each sample is taken as in equation (3)

$$S = \phi_1^2 + \phi_2^2 + \phi_3^2 + \dots + \phi_i^2 + \dots + \phi_m^2 \dots (3)$$

The given equation for sum of square error is solved so that the error value is minimized. From the solution of equation (3), regression coefficients are calculated using the least square method. If y_i is the actual value and \hat{y}_i is the estimated value of y. The sum of square error is measured using equation (4).

$$SSE = \sum_{i=1}^m (\hat{y}_i - y_i)^2 \quad \dots (4)$$

The value of SSE determines the goodness of fit of the curve. In general lower the value of SSE, better is fit. Similarly deviation from the mean value is measured using equation (5) and known as sum of square of regression [8].

$$SSR = \sum_{i=1}^m (\hat{y}_i - \bar{y})^2 \quad \dots (5)$$

From equation (4) and (5), sum of square deviation about the mean value is found using equation (6) as sum of square of total:

$$SST = SSR + SSE \quad \dots (6)$$

Most common regression measure coefficient for goodness of fit is R- square which is the measure of ratio of SSR and SST and is calculated using equation (7):

$$R\text{-square} = \frac{SSR}{SST} = 1 - \frac{SSE}{SST} \quad \dots (7)$$

The value of R-square varies from 0 to 1 with 1 indicating that the samples exactly fit on regression line. Apart from these measures, root mean square error is also used for performance measure of regression model. Lower the value of RMSE, better is the fit. For our developed model, we have calculated all these performances measure and based upon their values, the best model is suggested. Before we start with the model performance measure, we have briefly elaborated the experiment setup for our experiments.

III EXPERIMENTAL SETUP AND DATA CAPTURING

During our experimentation, we generated a large dataset of both indoor and outdoor videos. For our experiments we used Sony DCR-SX44E with Carl Zeiss Vario-Tessar (60 X Optical and 2000 X Digital), filter diameter: 30mm, F1.8~6.0 and focal length f=1.8~108mm. Frame rate of the captured video was 25 frames per second. We divided the data set into two categories depending upon the environment. *Data set 1* consisted of 10 videos captured under full light conditions and *Data set 2* consisted of 8 videos captured during dim light conditions, for both indoor and outdoor environment. Online video was acquired from the camera, projected centrally. The flow diagram of speed and scale estimation for online video is shown in figure 3 below. The background was subtracted using Gaussian Mixture Model [6]. We took three Gaussians with different mean and standard deviation. The pixels which were not assigned to any of these Gaussians were declared as the foreground pixels. Once the foreground was detected, centroid of the object was calculated. Area of bounding box which encloses the object was calculated for the estimation of the scale. Further, speed of the object was determined by measuring the distance travelled from frame to frame. This process was repeated for different 3D distance of the object from the camera. This data was then stored in an array. Once the object moved out of camera view angle, we applied the

regression analysis for modelling the scale and the speed of the object w.r.t the 3D distance from the camera. Different errors associated with the regression analysis were estimated and the best model was selected. In Video Data set 1 (Park_moving.avi), using the above mentioned algorithm, object was extracted. The position of object at different location is shown in Figure 4. From the analysis, it was revealed that the object is reasonably scaled form frame number 770 to 2050.

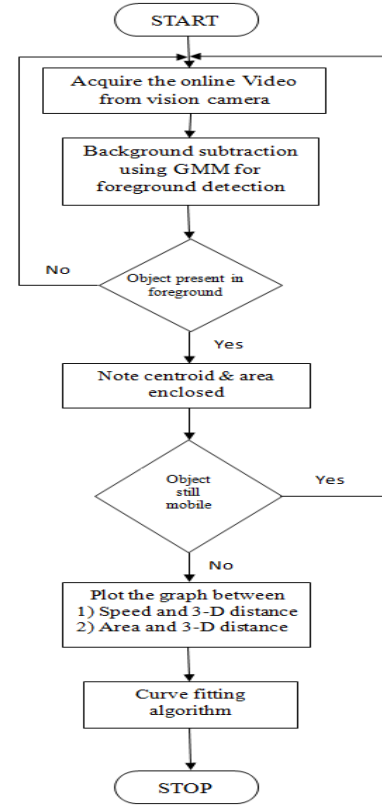


Figure 3: Flow Diagram of Speed and Scale Estimation

Estimated speed and area at different 3D distance from camera are tabulated in Table1. Analysis of the tabulated data revealed that the object speed decrease from 140 (pixel scaled) to 17 (pixel scaled) when 3D distance from camera is increased from 5m to 45m. Similarly in video data set 2 (road_eve.avi), the position of object at different location is shown in Figure 5. Frame by frame analysis showed that the object got reasonably scaled from frame no. 620 to 2525. The estimated speed and the estimated area at different 3D distances from the camera are tabulated in Table2. Analysis of the tabulated data revealed that object speed decrease from 100 (pixel scaled) to 11.16 (pixel scaled) when the 3D distance from the camera is increased from 8m to 64m. Using the algorithm discussed above, speed and area of the object are estimated for all the videos from Video Data set 1 (10Videos) and Video Data set 2 (8 Videos) . These data are further subjected for curve fitting for building a robust model for speed and area w.r.t. the 3D distance from the camera.



Figure 4: Target Location at Different Frames

S.No	DISTANCE (in meters)	SPEED (in pixels/sec)	CHANGE IN X	CHANGE IN Y	BOX AREA (in pixel square)
1	5	140	78	200	15600
2	10	88.8	48	150	7200
3	15	60	40	110	4340
4	18	47.82	33	97	3200
5	20	40.83	30	85	2650
6	22	37.34	27	80	2185
7	25	31	25	67	1645
8	27	28.83	22	62	1370
9	30	26.16	20	55	1050
10	33	23.27	15	53	812
11	35	23.00	13	46	720
12	38	20.51	12	45	552
13	40	19.50	11	43	470
14	43	18.74	10	40	398
15	45	17	10	34	340

Table 1: Target Location and Speed at Different Distance

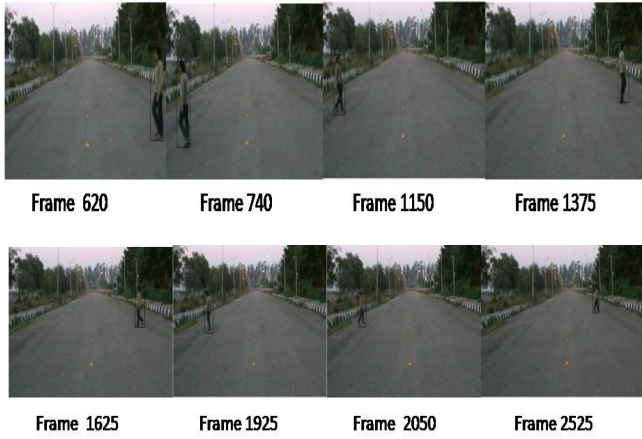


Figure 5: Target Location at Different Frames

S.No	DISTANCE (in meters)	SPEED (in pixels/sec)	CHANGE IN X	CHANGE IN Y	BOX AREA (in pixel square)
1	8	100	78	250	19500
2	12	74.63	45	171	7700
3	16	56.48	29	125	3625
4	20	43.95	23	95	2185
5	24	35.18	19	84	1596
6	28	28.26	17	74	1260
7	32	24.23	16	64	1020
8	36	20.07	14	59	829
9	40	16.91	13	51	670
10	44	15.64	12	47	559
11	48	14.17	11	42	462
12	52	13.16	10	38	378
13	56	12.27	8	38	310
14	60	11.60	7	36	258
15	64	11.16	6	34	210

Table 2: Target Location and Speed at Different Distance

IV RESULTS AND ANALYSIS

Using the extracted speed and scaling data for all the video sets, we have carried out regression analysis of data. We have compared four models for speed and scale factor and further residual error in each of the model is estimated using MATLAB tool. The details of various models are discussed as follow:

4.1 Regression Model for Speed of Object

Data from the 18 videos in data set 1&2 is analysed for building a robust model for speed of object w.r.t. 3D distance of the object from the camera.

a) Regression Analysis for Exponential Fit

The exponential fit for the video sequences captured is given as equation (8).

$$f(x) = ae^{bx} + ce^{dx} \quad \dots (8)$$

Average value of above regression coefficients are as follow: $a=185$, $b = -1$, $c = 19$ and $d=-0.03$. The average value of error for the data set 1&2 is as follows: SSE= 2.3, R-square = 0.9998 and RMSE = 0.67.

b) Regression Analysis for Power Fit

The power fit for the video sequences captured is given as equation (9).

$$f(x) = ax^b + c \quad \dots (9)$$

Average value of above regression coefficients are as follow: $a=496$, $b = -0.66$ and $c = -27$. The average value of error for the data set 1&2 is as follows: SSE= 48, R-square = 0.9980 and RMSE = 2.7.

c) Regression Analysis for Polynomial (4th degree) Fit

The power fit for the video sequences captured is given as equation (10).

$f(x) = k_1x^4 + k_2x^3 + k_3x^2 + k_4x + k_5 \dots$ (10) Average value of above regression coefficients are as follow: $k_1 = 0.000056$, $k_2 = -0.009$, $k_3 = 0.53$, $k_4 = -15$ and $k_5 = 192$. The average value of error for the data set 1&2 is as follows: SSE= 2.75, R-square = 0.9997 and RMSE = 0.8980.

d) Regression Analysis for Polynomial (5th degree) Fit
 The power fit for the video sequences captured is given as equation (11).

$$f(x) = k_1x^5 + k_2x^4 + k_3x^3 + k_4x^2 + k_5x + k_6 \dots (11)$$

Average value of above regression coefficients are as follow: $k_1 = 0.000056$, $k_2 = -0.009$, $k_3 = 0.53$, $k_4 = -15$, $k_5 = 192$, $k_6 = 202$. The average value of error for the data set 1&2 is as follows: SSE= 1.585, R-square = 0.9997 and RMSE = 0.63.

4.2 Regression Model for Scaling of Object

Data from the 18 videos in data set 1&2 is analysed for building a robust model for speed of object w.r.t. 3D distance of the object from the camera.

a) Regression Analysis for Exponential Fit
 The exponential fit for the video sequences captured is given as equation (12)

$$f(x) = ae^{bx} + ce^{dx} \dots (12)$$

Average value of above regression coefficients are as follow: $a = 12200000$, $b = -0.2016$, $c = 412$ and $d = -0.03$. The average value of error for the data set 1&2 is as follows: SSE= 570, R-square = 1 and RMSE = 10.5.

b) Regression Analysis for Power Fit
 The power fit for the video sequences captured is given as equation (13).

$$f(x) = ax^b + c \dots (13)$$

Average value of above regression coefficients are as follow: $a = 136000$, $b = -1.51$ and $c = -3$. The average value of error for the data set 1&2 is as follows: SSE= 77000, R-square = 0.9980 and RMSE = 97.

c) Regression Analysis for Polynomial (4th degree) Fit
 The power fit for the video sequences captured is given as equation (14).

$$f(x) = k_1x^4 + k_2x^3 + k_3x^2 + k_4x + k_5 \dots (14)$$

Average value of above regression coefficients are as follow: $k_1 = 0.0045$, $k_2 = -0.31$, $k_3 = 48$, $k_4 = -1455$ and $k_5 = 17000$. The average value of error for the data set 1&2 is as follows: SSE=8340, R-square = 0.9999 and RMSE =53.

d) Regression Analysis for Polynomial (5th degree) Fit
 The power fit for the video sequences captured is given as equation (15).

$$f(x) = k_1x^5 + k_2x^4 + k_3x^3 + k_4x^2 + k_5x + k_6 \dots (15)$$

Average value of above regression coefficients are as follow: $k_1 = -0.000036$, $k_2 = -0.01$, $k_3 = -2.1$, $k_4 = 95$, $k_5 = -2115$, $k_6 = 21500$. The average value of error for the data set 1&2 is as follows: SSE= 1075, R-square = 0.9999 and RMSE = 26. In Figure 6 Exponential, Power, Polynomial (4th degree) and polynomial (5th degree) curve fitting results are plotted along with 3D distance from camera for the video sequences for Data Set 1((Park_moving.avi). The error analyses for these curve fitting models are plotted as residual plots. In Figure 7 Exponential, Power, Polynomial (4th degree) and polynomial (5th degree) curve fitting results are plotted along with 3D distance from camera for the video sequences for Data Set 2(road_eve.avi). The error analyses for these curve fitting models are plotted as residual plots.

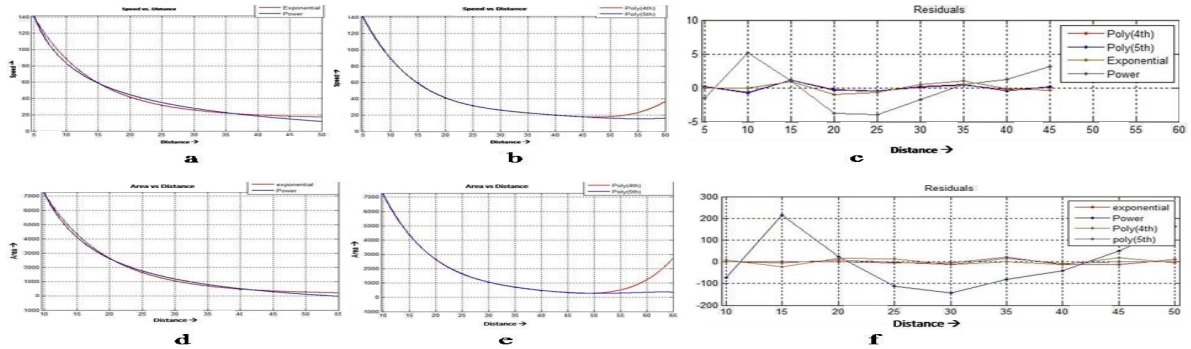


Figure 6: Speed vs distance relations are shown as (a) Exponential curve fitting and Power curve fitting (b) Polynomial(4th degree) and polynomial(5th degree). (c) Residual for above curve fitting **Area vs Distance** relations are shown (d) Exponential and Power (e) Polynomial(4th degree) and polynomial(5th degree). (f) Residual comparison for the above curve fitting.

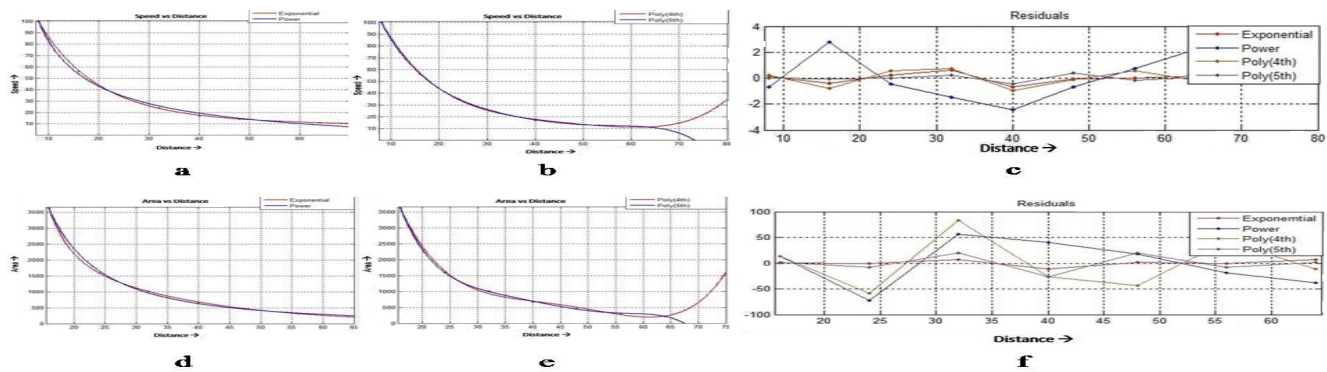


Figure 7: Speed vs Distance relations are shown as (a) Exponential curve fitting and Power curve fitting (b) Polynomial(4th degree) and polynomial(5th degree) (c) Residual for above curve fitting. Area vs Distance relations are shown (d) Exponential and Power (e) Comparison of Polynomial(4th degree) and polynomial(5th degree) (f) Residual comparison for the above curve fitting.

From the analysis of the plotted data, it was observed that polynomial plots gave a sharp increase in the error as the distance of the object from camera increases above 60m. Hence, one could faithfully conclude that the exponential regression model could be used for finding either speed or scale of the object when 3D distance from camera is known. The relation mentioned in equation 8 and 12 may be used for calculation of speed and scale of the object respectively.

V CONCLUSION AND FUTURE DIRECTION

Although, robust computer vision algorithm are developed for object classification, scene segmentation, activity recognition, video profiling and object tracking etc., improving the quality of video surveillance system still remain a challenging task. In our present work we have compared different regression models of speed and scale relation in reference to the 3D distance of the object from the camera. From analysis of different videos both indoor and outdoor, we can conclude that the speed and scaling could be better modelled as exponential fit in comparison to polynomial or power regression model. In field of computer vision where scaling and speed of the object greatly affects the tracking performance, the developed regression model could be embedded to handle occlusion better during tracking. It could also be used under multi-sensor environment where distance could be easily detected with radar sensor. It is also helpful for defence application for building automated armaments. However, we have conducted all experiment under the assumption that the speed of the object remains constant. In future, we are working for building model where speed of object varies with time and also multiple objects are present in scene. Also we are working on embedding this model for surveillance algorithm in order to enhance its performance.

REFERENCES

- [1] Jie Cao, Li Li "Vehicle Objects Detection of Video Images Based on Gray-Scale Characteristic" 2009 First International Workshop on Education Technology and Computer Science pp 936-940.
- [2] ESSA Technical Report ERL 101-ITS 73. "A method of smooth curve fitting by Hiroshi Akima.
- [3] Book Entitled "Methods of curve fitting" by Carlos Frasser.
- [4] Book Entitled, The Kaleida Graph Guide to Curve Fitting.
- [5] Fitting in Matlab by Klaus Betzler¹, Fachbereich Physik, University at Osnabruck.
- [6] C. Stauffer and W. Grimson, "Adaptive background mixture models for real-time tracking", IEEE Conf. on Computer Vision and Pattern Recognition, 2:2246, 1999. Vol. 2.
- [7] Book Entitled "Overview of Curve Fitting Models and Methods in LabVIEW" by National Instruments
- [8] Book Entitled 'Mathematical Statistics with Applications' by Kandethody M. Ramachandran and Chris P. Tsokos
- [9] S. S. Cheung and C. Kamath, "Robust techniques for background subtraction in urban traffic video," in Video Communications and Image Processing. SPIE Electronic Imaging, vol. 5308, 2004, pp. 881-892.
- [10] Book Entitled "Engineering Mathematics", Volume 2 by: E. Rukmangadachari, Publisher: Pearson Education India.
- [11] Javed, O. and Shah, M., "Tracking and Object Classification for Automated Surveillance," Proc. European Conf. on Computer Vision (ECCV), 2002.
- [12] Lipton, A.J., Fujiyoshi, H. and Patil, R.S., "Moving target classification and tracking from real-time video," Proc. IEEE Workshop on Applications of Computer Vision (WACV), 1998 pp 8-14
- [13] Criminisi, A., Reid, I. and Zisserman, A., "Single View Metrology," Proc. 7th Intl. Conf. on Computer Vision (ICCV), 1999 pp 434-441 vol1
- [14] Jaynes, C., "Multi-view Calibration from Planar Motion for Video Surveillance," Proc. Intl. Workshop on Video Surveillance, 1999 pp 59-66.
- [15] Lv, F., Zhao, T. and Nevatia, R., "Self-Calibration of a camera from video of a walking human," Proc. Intl. Conf. on Pattern Recognition (ICPR), 2001. PP 562-567 vol. 1
- [16] H. Nicolas, "Depth Analysis for Surveillance videos in H.26 Compress domain" Proc. European Signal Processing Conference (EUSIPCO), 2012 pp 146-149
- [17] Peng Li, Zhipeng Cai, Hanyun Wang, Zhuo Sun, Yunhui Yi, Cheng Wang, Jonathan Li, "Scale Invariant Kernel-Based Object Tracking" Proc. Computer Vision in Remote Sensing (CVRS), 2012, pp 252-255
- [18] Min Jiang, Lei Zhang, Yanli Huang "Object tracking based on particle filter and scale invariant feature transform". Proc. International Conference on Multimedia Technology (ICMT), 2010 pp 1-4.
- [19] Jie Hu, Huaxiong Zhang, Jie Feng, Hai Huang, Hanjie Ma, "A Scale Adaptive Kalman Filter Method Based On Quaternion Correlation In Object Tracking" Proc. Third International Conference on Networking and Distributed Computing (ICNDC), 2012 pp 170-174.

Design of Unity Power Factor Controller for Three-phase Induction Motor Drive Fed from Single Phase Supply

Rachana Garg¹, Priya Mahajan¹, Parmod Kumar², and Rohit Goyal¹¹Delhi Technological University, New Delhi 110042, India

²Maharaja Agrasen Institute of Technology, New Delhi 110085, India

Email: {rachana16100, pramodk2003}@yahoo.co.in, {priyamahajan.eed, rohitelect.goyal}@gmail.com

Abstract— This paper carves out the design of unity power factor controller for three phase variable speed induction motor drive. SPWM technique is used to improve the power factor of the system to unity and hysteresis controller is used for speed control of the drive. These control techniques lead to a unity power factor seen by the ac supply and minimize the power loss, audible noise, and motor torque ripple. A three level converter-inverter system employing advanced insulated gate bipolar transistors (IGBTs) is used.

Index Terms—Ac-dc-ac converter; vector controlled induction motor drive; unity power factor control, Hysteresis controller

I. INTRODUCTION

Induction motor is widely used in industry and agricultural sector due to the fact that it is relatively cheap, rugged and maintenance free. It needs reactive power for operation and working. Thus, a large reactive power is required to be supplied and transmitted which reduces the power factor of the system and hence the transmission lines capacity. It is therefore desirable to improve the power factor of supply side for induction motor drive. This can be achieved using unity power factor (upf) controller with sinusoidal pulse width modulation (SPWM) technique. In the present work, the authors have simulated the IGBT based power converter, connected to three phase induction motor drive. Hysteresis controller is used for variable speed control.

A lot of research has been going on to improve the performance and efficiency of the induction drive system. K. Thiagarajah, V. T. Ranganathan described an inverter/converter system operating from a single - phase supply using IGBT [1]. Adrian David Cheok, Shoichi Kawamoto, Takeo Matsumoto, and Hideo Obi described new developments in the design of high-speed electric trains with particular reference to the induction motor drive system [2]. Prasad N. Enjeti, and Ashek Rahman have proposed the new single-phase to three-phase converter for low-cost ac motor drive [3]. The different control strategy of induction motor drive system has been presented and discussed by various researchers [4]-[6].

II. PROBLEM FORMULATION

The induction motor drive comprises of (i) ac to dc converter, (ii) dc to ac inverter, and (iii) dc link capacitor between the converter and inverter. Fig. 1 shows the proposed configuration for unity power factor control towards power supply to induction motor drive. The front-end for the system used here is a full-bridge IGBT PWM converter with an ac reactor [7]. In order to maintain the supply current at unity power factor, unity power factor controller with SPWM technique is designed.

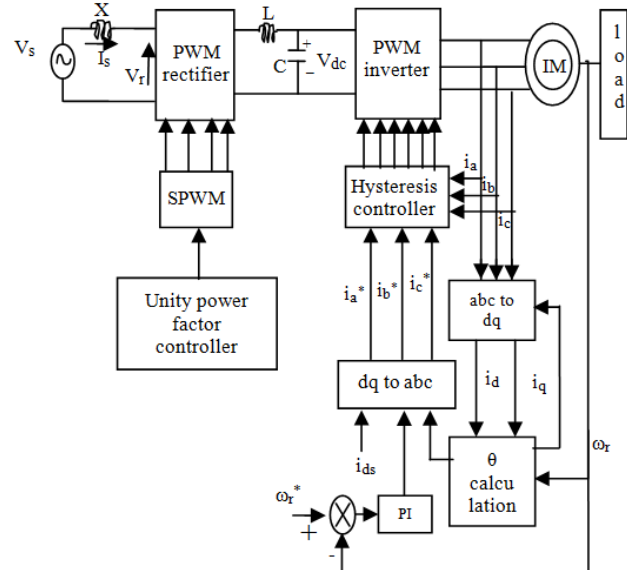


Figure 1. Block diagram of supply side unity power factor control of induction motor drive

On the machine side, a high switching frequency three phase PWM inverter using IGBT is used. This converter is controlled by hysteresis controller for variable speed drive. The entire system is fed from single-phase mains supply.

III. POWER FACTOR CONTROL ALGORITHM

To achieve unity power factor on supply side, input voltage to converter, V_r , is controlled with current and

voltage feedback to control the phase difference between the ac supply voltage and current. In the unity power factor case, the converter voltage amplitude is given by (1) [8]

$$V_r = \sqrt{V_s^2 + (I_s X_s)^2} \quad (1)$$

If the converter voltage can be controlled to the above value then unity power factor will be maintained. In the developed upf controller, a control system is used to maintain unity power factor by controlling the switching of converter. The upf controller maintains a constant dc link voltage, in order that a steady dc link voltage is fed to the inverter. The block diagram of unity power factor controller algorithm is shown in Fig. 2.

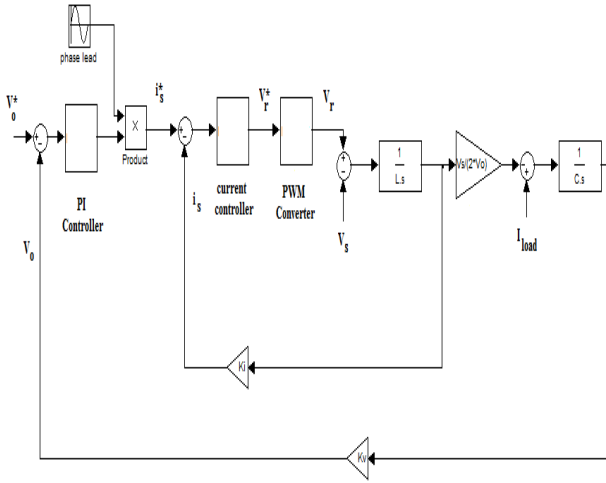


Figure 2. Block Diagram of Unity Power Factor Control Algorithm

IV. DYNAMIC MODEL OF INDUCTION MOTOR

The three phase squirrel cage induction motor in synchronous rotating reference frame can be represented as in Fig. 3[9].

Voltage and flux equations for the motor are given by (2)-(9)[9].

$$V_{qs} = R_s * i_{qs} + \frac{d\phi_{qs}}{dt} + \omega_e \phi_{ds} \quad (2)$$

$$V_{ds} = R_s * i_{ds} + \frac{d\phi_{ds}}{dt} - \omega_e \phi_{qs} \quad (3)$$

$$V_{qr} = R_r * i_{qr} + \frac{d\phi_{qr}}{dt} + (\omega_e - \omega_r) \phi_{dr} \quad (4)$$

$$V_{dr} = R_r * i_{dr} + \frac{d\phi_{dr}}{dt} - (\omega_e - \omega_r) \phi_{qr} \quad (5)$$

$$\phi_{qs} = L_{ls} * i_{qs} + (i_{qs} + i_{qr}) L_m \quad (6)$$

$$\phi_{qr} = L_{lr} * i_{qr} + (i_{qs} + i_{qr}) L_m \quad (7)$$

$$\phi_{ds} = L_{ls} * i_{ds} + (i_{ds} + i_{dr}) L_m \quad (8)$$

$$\phi_{dr} = L_{lr} * i_{dr} + (i_{ds} + i_{dr}) L_m \quad (9)$$

where V_{qs} & V_{ds} are the applied voltages to the stator; i_{ds} , i_{qs} , i_{dr} , & i_{qr} are the corresponding d & q axis currents; ϕ_{qs} , ϕ_{qr} & ϕ_{ds} , ϕ_{dr} are the rotor & stator flux component; R_s , R_r are the stator & rotor resistances; L_{ls} & L_{lr} denotes the

stator & rotor inductances, L_m is the mutual inductance.

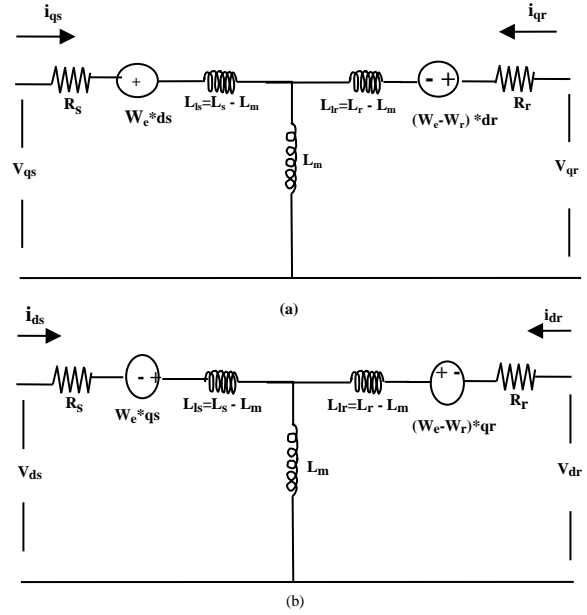


Figure 3. Equivalent circuit of Induction motor in synchronous rotating reference frame, a) q-axis circuit b) d-axis circuit

The electromagnetic torque equation is given by (10)

$$T_e = \frac{3 * P * L_m}{2 * 2 * L_r} * (\phi_{dr} i_{qs} - \phi_{qr} i_{ds}) \quad (10)$$

where P denotes the pole number of the motor

In case of vector control the q -component of the rotor field ϕ_{qr} would be zero. Then the electromagnetic torque is controlled only by q -axis stator current & (10) is reduced to (11)

$$T_e = \frac{3 * P * L_m}{2 * 2 * L_r} * (\phi_{dr} i_{qs}) \quad (11)$$

V. VECTOR CONTROL METHODOLOGY

There are large number of ways for speed control of induction motor among which vector or field oriented control is the most widely accepted methods now a day's[9]-[15]. In the present studies indirect vector control method is employed. Here, the unit vector is generated in an indirect manner using the measured speed ω_r and slip speed ω_{sl} . The following dynamic equations take into consideration to implement indirect vector control strategy. Equation 12 shows the rotor flux position.

$$\theta_e = \int \omega_e dt = \int (\omega_r + \omega_{sl}) dt = \theta_r + \theta_{sl} \quad (12)$$

The stator current i_a , i_b , i_c in the 3-phase coordinate is changed to 2-phase AC current in the static coordinate with 3/2 equivalent transformation. Then through synchronous rotating coordinate transformation, the 2-phase AC current will be equivalent as dc current i_d and i_q in the synchronous rotating coordinate. The abc - dq transformation is an essential part of this scheme. The direct-quadrature-zero (dqo) transformation or zero-

direct-quadrature (*odq*) transformation is a mathematical transformation used to simplify the analysis of three-phase circuits. The transformation of *abc-dq* involves the decoupling of variables with time-varying coefficients and refers all variables to a common *reference* frame. This transformation reduces the three line currents to two dc quantities in *dq* reference frame. The two dc quantities are orthogonal to each other. This allows the control of the two quantities independently. The three-phase transformation into two-phase is carried out through *abc-dq* transformation by using various methods like Stanley's transformation, Park's transformation etc. Park's transformation applied to three-phase currents is shown by (13)

$$I_{dgo} = T I_{abc} = \frac{2}{3} \begin{bmatrix} \cos \theta & \cos \left(\theta - \frac{2\pi}{3} \right) & \cos \left(\theta + \frac{2\pi}{3} \right) \\ -\sin \theta & -\sin \left(\theta - \frac{2\pi}{3} \right) & -\sin \left(\theta + \frac{2\pi}{3} \right) \\ 0.5 & 0.5 & 0.5 \end{bmatrix} \begin{bmatrix} I_a \\ I_b \\ I_c \end{bmatrix} \quad (13)$$

The inverse transform is shown by (14)

$$I_{abc} = T^{-1} I_{dgo} = \begin{bmatrix} \cos \theta & -\sin \theta & 1 \\ \cos \left(\theta - \frac{2\pi}{3} \right) & -\sin \left(\theta - \frac{2\pi}{3} \right) & 1 \\ \cos \left(\theta + \frac{2\pi}{3} \right) & -\sin \left(\theta + \frac{2\pi}{3} \right) & 1 \end{bmatrix} \begin{bmatrix} I_d \\ I_q \\ I_o \end{bmatrix} \quad (14)$$

VI. HYSTERESIS CURRENT CONTROL ALGORITHM:

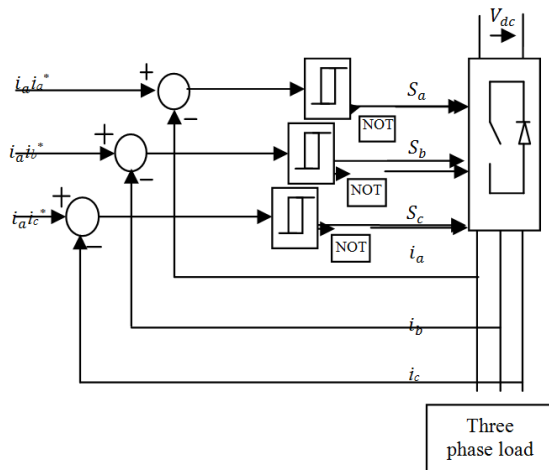


Figure 4. Block diagram of hysteresis current control

Fig. 4 shows the block diagram for hysteresis current control scheme for induction motor drive. In this circuit three phase load i.e induction motor in our case is connected to the PWM voltage source inverter. Hysteresis current algorithm is used to control the speed of induction motor. The load currents i_a , i_b and i_c are compared with the reference currents i_a^* , i_b^* and i_c^* and error signals are passed through hysteresis band to generate the firing pulses, which are operated to produce output voltage in manner to reduce the current error. The purpose of the current controller is to control the load

current by forcing it to follow a reference one. It is achieved by the switching action of the inverter to keep the current within the hysteresis band. The load currents are sensed & compared with respective command currents by three independent hysteresis comparators having a hysteresis band ' h '. The output signals of the comparators are used to activate the inverter power switches. The inverter current vector is given by (15)

$$i = \frac{2}{3} [i_a + \alpha i_b + \alpha^2 i_c] \quad (15)$$

where α is complex number operator

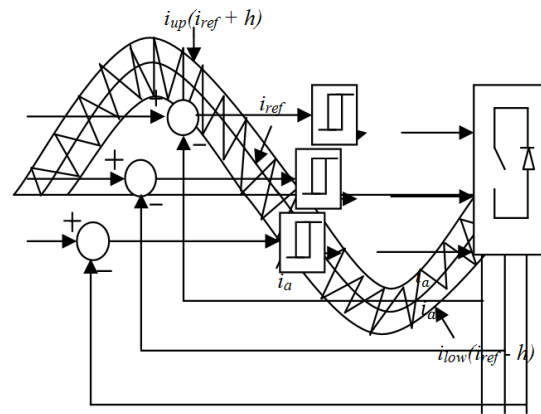


Figure 5 Fixed band shape of hysteresis controller

In this scheme, the hysteresis bands are fixed throughout the fundamental period. Fig. (5) Shows the fixed band shape of hysteresis controller. The algorithm for one phase of this scheme is given by (16)-(18)

$$i_{ref} = i_{max} \sin \omega t \quad (16)$$

Upper band limit of current

$$i_{up} = i_{ref} + h \quad (17)$$

Lower band limit of current

$$i_{low} = i_{ref} - h \quad (18)$$

where, h = Hysteresis band limit

If $i_a > i_{up}$, $V_{ao} = -V_{dc}/2$

If $i_a < i_{low}$, $V_{ao} = +V_{dc}/2$

VII. SIMULATION RESULTS AND DISCUSSION

The simulation has been carried on the 3-phase, 5hp (3.73KW), 1750rpm (183.33rad/sec), 50Hz squirrel cage induction motor with following parameters:

Stationary reference frame

Y- Connected

R_s (stator resistance) = 1.115 Ω

R_r (rotor resistance) = 1.083 Ω

L_s (stator inductance) = 0.005974H

L_r (rotor inductance) = 0.005974H

L_m (magnetizing inductance) = 0.2037H

J (moment of inertia) = 0.02Kg m²

P (number of poles) = 4

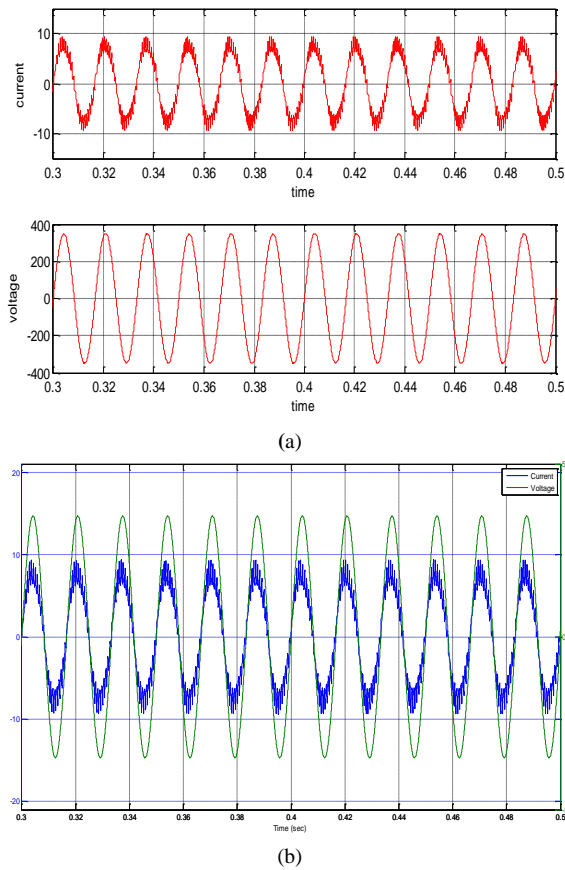


Figure 6. (a) and (b) Simulink plot showing supply side unity power factor control on "no load" at 60 rad/sec

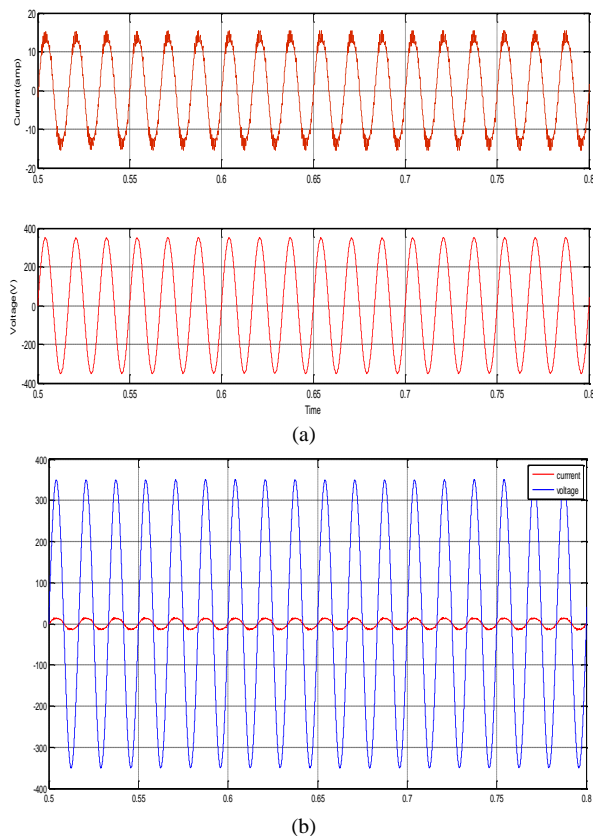


Figure 7. (a) and (b) Simulink plot showing supply side unity power factor control on "full load" at 60 rad/sec

Fig. 6-Fig. 9 shows the supply side unity power factor control on different speed and different load.

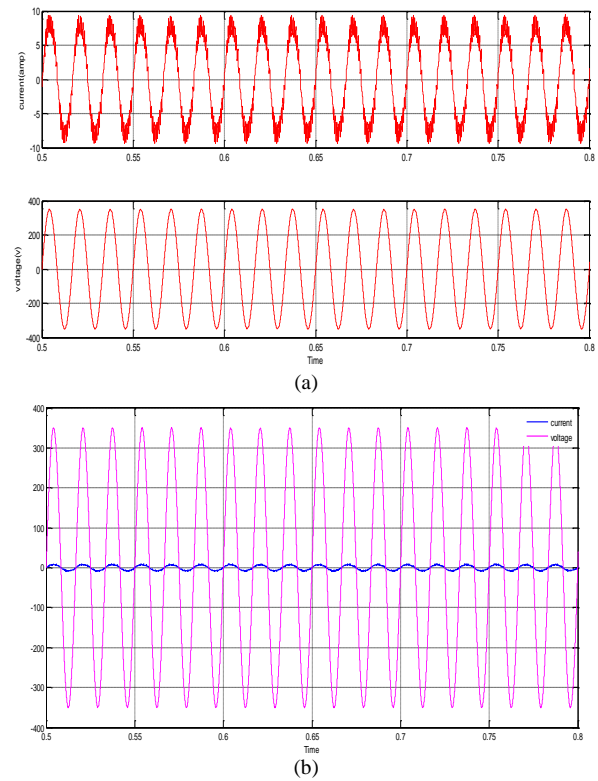


Figure 8. (a) and (b) Simulink plot showing supply side unity power factor control on "no load" at 150 rad/sec

Fig. 10-Fig. 13 shows the voltage (line-line), three phase stator current, speed and electromagnetic torque on different load and different speed with respect to time.

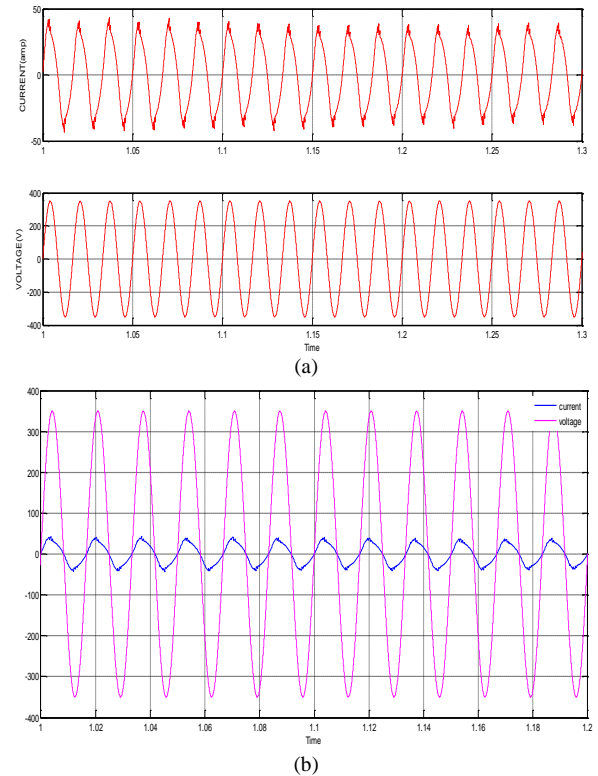


Figure 9. (a) and (b) Simulink plot showing supply side unity power factor control on "full load" at 140 rad/sec

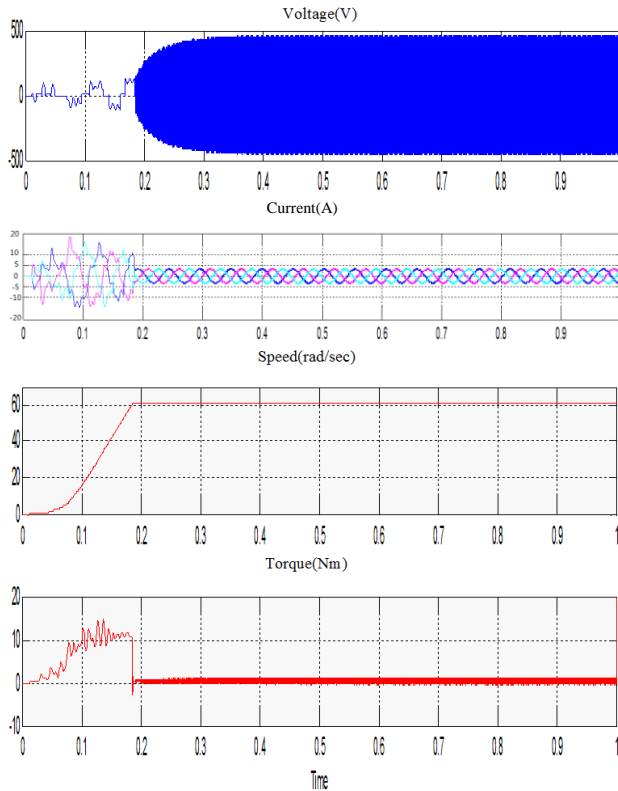


Figure 10. Simulink plot showing voltage (line-line), three phase stator current, speed and electromagnetic torque on "no load" at 60rad/sec speed with respect to time

Fig. 6 shows the simulink result of supply side unity power factor control of 5hp induction motor working on "no load" at 60 rad/sec. It has been observed that at no load supply side current is 8.1A peak current but at improved power factor of approximately unity. The current contains nominal harmonics.

Fig. 7 shows the simulink result of supply side unity power factor control of 5hp induction motor working on "full load" at 60 rad/sec, it has been observed that at full load supply side current is 12.1A peak current but at improved power factor of approximately unity. The current contains nominal harmonics.

Fig. 8 shows the simulink result of supply side unity power factor control of the 5hp induction motor working on "no load" at 150 rad/sec. It has been observed that at no load supply side current 8.1 A peak current but at improved power factor of approximately unity. The current contains nominal harmonics.

Fig. 9 shows the simulink result of supply side unity power factor control of 5hp induction motor working on "full load" at 140 rad/sec, it has been observed that at full load supply side current is 30A peak current but at improved power factor of approximately unity, the current contains nominal harmonics.

Fig. 10 shows voltage (line-line), three phase stator current, speed and electromagnetic torque of 5hp induction motor on "no load" at 60 rad/sec. The no load current per phase is 3.2A peak. The currents show a hysteresis band of variation. The three phase currents are perfectly sinusoidal, 120° apart from each other. At the time of starting the maximum current drawn by the

induction motor is as high as 18A peak. Initially current frequency is low due to this at the time of starting torque is more.

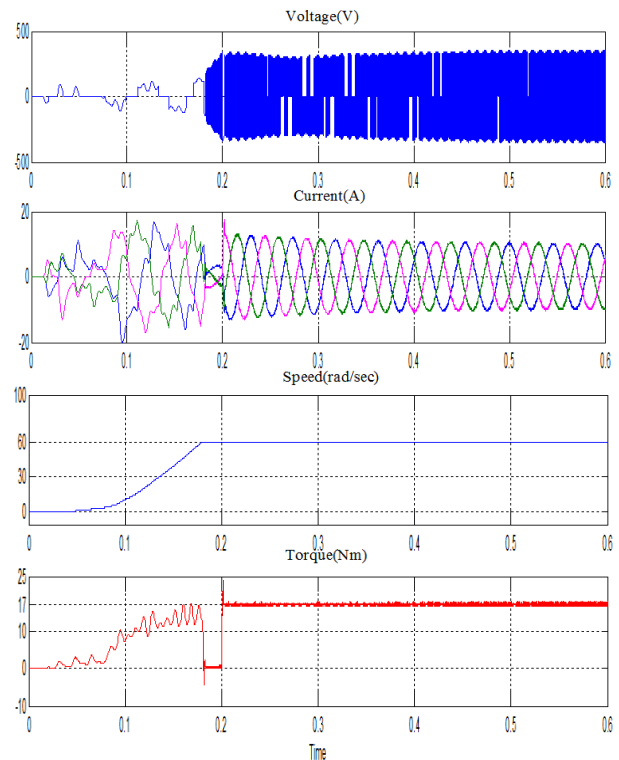


Figure 11. Simulink plot showing voltage (line-line), three phase stator current, speed and electromagnetic torque on "full load" at 60rad/sec speed with respect to time

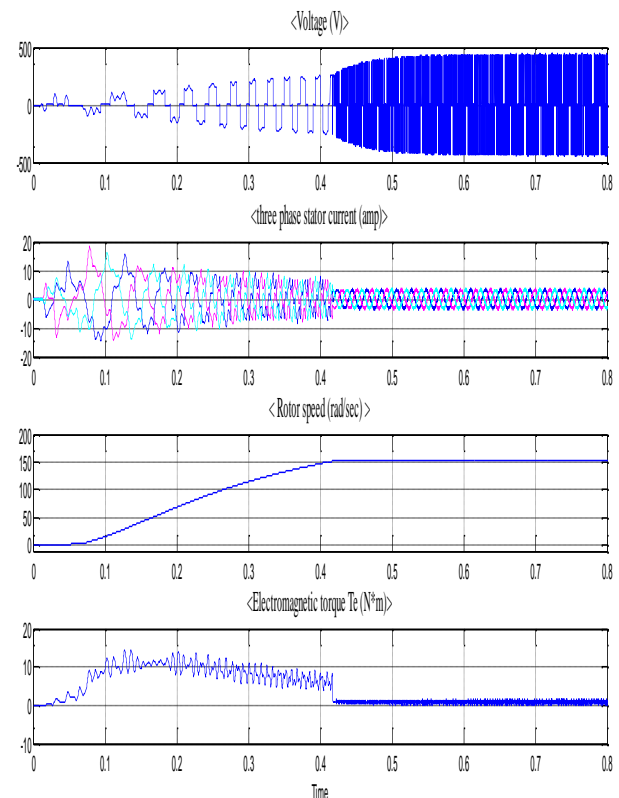


Figure 12. Simulink plot showing voltage (line-line), three phase stator current, speed and electromagnetic torque on "no load" at 150rad/sec speed with respect to time

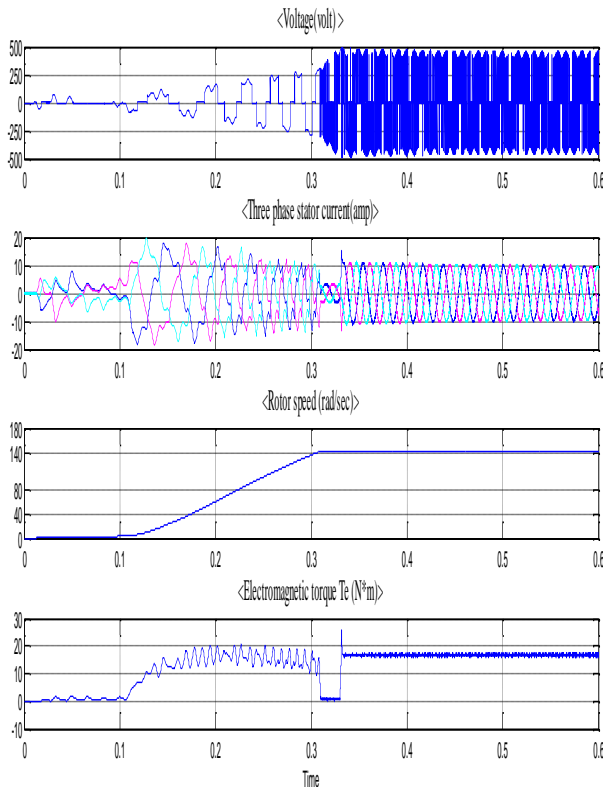


Figure 13. Simulink plot showing voltage (line-line), three phase stator current, speed and electromagnetic torque on "full load" at 140rad/sec speed with respect to time

Fig. 11 shows voltage (line-line), three phase stator current, speed and electromagnetic torque of 5hp induction motor on "full load" at 60 rad/sec. The full load current is 9.4A peak. The current shows a hysteresis band of variation. The three phase currents are perfectly sinusoidal, 120° apart from each other. At the time of starting the maximum current drawn by the induction motor is as high as 18A peak. Initially current frequency is low due to this at the time of starting torque is more.

Fig. 12 shows voltage (line-line), three phase stator current, speed and electromagnetic torque of 5hp induction motor on "no load" at 150 rad/sec. The no load current is 3.2 A peak. The currents show a hysteresis band of variation. The three phase currents are perfectly sinusoidal, 120° apart from each other. At the time of starting the maximum current drawn by the induction motor is as high as 18A peak. Initially current frequency is low. Due to this, at the time of starting, torque is more.

Fig. 13 shows voltage (line-line), three phase stator current, speed and electromagnetic torque of 5hp induction motor on "full load" at 140 rad/sec. The full load current per phase is 9.4 A peak. The current shows a hysteresis band of variation. The three phase currents are perfectly sinusoidal, 120° apart from each other. At the time of starting the maximum current drawn by the induction motor is as high as 18A peak.

VIII. CONCLUSIONS

Simulation studies have been carried out using MATLAB 7.7.0 (R2008b) to control the speed of

induction motor and improving the power factor of supply side to unity. The speed is controlled using hysteresis current controller, which controls the frequency of stator current. The results are taken for different values of speed under both no load and full load condition. It has been observed that the power factor can be controlled to unity at all speeds. The above studies are useful in improving the performance and efficiency of the supply system by decreasing the reactive power requirement of the system.

REFERENCES

- [1] K. Thiyagarajah, V. T. Ranganathan, and B. S. R. Iyengar, "A high switching frequency IGBT PWM rectified inverter system for ac motor drives operating from single phase supply," *IEEE Trans. on Power Electronics*, vol. 6, no. 4, October 1991.
- [2] A. D. Cheok, S. Kawamoto, T. Matsumoto, and H. Obi, "High power AC/DC converter and DC/AC inverter for high speed train applications," in *Proc. TENCON*, 2000, pp. 423-428.
- [3] P. Enjeti, and A. Rahman, "A new single phase to three phase converter with active input current shaping for low cost AC motor drives," *IEEE Trans. Industrial Applications*, vol. 29, no. 2, pp. 806-813, July 1993.
- [4] J. Itoh, and K. Fujita, "Novel unity power factor circuits using zero-vector control for single-phase input systems," *IEEE Trans. Power Electronics*, vol. 15, no. 1, pp. 36-43, Jan. 2000.
- [5] B. K. Lee, B. Fahimi, and M. Ehsani, "Overview of reduced parts converter topologies for AC motor drives," in *Proc. IEEE PESC*, 2001, pp. 2019-2024.
- [6] C. B. Jacobina, M. B. de R. Correa, A. M. N. Lima, and E. R. C. da Silva, "AC motor drive systems with a reduced switch count converter," *IEEE Trans. Industrial Applications*, vol. 39, no. 5, pp. 1333-1342, Sep./Oct. 2003.
- [7] J. R. Rodriguez, J. W. Dixon, J. R. Espinoza, J. Pontt, and P. Lezana, "PWM regenerative rectifiers: State of the art," *IEEE Trans. Industrial Electronics*, vol. 52, no. 1, pp. 5-22, Feb 2005.
- [8] C. W. Lander, *Power Electronics*, McGraw-Hill Book Company.
- [9] B. K. Bose, *Modern Power Electronics & AC Drives*, Prentice Hall.
- [10] R. G. W. Leonhard, and C. J. Nordby, "Field-Oriented control of a standard ac motor using microprocessors," *IEEE Trans. on Industrial Applications*, vol. IA-16, no. 2, pp 186-192, March 1980.
- [11] T. Matsuo, and T. A. Lipo, "A rotor parameter identification scheme for vector-controlled induction motor drives," *IEEE Trans. Industrial Applications*, vol. IA-21, no. 4, pp 624-632, May 1985.
- [12] M. Koyama, M. Yano, I. Kamiyama, And S. Yano, "Microprocessor-based vector control system for induction motor drives with rotor time constant identification function," *IEEE Trans. on Industrial Applications*, vol. IA-22, no. 3, pp 453-459, May 1986.
- [13] I. Takahashi, and T. Noguchi, "A new quick-response and high-efficiency control strategy of an induction motor," *IEEE Trans. on Industrial Applications*, vol. IA-22, no. 5, pp 820-827, Sept. 1986.
- [14] T. Murata, T. Tsuchiya, and I. Takeda, "Vector control for induction machine on the application of optimal control theory," *IEEE Trans. on Industrial Electronics*, vol. 31, no. 4, August 1990.
- [15] N. Mohan, T. M. Undeland, and W. P. Robins, *Power Electronics: Converters Applications and Design*, New York: Wiley, 1989.

Rachana Garg received the B.E. and M.E. degree in 1986 and 1989 from NIT, Bhopal respectively. She has obtained her Ph.D in Electrical Engg. from Delhi University in 2009. Presently, she is working as Associate Prof. in Delhi Technological University, Delhi. Her area of interest is modeling of transmission lines, power system operation and control.

Priya Mahajan received the B.E. and M.E. degree in 1996 and 1998 from Thapar Institute of Engg. & Tech., Patiala and Punjab Engg. College, Chandigarh respectively. Presently she is pursuing the Ph.D degree in electrical engineering from Delhi University, Delhi.

She is working as Assistant Prof. in Delhi Technological University, Delhi since last 13 years. Her area of interest includes power system and railway traction system.

Parmod Kumar received the B.E., M.E., and Ph.D. degrees in 1972, 1975, and 1982, respectively.

After post-graduation in measurement and instrumentation, he joined M.P. Electricity Board, M.P., India, as an Assistant Engineer and commissioned telemetry and SCADA instruments at substations, power stations, and the central control room. In 1983, he joined the Central Electricity Authority as a Dynamic System Engineer and designed and configured the load dispatch centers for electric utilities. Subsequently, he served on various capacities to Indian Railway Construction

Company, ERCON, ESPL, ESTC, and then entered academic life in 1991. His area of interest is smart and intelligent system design, operation, and control.

Rohit Goyal received B.E. degree in 2010 from M.B.M engineering college, Jodhpur and he is a M.tech student at Delhi Technological University, Delhi. He has completed the course work in M.tech and final result is awaited.

Presently, he is working as Assistant Prof. in Dehradun Institute Technology University, Dehradun. His areas of interest are railway traction system and control.

SHORT COMMUNICATION

Edge Strength based Fuzzification of Colour Demosaicking Algorithms

Seba Susan* and Deepak Aneja

Delhi Technological University, New Delhi-110 042, India

*E-mail: seba_406@yahoo.in

ABSTRACT

In this paper we fuzzify the bilinear colour interpolation and the non-linear colour differential correlative interpolation techniques of colour demosaicking, using the edge strength map of the mosaic image. In doing so we ensure that the edges have less participation in the interpolation thereby minimizing the interpolation error. The result is faster and more accurate colour demosaicking algorithms with application to high resolution images. The overall improvement is quite significant when it comes to colour interpolation of high definition/high resolution images containing a lot of detail or edges as proved by the extensive experimental results on state-of-the-art databases and state-of-the-art comparison.

Keywords: Colour demosaicking, colour filter array interpolation, edge strength, fuzzy membership

1. INTRODUCTION

Digital Cameras containing single chip sensors are increasingly becoming popular due to their savings in cost and size. In a single chip camera sensor, at each pixel location, only one of the R, G, B channels are captured in the layout of the Bayer pattern³ as shown in Fig. 1. The resulting image is called the mosaic image. Colour filter array interpolation (CFA) or demosaicking techniques^{1,2} are used to generate the missing colour values using the existing colour values in the mosaic image. Since green colour samples show least aliasing, the green channel is interpolated first followed by the red and the blue channels^{1,2}. Edge directed green channel interpolation was investigated before using both luminance and chrominance gradients^{4,5}. Chrominance gradients were also used for initial green channel interpolation⁷. The edge strength filter output has been used to improve the green channel interpolation in an iterative manner leading to computational overhead². It is established that high frequency details from the mosaic image are more informative than those from individual channels⁶. More recently, an adaptive threshold based on high frequency information was proposed for the interpolation of green pixels²¹. Colour demosaicking has also been achieved

by considering the spectral and spatial sparse representations of images jointly²². All these techniques highlight the fact that the presence of edges should be taken into account while interpolating. This forms the basis of our paper in which we use the edge strength information from the mosaic image in a non-iterative manner for determining the relative participation of pixels while interpolating. The result is a linear filter that achieves interpolation through fuzzy memberships.

2. PROPOSED FUZZY NON-LINEAR COLOUR DIFFERENTIAL CORRELATIVE INTERPOLATION FOR HIGH DETAIL IMAGES

There are a number of colour correlation based interpolation techniques which assume either colour ratio⁸ or colour difference⁵ to be constant. The latter technique which is called the colour differential correlative interpolation (CDC) gives excellent results for positive colour correlation but produces colour artifacts in the case of negative colour correlation or location of edge points. The non-linear CDC filter is used to reduce the artifacts that arise in the colour difference method¹. The non-linear CDC filter involves a directed interpolation process with constant scrutiny of edge information and consequent selective participation of the neighborhood pixels in the interpolation. We avoid this constant scrutiny of edges by including all the pixels in the interpolation process and assigning a weight to each pixel based on its edge strength. The lesser the edge strength at a pixel the more is its participation in the interpolation process.

The proposed fuzzy non-linear CDC filter is described below. Authors defined the edge strength for a mosaic image, as defined by Kuno & Sugiura². Consider a 3 x 3 neighbourhood of pixels labeled P_1 - P_9 (Fig.1). Then the edge strength² at the center pixel P_5 is given by

G_{00}	B_{01}	G_{02}	B_{03}	G_{04}	B_{05}	G_{06}
R_{10}	G_{11}	R_{12}	G_{13}	R_{14}	G_{15}	R_{16}
G_{20}	B_{21}	G_{22}	B_{23}	G_{24}	B_{25}	G_{26}
R_{30}	G_{31}	R_{32}	G_{33}	R_{34}	G_{35}	R_{36}
G_{40}	B_{41}	G_{42}	B_{43}	G_{44}	B_{45}	G_{46}
R_{50}	G_{51}	R_{52}	G_{53}	R_{54}	G_{55}	R_{56}
G_{60}	B_{61}	G_{62}	B_{63}	G_{64}	B_{65}	G_{66}

P_1	P_2	P_3
P_4	P_5	P_6
P_7	P_8	P_9

Figure 1. Bayer CFA Pattern and the 3 x 3 neighbourhood used to calculate the edge strength S.

Received 28 June 2013, revised 22 October 2013, online published 23 January 2014

$$S = \frac{|P_1 - P_9|}{2} + \frac{|P_3 - P_7|}{2} + |P_2 - P_8| + |P_4 - P_6| \quad (1)$$

For any pixel k in the mosaic image, the edge strength computed using Eqn. (1) is S_k , $k = 1, 2, \dots, M \times N$, where $M \times N$ is the size of the mosaic image. The fuzzy membership of the pixel k for participation in the interpolation process is given by

$$\mu_k = 1 - \frac{S_k}{\max_k(S_k)} \quad (2)$$

The fuzzy membership μ_k in Eqn. (2) has values in the range of 0 to 1. High membership indicates that k belongs to a smooth region (low edge strength S_k) and low membership indicates that k is an edge pixel (high edge strength S_k).

The fuzzy average of a set X with elements $x \in X$ having a set of associated memberships $\{\mu\}$ is defined as

$$\mu = \frac{\sum_{x \in X} \mu x}{\sum_{x \in X} \mu} \quad (3)$$

Now we replace the averaging in the interpolation process of the non-linear CDC filter by the fuzzy averaging of the interpolating pixels using Eqn. (3), instead of checking iteratively whether the correlation is maximum along horizontal (H) or vertical (V) direction and applying the interpolation only in that direction¹. Since each pixel is weighted by its membership, the participation of edge pixels in the negative correlation case is automatically reduced due to lower fuzzy memberships.

The steps of our fuzzy non-linear CDC filter method are outlined below on the lines of the process in¹ for the Bayer pattern in Fig. 1. Here the lower case letters are the interpolated signals and the upper case letters are the already existing ones in the mosaic image. Step 0 involves the computation of the gradients $divKv$ and $divKh$ in H and V directions respectively¹. This step is omitted in our method since the participation of the interpolating pixels is determined automatically through fuzzy memberships and not through a rigorous *if-else* procedure.

Step 1: G plane interpolation on R and B planes

At the R_{32} pixel location,

$$g_{32} = R_{32} + (G_{32\varepsilon} - R_{32\varepsilon}) \quad (4)$$

The subscript ε in Eqn. (4) denotes low frequency information computed by fuzzy averaging as shown below.

$$G_{32\varepsilon} = \frac{\sum_{ij} \mu_{ij} G_{ij}}{\sum_{ij} \mu_{ij}}, ij \in 22, 31, 33, 42 \quad (5)$$

$$R_{32\varepsilon} = \frac{\sum_{ij} \mu_{ij} R_{ij} + 4\mu_{32} R_{32}}{\sum_{ij} \mu_{ij} + 4\mu_{32}}, ij \in 12, 30, 34, 52 \quad (6)$$

The edge pixels thus contribute less to the computation of the second term in Eqn. (4) which is the offset value. The G values at B pixel locations are similarly computed.

Step 2: R and B plane interpolation on G plane.

At the G_{22} pixel location,

$$r_{22} = G_{22} + (R_{22ve} - g_{22ve}) \quad (7)$$

where

$$R_{22ve} = \frac{\sum_{ij} \mu_{ij} R_{ij}}{\sum_{ij} \mu_{ij}}, ij \in 12, 32 \quad (8)$$

$$g_{22ve} = \frac{\sum_{ij} \mu_{ij} g_{ij}}{\sum_{ij} \mu_{ij}}, ij \in 12, 32 \quad (9)$$

Similarly at the G_{33} pixel location,

$$r_{33} = G_{33} + (R_{33he} - g_{33he}) \quad (10)$$

The subscripts h and v in Eqn. (10) and Eqn. (7) denote the low frequency information in horizontal and vertical directions respectively. The B values at all G pixel locations are similarly computed.

Step 3: Interpolation of R and B planes on B and R planes respectively.

At the B_{23} pixel location,

$$r_{23} = g_{23} + (R_{23e} - g_{23e}) \quad (11)$$

where,

$$R_{23e} = \frac{\sum_{ij} \mu_{ij} R_{ij}}{\sum_{ij} \mu_{ij}}, ij \in 12, 14, 32, 34 \quad (12)$$

$$g_{23e} = \frac{\sum_{ij} \mu_{ij} g_{ij}}{\sum_{ij} \mu_{ij}}, ij \in 12, 14, 32, 34 \quad (13)$$

The B values at all R pixel locations are similarly computed.

3. THE FUZZY BILINEAR INTERPOLATION FILTER FOR REAL TIME APPLICATIONS

Authors presents a simplified version method for faster processing. In this method we simply interpolate the colours in the same plane without adding any offset to the existing center pixel. This is equivalent to a fuzzification of the bilinear interpolation filter¹¹ method of colour demosaicking, which averages the colour samples without checking for any edges. The edge strength is used to compute the fuzzy memberships as in Eqn. (2). The fuzzy memberships obtained from the edge strength using Eqn. (2) constrain the contribution of edge pixels in the weighted averaging.

The steps of our fuzzy bilinear interpolation method are given below for the Bayer pattern in Fig. 1.

Step 1: G plane interpolation on R and B planes

At the R_{32} pixel location

$$g_{32} = \frac{\sum_{ij} \mu_{ij} G_{ij}}{\sum_{ij} \mu_{ij}}, ij \in 22, 31, 33, 42 \quad (14)$$

Step 2: R and B plane interpolation on G, B planes and G,R planes respectively.

At the G_{22} pixel location,

$$r_{22} = \frac{\sum_{ij} \mu_{ij} R_{ij}}{\sum_{ij} \mu_{ij}}, ij \in 12, 32 \quad (15)$$

At the B_{23} pixel location,

$$r_{23} = \frac{\sum_{ij} \mu_{ij} R_{ij}}{\sum_{ij} \mu_{ij}}, ij \in 12, 14, 32, 34 \quad (16)$$

The B values at all G and R pixel locations are similarly computed. In the case of the Bilinear interpolation filter the memberships in Eqns. (14)-(16) are equal to 1.

4. EXPERIMENTAL RESULTS

The experiments are conducted on the high definition images, 'Fungi', 'Insect', 'Painting', 'Fruits', 'Stones' downloaded from the web shown in Fig. 2, and also on state of the art databases – Berkeley (100 test images of size 481 x 321)⁹, high resolution and high dimensional Landsat satellite images¹⁷, 700 x 504 Nikon fluorescent microscopy images¹⁸ and the 512 x 712 Kodak true colour loss less images¹⁹. For each image, the mosaic is obtained in the layout of the Bayer pattern in Fig. 1. The coding is done in MATLAB 7.9 on a 2.3 GHz Pentium processor. The PSNR and runtime of the proposed fuzzy bilinear interpolation filter (labeled as (k)) and

the proposed fuzzy Non-linear CDC filter (labeled as (l)) are compared with a slew of state-of-the-art colour demosaicking methods namely,

- (a) Nearest neighbor replication¹²
- (b) Bilinear interpolation¹¹
- (c) Smooth hue transition interpolation¹³
- (d) Pattern matching algorithm¹⁴
- (e) Edge directed interpolation¹⁵
- (f) Colour interpolation using Laplacian second order colour correction⁷
- (g) Threshold based variable number of gradients¹⁶
- (h) Gradient corrected linear interpolation²⁰
- (i) Edge strength based CFA interpolation² and
- (j) Non-linear CDC filter¹.

The colour demosaicking results of the five high-definition images are shown in Table 1 for all methods. It is seen that for

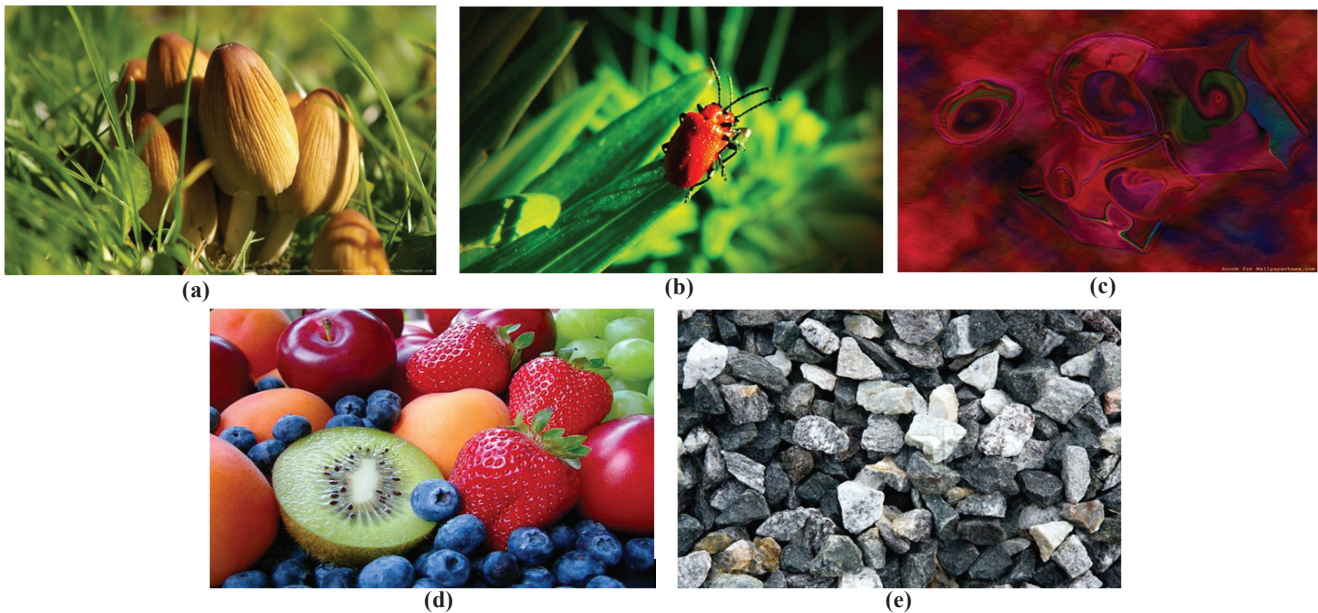


Figure 2. The high definition images used for the experimentation, (a) Fungi, (b) Insect, (c) Painting, (d) Fruits, (e) Stones.

Table 1. Results of real-time colour filter array interpolation on the high definition images in Fig. 2 in terms of PSNR and running time in seconds.

Methods	Fungi 2560 x 1600		Insect 1680 x 1050		Painting 1024 x 768		Fruits 495 x 370		Stones 480 x 320	
	PSNR	Time	PSNR	Time	PSNR	Time	PSNR	Time	PSNR	Time
(a)	46.7	0.23	35.9	0.02	47.8	0.09	38.6	0.03	48.0	0.07
(b)	50.3	0.77	36.9	0.03	50.2	0.40	40.3	0.04	51.6	0.17
(c)	41.4	43.1	38.2	1.69	42.3	18.3	38.9	1.97	46.4	8.25
(d)	43.2	124.7	34.9	4.60	46.7	52.6	36.2	5.46	47.3	24.5
(e)	51.1	12.4	37.0	0.43	50.6	5.13	40.6	0.52	51.9	2.29
(f)	39.0	34.2	34.8	1.47	42.2	13.3	35.0	1.78	49.5	4.67
(g)	40.1	351.9	35.4	14.6	42.1	145.9	35.7	17.5	45.1	64.2
(h)	52.3	0.22	39.2	0.01	51.1	0.05	42.3	0.01	49.6	0.03
(i)	Too large computations									
(j)	54.0	58.1	39.4	1.93	51.5	23.2	42.3	2.41	49.3	10.3
(k)	50.9	26.8	37.0	0.94	50.5	11.2	40.6	1.12	51.9	5.36
(l)	53.5	65.7	40.1	2.46	52.0	29.7	42.8	2.91	50.0	12.6

all images except Fungi, the proposed fuzzy filters outperform the other methods, with our fuzzy bilinear interpolation filter (k) providing the lesser execution time, albeit at a reduced picture quality. The fuzzy bilinear interpolation filter however gives best results for the ‘Stones’ image where colour contrast and colour edges are few. The results for the Edge strength filter² are not included since the runtime (several hours for each image)

for these images is too considerable for real-time applications. Fig. 3 shows the mosaic image and its edge strength map for the ‘Fruits’ image. A small segment of the ‘Fruits’ image, highlighted in Fig. 3, is used for visual comparison of the reconstructed results of all methods in Fig. 4. As observed, the fuzzy non-linear CDC filter (l) gives the best visual match to the original image in Fig. 3 and the highest PSNR in Table 2.

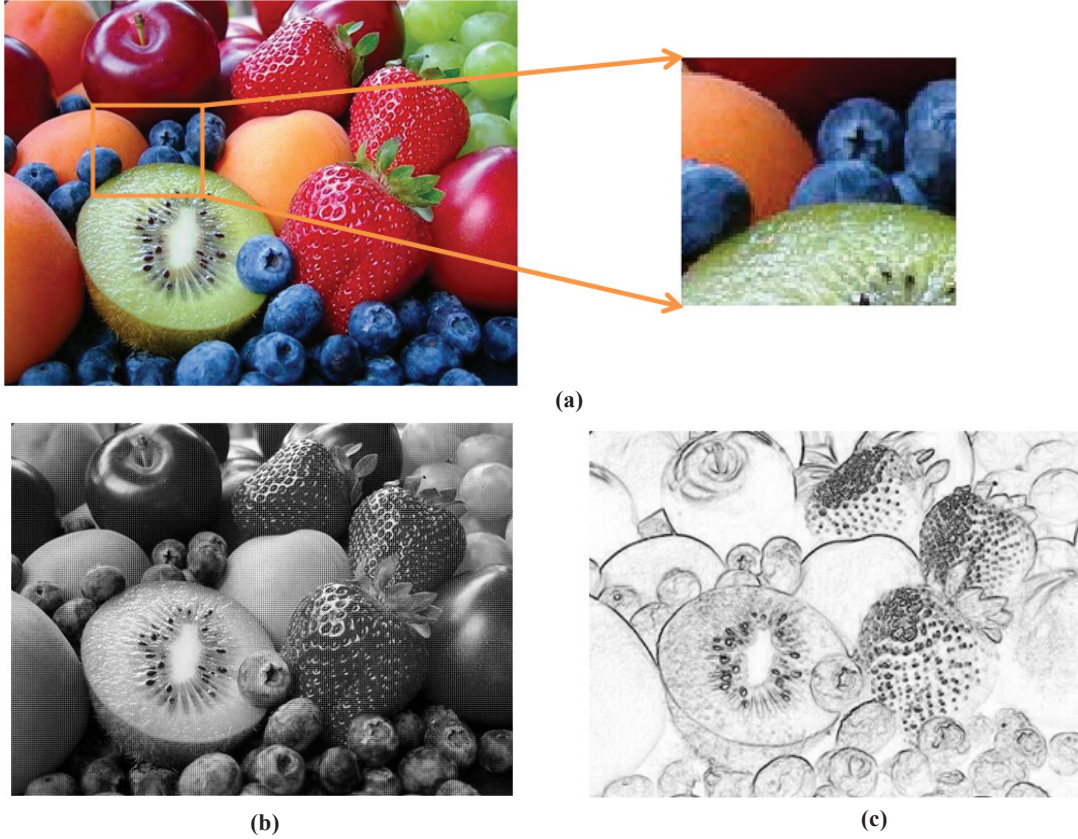


Figure 3. (a) The original ‘Fruits’ image with a small section shown highlighted, (b) The original mosaic image, and (c) The edge strength map of the mosaic image.

Table 2. Results of real-time colour filter array interpolation on various datasets in terms of the (average PSNR \pm Standard deviation, average time in seconds \pm Standard deviation).

Methods	Berkeley images (100 images)		Landsat satellite images (23 images)		Nikon fluorescent microscopy images (24 images)		Kodak loss-less colour images (24 images)	
	PSNR	Time	PSNR	Time	PSNR	Time	PSNR	Time
(a)	40.2 \pm 1.2	0.008 \pm 0.004	39.0 \pm 2.6	0.08 \pm 0.05	41.8 \pm 1.8	0.02 \pm 0.02	40.1 \pm 1.8	0.04 \pm 0.005
(b)	44.0 \pm 2.2	0.09 \pm 0.03	41.1 \pm 3.6	0.4 \pm 0.22	42.2 \pm 2.1	0.07 \pm 0.012	41.2 \pm 2.1	0.13 \pm 0.01
(c)	42.5 \pm 2.3	1.91 \pm 0.28	39.1 \pm 2.0	15.9 \pm 8.7	41.8 \pm 2.2	3.6 \pm 0.09	41.0 \pm 2.2	4.6 \pm 0.2
(d)	37.8 \pm 1.8	5 \pm 0.4	37.5 \pm 2.0	56.1 \pm 29.2	41.7 \pm 1.5	9.8 \pm 0.46	37.6 \pm 1.1	10.6 \pm 0.3
(e)	44.7 \pm 2.6	0.5 \pm 0.07	41.5 \pm 3.8	5.5 \pm 3.0	44.3 \pm 2.2	0.92 \pm 0.04	42.3 \pm 2.2	1.1 \pm 0.08
(f)	36.1 \pm 3.1	1.6 \pm 0.17	36.7 \pm 2.2	12.6 \pm 6.8	40.2 \pm 1.2	2.0 \pm 0.31	36.6 \pm 2.0	4.4 \pm 0.7
(g)	37.2 \pm 2.2	15 \pm 2	36.2 \pm 1.7	129.5 \pm 68.2	39.4 \pm 1.4	24.9 \pm 2.4	35.9 \pm 1.7	48.4 \pm 4
(h)	45.6 \pm 2.1	0.006 \pm 0.001	43.7 \pm 3.9	0.05 \pm 0.02	43.3 \pm 2.2	0.01 \pm 0.0	44.4 \pm 2.3	0.03 \pm 0.02
(i)	46.0 \pm 2.3	228 \pm 34	Too large computations		42.6 \pm 2.1	275.0 \pm 17.5	44.8 \pm 2.3	403 \pm 60
(j)	45.0 \pm 2.0	2 \pm 0.11	44.2 \pm 4.0	18.7 \pm 9.6	43.0 \pm 2.1	4.3 \pm 0.08	46.0 \pm 2.4	6.9 \pm 0.1
(k)	44.3 \pm 2.5	0.95 \pm 0.06	41.3 \pm 3.8	14.2 \pm 7.5	44.4 \pm 2.2	1.9 \pm 0.03	42.0 \pm 2.2	3.4 \pm 0.09
(l)	46.3 \pm 2.4	2.5 \pm 0.2	44.4 \pm 4.0	23.0 \pm 11.8	43.1 \pm 2.2	5.1 \pm 0.12	45.3 \pm 2.3	8.7 \pm 0.07

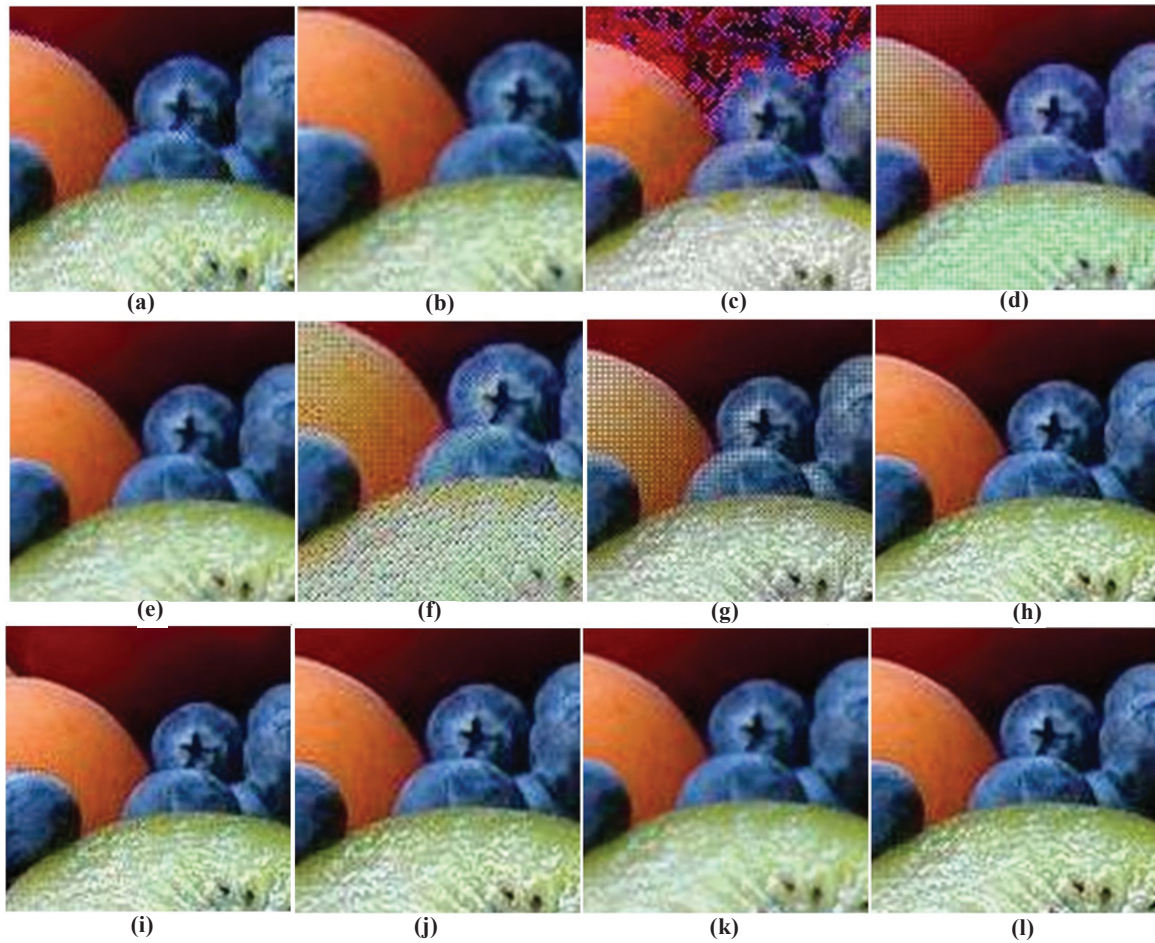


Figure 4. The reconstructed colour images for the highlighted section of Fruits image in Fig. 3 for the 12 colour demosaicking methods labeled (a) to (l) in the results section.

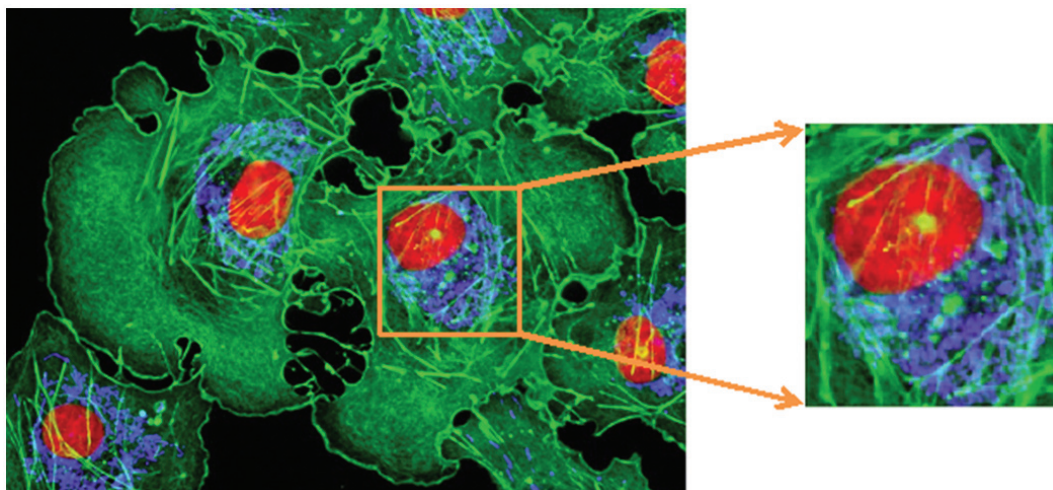


Figure 5. An example from the Nikon Microscopy database with a highlighted section shown for subsequent comparison of demosaicking results.

The results for the Berkeley, Landsat, Nikon Microscopy, and Kodak datasets are summarized in Table 2 for methods (a) to (l) and these once again ascertain the efficiency of the fuzzy colour demosaicking algorithms proposed in this paper in terms of the highest possible PSNR achieved at the lowest runtime. The proposed Fuzzy bilinear interpolation method

is a good option for colour interpolation in real-time with acceptable visual quality, whereas for high resolution images the Fuzzy non-linear CDC filter can be relied on for obtaining highly efficient results in a very short time. Fig. 6 shows the interpolated results of the zoomed in image of the microscopy image shown in Fig. 5. The results indicate the best visual

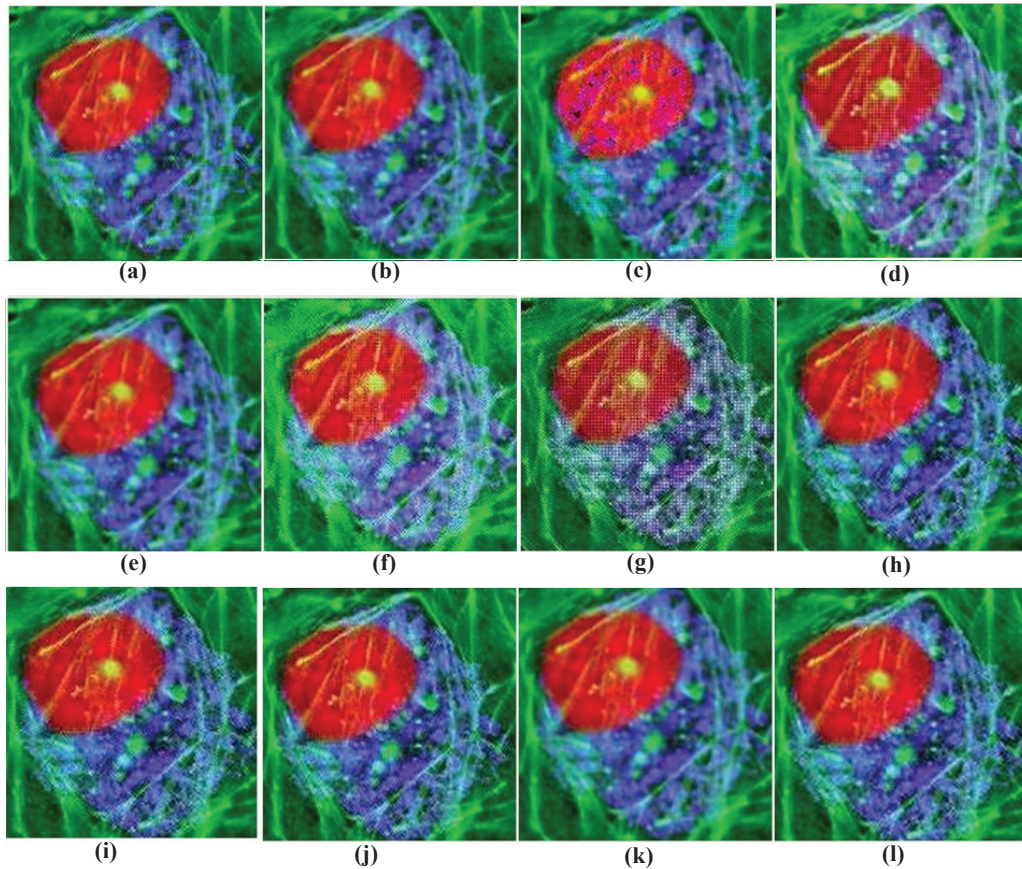


Figure 6. Results of 12 demosaicking methods (a)-(l) on an example from the Nikon Microscopy database the highlighted section in Fig. 5.

quality for the proposed fuzzy bilinear interpolation method as compared to all other methods. The Gradient corrected linear interpolation (method (h)) provides the lowest runtime but its PSNR is relatively low. The Fuzzy bilinear interpolation is found to excel for the Microscopy images in terms of highest PSNR with an average execution time of only 2 s. The Fuzzy non-linear CDC method is found best for the high resolution satellite images and marginally close to the non-linear CDC filter for the Kodak images, outperforming all other methods in a consistent manner.

5. CONCLUSION

In this study, authors fuzzify the non-linear CDC colour filter array interpolation and the bilinear interpolation techniques for colour demosaicking. The fuzzy memberships used are derived from the edge strength map of the mosaic image. We observe a rise in PSNR values and reduction in execution time for high resolution images where the edge information is significant.

REFERENCES

1. Kuno, Tetsuya & Sugiura, Hiroaki. Practical colour filter array interpolation part 2 with non-linear filter. *IEEE Trans. Consumer Electron.*, 2006, **52**(4), 1409-1417.
2. Pekkuksen, Ibrahim & Altunbasak, Yucel. Edge strength Filter based colour filter array interpolation. *IEEE Trans. Image Process.*, 2012, **21**(1), 393-397.
3. Bayer, B.E. Colour Imaging Array, U.S. 3 971 065, Jul. 1976.
4. Hibbard, R.H. Apparatus and method for adaptively interpolating a full colour image utilizing luminance gradients, U.S. Patent 5 382 976, Jan. 17, 1995.
5. Laroche, C.A. & Prescott, M.A. Apparatus and method for adaptively interpolating a full colour image utilizing chrominance gradients, U.S. Patent 5 373 322, Dec. 13, 1994.
6. Lian, N.X.; Chang, L.; Tan, Y.P. & Zagorodnov, V. Adaptive filtering for colour filter array demosaicking, *IEEE Trans. Image Process.*, 2007, **16**(10), 2515-2525.
7. Hamilton, J.F. & Adams, J.E. Adaptive colour plane interpolation in single sensor colour electronic camera, U.S. Patent 5 629 734, Mar. 13, 1997.
8. Lukac, R. & Plataniotis, K.N. A normalized model for colour-ratio based demosaicking schemes. *In the International Conference on Image Processing*, 2004, **3**, pp.1657-1660.
9. The Berkeley segmentation dataset and benchmark. <http://www.eecs.berkeley.edu/Research/Projects/CS/vision/bsds/> (Accessed online on 1st October 2013)
10. Okada, S.; Matsuda, Y.; Yamada, T. & Kobayashi, A. System on a chip for digital still camera. *IEEE Trans. Consumer Electron.*, 1999, **45**(1), 259-267.
11. Adams, James E. Jr. Interactions between colour plane interpolation and other image processing functions in

- electronic photography. *In the Proceedings of the SPIE Electronic Imaging Conference*, 1995, **2416**, 144-151.
12. Sakamoto, Tadashi; Nakanishi, Chikako & Hase, Tomohiro. Software pixel interpolation for digital still cameras suitable for A 32-bit MCU. *IEEE Trans. Consumer Electron.*, 1998, **44**(4), 1342-1352.
 13. Cok, David R. Signal processing method and apparatus for producing interpolated chrominance values in a sampled colour image signal, U.S. Patent 4,642,678, Eastman Kodak Company, 1987.
 14. Wu, X.; Choi, W. K. & Bao, P. Colour restoration from digital camera data by pattern matching. *In the Proceedings of the SPIE's Electronic Imaging Conference Colour Imaging: Device- Independent Colour*, Colour Hardcopy, and Graphic Arts II, 1997, **3018**, pp. 12-17.
 15. Laroche, C.A. & Prescott, M.A. Apparatus and method for adaptively Interpolating a full colour image utilizing chrominance gradients, U.S. Patent 5 373 322, Dec. 13, 1994.
 16. Chang, Edward; Cheung, Shiufun & Davis, Y. Pan. Colour filter array recovery using a threshold-based variable number of gradients. *In the Proceedings of SPIE.*, 1999, **3650**.
 17. <http://www.landsat.org/> (Accessed online on 1st October 2013)
 18. <http://www.microscopyu.com/articles/fluorescence/index.html> (Accessed online on 1st October 2013)
 19. Franzen, Rich. Kodak lossless true colour image suite, URL: <http://r0k.us/graphics/kodak/> (Accessed online on 1st October 2013)
 20. Côté, Guy & Jeffrey, E. Frederiksen. System and method for Demosaicking image data using weighted gradients. European Patent No. EP 2491721. 29 Aug. 2012.
 21. Newlin, Dev R. & Monie, Elwin Chandra. Edge sensing Demosaicking using adaptive weighted interpolation. *Am. J. Applied Sci.*, 2013, **10**(4), 418.
 22. Dahua, Gao; Wu, Xiaolin; Shi, Guangming & Zhang, Lei. Colour demosaicking with an image formation model and adaptive PCA. *J. Visual Commun. Image Representation*, 2012, **23**(7), 1019-1030.

CONTRIBUTORS



Dr Seba Susan received her PhD (Image Processing) from the Indian Institute of Technology (IIT), Delhi. She is currently Assistant Professor in the Department of Information Technology, Delhi Technological University (DTU), Delhi. Her research areas are statistical pattern recognition and soft computing.



Mr Deepak Aneja is a postgraduate student of the Department of Information Technology, Delhi Technological University, Delhi. His areas of interest include colour image processing and fuzzy systems.

Field Characteristics in Dielectric Rectangular Wave Guide with harmonics

Deepender Dabas,
ECE Deptt. JIIT University, Noida, UP, India.
dsdabas@gmail.com,

Savita
CS Department, BCAS, Delhi University, India
savita.dabas@gmail.com

N S Raghava
ECE Deptt. Delhi College of Engineering, Delhi, India
nsraghava@dce.ac.in,

Abstract - In this paper field distribution inside rectangular dielectric waveguide has been studied assuming square wave field incidence for its dominant and other modes. Incident square wave field can be seen as made up of various harmonics of sine and cosine functions. Here up to five harmonics of sine and cosine function are taken to represent the field distribution and mathematical equations are derived. Field distribution inside and outside the wave guide are plotted using Mat Lab application for even and odd symmetric fields. Two modes, E_{mn}^y and E_{mn}^x of propagation are considered inside the dielectric wave guide, having most of the electric field in y direction and x direction respectively. From these, Eigen equations and propagation constant can be calculated for harmonics of the incidence wave function. For frequencies above cut-off, field is assumed to be confined inside the waveguide and decaying exponentially outside, as assumed in Marcatili's method to find the wave guide solution.

Keywords- Field generated in E_{mn}^y and E_{mn}^x mode, Rectangular dielectric waveguide, square wave incidence, harmonic of sine (cosine) function for square wave.

I. INTRODUCTION

Dielectric waveguides restrict and direct the signal in particular direction and find their applications in many communication circuits, at millimeter and sub millimeter frequencies. It is important to study their modes of propagation and its propagation characteristics. The modes of dielectric waveguides are more difficult to analyze than those of the metallic rectangular waveguide because they don't have metallic boundaries [1]. A lot of study has been done in wave guides by assuming co-sinusoidal field as incidence field [2], [3] but very less by assuming square wave field or harmonics field as incidence. In the present analysis, distribution of electric and magnetic field as square wave form is represented by the harmonics of the sine (cosine) wave field inside the core and exponential decaying field outside the waveguide.

The dielectric rectangular wave guide material is assumed to have relative dielectric constant, $\epsilon_r > 1$ and surrounding material is air. Because of absence of conducting boundaries the EM field exists inside and outside the wave guide [2], [11].

E_{mn}^y and E_{mn}^x as well as hybrid modes (all six components E_x , E_y , E_z , H_x , H_y , H_z) are supported by rectangular dielectric waveguide [4], [5]. Modes are designated as E_{mn}^y , if the electric field is parallel to the y-axis, and as E_{mn}^x if electric field is parallel to x-axis. m and

n subscript designate the number of maxima in x and y direction. E_{mn}^x modes have components namely E_x , E_y , E_z , H_x , and H_z , with $H_x = 0$ which can be visualized as the TM_x modes. Similarly, E_y , E_z , H_x , H_y , and H_z , with $E_x = 0$ are the components of the E_{mn}^y modes which can be visualized as TE_x modes [13] - [15]. In dielectric waveguide the dominant modes correspond to $m=n=1$.

II. EQUATIONS WITH SQUARE WAVE INCIDENCE

Taking square wave as incident field on rectangular dielectric waveguide and propagation along z-axis as shown in figure 1.

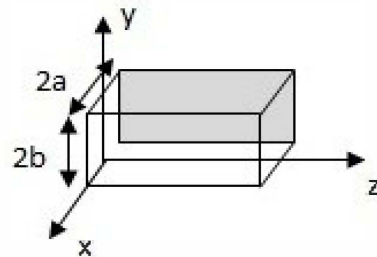


Fig. 1. Wave propagation in rectangular dielectric wave guide in + z- axis

The incident wave function can be written in two forms; One in even symmetric and other odd symmetric (asymmetric) field [4, 20].

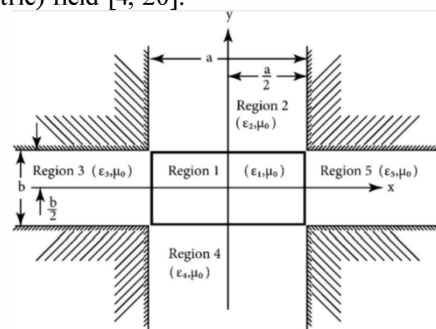


Fig. 2. Various regions defined in Marcatalli approximation method [2]

Using the Marcatili's approximation method, assuming most of the field is confined inside the core of the waveguide and the field in corners is neglected as shown in figure 2 [2]. The field potentials for even symmetric and odd symmetric (asymmetric) fields can be written as described in subsequent sections.

A. Equations for even symmetry

$$\begin{aligned}\Psi_{\text{even}} &= A_1 \text{Rect}^e(ux) \text{Rect}^e(u_1y) e^{-jk_z z} \\ &= B_1 e^{-\nu x} \text{Rect}^e(u_1y) e^{-jk_z z} \quad |x| \leq a, |y| \leq b \text{ (inside guide)} \\ &= C_1 \text{Rect}^e(ux) e^{-\nu_1 y} e^{-jk_z z} \quad |x| \geq a, |y| \leq b \text{ (outside guide)} \\ &= C_1 \text{Rect}^e(ux) e^{-\nu_1 y} e^{-jk_z z} \quad |x| \leq a, |y| \geq b \text{ (outside guide)} [7]\end{aligned}\quad (1)$$

The function $\text{Rect}^e()$ is taken for representing even rectangular field. Also u, u_1, K_z are propagation constant inside the dielectric in x, y and z direction and ν, ν_1 are attenuation constant in x and y directions outside the dielectric region. A_1, B_1 and C_1 are the amplitude values of the function. The $\text{Rect}()$ function can be seen in the form of harmonics of cosine and sine function for symmetric and asymmetric fields. The regions $x > a$ and $y > b$ have been neglected as fields are very weak at these corners, this has been done by applying Marcanti's and Goell's approximate methods [1-2].

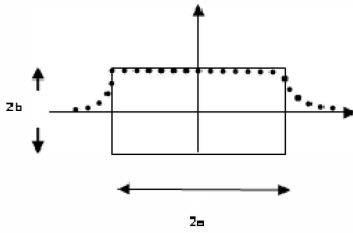


Fig. 3. Even symmetric rectangular function across the dielectric waveguide

Figure 3 shows the rectangular field as even symmetric distribution to origin. The even $\text{Rect}^e()$ function can be written as harmonics of cosine functions. The harmonics equations for n up to 9 can be written as:-

$$\begin{aligned}(n=3) \quad F(x) &:= \frac{4b}{\pi} \cos\left(\frac{\pi x}{a}\right) - \frac{4b}{3\pi} \cos\left(\frac{3\pi x}{a}\right) \\ (n=5) \quad F(x) &:= \frac{4b}{\pi} \cos\left(\frac{\pi x}{a}\right) - \frac{4b}{3\pi} \cos\left(\frac{3\pi x}{a}\right) + \frac{4b}{5\pi} \cos\left(\frac{5\pi x}{a}\right) \\ (n=9) \quad F(x) &:= \frac{4b}{\pi} \cos\left(\frac{\pi x}{a}\right) - \frac{4b}{3\pi} \cos\left(\frac{3\pi x}{a}\right) + \frac{4b}{5\pi} \cos\left(\frac{5\pi x}{a}\right) - \frac{4b}{7\pi} \cos\left(\frac{7\pi x}{a}\right) + \frac{4b}{9\pi} \cos\left(\frac{9\pi x}{a}\right)\end{aligned}\quad (2)$$

Where $F(x)$ is rectangular function in terms of harmonics of cosine only and b is the amplitude values of the function. Taking even symmetric rectangular function in terms of five harmonics from eq. 2, the field equations (1) can be written as

$$\begin{aligned}\Phi_{\text{even}} &:= A_1 \left(\cos(ux) - \frac{1}{3} \cos(3ux) + \frac{1}{5} \cos(5ux) \right) + \\ &\quad \left(\cos(u_1 y) - \frac{1}{3} \cos(3u_1 y) + \frac{1}{5} \cos(5u_1 y) \right) (e)^{-jk_z z} \\ &:= B_1 (e)^{-\nu x} \left(\cos(u_1 y) - \frac{1}{3} \cos(3u_1 y) + \frac{1}{5} \cos(5u_1 y) \right) (e)^{-jk_z z} \\ &:= C_1 \left[\cos(ux) - \frac{1}{3} \cos(3ux) + \frac{1}{5} \cos(5ux) \right] (e)^{-\nu_1 y} (e)^{-jk_z z}\end{aligned}\quad (3)$$

Constant A, B and C are the normalized amplitude values. From these derived mathematical harmonics equations (3) graphical distribution of fields can be plotted using 3-D graphical tool of Mat lab.

B. Equations for odd symmetry

Rectangular field equations for asymmetric (odd) distribution can be written as

$$\begin{aligned}\Psi_{\text{odd}} &= A_1 \text{Rect}^o(ux) \text{Rect}^o(u_1y) e^{-jk_z z} \\ &= B_1 e^{-\nu x} \text{Rect}^o(u_1y) e^{-jk_z z} \quad |x| \leq a, |y| \leq b \text{ (inside guide)} \\ &= C_1 \text{Rect}^o(ux) e^{-\nu_1 y} e^{-jk_z z} \quad |x| \geq a, |y| \leq b \text{ (outside guide)} \\ &= C_1 \text{Rect}^o(ux) e^{-\nu_1 y} e^{-jk_z z} \quad |x| \leq a, |y| \geq b \text{ (outside guide)} [7]\end{aligned}\quad (4)$$

Here, the function $\text{Rect}^o()$ is taken for representing odd rectangular field and other terms remain same, as defined earlier. Figure 4 shows the odd symmetric rectangular field to origin.

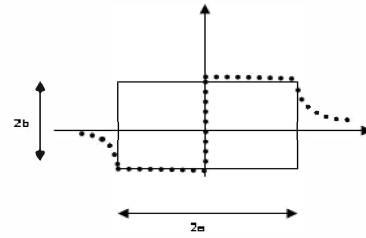


Fig. 4. Odd symmetric rectangular function across the dielectric waveguide

The odd rectangular field can be written with harmonics of sine function. For n ranging from 3 to 9 the odd rectangular function are:-

$$\begin{aligned}(n=3) \quad F(x) &:= \frac{4b}{\pi} \sin\left(\frac{\pi x}{a}\right) + \frac{4b}{3\pi} \sin\left(\frac{3\pi x}{a}\right) \\ (n=5) \quad F(x) &:= \frac{4b}{\pi} \sin\left(\frac{\pi x}{a}\right) + \frac{4b}{3\pi} \sin\left(\frac{3\pi x}{a}\right) + \frac{4b}{5\pi} \sin\left(\frac{5\pi x}{a}\right) \\ (n=9) \quad F(x) &:= \frac{4b}{\pi} \sin\left(\frac{\pi x}{a}\right) + \frac{4b}{3\pi} \sin\left(\frac{3\pi x}{a}\right) + \frac{4b}{5\pi} \sin\left(\frac{5\pi x}{a}\right) \\ &\quad + \frac{4b}{7\pi} \sin\left(\frac{7\pi x}{a}\right) + \frac{4b}{9\pi} \sin\left(\frac{9\pi x}{a}\right)\end{aligned}\quad (5)$$

Similarly, putting the odd rectangular fields of Eqn 5 for five harmonics the field equations (4) becomes

$$\begin{aligned}\Phi_{\text{odd}} &:= A_1 \left(\sin(ux) + \frac{1}{3} \sin(3ux) + \frac{1}{5} \sin(5ux) \right) + \\ &\quad \left(\sin(u_1 y) + \frac{1}{3} \sin(3u_1 y) + \frac{1}{5} \sin(5u_1 y) \right) (e)^{-jk_z z} \\ &:= B_1 (e)^{-\nu x} \left(\sin(u_1 y) + \frac{1}{3} \sin(3u_1 y) + \frac{1}{5} \sin(5u_1 y) \right) (e)^{-jk_z z} \\ &:= C_1 \left(\sin(ux) + \frac{1}{3} \sin(3ux) + \frac{1}{5} \sin(5ux) \right) (e)^{-\nu_1 y} (e)^{-jk_z z}\end{aligned}\quad (6)$$

From the mathematical equations (3) and (6) graphical distribution of fields can be plotted by using 3-D graphical tool of Mat lab. This field distribution gives a better understanding of 3-D visualization of harmonics of a wave.

The 3-D graph plotted are with the field varying as even and odd function around origin in x and y direction inside the dielectric and decaying exponentially outside the boundary of dielectric. The propagation constant and attenuation constant inside and outside the waveguide are assumed with certain values and different propagation mode graphs are plotted.

III. EVEN SYMMETRIC FIELDS WITH VARIOUS HARMONICS

A. Inside the waveguide

The even symmetric square fields E_{mn}^x with E_x and E_y harmonics components in x and y direction and propagation in z direction, are shown in figure 5. The derived mathematical equation 3 has been normalized with respect to amplitude. Wave fields inside the dielectric for 1, 3 and 5 harmonics function are plotted for mode $m=n=1$.

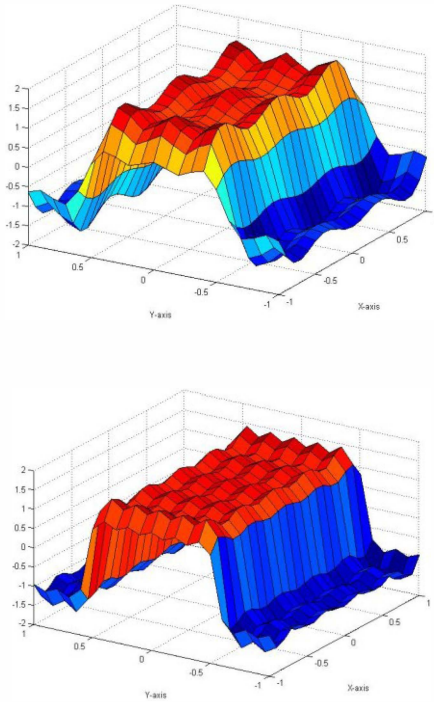


Fig. 5. E_{mn}^x mode even symmetric fields inside the waveguide with harmonics (1-5 harmonics)

B. Outside the waveguide

Exponentially decaying field outside wave guide derived in equation 3 for same mode are shown in figure 6. The wave function plots are shown for third and fifth harmonics.

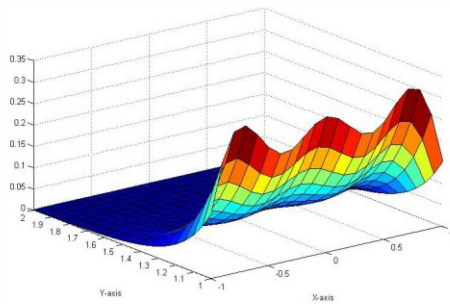


Fig. 6 (a)

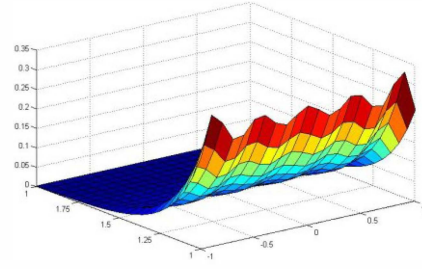


Fig. 6 (a) and (b). E_{mn}^x mode even symmetric fields outside the waveguide with harmonics (3 and 5 harmonics)

IV. ODD SYMMETRIC FIELDS WITH VARIOUS HARMONICS

A. Inside the waveguide

Similarly, the odd symmetric fields of E_{mn}^x mode are plotted by taking the equation 6. For the dominant mode ($m=n=1$) waveform plots for 1, 3 and 5 harmonics are shown in figure 7.

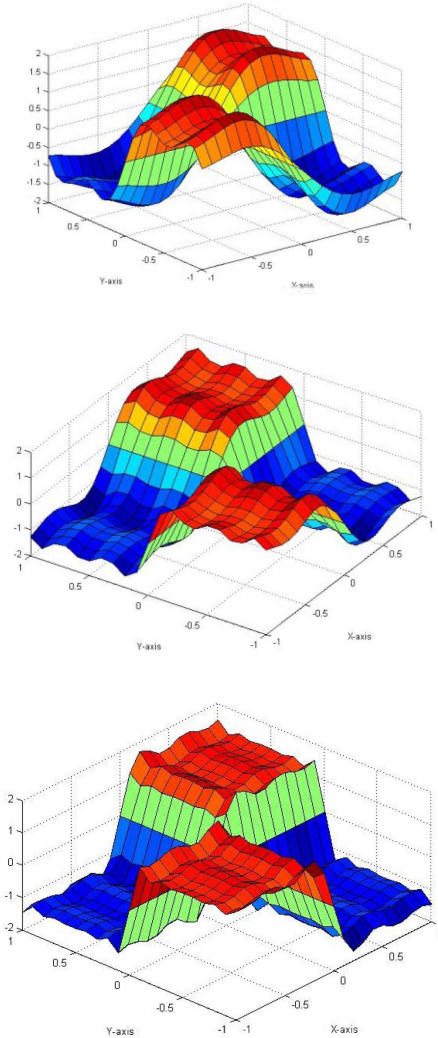


Fig. 7. E_{mn}^x Odd symmetric fields inside the waveguide with harmonics (1-5 harmonics)

B. outside the waveguide

Outside decaying field plot for odd symmetric function for E_{mn}^x mode is shown in figure 8. The wave function plot shown is for third harmonics.

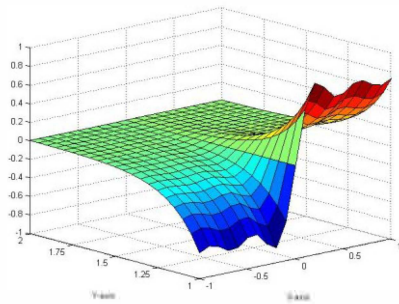


Fig. 8. E_{mn}^x mode odd symmetric fields outside the waveguide with 3 harmonics

V. FIELD DISTRIBUTION OF SOME OTHER MODES

Field distribution mode $m=1$ and $n=3$ ie E_{13}^x inside the wave guide are also drawn from same equations. Figure 9 depicts the field distribution of even symmetric field and figure 10 shows the odd symmetric field. These fields are shown only for fifth harmonics.

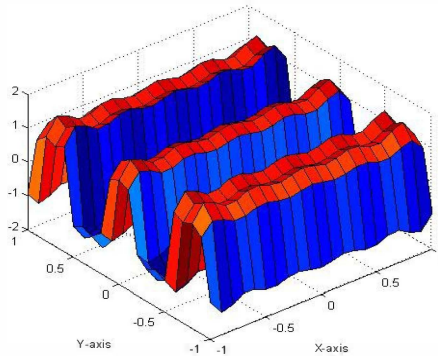


Fig. 9. Even field distribution for E_{13}^x mode inside waveguide with five harmonics

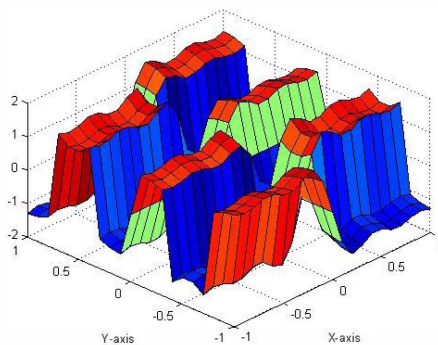


Fig. 10. Odd field distribution for E_{13}^x mode inside waveguide with five harmonics

V. RESULT AND DISCUSSIONS

The rectangular symmetric or asymmetric field basically consists of various harmonics of the cosine or sine functions. Field equations for up to five harmonics are being taken and the waveform plots for these harmonics inside and outside the wave guide are plotted using 3-D tool of Matlab. The waveform plot of up to fifth harmonics inside the wave guide looks like a square waveform. These 3-D plots give a clear understanding of all the fields inside as well as outside

the waveguide for various harmonics. Waveform plots, for not only these modes but for any other mode can also be plotted by using the same equations. From these wave function equations the characteristic equation with harmonics can be written and value of propagation constant can be found. This propagation constant can be compared with the propagation constant found by single sine or cosine field [24].

REFERENCES

- [1] J. E. Goell, "A circular harmonic computer analysis of rectangular dielectric waveguide," Bell Syst. Tech J., Vol 48, pp 2133-2160, Sept 1969.
- [2] E. A. J. Marcattili, "Dielectric rectangular wave guide and directional coupler for integrated optics," Bell Syst. Tech J., Vol 48, pp 2071-2102, Sept 1969.
- [3] W. Schlosser, and H.G. Unger, "Partially filled waveguide and surface waveguide of rectangular cross section," Advances in Microwave, New York, Academic press 1966, pp. 319-387.
- [4] T. E. Rozzi, M. Mongiardo, "Open electromagnetic waveguides," Issue 43 of IEE publication series. IET 1997.
- [5] C. Yeh, F. Shimabukuro, "The Essence of dielectric waveguides", Springer 2008.
- [6] R. F. Harrington, "Time harmonic Electromagnetic fields," IEEE press series on Electromagnetic wave theory.
- [7] S. K. Koul, "Millimeter wave and optical dielectric integrated guides and circuits," Wiley series in microwave and optical engineering. 1997.
- [8] J. Sharma, and A. De, "Full wave analysis of dielectric rectangular waveguide," Progress in Electromagnetics Research, vol.13,121-131, 2010.
- [9] R. Mittra, Y. Hou, and V. Jamnejad, "Analysis of open dielectric waveguides using mode-matching technique and variational methods," IEEE trans. on microwave theory and tech., MTT-28 vol. 1, pp. 36-43, January 1980.
- [10] K. Solbach, and I. Wolff, "The electromagnetic fields and the phase constants of dielectric image lines" IEEE transaction on microwave theory and techniques vol. 26, Issue 4, pp 266-274, April 1978.
- [11] K. Ogusu, "Numerical Analysis of rectangular dielectric waveguide and its modifications" IEEE transaction on microwave theory and techniques vol. 25, Issue 11, pp 874-885, 1977.
- [12] R. M. Knox, "Dielectric waveguide microwave integrated circuits – an overview," IEEE transaction on microwave theory and techniques vol. 24, Issue 11, pp 806-814, 1976.
- [13] R. Mittra, and S. W. Lee, "Analytical techniques in the theory of guided waves. New York, Macmillan, 1971.
- [14] R. E. Collin, "Field theory of guided wave". New York, IEEE press 1991.
- [15] L. Eyges, and P. Gianino, and P. Wintersteiner, "Modes of dielectric waveguide of arbitrary cross sectional shape," J. Opt. Soc. Amer. Vol. 69, 1226-1235, 1979.
- [16] W. Schollosser, and H.G. Unger, "Advances in Microwaves," Academic press New York, 1966.
- [17] C.B. Shaw, B.T. French, and C. Warner, "Further research on optical transmission lines," Science rep no2, automatics report No C7-929/501, Air force contract AF 449(638)-1504 AD635501.
- [18] J.C. Maxwell, "A treatise on electricity and magnetism," Dover, New York, 1954.
- [19] K. Sabetfakhri, and L.P.B. Katehi, "An integral transform technique for analysis of planar dielectric structures," IEEE transaction on microwave theory and techniques MTT vol. 42, 1052-1062, 1994.
- [20] S. Peng, T. Tamir, and H.L. Bertoni, "Theory of periodic dielectric waveguide," IEEE Transaction on Microwave Theory and Techniques, vol. 23, 123-133, 1975.
- [21] E.W. Kolk, N.H.G. Baken, and H. Blok, "Domain integral equation analysis of integrated optical channel and ridged waveguide in stratified media," J. Lightwave Technology, vol. 38, pp. 78-85, 1990.
- [22] G. Athanasoulas, and K. Uzunoglu, "An accurate and efficient entire-domain basis Galerkin's method for integral equation analysis of integrated rectangular dielectric waveguides," IEEE Transaction on Microwave Theory and Techniques, vol. 43, pp. 2794-2804, 1995.
- [23] D. Lioubtchenko, S. Tretyakov, and S. Dudorov, "Millimeter wave waveguide," Kluwer Academic publishers, 2003.
- [24] D. Dabas, J. Sharma and N. S. Raghava, and A. De, "Square wave analysis of dielectric rectangular waveguide," SPIE 8760, International Conference on Communication and Electronics System Design, January, 2013.

Glowworm Swarm Optimization Technique for Optimal Power Flow

Rahul Dogra¹ and Nikita Gupta²

¹Executive Engineer, Siemens Limited India.

*²M.Tech Power Systems, Delhi Technological University, Delhi, India.
E-mail: ¹rahul.robby@gmail.com, ²guptanikita08@gmail.com*

Abstract

This paper presents Glowworm Swarm Optimization (GSO) algorithm to solve the optimal power flow (OPF) problem. The objective is to minimize the fuel cost and keep the power outputs of generators, bus voltages, shunt capacitors/reactors and transformers tap-setting in their secure limits. Glowworm Swarm Optimization algorithm, enables a swarm of agents to split into subgroups, exhibit simultaneous taxis towards each other, and rendezvous at multiple optima (not necessarily equal) of a given multimodal function. In our problem the agents are generation values of the generator. The incorporation of the proposed method using GSO has been examined and tested for standard IEEE 30 bus system in MATLAB and its effectiveness is illustrated.

Keywords: Glowworm Swarm Optimization, optimal power flow, fuel cost.

1. Introduction

The optimal power flow of OPF has had a long history in its development. It was first discussed by Carpentier in 1962 and took a long time to become a successful algorithm that could be applied in everyday use. [1] In an OPF, the values of some or all of the control variables need to be found so as to optimize (minimize or maximize) a predefined objective. Objective function takes various forms such as fuel cost, transmission losses and reactive source allocation. The OPF methods are broadly grouped as Conventional and Intelligent.[2] The conventional methodologies include the well known techniques like Gradient method, Newton method Quadratic Programming method, Linear Programming method and Interior point method. They

have poor convergence, may get stuck at local optimum, they can find only a single optimized solution in a single simulation run and they become too slow if number of variables are large. To overcome the limitations and deficiencies in analytical methods, *intelligent methods* based on *Artificial Intelligence* (AI) techniques have been developed in the recent past. Intelligent methodologies include the recently developed and popular methods like Genetic Algorithm, Particle swarm optimization. The main advantages of Intelligent methods are: Possesses learning ability, fast, appropriate for non-linear modeling, etc [3].

In this paper optimal power flow using one of novel nature inspired technique known as Glowworm Swarm Optimization (GSO) is used. GSO is a popular swarm intelligent optimization technique proposed by K.N.Krishnanad and D.Ghose in 2005, which has received some interest recently, and mimics the behavior of glowworms glow to attract companions that can successfully find the global optimum and searching multiple optimum of multimodal function[4]. Now GSO algorithm is widely used in some spheres. Glowworm Swarm Optimization algorithm, enables a swarm of agents to split into subgroups, exhibit simultaneous taxis towards, and rendezvous at multiple optima (not necessarily equal) of a given multimodal function. This was basically inspired from the modified Ant Colony Optimization (ACO) with some significant differences. OPF using GSO helps us to find out the optimal value of generation of generators which will help us to minimize the cost function which is the objective function in our problem, keeping in view the different constraints that come in OPF [5].

2. Optimal Power Flow Problem Formulation

The standard OPF problem can be written in the following form, Minimize $F(x)$ (the objective function) subject to:

$$\begin{aligned} h_i(x) &= 0, i = 1, 2, \dots, n \text{ (equality constraints)} \\ g_j(x) &= 0, j = 1, 2, \dots, m \text{ (inequality constraints)} \end{aligned} \quad (1)$$

where x is the vector of the control variables, that is those which can be varied by a control center operator (generated active and reactive powers, generation bus voltage magnitudes, transformers taps etc.) [5], [8] & [11]; the essence of the optimal power flow problem resides in reducing the objective function and simultaneously satisfying the load flow equations (equality constraints) without violating the inequality constraints. The most commonly used objective in the OPF problem formulation is the minimization of the total cost of real power generation. The individual costs of each generating unit are assumed to be function, only, of active power generation and are represented by quadratic curves of second order. The objective function for the entire power system can then be written as the sum of the quadratic cost model at each generator [1] [2] & [3] given by eqn(1).

$$F(x) = \sum_{i=1}^{ng} (a_i + b_i P_{gi} + c_i P_{gi}^2) \quad (2)$$

Where ng is the number of generation including the slack bus. P_{gi} is the generated active power at bus i . a_i , b_i and c_i are the unit costs curve for i th generator. While minimizing the cost function, it's necessary to make sure that the generation still

supplies the load demands plus losses in transmission lines. Usually the power flow equations are used as equality constraints, active and reactive power injection at bus i are defined in the following equation:

$$\begin{aligned} P_i(V, \theta) &= \sum_{j=1}^{nbus} V_i V_j (g_{ij} \cos \theta_{ij} + b_{ij} \sin \theta_{ij}) ; i = 2, nbus \\ Q_i(V, \theta) &= \sum_{j=1}^{nbus} V_i V_j (g_{ij} \sin \theta_{ij} + b_{ij} \cos \theta_{ij}) ; i = npv + 1, nbu \end{aligned} \quad (3)$$

The inequality constraints of the OPF reflect the limits on physical devices in the power system as well as the limits created to ensure system security. The most usual types of inequality constraints are upper bus voltage limits at generations and load buses, lower bus voltage limits at load buses, var. limits at generation buses, maximum active power limits corresponding to lower limits at some generators, maximum line loading limits and limits on tap setting of TCULs and phase shifter. Upper and lower bounds on the active generations at generator buses can be given by eqn (3)

$$P_{gi} \min \leq P_{gi} \leq P_{gi} \max, i=1, ng. \quad (4)$$

Applications of a conventional optimization technique such as the gradient-based algorithms to a large power distribution system with a very non-linear objective functions and great number of constraints are not good enough to solve this problem.[6] Because it depend on the existence of the first and the second derivatives of the objective function and on the well computing of these derivative in large search space[12].

3. Glowworm Swarm Optimization

In the glowworm swarm optimization algorithm, glowworms are randomly placed in the objective function space, which contain a luminescent quantity called luciferin. The intensity of luciferin is associated with the objective function of glowworm's location, and a greater luciferin mean better location and objective function value of glowworms[4]. Each glowworm has a local-decision domain that is bound by a radial sensor range. In the local decision domain, each glowworm finds neighbor and is attracted by the brighter glow of other glowworms in the neighborhood set, and the neighbor has the greater luciferin. The glowworm moves toward the brighter glowworm using a probabilistic mechanism. Also, local-decision domain size is variable that is affected by the number of neighbors. When the neighbor has the lower density, the local-decision domain will enlarge in favor of finding more neighbors; when the neighbor density is higher, the local-decision domain will reduce. Finally, the movement of glowworms will lead to majority gathering to multiple optima[5]&[6].

Entire process of GSO algorithm includes four steps: deployment of glowworms phase, luciferin-update phase, movement phase and local-decision domain update phase. Deployment of glowworms phase: in the phase, the purpose is to enable the glowworms to be dispersed in the entire objective space. Each glowworm contains equal quantity of luciferin and sensor range. Luciferin-update phase: during the luciferin update phase, each glowworm changes luciferin value according to the objective function value of their current location. The luciferin update rule is given by eqn(4):

$$l_i(t+1) = (1 - \rho)l_i(t) + \gamma J_i(t+1) \quad (5)$$

Where ρ ($0 < \rho < 1$) is the luciferin decay constant, $l_i(t)$ is the luciferin enhancement constant and $J_i(t)$ indicates the objective function value at glowworm i's location at time t . Movement phase: during the movement phase, each glowworm selects a neighbor that has higher luciferin value and moves toward it using a probabilistic mechanism. The probability of glowworms i moving towards a neighbor j is based on the Eq. (2) at iteration t given by eqn(5):

$$\rho_j(t) = \frac{(l_j(t) - l_i(t))}{\sum_{k \in N_j(t)} (l_k(t) - l_i(t))} \quad (6)$$

Where $l_i(t)$ is the luciferin value of glowworm i , $d(i, j)$ is the Euclidian distance between glowworms i and j . The movement of glowworms i is as follows in eqn(6):

$$x_i(t+1) = x_i(t) + s \frac{x_j(t) - x_i(t)}{\|x_j(t) - x_i(t)\|} \quad (7)$$

Where s is the step-size. Local-decision domain update phase: when the number of neighbor changes, local-decision domain needs update at each of iteration, local-decision domain update rule can be presented by the following equation (7)

$$r_d^i(t+1) = \min \{r_s, \max \{0, r_d^i(t) + \beta(n_t - (N_i(t)))\}\} \quad (8)$$

Where $r_d^i(t+1)$ is the local-decision domain of glowworm i at the $t+1$ iteration, β is a constant parameter that affects the rate of change of the neighbor domain, n_t is threshold that is used to control the number of neighbors [5].

4. GSO Applied to Optimal Power Flow

The GSO-based approach for solving the OPF problem to minimize the cost takes the following steps: First we fix the minimum and maximum value of each generator using the IEEE-30 bus system data that is we fix our workspace. Then we deploy the agents randomly in the workspace (here in our problem the agents are generation values of the generator). Then we give the parameters of GSO in our program for OPF using GSO, which are always fixed for every experiment. Then we formulate the objective function of the six generators (here in our problem formulation the objective function has been taken as cost function). Then we apply the stage of GSO named Luciferin Update phase using its standard formula. This step helps in updating the generation values of the entire individual generator. Then we calculate the probability of movement of agents towards each other. Then accordingly we give the movement step to the agents in the movement phase of OPF using GSO. Then we set the constraints required for the OPF, using the IEEE-30 bus data. Then we give the last phase of our algorithm i.e. the local decision domain range update rule, which helps in effective movement of agents so that they can capture the optimal value effectively. Then we simulate our program in MATLAB and get the final results.

5. Result of OPF Using GSO

The proposed GSO algorithm is tested on standard IEEE 30 bus system. The test system consists of 6 thermal units. The program was written and executed on Intel Core 2 Duo having 2.4 GHZ 3GB RAM. The optimal setting of the GSO control parameters are: $\rho = 0.4$, $\gamma = 0.6$, $\beta = 0.08$ and sensor range is 200.

Table 1: Values of parameters achieved using Glowworm optimization technique.

Parameters	Values
Initial Cost of Generation	742.30 \$/hr
Final Cost of Generation	425.90 \$/hr
P1	61.37 MW
P2	23.23 MW
P3	33.37 MW
P4	29.47 MW
P5	28.68 MW
P6	15.63 MW
Time Taken	45.06 seconds

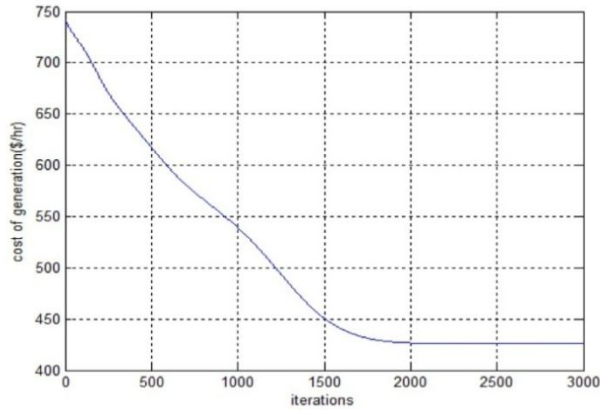


Fig. 1: Fuel cost variation.

6. Conclusion

In this paper for the sake of solving optimal power flow (OPF) problems one of novel nature inspired technique known as Glowworm Swarm Optimization (GSO) has been used for solution of optimal power flow problem of large distribution systems via a simple genetic algorithm. The objective was to minimize the fuel cost and keep the power outputs of generators, bus voltages, shunt capacitors/reactors and transformers tap-setting in their secure limits. GSO has been examined and tested for standard IEEE 30 bus system in MATLAB. We saw that our objective function i.e. cost function was minimized under the constraints and also we got the values of generation of different generator which would give optimum generation under different constraints.

References

- [1] J.A. Momoh, R. J. Koessler, M. S. Bond, B. Stott, D. Sun, A. Papalexopoulos, and P. Ristanovic, "Challenges to optimal power flow," *IEEE Trans. Power Syst.*, vol. 12, pp. 444–455, Feb. 1997.
- [2] M.A.Abido, "Optimal Power flow using particle swarm optimization", Electrical power and energy systems, 2002.
- [3] H.W. Dommel and W. F. Tinney, "Optimal power flow solutions," *IEEE Trans. Power Appar. Syst.*, vol. PAS-87, pp. 1866–1876, Oct. 1968.
- [4] K.N. Krishnanand, D. Ghose, Glowworm swarm optimization For simultaneous capture of multiple local optima of multimodal functions, *Technical Report GCDSL 2006/04, Department of Aerospace Engineering, Indian Institute of Science, July 2006.*
- [5] K.N. Krishnanand, D. Ghose, Detection of multiple source locations using a glowworm metaphor with applications to collective robotics, in: *Proceedings of IEEE Swarm Intelligence Symposium*, Pasadena, CA, June 2005, pp. 84–91.
- [6] K.N. Krishnanand, D. Ghose, Glowworm swarm based optimization algorithm for multimodal functions with collective robotics applications, in: *Recent Progress in Distributed Intelligence, Multiagent and Grid Systems 2 (3)* 209–222 (special issue).
- [7] M. H. Bottero, F. D. Galiana, and A. R. Fahmideh-Vojdani, "Economic dispatch using the reduced Hessian," *IEEE Trans. Power Appar. Syst.*, vol. PAS-101, pp. 3679–3688, Oct. 1982.
- [8] J. A. Momoh, "A generalized quadratic-based model for optimal power flow," *IEEE Trans. Syst., Man, Cybern.*, vol. SMC-16, 1986.
- [9] G. F. Reid and L. Hasdorf, "Economic dispatch using quadratic programming," *IEEE Trans. Power Appar. Syst.*, vol. PAS-92, pp. 2015–2023, 1973.
- [10] Poli, R., Kennedy, J., & Blackwell, T. (2007). Particle swarm optimization: an overview. *Swarm Intelligence*, 1(1), 33–57.
- [11] Jason Yuryewich, Kit Po Wong, "Evolutionary programming based optimal power flow algorithm", *IEEE Transactions on Power Systems*, Vol. 14, No. 4, November 1999.
- [12] Singh, G., & Deb, K. (2006). Comparison of multi-modal optimization algorithms based on evolutionary algorithms. In *Proceedings of the genetic and evolutionary computation conference* (pp. 1305–1312). New York ACM Press.

Kinetics Studies on the Catalytic Thermal Degradation of High Density Polyethylene

Vandana^{1*}, Pratibha Chaudhary², Ramesh Chander Sharma³

¹Research Scholar, ²Professor, Department of Chemistry, Deenbandhu Chhotu Ram University of Science and Technology, Murthal, Haryana, India

³Professor, Department of Applied Chemistry and Polymer Technology, Delhi Technological University, Delhi, India

*Corresponding author email id: vandana1582@gmail.com

ABSTRACT

Thermogravimetric analysis of high density polyethylene and Co^{3+} catalyst mixtures was studied under non-isothermal conditions. The mixtures used in this study consist of blends of HDPE: Co^{3+} in 3:1 and 5:1 ratios. The pyrolysis was carried out over a temperature range of 30 to 800 °C in an inert atmosphere of nitrogen, with a heating rate of 10°C/min. The kinetic parameters were evaluated using the Coats and Redfern method. The activation energy of raw HDPE was decreased by Co^{3+} catalyst by nearly 80% within the given temperature ranges. A reduction in the activation energy of the blended mixture was observed, which clearly indicates the synergism in the co-cracking/co-processing reactions. The reaction is defined as zero order reaction. The catalyst chosen for pyrolysis shows effective aspects on HDPE degradation.

Keywords: Degradation, Catalyst, HDPE, Kinetics, Non-isothermal

1. INTRODUCTION

The global production of plastics in 2010 was 265MMT and in 2011, it was 280 MMT. Europe produced 21.5% and China 23.5% of the global production. India's share is just 4.25%. An exponential increase in production and consumption of plastics has put lot of pressure on recycling and management. Though recycled plastics have found applications in protecting lands and fields, construction of buildings and many more, the emphasis has been on the sustainable energy recovery[1]. More emphasis has been laid on making plastics a high-quality secondary raw material for diversified applications.

The thermal treatment of plastics wastes by pyrolysis or incineration has received considerable attention. A proper thermal treatment system not only resolves the disposal problems, but also recovers energy as well as several organic compounds which may find applications as raw materials. High-temperature pyrolysis processes have been developed in the past[2,3]. However, absence of reliable data on hydrodynamics, heat transfer and kinetics required to develop high temperature pyrolysis reactors hampered their optimal design and operation. Therefore, the kinetics of thermal degradation of such solid plastics wastes must be studied to provide a more detailed thermal and flow analysis[4].

Dynamic thermogravimetric analysis (TGA) has been frequently used to study the kinetics and mechanism of thermal degradation of polymers, as it provides reliable information on the frequency factor, the activation energy, and the reaction order[5-10]. Ahmaruzzaman and Sharma[11-17] have described the advantages of studying non-isothermal kinetics over the isothermal kinetic studies. In this paper, the kinetics of pyrolysis of high density polyethylene (HDPE) in the presence of cobalt trichloride was studied under non-isothermal heating in nitrogen media using TGA curves. The kinetic parameters of the process were calculated using the method of Coats-Redfern[18] and kinetic equations.

2. MATERIALS AND METHOD

The HDPE (MWZ 4,20,000) were procured from the BIs Ethanol Private Limited, New Delhi, India. The property of raw plastic is given in Table 1. The catalyst cobalt tri-chloride used in the study was of AnalaR grade. TGA

analysis of the samples is done using a STA6000, thermogravimetric analyser under non-isothermal conditions, over a temperature range of 30 °C to 700 °C and at a heating rate of 10 °C/min. About 10 mg of the sample was used for the study, in an inert nitrogen atmosphere having 20 ml/min nitrogen flow. The weight loss data were recorded as a function of time and temperature using special software in computer. Pyrolysis was carried out at non-isothermal conditions[18]. As slow heating rate was used, the heat transfer limitation was ignored.

Table 1: Properties of raw HDPE sample used

Property	HDPE
Manufacturer	Bls Ethanol Private Limited, New Delhi
Form	Pellets
Density, kg/m ³ at 296 K	950–956
Melting point (°C)	399–405
Melt flow rate, g/10 min	0.3–0.5

2.1. Analysis of Weight Loss Data

Assuming first-order decomposition reaction, an integral method was used to evaluate the kinetic parameters. Details of the mathematical procedure used in the analysis of the TGA data can be found elsewhere[17,18]. The extent of conversion, or the fraction of material pyrolysed, x , may be defined using the expression:

$$x = \frac{w_0 - w_t}{w_0 - w_\infty} \quad (1)$$

Where, w_0 is the initial weight (in mg), w_t is the weight after t minutes (in mg) and w_∞ is the weight after pyrolysis (in mg). The rate expression can be written as:

$$\frac{dx}{dt} = k(1 - x) \quad (2)$$

With a linear heating rate of a , (K /min),

$$a = \frac{dT}{dt} \quad (3)$$

The integrated rate expression for $n = 1$ will be,

$$\ln \left[\frac{-\ln(1-x)}{T^2} \right] = \ln \left\{ \left(\frac{AR}{aE} \right) \left(1 - \frac{2RT}{E} \right) \right\} - \frac{E}{RT} \quad [n = 1] \quad (4)$$

and integrated rate expression for $n \neq 1$ will be,

$$\ln \left[\frac{1 - (1-x)^{(1-n)}}{(1-n)T^2} \right] = \ln \left\{ \left(\frac{AR}{aE} \right) \left(1 - \frac{2RT}{E} \right) \right\} - \frac{E}{RT} \quad [n \neq 1] \quad (5)$$

In these expressions, T = temperature, A = frequency factor, R = gas constant, a = heating rate and E = activation energy of the reaction. In the present study, the order of the reaction is assumed between $n = 0$ to $n = 4$. The parameters of the Equations- 5 were calculated for $n=0, 0.5, 1, 1.5, 2, 2.5, 3, 3.5$ and 4.0 . Then, the plots of $\ln[-\ln(1-X)/T^2]$ against $1/T$ for $n=1$ and $\ln [1-(1-X)^{1-n}/(1-n)T^2]$ against $1/T$ for $n \neq 1$ were drawn. Where these plots correspond to each other, the same will be the order of the reaction.

The value of n which gives the value of highest R^2 (regression coefficient) indicates the reaction order. From the

slope ($y = mx + C$) activation energy ($-E/R = m$) of the reaction is calculated. Frequency factor A can be calculated from the intercept. As R , a and E are known, then A can be determined.

$$\ln\left(\frac{AR}{aE}\right) = \text{INTERCEPT} \quad (6)$$

3. RESULTS AND DISCUSSION

The TGA of HDPE, HDPE- cobalt trichloride (3:1) and HDPE- cobalt trichloride (5:1) are carried out under non-isothermal conditions- [18-21] in nitrogen medium over a temperature range of 30-700 °C and at a heating rate of 10 °C/min. About 10 mg of each sample was used for the study. An inert atmosphere was maintained using flowing N_2 at 20 ml/min. The weight loss data were recorded as a function of time and temperature and presented in Figures 1- 3.

All the weight loss curves are smooth, with one inflection point during reaction under nitrogen atmosphere. In all experiments, the final temperature was nearly 500 °C. Although the decomposition curves of HDPE- $CoCl_3$ (3:1) given in Figure 2 shows that HDPE degrades nearly 100% at 460 °C the decomposition curves of HDPE: $CoCl_3$ (5:1) given in Figure 3 shows that HDPE degrades nearly 70% at 515°C and the decomposition of raw HDPE occurs at 490 °C. The pyrolysis study reveals that 3:1 ratio of catalyst is more favourable for the decomposition of HDPE.

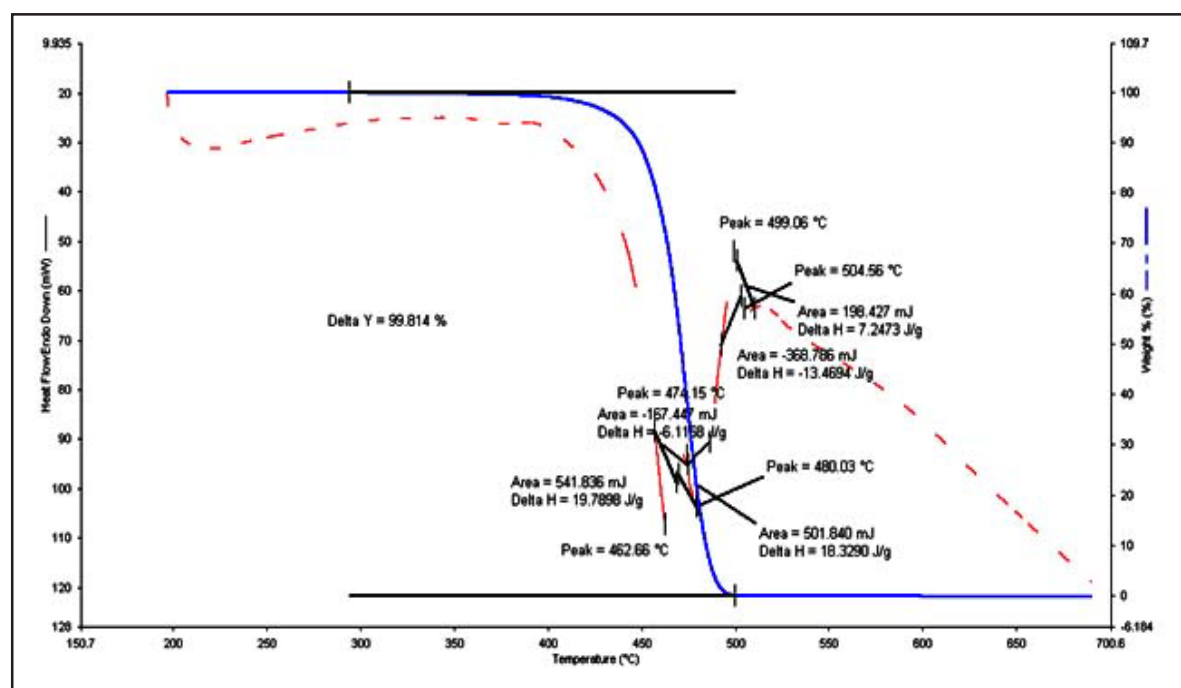
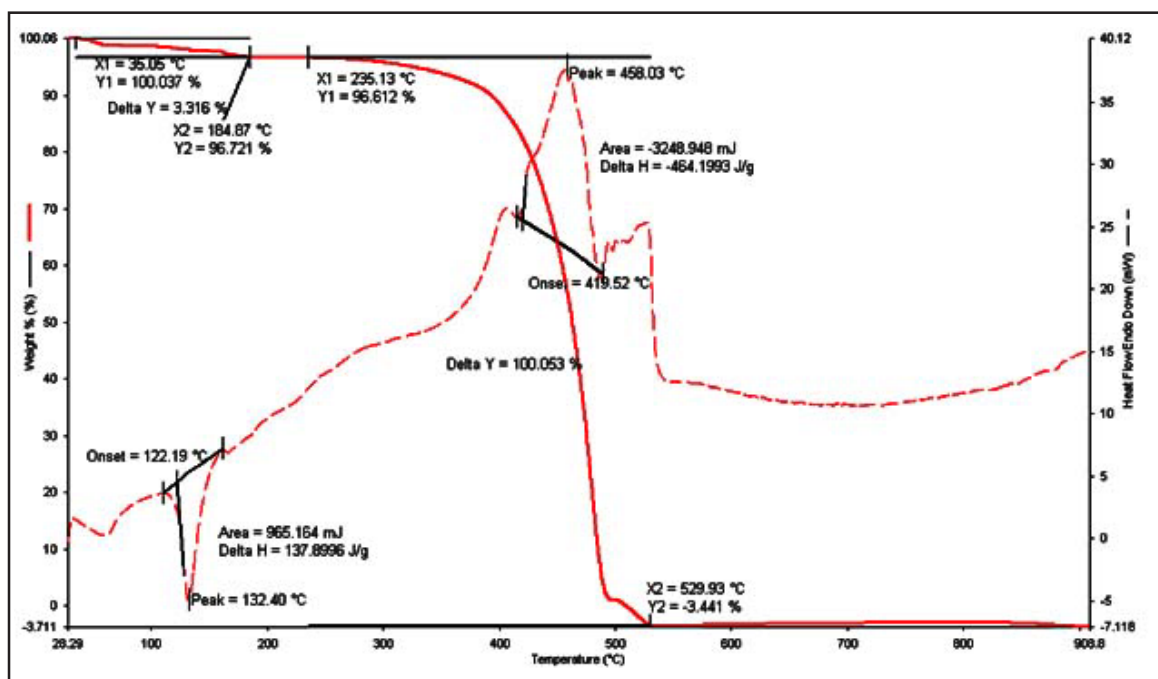
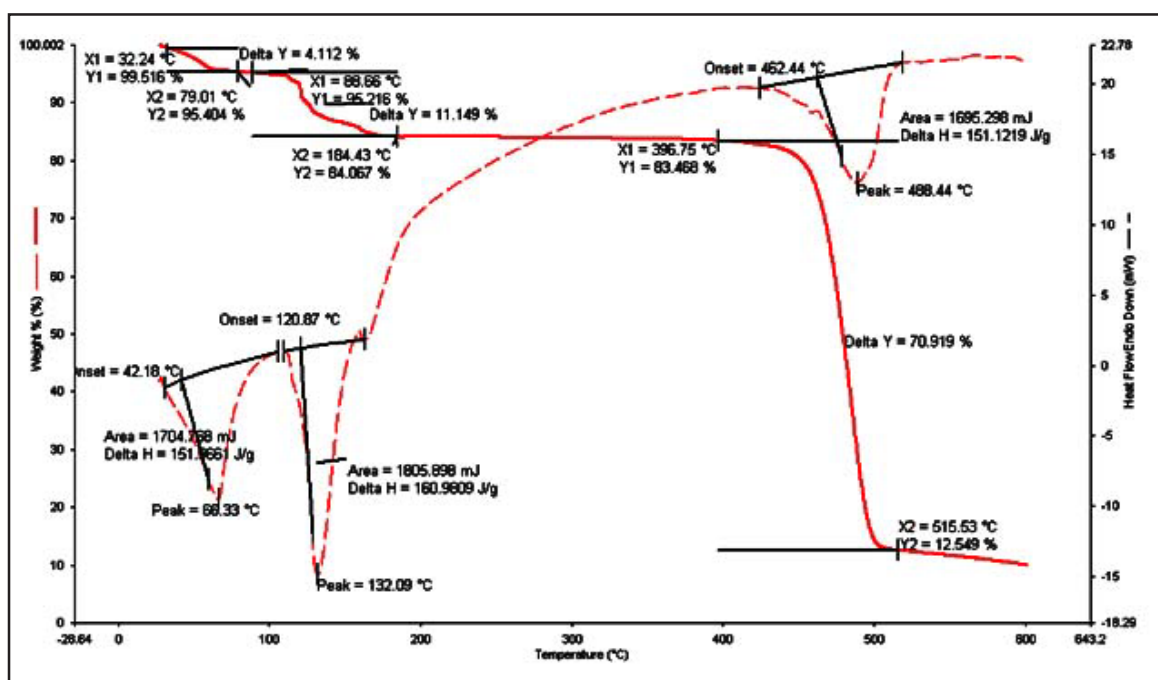


Figure 1: Thermogram of HDPE

Upon analysing the TGA data, it was revealed that a linear curve of Equation- 5 for $n = 0$ is the most appropriate as the regression coefficient is highest for $n=0$; the curves of Equation- 5 for raw HDPE, HDPE- $CoCl_3$ (3:1) and HDPE- $CoCl_3$ (5:1) under non-isothermal conditions are presented in Figures 4-6. In these figures, the entire range of the plots of $\ln[-\ln(1-X)/T^2]$ against $1/T$ for $n=1$ and of $\ln[1-(1-X)^{1-n}/(1-n)T^2]$ against $1/T$ for $n \neq 1$ correspond to a linear graph. The value of n which gives the value of highest R^2 (regression coefficient), indicates that reaction is of zero order for all the three samples at a heating rate of 10 °C/min.

Reasonable fits of data to straight lines in these figures indicate that the assumption of first order kinetics for thermal decomposition of HDPE, as proposed by the Coats and Redfern[18] in presence of cobalt tri-chloride is

Figure 2: Thermogram of HDPE-CoCl₃(3:1)Figure 3: Thermogram of HDPE-CoCl₃(5:1)

not acceptable. The analysis of TGA data presented reveals that the thermal decomposition of HDPE and its blend can be described by a zero-order reaction. The apparent kinetic parameters are shown in Table 2. The activation energy values found in this study are not in agreement with earlier studies wherein it ranged from 28 to 350 kJ/mol for different forms of Polyethylene[21], which appears to be reasonable due to difference in molecular weight of the HDPE. The calculated activation energy value is minimum for HDPE-CoCl₃(3:1), which indicates that this blend is most favourable for thermal degradation of HDPE.

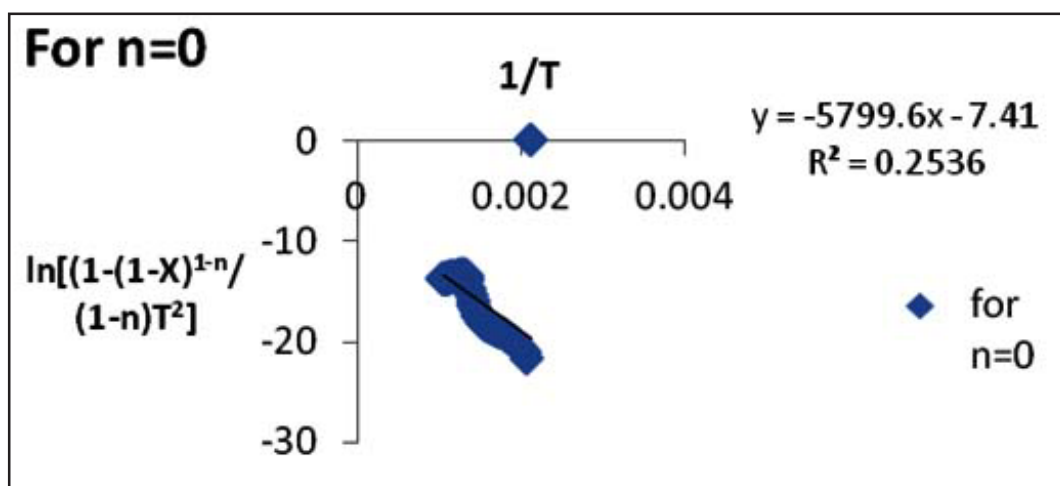


Figure 4: Curve based on the integrated rate expression (Equation 5) for $n = 0$ for Raw HDPE

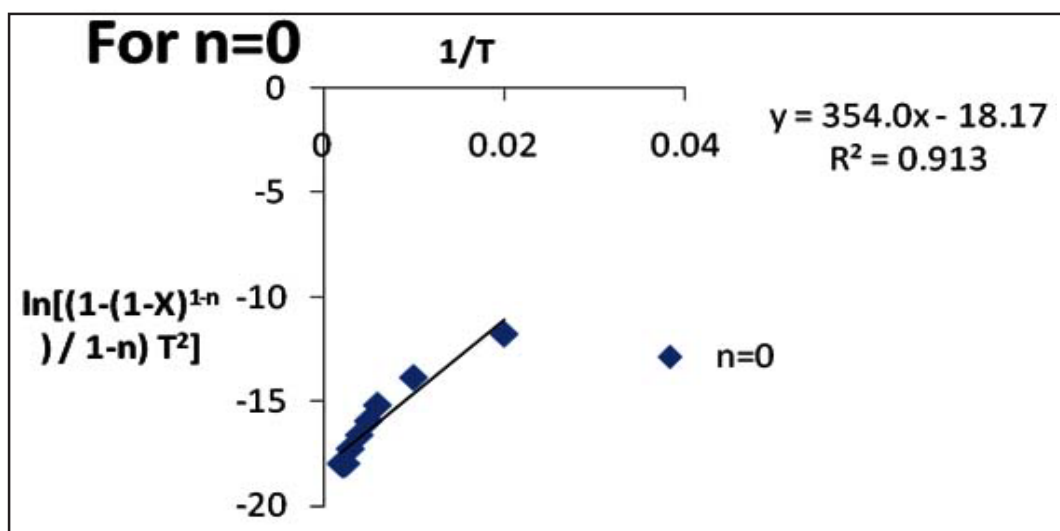


Figure 5: Curve based on the integrated rate expression (Equation 5) for $n = 0$ for HDPE- CoCl_3 (3:1)

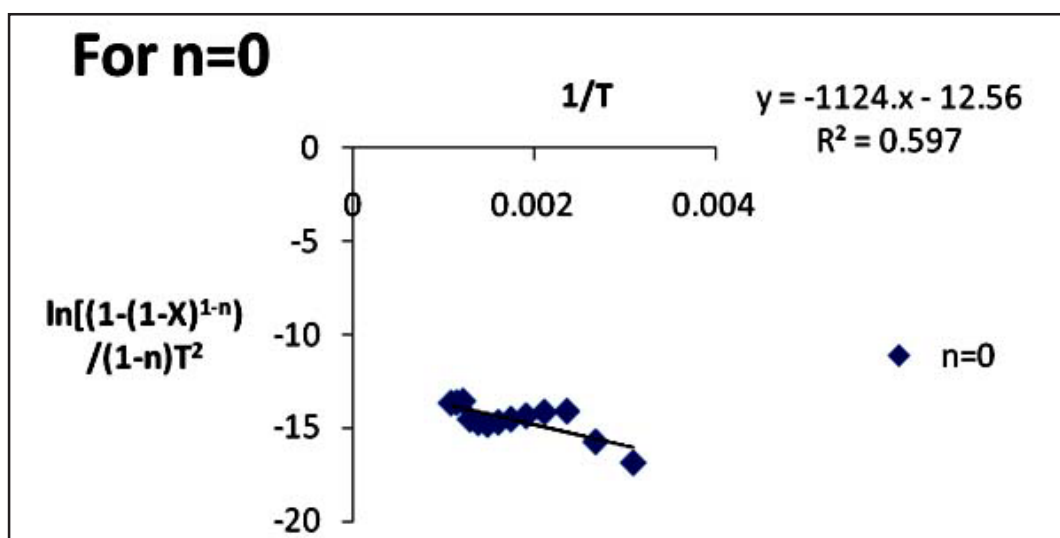


Figure 6: Curve based on the integrated rate expression (Equation 5) for $n = 0$ for HDPE- CoCl_3 (5:1)

Table 2: Apparent kinetic parameters determined by the Coats and Redfern method under non- isothermal conditions for raw HDPE, HDPE-CoCl₃(3:1) and HDPE- CoCl₃(5:1)

Material	Order of reaction(<i>n</i>)	Activation Energy (<i>E_a</i>) (kJ/mol)	Frequency factor (<i>A</i>)
HDPE	0	41.21	0.00732
HDPE-CoCl ₃ (3:1)	0	7.11	0.32222
HDPE-CoCl ₃ (5:1)	0	9.34	0.03944

4. CONCLUSION

From the study, the following points can be concluded-

- Kinetics studies under non-isothermal conditions confirmed that Co³⁺ is a good catalyst for thermal decomposition of HDPE.
- The activation energy data from the TGA study revealed that the HDPE-CoCl₃ (3:1) blend has the lowest activation energy and so this ratio is favourable.
- The kinetics of thermal degradation of HDPE in the presence of cobalt tri-chloride under non-isothermal conditions is of zero order.

ACKNOWLEDGEMENT

The author would like to thank USIC, Delhi University, Delhi for their technical support to carry out this research work.

REFERENCES

1. Association of Plastics Manufacturers in Europe (APME), Summary Report, APME, Brussels; **2003**.
2. Cooney, J.D., Day, M. and Wiles, D.M. Thermal degradation of poly (ethylene terephthalate): A kinetic analysis of thermogravimetric data. *Journal of Applied Polymer Science*. **1983**; 28: 2887.
3. Ebbinghaus, B.B. Thermodynamics of gas phase chromium species: The chromium chlorides, oxychlorides, fluorides, oxyfluorides, hydroxides, oxyhydroxides, mixed oxyfluorochlorohydroxides and volatility calculations in waste incineration processes. *Combustion and Flame*. **1995**; 101: 311.
4. Arisawas, H. and Brill, T.B. Kinetics and mechanisms of flash pyrolysis of poly(methyl methacrylate) (PMMA). *Combustion and Flame*. **1997**; 109: 415.
5. Park, S.W., Lee, J.L. and Seul, S.D. Thermal Degradation of Polymer Material by Thermogravimetry-A Kinetic Data Analysis of Poly(methyl methacrylate). *Hwahak Konghak*. **1985**; 23: 125.
6. Petrovic, Z.S. and Zavargo, Z.Z. Reliability of methods for determination of kinetic parameters from TGA and DSC. *Journal of Applied Polymer Science*. **1986**; 32: 4353.
7. Nam, J.D. and Seferis, J.C. A Composite Methodology for Multi-Stage Degradation of Polymers, *Journal of Polymer Science Part B: Polymer Physics*. **1991**; 29: 601.
8. Nam, J.D. and Seferis, J.C. Generalised composite degradation kinetics for polymeric systems under isothermal and non-isothermal conditions. *Journal of Polymer Science Part B: Polymer Physics*. **1992**; 30: 455.
9. Jimenez, A., Berenguer, V., Lopez, J. and Sanchez, A. Thermal degradation study of poly(vinyl chloride): Kinetic analysis of thermogravimetric data. *Journal of Applied Polymer Science*. **1993**; 50: 1565.

10. Salin, J.M. and Seferis, J.C. Kinetic analysis of high-resolution TGA variable: Heating rate data. *Journal of Applied Polymer Science*. **1993**; 47: 847.
11. Ahmaruzzaman, M. and Sharma, D.K. Non-isothermal kinetic studies on co-processing of vacuum residue, plastics, coal and petrocrop. *Journal of Analytical and Applied Pyrolysis*. **2005**; 73: 263.
12. Ahmaruzzaman, M. and Sharma, D.K. Characterization of liquid products obtained from co-cracking of petroleum vacuum residue with plastics. *Energy Fuels*. **2006**; 21: 2498.
13. Ahmaruzzaman, M. and Sharma, D.K. Kinetic studies on cocracking of petroleum vacuum residue with thermoplastics and biomass (Petrocrop). *Petroleum Science Technology*. **2007**; 25: 925.
14. Ahmaruzzaman, M. and Sharma, D.K. chemical reaction engineering studies on cocracking of petroleum vacuum residue with coal, plastics, and biomass (Bagasse and Petrocrop). *Petroleum Science Technology*, **2007**; 25: 937.
15. Ahmaruzzaman, M. and Sharma, D.K. Co-processing of petroleum vacuum residue with coal, plastics and biomass and its synergistic effects. *Energy Fuels*. **2007**; 21: 891.
16. Ahmaruzzaman, M. and Sharma, D.K. Characterization of liquid products from the co-cracking of ternary and quaternary mixture of petroleum vacuum residue, polypropylene, Samla coal and Calotropis procera. *Fuel*. **2008**; 87: 1967.
17. Ahmaruzzaman, M. and Sharma, D.K. Characterization of liquid products obtained from co-cracking of petroleum vacuum residue with coal and biomass. *Journal of Analytical and Applied Pyrolysis*. **2008**; 81: 37.
18. Coats, A.D. and Redfern, J.P. Kinetic parameters from thermogravimetric data. *Nature*. **1964**; 201: 68.
19. Gersten, J., Fainberg, V., Hetsroni, G. and Shindler, Y. Kinetic study of the thermal decomposition of polypropylene, oilshale and their mixture. *Fuel*. **2000**; 79: 1679.
20. Doğan, Ö.M. and Uysal, B.Z. Non-isothermal pyrolysis kinetics of three Turkish oil shales. *Fuel*, **1996**; 75: 1424.
21. Bockhorn, H., Hornung, A., Hornung, U. and Schawaller, D. Study on the thermal degradation of polypropylene and polyethylene. *Journal of Analytical and Applied Pyrolysis*, **1999**; 48: 93.



Abhimanu Singh, Datta, C. K.

LOSS MINIMIZATION POLICY FOR A PRODUCTION LINE WITH IMMEDIATE FEEDBACK AND MULTI SERVER FACILITY AT ALL PROCESSING UNITS

Received: 7 April 2013 / Accepted: 09 May 2013

Abstract: In this paper, we have derived mathematical expressions for the loss caused by ill processing of items or jobs at various processing units in a production line. On the basis of the expressions, we concluded a policy for minimization of the loss caused by ill processing of jobs or items at various processing units. In the production line, each of the processing units has multi-server facility. Arrivals to the first processing unit are according to Poisson distribution. Service times at each of the processing units are exponentially distributed. At each of the processing units, we have taken into account immediate feedback and the rejection possibility. Considering the processing cost at each of the processing units, the average loss to the system due to rejection, caused by ill processing at various processing units, is obtained.

Keywords: Queuing Network, Processing Units, Production Line, multi-server, Immediate Feedback

Politika minimizacije gubitka za proizvodnu liniju sa trenutnom povratnom vezom u multi serverskom okruženju za sve proizvodne jedinice. U ovom radu je izveden matematički izraz za gubitak usled neadekvatne obrade delova ili radnih pozicija na različitim proizvodnim jedinicama na proizvodnoj liniji. Na početku eksperimenta je usvojena politika minimizacije gubitka usled neadekvatne obrade delova ili radnih pozicija na različitim proizvodnim mestima. Na proizvodnoj liniji svaka proizvodna jedinica ima multi serversko postrojenje. Dolazak do prvih proizvodnih jedinica se odvija shodno Poasonovoj raspodeli. Servisna vremena na svakoj proizvodnoj jedinici su eksponencionalno raspoređena. Na svakoj proizvodnoj jedinici je uzeta u obzir trenutna povratna sprega i moguće odbacivanje. Uzimajući u obzir troškove obrade na svakoj proizvodnoj jedinici, prosečan gubitak sistema usled odbacivanja, usled neadekvatne obrade na različitim proizvodnim jedinicama, je održan.

Ključne reči: čekajuća mreža, proizvodne jedinice, proizvodna linija, multi server, trenutna povratna sprega

1. INTRODUCTION

A production line as shown in fig.1 is a sequence of a finite number of processing units arranged in a specific order. At each of the processing units, service may be provided by one person or one machine that is called single- server facility, or it can be provided by more than one persons or more than one machines that is called multi-server facility at the respective processing units. In this paper we have considered multi-server facility at each of the processing units. At each of the processing units, a specific type of processing is performed i.e. at different processing units material is processed differently. At a processing unit, the processing times of different jobs or items are independent and are distributed exponentially around a certain value, called mean processing time.

In a production line the processing of raw material or a job starts at the first processing unit. It is processed for a certain time interval at the first processing unit and then it is transferred to the second processing unit for other type of processing, if its processing is done correctly at the first processing unit. This sequence is followed until the processing at the last processing unit is over. In a production line raw material is processed at a series of processing units one after the other and finally it is transformed into finished goods ready for use.

End of processing at each of the processing units give rise to the following three possibilities:

- (a) Processing at a unit is done correctly and the job or material is transferred to the next processing unit for other type of processing.
- (b) Processing at a unit is not done correctly but can be reprocessed once more at the same processing unit.
- (c) Processing at a unit is neither done correctly nor it can be reprocessed at the same processing unit i.e. this job or material is lost, in this situation the job or material is rejected and put into the scrap.

We are applying Queuing Theoretical approach to study the production line and hence to derive the policy for minimization of the said loss. Several researches have studied the queues in series having infinite queuing space before each servicing unit. Specifically, J. R. Jackson [1] had studied network of waiting lines, R.R. P. Jackson [2] studied finite and infinite queuing space with phase type service taking two queues in series. In, K.L. Arya [3] has found that the steady state distribution of queue length taking two queues in the system, where each of the two non- serial servers is separately in service. O.P. Sharma [4] studied the stationary behavior of a finite space queuing model consisting of queues in series with multi-server service facility at each node.

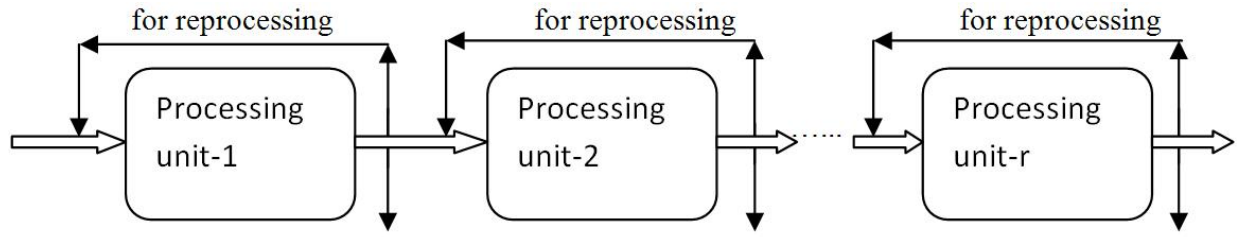


Fig. 1. A production line

2. MODELING

We consider a production line as shown in fig.2 consisting of an arbitrary number(r) of processing units arranged in a series in a specific order. Each of the processing units has multi- server facility and immediate feedback.

Let

λ = Mean arrival rate to the first processing unit from an infinite source, following Poisson's rule.

μ_i = Mean service rate of an individual server at the i^{th} processing unit having exponentially distributed service times.

S_i = Number of servers at the i^{th} processing unit.

n_i = Number of unprocessed jobs before the i^{th} processing unit waiting for service, including one in service, if any, at any time t .

$p_{i,i+1}$ = Probability that the processing of a job or material at the i^{th} processing unit is done correctly and it is transferred to the $(i+1)^{st}$ processing unit.

$p_{i,i}$ = Probability that the processing of a job or material at the i^{th} processing unit is not done correctly but it can be reprocessed once more, so, it is transferred to the same processing unit for processing once more.

$p_{i,o}$ = Probability that the processing of a job or material at the i^{th} processing unit is neither done correctly nor it remains suitable for reprocessing.

C_i = Processing cost per unit at the i^{th} processing unit.

L = Average loss per unit time, to the system due to rejection of items at various processing units due to ill-processing.

$P(n_1, n_2, \dots, n_r, t)$ = Probability that there are n_1 jobs waiting for processing before the first processing unit including one in service, if any, n_2 jobs before the second processing unit waiting for service including one in service, if any, and so on, n_r jobs before the r^{th} processing unit waiting for service including one in service, if any at time t , with $n_i \geq 0 (1 \leq i \leq r)$, and $P(n_1, n_2, \dots, n_r, t) = 0$, if some $n_i < 0$ (because number of jobs cannot be negative).

The above production line can be represented by a serial network of queues in which each processing unit is equivalent to a queue with the same number of similar servers and the same numbers of jobs waiting for service.

In the above serial network of queues, each queue has immediate feedback. To analyze this serial network of queues firstly we remove the immediate feedback.

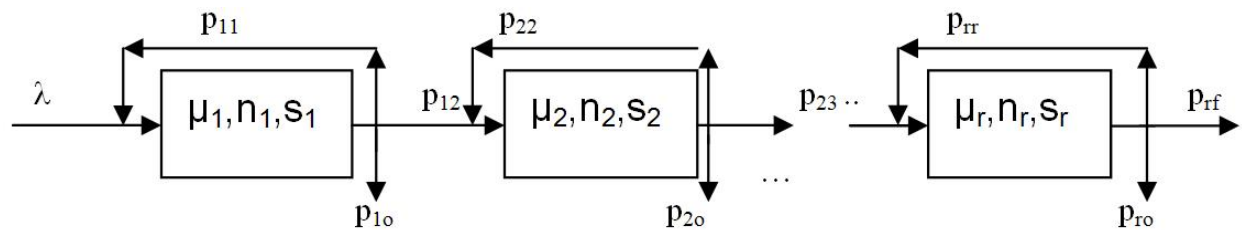


Fig. 2. Proposed production line

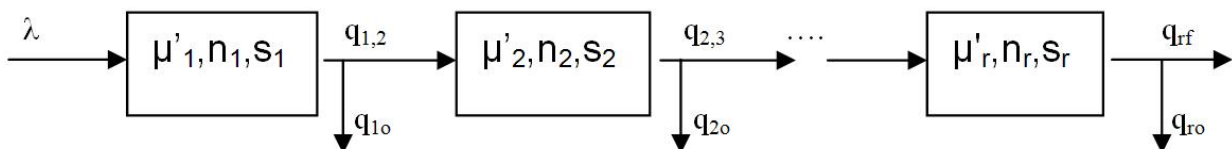


Fig.3. Equivalent serial network of queues

After the removal of immediate feedback the above serial network of queues is replaced by one, as shown in Fig. 3.

Here $\mu'_i = \mu_i(1 - p_{i,i})$, where μ'_i is the effective service at the i^{th} processing unit after the removal of the immediate feedback [5].

And the respective probabilities become as follows

$$q_{io} = \frac{p_{io}}{(1 - p_{ii})}, q_{ii+1} = \frac{p_{ii+1}}{(1 - p_{ii})} \quad (1)$$

3. EQUATIONS GOVERNING THE QUEUING SYSTEM

Under the steady state conditions, we have [6, 7, 8] :

$$[\lambda + s_1\mu'_1 + s_2\mu'_2 + \dots + s_r\mu'_r].$$

$$\begin{aligned} P(n_1, n_2, \dots, n_r) &= \lambda P(n_1 - 1, n_2, \dots, n_r) + \\ &\sum_{i=1}^r s_i \mu'_i q_{i,i+1} P(n_1, n_2, \dots, n_i + 1, n_{i+1} - 1, \dots, n_r) + \\ &\sum_{i=1}^r s_i \mu'_i q_{i,o} P(n_1, n_2, \dots, n_i + 1, n_{i+1}, \dots, n_r) \end{aligned} \quad (2)$$

4. SOLUTION FOR INFINITE QUEUING SYSTEM

Under the steady state conditions all the queues behave independently and thus the solution of steady state equation in product form is given by [9,10]

$$\begin{aligned} P(n_1, n_2, \dots, n_r) &= \prod_{i=1}^r (1 - \rho_i) \rho_i^{n_i}, \quad \text{where} \\ n_i &\geq 0 (1 \leq i \leq r) \text{ and } \rho_i < 1 (1 \leq i \leq r) \end{aligned} \quad (3)$$

If any $\rho_i (1 \leq i \leq r) > 1$ then the stability is disturbed and the behavior of the system will not remain stationary consequently solution will not be given by Eq. (3).

Here, we have

$$\rho_i = \frac{\lambda_i}{s_i \mu'_i},$$

$$\text{Where } \lambda_i = \lambda \prod_{k=1}^i \frac{p_{k-1,k}}{(1 - p_{k-1,k-1})}, p_{0,0} = 0$$

Thus

$$\rho_i = \frac{\lambda}{s_i \mu'_i} \prod_{k=1}^i \frac{p_{k-1,k}}{(1 - p_{k,k})} \quad (4)$$

With $p_{0,1} = 1$

It is observed that

$$\sum_{i=1}^r \lambda_i q_{i,o} + \lambda_r q_{r,f} = \lambda \quad (5)$$

5. EVALUATION OF AVERAGE LOSS:

Let c_1 be the processing cost at the first processing unit, c_2 the processing cost at the second processing unit and so on $\dots c_r$, the processing cost at the r^{th} processing unit.

If an item is rejected just after its processing at the first processing unit is over, then it causes a loss c_1 to the system. If an item is rejected just after its processing at the second processing unit is over, then it causes a loss $(c_1 + c_2)$ to the system. Thus, in general if an item is rejected just after its processing at the r^{th} processing unit is over, then it causes a loss $(c_1 + c_2 + c_3 + \dots + c_r)$ to the system.

L, the average loss per unit time to the system due to rejection of items just after the processing at various processing units due to ill-processing (processing of an item is neither done correctly nor it can be reprocessed) is

$$\begin{aligned} L &= c_1 \lambda q_{1,o} + (c_1 + c_2) \lambda q_{1,2} q_{2,o} + \dots \\ &+ (c_1 + c_2 + \dots + c_r) \lambda q_{1,2} q_{2,3} \dots q_{r-1,r} q_{r,o} \\ &= \sum_{i=1}^r (c_1 + c_2 + \dots + c_i) \lambda q_{1,2} q_{2,3} \dots q_{i-1,i} q_{i,o}, \\ &\text{With } q_{0,1} = 1 \\ &= \sum_{i=1}^r (c_1 + c_2 + \dots + c_i) \lambda \frac{p_{1,2}}{1 - p_{1,1}} \frac{p_{2,3}}{1 - p_{2,2}} \dots \\ &\frac{p_{i-1,i}}{1 - p_{i-1,i-1}} \frac{p_{i,o}}{1 - p_{i,i}}, \\ &= \lambda \sum_{i=1}^r (c_1 + c_2 + \dots + c_i) \prod_{k=1}^i \left(\frac{p_{k-1,k}}{1 - p_{k-1,k-1}} \right) \frac{p_{i,o}}{(1 - p_{i,i})} \end{aligned}$$

$$\text{With } p_{0,0} = 0, \text{ and } p_{0,1} = 1 \quad (6)$$

On the basis of the above expressions, it is clear that later the stage of rejection of an item from the assembly line greater the loss to the system.

6. POLICY TO MINIMIZE THE LOSS

There are two types of losses.

1. First Type-

one-when the processing of an item or job is not done correctly and it is reprocessed at the same production line. In this type the time spent by the machine goes waste and creates loss to the system.

2. Second Type-

when the processing of an item or job at a processing unit is not correctly as well as it can not be reprocessed once more, it then is put into the scrap. In this type, the cost of bringing the item or job into the present form goes waste. This loss includes the cost occurred due to processing at the earlier stages and the cost occurred on the material in making it suitable for processing at the first processing unit.

In this study, we are considering the second type loss caused as the cost occurred due to processing at the earlier stages

Average loss i.e. the sum in equation (6), can be minimized by minimizing the individual terms. This we can do in three ways:

- (i) It is obvious from the equation (6) that if an item (or a job) is rejected from the production line at a later stage it causes more and more loss to the system. Thus, emphasis should be given to install comparatively much efficient machines at later stages.
- (ii) The sum in equation (6) can be minimized by minimizing the term P_{i0} . Thus loss can be minimized by installing machines with minimum rejection rate.
- (iii) The sum in equation (6) can be minimized by maximizing the term $(1-P_{ii})$ i.e. by minimizing P_{ii} . Thus, loss can be minimized by installing machines with minimum reprocessing rate.

7. ACKNOWLEDGEMENT

The corresponding author is thankful to Prof. C.K. Datta, [Formerly Professor at Delhi Technological University], and Prof. B.D. Acharya, [Formerly Sci.'G' & Senior Advisor to Govt. of India, DST, New Delhi], for encouragement. I am thankful to the management of BPIT, Rohini, Delhi, also, for providing creative and learning environment in the institute and my colleagues for cooperation and support they extended all the time

8. REFERENCES

- [1] Jackson, J. R., (1957), "Networks of waiting lines", Oper. Res.,5, pp. 518-521.
<http://or.journal.informs.org/content/5/4/518.full.pdf>
- [2] Jackson, R.R.P.,(1954) "Queueing Systems with Phase Type Service," Operations Research Quarterly, 5(2), pp. 109-120.
- [3] Arya,K. L., (1972), *Study of a Network of Serial and Non-serial Servers with Phase Type Service and Finite Queueing Space*, Journal of Applied Probability [online] 9(1), pp198-201.
<http://www.jstor.org/stable/3212649>
- [4] Sharma, O.P., (1973), *A Model for Queues in Series*. Journal of Applied Probability [Online] 10(3), pp. 691-696.
<http://www.jstor.org/stable/3212791>
- [5] J. Walrand, *An Introduction to Queueing Networks*, Prentice Hall, Englewood Clifs, New Jersey, (1988), ch 4, pp. 160.
- [6] Saaty, T. L., *Elements of Queueing Theory*, McGraw-Hill, New York, 1961, ch. 12, pp. 260.
- [7] Gross ,D. and Harris, C. M., *Fundamentals of Queueing Theory*, John-Wiley New York, 1985, ch. 4, pp. 220-226
- [8] Guy, L., Curry. Richard M. Feldman, *Manufacturing System*, Springer-Verlag, Berlin Heidelberg, 2011, ch. 3, pp. 77-80.
- [9] Bhat, U.N., *An Introduction to Queueing Theory*, Birkhäuser, Boston, 2008, ch. 7, pp 144-147.
- [10] Kishor.S.Trivedi., *Probability & Statistics with Reliability, Queuing and Computer Science Applications*. Wiley India (P.) Ltd., 4435/7, Ansari Road, Daryaganj, New Delhi, (2002), ch. 9, pp. 564

Authors: Mr. Abhimanu Singh, Assistant Professor, Applied Mathematics, BPIT, Sector-17, Rohini, Delhi, India, **Prof., Dr., C. K. Datta**, Deptt. of Mechanical Engineering, PDM College of Engineering, Bahadurgarh, Haryana, India(Formerly Professor in Production Engineering at Delhi Technological University, Delhi, India).

E-Mail: asingh19669@yahoo.co.in

Membrane Technique for Leachate Treatment- A Literature Review

Arpita Anand and Shashank Shekhar Singh

*Department of Environmental Engineering,
Delhi Technological University, Delhi-110042.*

Abstract

Rapid increase in population and industrialization leads to huge generation of solid waste throughout the country with landfilling as the most common practice for management of these solid waste. It is estimated that out of 3267 MLD of sewage is generated in Delhi. Concentrations of COD, BOD₅, heavy metals, NH₄N, low BOD₅/COD ratio and the lack of nutrients in the methanogenic phase have restricted the application of biological treatment processes like aerated lagoons, activated sludge, sequence batch reactors, trickling filter, rotational biological contactors, thereby membrane technology is now days being used. Membrane filtration can be defined as the separation of solid immiscible particles from a liquid or gaseous stream based primarily based on size difference. It includes processes such as reverse osmosis (RO), nanofiltration (NF), ultrafiltration(UF) and microfiltration (MF). MF cannot be use alone in leachate treatment, used as pre-treatment for other membrane processes e.g. UF, NF or RO. MF alone, the COD removal is between 25-35%. Using the UF step alone 50% of organic matter can be separated. Nanofiltration removes up to 60-70% COD as well as about 50% ammonia from leachates while its combination with physicochemical methods further improves leachate treatment bringing the COD removal (refractory COD inclusive) to a range of (70-80%). Reverse Osmosis process has been reported to be a very efficient and promising method for leachate treatment. RO membranes can remove more than 99% organic macromolecules and colloids from feed water and up to 99% of the inorganic ions. Due to high rejection ability, reverse osmosis membranes retain both organic and inorganic dissolved in water with rejection rates of 98 - 99% thus being useful for purifying of liquid

wastes, i.e. leachate. Permeate generated from the reverse osmosis unit is low in inorganic and organic contaminants which meet the discharge standards.

1. Introduction

Due to rapid urbanization and uncontrolled growth rate of population, Solid Waste Management (SWM) has become acute in India. The waste characteristics are expected to change due to urbanization, increased commercialization and standard of living. Waste disposal is one of the major problems being faced by all nations across the world. It is more than a menace in our country. In Indian cities the waste is generally not weighed. It is measured by volume to determine the quantity of waste disposed. Several studies conducted by National Environmental Engineering Research Institute (NEERI) and other consultants have shown that the waste generation rates are low in smaller towns whereas they are high in cities over 20 lac population. The range is between 200 gms / capita / day and 500 gms / capita / day. Leachate is the liquid waste which leaches out from solid waste. It varies widely in composition regarding the age of the landfill and the type of waste that it contains. It can usually contain both dissolved and suspended material. In a landfill that receives a mixture of municipal, commercial, and mixed industrial waste, but excludes significant amounts of concentrated specific chemical waste, landfill leachate may be characterized as a water-based solution of four groups of contaminants dissolved organic matter (alcohols, acids, aldehydes, short chain sugars etc.), inorganic macro components (common cations and anions including sulfate, chloride, Iron, aluminium, zinc and ammonia), heavy metals (Pb, Ni, Cu, Hg etc.), and xenobiotic organic compounds such as halogenated organics. The physical appearance of leachate when it emerges from a typical landfill site is a strongly odoured black, yellow or orange colored cloudy liquid. The smell is acidic and offensive and may be very pervasive because of hydrogen, nitrogen and sulfur rich organic species. Biologically refractory organic constituents, ammonia, and heavy metals in leachate are three principal issues with regard to treatment and disposal. The organic content in leachate is usually described by COD, 5-day BOD, or total organic carbon (TOC). Generally, high COD (3000–60,000), high BOD5/COD ratio (> 0.6), a high fraction of low-molecular organics characterize leachate from young landfills (1–2 years old). In contrast, moderate COD (100–500 mg/L), low BOD5/COD ratio (< 0.3), and a high fraction of high molecular-weight organics characterize mature leachate from old landfills (> 10 years old).

2. Materials and Methods

Microfiltration membrane size ranges between 0.02-10 μm and size range of ultrafiltration between 0.001-0.02 μm . Nanofiltration size range is from 0.0001-0.005 μm and for reverse osmosis it varies from 0.0001-0.003 μm .

3. Result and Discussion

Leachate consists of many different organic and inorganic compounds that are typically either dissolved or suspended in the wastewater. High concentrations of chemical oxygen demand (COD) associated, BOD, nitrogen, phenols, pesticides, solvents and heavy metals are common in these systems. Due to these characteristics leachate treatment technologies fall into these basic types biological and physicochemical and membrane process of treatment.

Biological treatment is firmly established as the standard method of waste treatment for some wastes. Biological purification processes can be aerobic type or anaerobic depending on whether or not the biological processing medium requires O₂ supply. The Moving Bed Biofilm Reactor (MBBR) is a highly effective biological treatment process that was developed on the basis of conventional activated sludge process and bio filter process. The most notable developments in anaerobic treatment process technology was the upflow anaerobic sludge blanket (UASB) reactor in the late 1970s in the Netherlands by Lettinga and his coworkers. Membrane filtration is used to remove particles that are too small for ordinary filters to remove. Most membrane filtration systems use cross flow filtration where the feed waste liquid flows across the membrane rather than through it, as in conventional filtration. The common membrane materials used for this process are Polysulfone (PSUF), Dynel, Cellulose acetate (CA). In nanofiltration process the membrane used also has Asymmetric micro porous structure. The size is in the range of 0.01–5nm. The driving force applied at pressure 5–50atm and sieving mechanism followed. The common membrane material used for this process is Polyvinylidene fluoride (PVDF).

The biological treatment processes including the aerobic and anaerobic treatment provide a good to average treatability for young to not so old leachates but are affected by excess biomass. The physio-chemical treatment processes have an average effect on the treatment of heavy metals and organic waste. The coagulation flocculation treatment process has average removal efficiency of heavy metals for medium to old leachates with high sludge production and consequent disposal. The chemical precipitation gives the same results for medium aged leachate. Adsorption gives a good result in removal of organic wastes from old leachates but with carbon fouling problem and is expensive too. The UASB technology needs constant monitoring when put into use to ensure that the sludge blanket is maintained, and not washed out (thereby losing the effect) UASB reactors, when they are submitted to high volumetric organic loading rate values, have exhibited higher performances compared to other kinds of anaerobic reactors. The membrane filtration processes provides an efficient removal technique for sulphate salts and ions, organic and inorganic compounds, but are costly. The nanofiltration process is effective in removing sulphate salts and ions, while reverse osmosis is good in removing of organic and inorganic compounds but require pretreatment. Activated sludge is not efficient for compounds with MW higher than 5000 and nutrients additions may be required. Trickling filter requires a clarifier for sloughed off solid and oxygen transfer is a limiting factor for BOD > 450 mg/l.

Activated carbon Adsorption necessitate regeneration of carbon or it is wasted with the sludge.

References

- [1] Alexander C. Demetracopoulos, A. M. ASCE and Lily Sehayek (1985)–“Design Considerations for a Novel Landfill Liner”. Journal of Environmental Engineering, Vol. 111, No. 4, August, 1985. ©ASCE, ISSN 0733-9372/85/0004-0528. From ASCE.
- [2] CHEN Shaohua & LIU Junxin (2006)–“Landfill leachate treatment by MBR: Performance and molecular weight distribution of organic contaminant”, Chinese Science Bulletin 2006 Vol. 51 No. 23 2831—2838.
- [3] Despina Fatta, Achilleas Papadopoulos and Maria Loizidou (1999)–“A Study on the Landfill Leachate and Its Impact on the Groundwater Quality of the Greater Area”. Environmental Geochemistry and Health 21: 175–190, 1999. From Springer link.
- [4] Dr. Vinod Tare and Asit Nema (2004)–“UASB Technology–Expectations and Reality”. Dept. of Env. Engg IIT Kanpur, Foundation for Greentech Environmental Systems New Delhi.
- [5] Ferhan Çeçen* & DidemÇakıroğlu (2001)–“Impact of landfill leachate on the co-treatment of domestic wastewater” Biotechnology Letters 23: 821–826, 2001. From Springer link.

PERFORMANCE AND EMISSION CHARACTERISTICS OF CASTOR SEED OIL BIODIESEL ON MEDIUM CAPACITY DIESEL ENGINE

Harveer Singh Pali

Ph. D. Scholar, Department of Mechanical Engineering,
Delhi Technological University
Delhi-110042, India
E- mail id: harvirpali@gmail.com

Naveen Kumar

Professor, Department of Mechanical Engineering,
Delhi Technological University
Delhi-110042, India
E-mail :naveenkumardce@gmail.com

Vipul Vibhanshu

M.Tech. Scholar, Department of
Mechanical Engineering,
Delhi Technological University
Delhi-110042, India
E- mail id: Vipuldonlyi@gmail.com

ABSTRACT

This paper presents the performance and emission characteristics of a medium capacity diesel engine fueled with castor seed oil biodiesel were conducted. The result of the performance studies showed an improved performance of the Brake Thermal Efficiency for B10 was higher than that of B0 while the maximum was obtained as B0 (24.53%) and B10 (25.87%) respectively. The Brake Specific Energy Consumption was also found lowest for B10 blend which was found to be marginally different from the fossil diesel. The emission studies showed that the CO, CO₂, NO_x and Smoke opacity increase with increase in blending ratio. Hence, B20 was the highest for these values. It could be concluded that the castor oil methyl ester blends can be used in CI engines in rural area for meeting energy requirement in various agricultural operations such as irrigation, transportation and so on.

Key Words: Biodiesel, Castor Oil, Emission, Performance, Tran-esterification.

NOMENCLATURE

%	Percentage.
bhp	Brake Horse Power
BMEP	Brake Mean Effective Pressure.
BP	Brake power
BSEC	Brake Specific energy Consumption
BTE	Brake Thermal Efficiency.
CO	Carbon Monoxide
CO ₂	Carbon Dioxide.
cst	Centi Stroke
FFA	Free Fatty Acid.
h	hour
HC	Hydrocarbon
kW	Kilo Watt
kWh	Kilo Watt Hour
L	Liter
B 0	Neat Diesel

B 5	5% COME and 95% Neat Diesel
B 5	10%COME and 90% Neat Diesel
B 5	15% COME and 85% Neat Diesel
B 20	20% COME and 80% Neat Diesel
m _f	mass flow rate
mm	Millimeter
COME	Castor Oil Methyl Ester
NO _x	Nitrogen Oxides.
ppm	Parts Per Million.
PM	Particulate matter
rpm	Revolution Per Minute.
Sec	Second
UHC	Unburned hydrocarbon
V	volt

INTRODUCTION

According to the international energy agency (IEA) report the world will need 50% more energy in 2030 than today, of which 45% will be accounted for by China and India [1]. In the quest for this, the non-oil producing countries like India have initiated efforts to lessen their dependency on fossil fuels by encouraging the development of alternative energy sources such as the production of biodiesel using locally available crops, thereby converting unutilized agricultural land to produce high oil-yield crops that are cheap, abundant and can be grown rapidly [2].

Biodiesel is a renewable clean bio-energy as it can be produced from vegetable oils, animal fats and micro-algae oil thus becoming a promising alternative to diesel fuel with prior advantages such as its biodegradability, non-toxic, and has low emission profile [3]. Biodiesel unlike fossil diesel has no aromatics, and contains about 10-11% oxygen by weight which on combustion on compression engine showed performance and characteristics of biodiesel-fueled engine are something crucial and was found to be responsible for reduced exhaust gas emissions, including Carbon monoxide (CO), Carbon dioxide

(CO₂), unburned hydrocarbon (UHC) and Particulate Matter (PM) on the positive side and reported increase in nitrous oxide (NO_x), low calorific value and high viscosity on the negative side [4-5].

The performance of a diesel engine is directly affected by the presence of metals and metalloids in fuel depending on their concentrations, these species can cause several problems such as corrosion of engine parts and shortening of machinery lifetime [6]. It is therefore imperative to use a vegetable oil of high quality and specific properties that can improve performance of biodiesel on the engine. One of such vegetable oils is castor seed oil which is slight viscosity, odor, Pale-yellow, non-volatile and non-drying with an average oil content of about 46-55% [7].

An intensive review of literature indicated quit reasonable literature exist on the use of castor seed oil in biodiesel production. For examples, *Panwar et al* [8] investigated important properties of methyl ester of castor seed oil are compared with diesel fuel. The authors analyzed the engine performance with different blends of biodiesel and was compared with mineral diesel and concluded that the lower blends of biodiesel increased the break thermal efficiency and reduced the fuel consumption. The results proved that the use of biodiesel (produced from castor seed oil) in compression ignition engine is a viable alternative to diesel.

Bello et al [9] also discussed the use of castor oil methyl ester as possible alternative fuel for diesel engines. To overcome the high kinematic viscosity of the neat oil, a high molar ratio of 6:1 was used to produce the methyl ester. The results obtained gave properties, torque outputs and specific fuel consumption that are close to those of diesel fuel thus confirming that it can be used as alternative fuel for diesel engines.

Palligarnai et al [10] examined different biodiesel sources (edible and non-edible), virgin oil versus waste oil, algae-based biodiesel that is gaining increasing importance, role of different catalysts including enzyme catalysts, and the current state-of-the-art in biodiesel production.

Gwi-Taek & Don-Hee [11] applied response surface methodology in order to optimize the reaction factors for biodiesel synthesis from inedible castor oil. Specifically, the effects of multiple parameters and their reciprocal interactions using a five-level three-factor design and optimized the reaction temperature, oil-to-methanol molar ratio, and quantity of catalyst were evaluated. Subsequent empirical analyses of the biodiesel generated under the predicted conditions showed that the model equation accurately predicted castor biodiesel yields within the tested ranges.

MATERIAL AND METHODS

Biodiesel Production

The biodiesel was produced by a two-stage esterification and transesterification of a required quantity of the oil and ethanol the molar ratio of 1:6 was used. The catalyst (KOH) weight of 0.75 % of the weight of the oil was used. The reaction temperature was maintained at 65°C±1 for 90 minutes reaction time under a constant stirring speed using a magnetic stirrer hot plate. The sample was allowed to get separated over night and

the COME layer at the top was washed gently with water and excess methanol was evaporated [12].

Fuel Properties of Castor Methyl Ester

The physico-chemical properties evaluated in respect of Diesel are summarized in Table 1. The density (kg/m³) and specific gravity were determined by Anton Parr DMA 4500 density meter at operating temperature of 15.25°C. The Kinematic viscosity (mm²/s or cst) was determined at 40°C with TOLEDO Mettler apparatus. The calorific value (MJ/kg) of the biodiesel was measured by oxygen bomb calorimeter PARR 600. The oxidation stability index (h) was measured by the induction period of the sample using the biodiesel Rancimat 873 and finally, the acid value and the % Free Fatty Acids (FFA) were also measured using 0.1N NaOH titration.

Table 1: Fuel properties of Castor Oil and its FAME in comparison with Diesel.

Properties	Unit	ASTM Method	Castor oil	CME	Diesel
Kinematic Viscosity at 40 °C	cSt	D-445	222.4	10.5	4.3
Density	gm/cc	D-4052	0.96	0.91	0.83
Calorific value	MJ/kg	D-4809	36.3	39.25	45.3
Flash point	0C	D-93	320	165	47
FFA	%	D974	2.67	0.41	NA
Acid Value	mg KOH/g	D-664	1.63	0.92	NA

Analysis of Fatty Acids of Castor Oil

The gas chromatography was conducted by injection of 20mg of the COME into the gas chromatographic equipped with a split/split-less injection port using flame ionization detector and N₂ as the carrier gas flowing at a rate of 8ml/min. The split ratio was 50:1 while the injection temperature was kept at 350°C and sample elution time of 45 mins. The percentage composition by mass of the individual acids was computed as shown in table 3.

ENGINE EXPERIMENT

A single cylinder- medium capacity, four-stroke, vertical, Air cooled, diesel engine of Kirloskar was used. An electrical dynamometer coupled to the engine was used as a loading device operated at no load, 20, 40, 60 and 100% load condition for engine while fuel consumption was measured with the help of a digital stopwatch and burette. Engine emissions like HC, NO_x and CO were recorded using AVL Di gas analyzer. Engine smoke was carried out using AVL smoke meter. The engine was started using neat diesel and allowed to attain stability for at least 30 minutes before taking the baseline data. In the subsequent stages, diesel line was swapped with Castor oil methyl ester blends (or bio Diesel tank) and respective parameters were noted. The detailed layout of the engine test set up is shown in Fig. 1 while the details of test rig instrumentation are shown in Table 2.

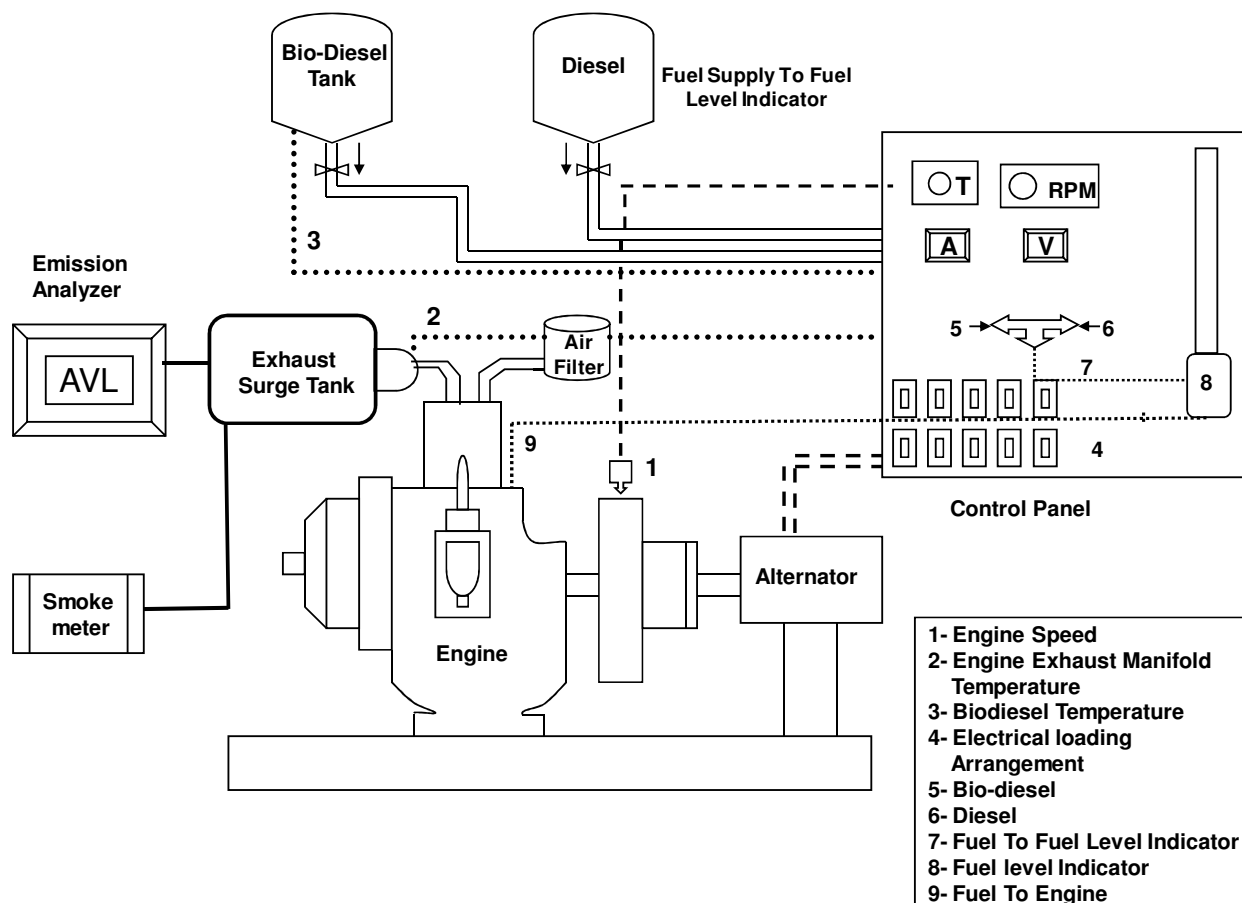


Figure 1: Line diagram of engine set-up.

RESULTS AND DISCUSSION

Fuel Properties of COME

The results of the of the fuel properties of the castor seed oil and COME were presented in table 2. From the results, it was evident that the viscosity of both the oil (222.4) and FAME (10.5) were relatively high. High kinematic viscosity affects the operation of fuel injection equipment, particularly at low temperatures when the increase in viscosity affects the fluidity of the fuel [13]. The calorific value (39.25 MJ/Kg) and flash point (165 °C) of FAME on the other hand were found to be within the range reported by literature. The acid value and the FFA values the maximum acid value of biodiesel according to ASTM D6751-08 is 0.5 (mg/KOH/g) which means that the pure oil has not exceeded this limit even before the transesterification reaction. The difference in acid value of the same feedstock and attributed it to quality of the oil as well as factors such as immature seeds and poor storage conditions.

The COME on the positive side has high oxidation stability of greater than eight hours which could be attributed to high degree of unsaturation as highlighted in the fatty acids profile. The results in this study were slightly different than that reported [14] for the same oil FAME, the authors the Kinematic viscosity was (15.94 cSt), the density (926.6), calorific value (37.8 MJ/Kg) and flash point (189.3 °C).

Fatty Acid Profile

The fatty acid profile of COME in table 3, revealed that ricinoleic acid constituted about 90% of the fatty acids present in the oil. This unsaturated fatty acid (97.7%) gives castor seed oil unique properties such as improved lubricity due to the presence of –OH attached to the oleic fatty acid structure. Other fatty acids in the oil include oleic and linoleic acids were also present.

Engine Performance

The performance of an engine is important in determining the application of biodiesel or any other alternative fuels on engine. The blending of non-edible biodiesel with mineral diesel can be applied directly to CI diesel engines but the effect of using this biodiesel must be evaluated by determining engine power, brake thermal efficiency, brake specific fuel consumption and emission products as regular as possible.

Table 2: Specification of the engine and the Dynamometer.

Engine Specification	
Engine model	DAF8,
No. of cylinder	1
Bore x stroke	95 x 110
Compression ratio	17.5:1
Rated output	5.9 KW at 1500 rpm.
S.F.C	251 gm/KWh
Swept volume	780 cc.
Dynamometer specification	
Manufacturer	Kirloskar Electric Co. Ltd., India
Dynamometer Type	Single phase, 50 Hz, AC alternator
Rated Output	5KVA@1500rpm
Rated Voltage	230V
Rated Current	32.6 A

Brake Thermal Efficiency: In all cases, brake thermal efficiency (BTE) was increasing with increase in applied load due to the reduction in heat loss and increase in power developed with increase in load. The full load BTE for B10 was 25.87% which was higher than that of the baseline diesel operation which stood at 24.53%. Hence B10 yields good thermal efficiency compared to B0, B05 and B20. Initially the thermal efficiency of the engine was improved with increasing concentration of the biodiesel blend. The possible reason for this is the additional lubricity provided by the biodiesel. The molecules of biodiesel (i.e. methyl esters of the oil) contain some amount of oxygen, which takes active part in the combustion process. It is noticed that after a certain limit with respect to diesel ester blend, the thermal efficiency trend was reverted and it started decreasing as a function of the concentration of blend. This lower BTE was obtained for B20 which could be due to the reduction in calorific value and increase in fuel consumption as compared to B10. The result of this study were consistent with results of Raheman and Ghadge [15] who reported the decrease in BTE with increase in the proportion of biodiesel in the blends at all compression ratios and injection timings using a Ricardo E6 engine fueled with Mahua FAME.

Brake Specific Energy Consumption (BSEC): The variation of brake specific Energy consumption (BSEC) with respect to load for different blends is presented in figure 3 showing the change in BSEC was almost similar for all blends. BSEC was also found lowest for B05 blend which was found to be marginally different from the fossil diesel. It could be concluded that BSEC was best improved by 20% blend. This was consistent with the results of other authors for example, Saboo [17], reported a decrease in BSCE and exhaust emissions for Polanga oil methyl ester fueled in a single cylinder engine.

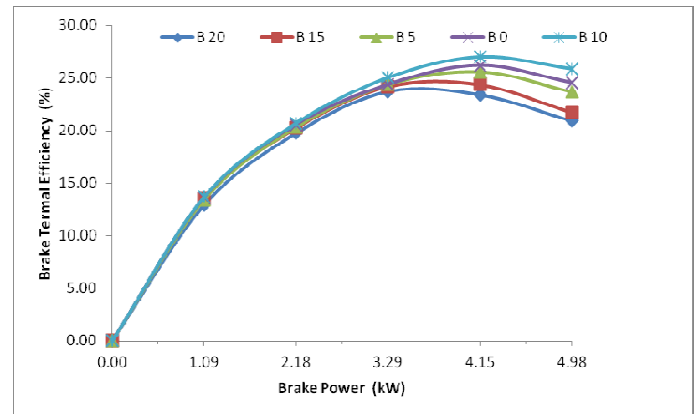


Figure 2: Brake Thermal Efficiency of Biodiesel Blends versus Brake Power

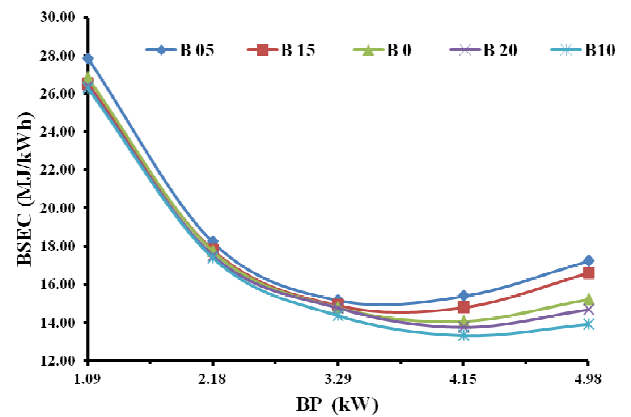


Figure 3: Brake Specific Energy Consumption of Biodiesel Blends versus Brake Power

Emission Characteristics

Carbon dioxide (CO₂), Carbon monoxide (CO) and Nitrous Oxide (NO_x) are important compounds to measure in emission studies due to their high toxicity and can be detrimental to the peoples on cumulative effect. In a summary form, the largest decreases in the amounts of CO₂, CO, HC, and smoke existing in emission gas were observed for B20, which means that increasing the amount of biodiesel in the fuel blend can lower the amount of the released pollutant after combustion as shown in figure 4, figure 5 and figure 6 respectively. Thus, it can be concluded that B20 is the best candidate as green fuel among all the blends studied in the above experiment.

Nitrogen Oxide (NO_x) emissions: It is found that the exhaust temperature increases with increase of COME in blends and is higher than that with diesel for all blends at all loads. Also a corresponding increase in NO_x emission is observed. This may be due to higher combustion chamber temperature, which in Table 3: Characteristics of Fatty Acids in Castor Seed Oil FAME

turn is indicated by the prevailing exhaust gas temperature. With increase in the value of exhaust gas temperature, NO_x emission also increased. Biodiesel fuel has the potential to emit more NO_x as compared to that of diesel fueled engines as shown in figure 7.

S.No.	Name of Fatty Acid	Chemical name of fatty acids	Degree of unsaturation	Chemical Formula	% value
1	Dihydroxyst	Dihydroxyst	-	-	0.7
2	Palmitic	Hexadecanoic	16:0	$C_{16}H_{32}O_2$	1.0
3	Stearic	Octadecanoic	18:0	$C_{18}H_{36}O_2$	1.0
4	Oleic	Octadecenoic	18:1	$C_{18}H_{34}O_2$	3.0
5	Linoleic	Octadecadienoic	18:2	$C_{18}H_{32}O_2$	4.2
6	Arachidic	Eicosanoic	20:0	$C_{20}H_{40}O_2$	0.3
7	Ricinoleic	Ricinoleic	18:1	$C_{18}H_{34}O_3$	89.5
8	Linolenic	Octadecadienoic	18:3	$C_{18}H_{30}O_2$	0.3
9	Saturated	-	-	-	2.3
10	Unsaturated	-	-	-	97.7

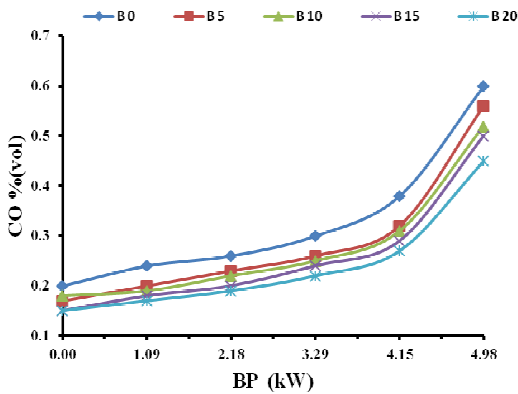


Figure 4: Variation of CO with respect to Brake Power.

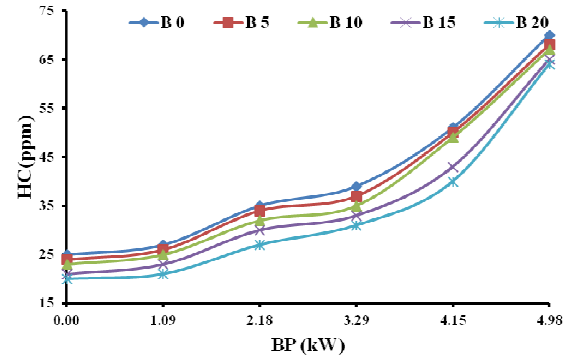


Figure 6: Variation of HC with respect to Brake Power.

Biodiesel due to its higher cetane number than petroleum diesel contains no aromatics, and less oxygen which makes it to exhibit reduced carbon monoxide (CO), unburned hydrocarbons (HC) and particulate matter (PM) in its exhaust but showed increase nitrous oxide emissions [18].

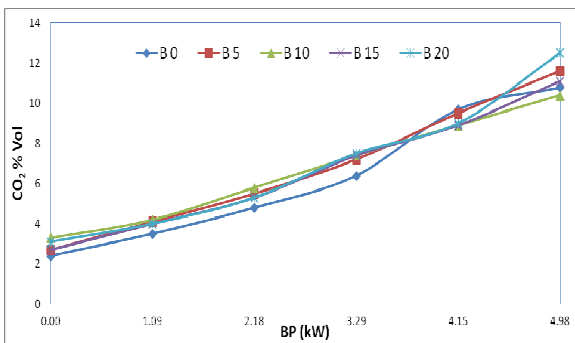


Figure 5: Variation of CO_2 with respect to Brake Power.

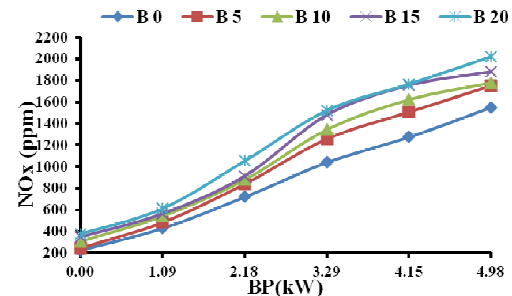


Figure 7: Variation of NO_x with respect to Brake Power.

Smoke opacity: Figure 8 shows the variation of smoke opacity of COME blends and diesel fuel. From the test results, it was found that the smoke opacity of neat diesel fuel is higher to that of biodiesel blends. At lower loads, the opacity difference is comparable but for full load condition B 20 shows lower smoke opacity than that of diesel fuel.

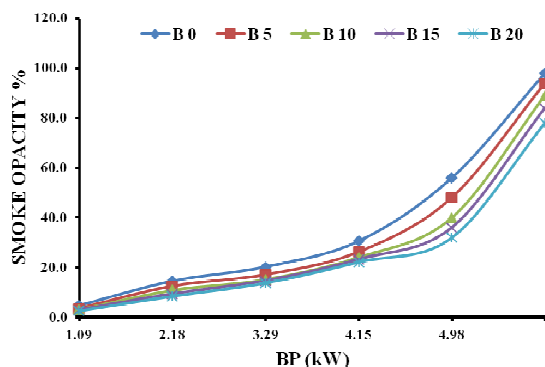


Figure 8: Variation of Smoke Opacity with respect to Brake Power.

This occurs due to longer ignition delay period (keeping all parameters constant) because of more fuel injection before ignition, higher temperature in the cycle and earlier termination of combustion process. The residence time is therefore increased. All these factors have found to reduce smoke opacity in exhaust.

CONCLUSION

The performance and emission characteristics of a medium capacity diesel engine fueled with the blends of Castor seed oil methyl esters were conducted. The results indicated that B10 blend resulted in highest full load BTE of 25.87% which was followed by B0 (24.53%), B5 (23.67%), B15 (21.71%) and B20 (20.89%) respectively. Similarly, full load BSEC exhibited by B10 was the least amongst the test fuels and stood at 13.91 MJ/kWh as compared to 15.21 MJ/kWh exhibited by the baseline data of diesel. Volumetric emissions of CO were found to get reduced with increase in volume fraction of the biodiesel in the test fuel. The full load CO emission for neat diesel was 0.6% which was dropped to 0.45% for B20. The rest of the test fuels exhibited CO emission trends within that range. Similarly, emissions of CO₂ were found to increase with increased biodiesel composition in the test fuel indicating superior combustion behavior with increased biodiesel volume fractions. Full load HC emission for the baseline was 70ppm which was reduced continuously with increase in biodiesel composition in the test fuel and finally B20 exhibited 64ppm of HC emission. Smoke opacity was reduced for higher biodiesel volume fractions. Opacity was found to be 78% for B20, 84% for B15, 89% for B10, 94% for B05 as compared to 98% exhibited by the baseline data of diesel. However, the emission of NO_x took an upward trend with increase in biodiesel volume fraction in the test fuel. Emission of NO_x was increased to 1748 ppm for B05, 1780 ppm for B10, 1882 ppm for B15 and 2022 ppm for B20 as compared to 1550 ppm exhibited by the baseline data of diesel. As an outcome of the exhaustive engine trial and the subsequent analysis, it may be concluded that the castor oil methyl ester blends can be used in unmodified CI engines leading to reduced emissions of CO, THC, smoke with marginal increase in NO_x emissions. The biodiesel can be of great help to provide energy security in remote rural areas of the country.

ACKNOWLEDGMENTS

The authors wish to acknowledge Center for Advanced Studies and Research in Automotive Engineering (CASRAE), Delhi Technological University, Delhi. The authors wish to thank Dr. (Prof.) Naveen Kumar, Head CASRAE and Mr. Alhassan Yahaya & Mr. Chinmaya Mishra, members of CASRAE by their contributions and support to the discussion of key issues.

REFERENCES

1. World Energy Issues, Monitor published by World Energy Council in February 2013
2. Pillay A. E. and S. C. Fok, Engine Emissions and Performances with Alternative Biodiesels: A Review. *Journal of Sustainable Development*, Vol. 5 No. 4. 2012. Pp 59-73 available online www.ccsenet.org/jdsd.
3. Abbaszaadeh A., Barat G., Omidkhah M. R. and Najafi G. Current biodiesel production technologies: A comparative review. *Energy Conversion and Management*, Vol. 63. 2012. pp 138-148
4. Wiznia D., Geist G and Ellis H. Biofuels: Implementation and Emission Analysis. 2006. Pp 1-8
5. Aman Hira and Shailendra Singh. Performance & Emission Characteristics of CI Engine, Fuel, Vol. 72, 2011, pp 1145-52.
6. Amais R. S., G. L. Donati, Schiavo D. and J. A. Nobrega. A simple dilute-and-shoot produce for Si determination in diesel and biodiesel by microwave-induced plasma optical emission spectrometry, *Microchemical Journal* Vol. 106 2013, pp 318-322, doi:10.1016/j.microc.2012.09.001
7. Ogunniyi D.S. Castor oil: a vital industrial raw material. *Bioresources Technology*, Vol. 97(9) 2006, pp 1086-91.
8. Panwar, N.L., Hemant Y. Shrirame, N.S. Rathore, Sudhakar Jindal, A.K. Kurchania. Performance evaluation of a diesel engine fueled with methyl ester of castor seed oil. *Applied Thermal Engineering*, Vol. 30, 2010. pp 245-249.
9. Bello E.I and Mekanju A. Production, Characterization and Evaluation of Castor oil Biodiesel as Alternative Fuel for Diesel Engines. *Journal of Emerging Trends in Engineering and Applied Sciences*, Vol. 2 (3), 2011. pp 525-530
10. Palligarnai T. Vasudevan E. and Michael Briggs. Biodiesel Production—Current state of the art and challenges, *Review of J Ind Microbiol Biotechnol*, Vol. 35, 2008 pp 421-430.
11. Gwi-Taek Jeong Don-Hee Park. Optimization of Biodiesel Production from Castor Oil Using Response Surface Methodology. *Appl Biochem Biotechnol*, Vol. 156, 2009. pp 431-441.

12. Karnwal Ashish, Naveen Kumar, M.M. Hasan, Rajeev Chaudhary, Arshad Noor Siddique and Zahid A, Khan. Production of Biodiesel from Thumba Oil: Optimization of Process Parameters, *Iranica Journal of Environment* **1(4)**, 2010: ISSN 2079-2011 PP 352-358.
13. Demirbas A. Progress and recent trends in biodiesel fuels. *Energy Conversion and Management*, 2009, Vol. **50** (1) pp 14-34
14. Chandu S. M., Pradhan S. and S. N. Naik. Parametric study of reactive extraction of castor seed (*Ricinus communis* L.) methyl ester production and its potential use as bio-lubricant, *Industrial Crops and Products*, Vol.**43**,2013,pp283-290.
<http://dx.doi.org/10.1016/j.indcrop.2012.07.010>.
15. Raheman H. and Ghadge S.V. Performance of diesel engine with biodiesel at varying compression ratio and ignition timing, *Fuel*, Vol. 87 (12) 2008, pp 2659-66.
16. Ramadhas AS. Muraleedharan C, Jayaraj S. Performance and emission evaluation of a diesel engine fueled with methyl esters of rubber seed oil. *Renewable Energy*; Vol. 30(12) 2005, pp 1789-800.
17. Saboo P.K., Das L.M., Babu M.K.G, Naik S.N. Biodiesel development from high acid value polanga seed oil and performance evaluation in a CI engine, *Fuel*, Vol. 86(3) 2007, pp 448-54.

PERFORMANCE COMPARISON OF FILTER CIRCUITS BASED ON TWO DIFFERENT CURRENT CONVEYOR TOPOLOGIES

Garima Varshney, Neeta Pandey, Rajeshwari Pandey, Asok Bhattacharyya
Department of Electronics and Communication Engg.
Delhi Technological University
Delhi, India

gvarshn1@gmail.com, n66pandey@rediffmail.com, rajeshwaripandey@gmail.com, bh_asok@ieee.org

Abstract—This paper investigates the effect of two different second generation current conveyor (CCII) topologies on the behaviour of low pass, high pass and band pass filters. One of the current conveyor topology is based upon CMOS inverters and the other realization is based on translinear loop. 3-db bandwidth, Total Harmonic Distortion (THD) and output noise are used as comparison parameters. Simulation results show that THD of CMOS inverter's based filters is lesser than that of the translinear loop based CCII filters. The former topology also enjoys better noise throughout its bandwidth against the latter one. All the simulations are done on PSPICE using typical BSIM3V3 0.35 μ m CMOS process parameters.

Keywords— Second generation current conveyor, CMOS inverter, translinear loop, filters, transconductance mode.

I. INTRODUCTION

There has been substantial emphasis on the development of current mode signal processing circuits such as filters and oscillators. This is due to increased bandwidth, simple circuitry, better linearity, dynamic range performances and lower power consumption as compared to their voltage mode counterparts. A variety of current mode building blocks are developed at the same time to keep the pace with current mode circuits. The current conveyor (CCII) is one among such blocks which has received significant attention. It is hybrid block and has basic construction containing a voltage follower (VF) interconnected with either current mirror or current follower.

The CCII is three-terminal devices with the terminals designated X, Y and Z. The potential at X follows the voltage applied to Y. The current flowing into X is copied at Z with high output impedance. There is no current flow through terminal Y.

A variety of topologies are proposed for CCII in [1], [2] and references cited therein. The topology reported in [1] is on CMOS inverters. In this topology the inverters operate in transconductance mode. The other current conveyor topology is translinear loop based [2]. In this paper, a performance comparison is carried out for CCII based low pass, high pass and band pass filters constructed with these two topologies. Performance comparison is done using 3-dB bandwidth, THD and Noise with respect to frequency as parameters. All the

PSPICE simulations are done using typical BSIM3V3 0.35 μ m CMOS process parameters.

In Section II and III, CMOS inverter based current conveyor and translinear loop based current conveyor topologies [1, 2] are reviewed briefly. Section IV presents the High-Pass, Low-Pass and Band-Pass filters design [3]. The simulation results are presented in section V which is followed by conclusion in section VI.

II. CMOS INVERTER BASED CURRENT CONVEYOR

The positive type second generation current conveyor based on CMOS inverter topology is shown in Fig. 2 [1]. It employs the CMOS inverters in transconductance mode of operation.

A. CMOS Inverter in Transconductance Mode

The transistor sizes W_N/L_N (nmos transistors) and W_P/L_P (pmos transistors) of the CMOS inverters are set in order to obtain a voltage transition around $V_{IN} = V_{OUT} = (V_{DD} + V_{SS})/2$. This condition leads to a common mode voltage V_{CM} about $V_{CM} = 0$ for $V_{SS} = -V_{DD}$, for small signal amplitudes about V_{CM} all the inverters behave as a transconductor [4]. In this mode of operation, the small signal output current (i_{out}) of inverter is given by $i_{out} = -g_m v_{in}$, where g_m is the inverters transconductance and v_{in} is the inverter small signal input voltage. The CMOS inverter I-V characteristics in transconductance mode are shown Fig. 1.

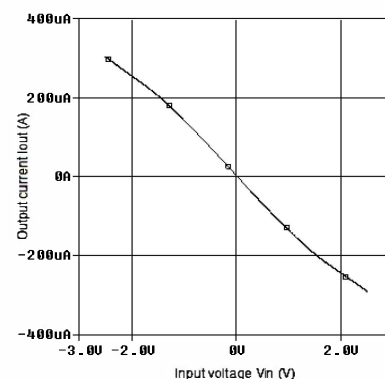


Fig. 1 CMOS Inverter in transconductance mode of operation

B. CMOS Inverter Based Current Conveyor

Fig. 2 [1] shows positive type second generation current conveyor based upon CMOS inverters only. Consider transconductance of all the inverters are same in Fig. 2 (g_{m_i} of each $I_i = g_m$). The relationship between voltages of terminals X and Y is obtained by analysing the path between inverters I1, I2, I3 and I4 as

$$V_X = \frac{R_L}{R_L + R_X} V_Y \quad (1)$$

Where $gm = 1/R_X$. It is clear from Fig. 2 that $I_Z = I_4 + I_5$, and $I_X = I_2 + I_3$. We have $I_4 = I_2$ and $I_5 = I_3$, which leads to $I_Z = I_X$.

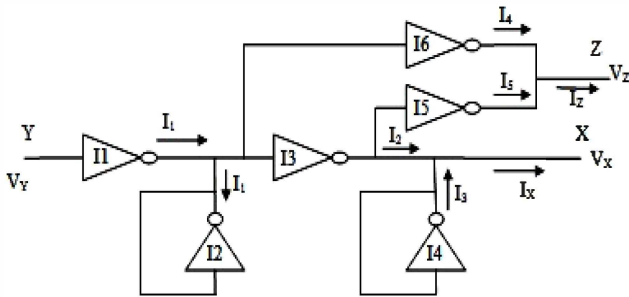


Fig. 2 CMOS Inverter based CCII+ [1]

III. TRANSLINEAR LOOP BASED CURRENT CONVEYOR

An implementation of translinear loop based positive type second generation current conveyor is shown in Fig.3 [2].

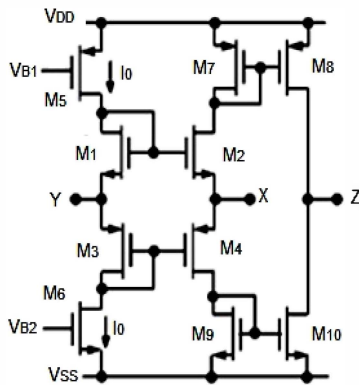


Fig. 3 Translinear loop based CCII+ [1]

CCII⁺ shown in Fig. 3 allows the function of voltage follower between points X and Y due to the translinear loop formed by M_1 , M_2 , M_3 and M_4 ($V_X = V_Y$). The transistors M_5 and M_6 provide the biasing to the loop. The output NMOS and PMOS current mirrors (M_7 , M_8 , M_9 and M_{10}) duplicate the current from port X to port Z ($I_Z = I_X$).

IV. FILTERS

The filter structures used for comparison of current conveyor topologies, mentioned in section II and III are shown in below subsections. All the three filters, low pass, high pass and band pass, consist of two capacitors, two resistors and one positive type second generation current

conveyor [3]. The cut-off frequency is same for all the filters and calculated as

$$\omega_0 = \sqrt{\frac{G_1 G_2}{C_1 C_2}} \quad (2)$$

A. Low-Pass Filter

A second order low pass filter is shown in Fig. 4.

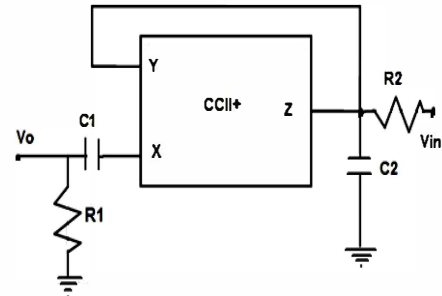


Fig. 4 CCII+ based Low pass filter

The low pass filter is having a voltage transfer function for $G_1 = G_2 = G$ as given below

$$\frac{V_o}{V_{in}} = \frac{G^2}{s^2 C_1 C_2 + s C_2 G + G^2} \quad (3)$$

B. High-Pass Filter

Fig. 5 shows a second order high pass filter.

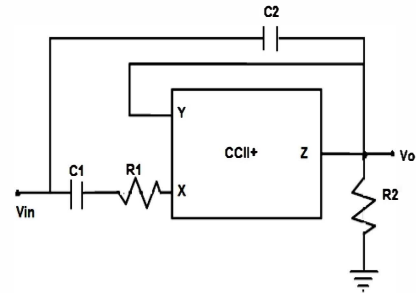


Fig. 5 CCII+ based High pass filter

The voltage transfer function of high pass filter for $C_1=C_2=C$ is given as

$$\frac{V_o}{V_{in}} = \frac{s^2 C^2}{s^2 C^2 + s C G_2 + G_1 G_2} \quad (4)$$

C. Band-Pass Filter

The second order band pass filter is shown in Fig. 6. The voltage transfer function of the filter for $G_1 = G_2 = G$ is given as below

$$\frac{V_o}{V_{in}} = \frac{sC_2G}{s^2C_1C_2 + sC_2G + G^2} \quad (5)$$

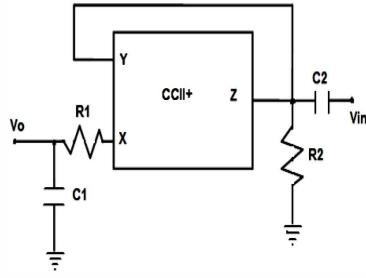


Fig. 6 CCII+ based Band pass filter

V. SIMULATION RESULTS

The filter structures of Figs. 4 - 6 are simulated to see the effect of CCII topologies on filter performance. The typical BSIM3V3 0.35 μm CMOS process parameters and power supply of $\pm 2.5\text{V}$ are used. The aspect ratios of the transistors used in CCII+ implementation are given in Table I. The filters are designed for pole frequency of 15.9MHz and quality factor of 1. The component values for the resistors (R_1 , R_2) and capacitors (C_1 , C_2) are taken as 10 K Ω each and 1 pF each respectively. The filter responses are shown in Figs. 7 - 9 which conform to the transfer functions given by (3) - (5). The inverter based CCII+ consumes almost half area than its translinear counterpart.

TABLE I
ASPECT RATIO OF TRANSISTORS

CMOS inverter based CCII+ in Fig. 2 W_N, W_P $L_N = L_P$	1.5 μm , 3 μm 2 μm
Translinear loop based CCII+ in Fig. 3 $W_1 = W_2 = W_6 = W_9 = W_{10}$ $W_3 = W_4 = W_5 = W_7 = W_8$ $L_1 = L_2 = L_3 = L_4 = L_5 = L_6 = L_7 = L_8 = L_9 = L_{10}$	3 μm 9 μm 2 μm

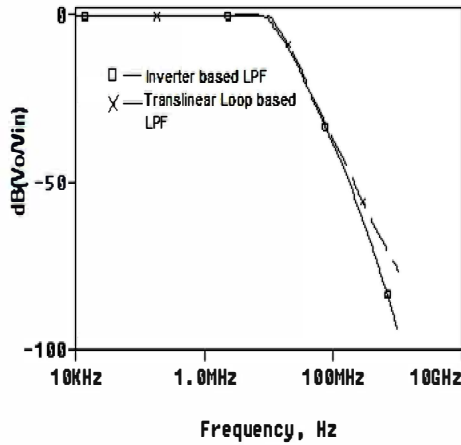


Fig. 7 Frequency response of Low pass filter

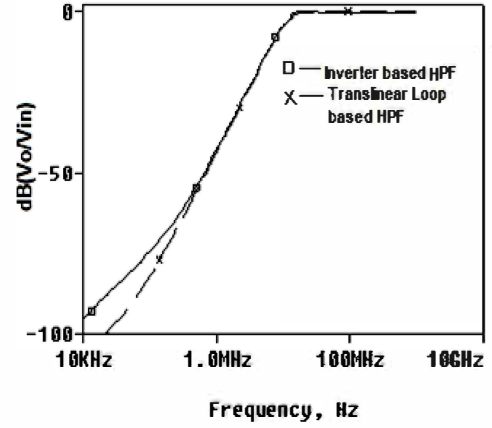


Fig. 8 Frequency response of High pass filter

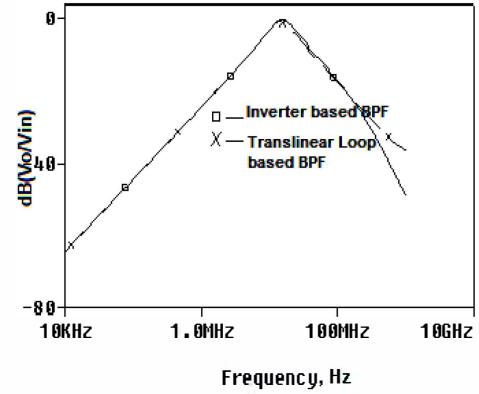


Fig. 9 Frequency response of Band pass filter

The following subsections describe the dynamic range, THD and noise with respect to frequency.

A. 3-dB Bandwidth

The bandwidth response for current transfer from x to z terminal is shown in Fig. 10. The bandwidth for translinear and inverter based CCII are reported as 200 MHz and 400 MHz respectively. The bandwidth for voltage transfer is found to be high for both the topologies.

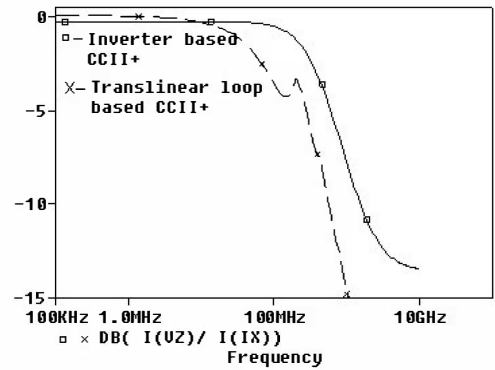


Fig. 10 Bandwidth response of CCII+

B. THD

An input sinusoidal excitation of frequency 3MHz is applied to see the effect of CCII topologies on THD. Fig. 11 shows the THD variations with respect to the input sinusoidal voltage signal amplitude for low pass filter. It may be noted that THD is comparable for low signal amplitudes but the inverter based topology gives better performance for higher signal amplitudes.

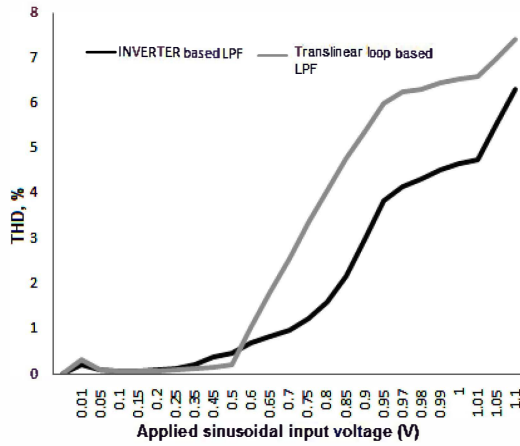


Fig. 11 THD variation of Low pass filter versus amplitude of applied sinusoidal signal

C. Noise Analysis

An input ac excitation having amplitude 200mV is applied to see the effect of CCII topologies on output noise. Figures 12 - 14 show the equivalent output noise against frequency for low pass, high pass and band pass filters. A close observation of these curves reveals that inverter based topology gives better performance. Table II shows the output noise value (nV) at 15.9 MHz frequency for all three filters.

TABLE II
OUTPUT NOISE COMPARISON FOR 15.9MHz FREQUENCY

Filter	LPF	HPF	BPF
Topology			
Translinear loop based	26.47	37.78	40.22
CMOS Inverter based	19.67	29.57	19.67

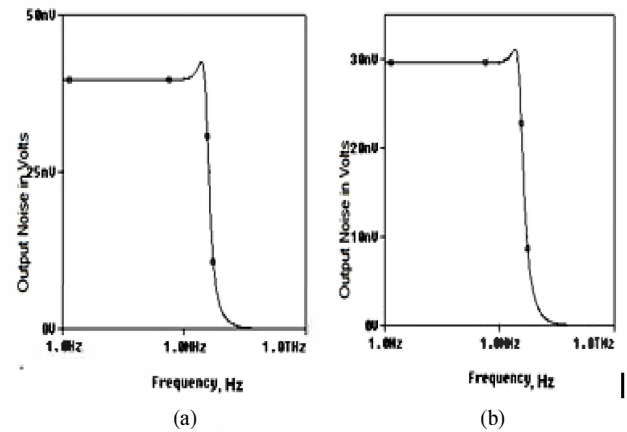


Fig. 12 Output noise of Low pass filter versus frequency (a) Translinear loop based (b) CMOS inverter based

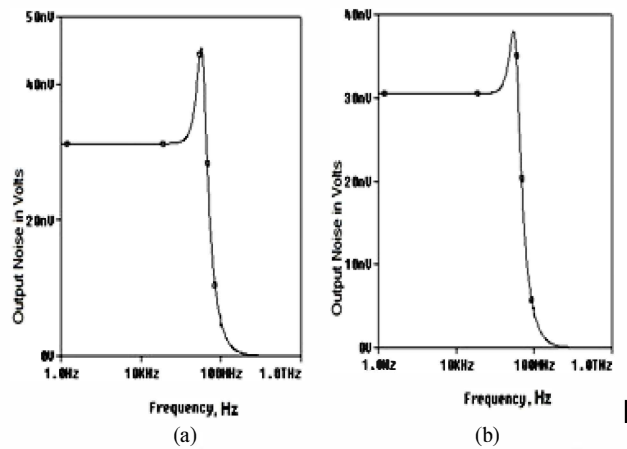


Fig. 13 Output noise of High pass filter versus frequency (a) Translinear loop based (b) CMOS inverter based

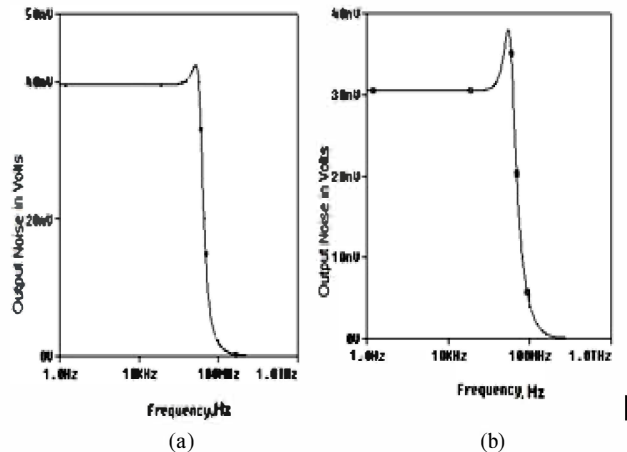


Fig. 14 Output noise of Band pass filter versus frequency (a) Translinear loop based (b) CMOS inverter based

VI. CONCLUSION

The effect of CCII topologies on the filter performance is evaluated on the basis of 3-dB bandwidth, THD and output noise in this paper. Bandwidth response for current transfer is found to be twice for CMOS inverter based CCII than that of

translinear loop based CCII. The THD of CMOS inverter's based topology is better than that the one based on traditional translinear loop. The former topology also has lesser noise against the latter one. The area of silicon required for CMOS inverter based CCII is approximate half of the silicon area for translinear loop based CCII, which is a clear advantage of CMOS inverter based CCII. At low power supply the traditional CCII deviates from its characteristics while CMOS inverter based CCII is able to operate under such conditions. The traditional CCII requires additional biasing circuitry. One more advantage of CMOS inverter based circuit is that they can be synthesized using digital inverter ICs.

REFERENCES

- [1] H. Barthelemy, M. Fillaud, S. Bourdel, and J. Gaubert, "CMOS inverters based positive second generation current conveyor," *Analog Integr. Circ Sig Process*, pp. 141–146, 2007.
- [2] S.B. Salem, A. Fakhfakh, M. Loulou, P. Loumeau, and N. Masmoudi, "A 2.5V 0.35 μ m CMOS Current conveyor and high frequency high-Q band-pass filter," in *2004 Proc. of ICM*, 2004, pp. 328 – 333.
- [3] J.W. Horng, "Voltage/Current-mode universal biquadratic filter using single CCII+" *Indian J. Pure & Appl. Phys.*, vol. 48, pp. 749-756, 2010.
- [4] B. Nauta, and E. Seevinck, "Linear CMOS transconductance element for VHF filters," *Electronics Letter*, vol. 25, pp. 448–450, 1989.

Phase control of nanostructured iron oxide for application to biosensor†

Cite this: *J. Mater. Chem. B*, 2013, **1**, 464

Rachna Sharma,^{ac} Ved Varun Agrawal,^{*a} A. K. Srivastava,^a Govind,^a Lata Nain,^b Mohd Imran,^a Soumya Ranjan Kabi,^b R. K. Sinha^c and Bansi D. Malhotra^{*d}

We report results of the studies relating to the phase transformation of bare Fe₃O₄ nanoparticles (NPs) to α -Fe₂O₃ NPs obtained during electrophoretic film deposition onto indium-tin oxide coated glass plates. The *in situ* oxidation of NPs during electrophoretic deposition can be circumvented using surface passivation of the Fe₃O₄ NPs with an organic shell (carbon) as well as an inorganic shell (silica), while retaining the biocompatibility of the Fe₃O₄ NPs. XRD and XPS studies reveal the transformation of Fe₃O₄ NPs to α -Fe₂O₃ NPs upon electrophoretic deposition, and the retention of the phase of the Fe₃O₄ NPs upon encapsulation with carbon and silica, respectively. The results of SEM studies indicate decreased agglomeration of the Fe₃O₄ NPs upon encapsulation during film deposition. Attempts have been made to compare the characteristics of cholesterol biosensors fabricated using Fe₃O₄@C and α -Fe₂O₃ NPs, respectively. The Fe₃O₄@C NPs based cholesterol biosensor shows response time of 60 s, a linearity range of 25–500 mg dl⁻¹, a sensitivity of 193 nA mg⁻¹ dl cm⁻² and a Michaelis–Menten constant of 1.44 mg dl⁻¹.

Received 1st October 2012

Accepted 9th October 2012

DOI: 10.1039/c2tb00192f

www.rsc.org/MaterialsB

Introduction

Nanostructured iron oxides (Fe₃O₄, γ -Fe₂O₃ and α -Fe₂O₃) owing to their multifunctional properties, such as small size, superparamagnetism, low toxicity *etc.*, are being widely investigated for applications in high-density information storage,¹ electronic devices,² ferrofluid technology,³ catalysis,⁴ pharmaceuticals⁵ and biotechnology.⁶ Among these, the application of nanostructured iron oxides in clinical diagnostics and biomedicine have aroused much interest because of their biocompatibility and stability under physiological conditions.^{7,8} They can also be used as contrast agents in magnetic resonance imaging,^{9,10} as mediators in hyperthermia,¹¹ as carriers for guided drug delivery^{12–14} and as immobilization supports for desired biomolecules for the diagnosis of various pathogens and diseases, and estimation of various biochemical analytes such as glucose, urea *etc.*^{15–17} Besides this, the particle size of the

nanostructured iron oxide can be controlled to a similar size as that of a biomolecule (protein 5–50 nm; virus 20–450 nm; cell 10–100 μ m).¹⁸

Despite several advantages, the susceptibility of Fe₃O₄ NPs towards oxidation and their tendency to agglomerate due to strong dipole–dipole attractions between particles, have limited their applications to date.¹⁹ It is anticipated that encasing colloids in a shell of a different material may perhaps protect the core from extraneous chemical and physical changes. Core–shell nanostructures are known to exhibit improved physical and chemical properties over their single-component counterparts, and hence are potentially useful for a range of applications. To improve the stability of the deposited NPs, many molecules, such as carbon and silica, have been considered as interesting encapsulants.^{20–22} Compared to polymer and inorganic shells, carbon shells exhibit much higher stability in various chemical and physical environments such as acid or base media, as well as at high temperatures and pressures.²³ Thus, carbon coated Fe₃O₄ NPs may perhaps ensure prolonged activity of the biomolecules and enhanced stability of the biosensors.

Among various methods, the formation of nanocrystalline films using electrophoretic deposition has recently gained much interest since it is cost effective²⁴ and can be used to obtain uniform thin films by optimizing parameters such as solution concentration, applied potential, pH of the solution *etc.*^{24,25} The fabrication of nanostructured iron oxide films using electrophoretic deposition and its characterization may perhaps yield important information relating to the phase change of nanostructured iron oxide. Also, the utilization of

^aNational Physical Laboratory, New Delhi-110012, India. E-mail: agrawalvv@nplindia.org; Tel: +91-11-45609489

^bDivision of Microbiology, Indian Agricultural Research Institute, New Delhi-110012, India

^cDepartment of Applied Physics, Delhi Technological University, New Delhi-110042, India

^dDepartment of Biotechnology, Delhi Technological University, New Delhi-110042, India. E-mail: bansi.malhotra@gmail.com

† Electronic supplementary information (ESI) available: SEM studies showing the immobilization of cholesterol oxidase onto nanostructured iron oxide films, shelf life, reproducibility and response time studies of the fabricated cholesterol biosensors. See DOI: 10.1039/c2tb00192f

nanostructured iron oxide films for the fabrication of biosensors may perhaps result in enhanced electrocatalytic activity of the given biomolecule and improved sensitivity for detection of the desired analyte.

We report a novel method of controlling the phase of iron oxide NPs obtained during electrophoretic deposition. It is shown that the phase of the nanostructured iron oxide during electrophoretic deposition can be tuned to the desired requirements by using bare Fe_3O_4 NPs or capped Fe_3O_4 NPs as the starting material. The nanocrystalline films of Fe_3O_4 @C and $\alpha\text{-Fe}_2\text{O}_3$ NPs have been employed for the fabrication of a biosensor using cholesterol oxidase as a model enzyme and the biosensing characteristics have been investigated using electrochemical techniques such as cyclic voltammetry and electrochemical impedance spectroscopy. To the best of our knowledge, there is as yet no report on the phase transformation of Fe_3O_4 NPs during electrophoretic deposition, its prevention and further application in biosensing.

Experimental methods

Materials and methods

Ferrous sulphate heptahydrate ($\text{FeSO}_4 \cdot 7\text{H}_2\text{O}$), ferric chloride (FeCl_3), sodium hydroxide (NaOH), fructose ($\text{C}_6\text{H}_{12}\text{OH}$) powder and tetraethyl orthosilicate ($\text{Si}(\text{OC}_2\text{H}_5)_4$) have been purchased from Sigma-Aldrich. All reagents are of analytical grade and have been used without further purification. De-ionized water (Milli-Q 10 TS) with resistivity $>18.2 \text{ M}\Omega \text{ cm}$ has been used for preparing all aqueous solutions. Indium-tin-oxide (ITO) coated glass plates have been obtained from Balzers, UK, (Baltracom 247 ITO, 1.1 mm thick) with a sheet resistance and transmittance of $25 \Omega \text{ sq}^{-1}$ and 90%, respectively. Cholesterol powder and cholesterol oxidase (EC 1.1.36 from *Pseudomonas fluorescens*) with a specific activity of 26 U mg^{-1} have been purchased from Sigma-Aldrich (USA). The stock solution of cholesterol has been prepared in 10% triton X-100 and stored at 4°C .

(a) Preparation of Fe_3O_4 , Fe_3O_4 @C and Fe_3O_4 @ SiO_2 NPs

(i) Fe_3O_4 NPs. The Fe_3O_4 NPs have been prepared *via* hydrolytic reaction based on chemical co-precipitation of metal salts with an alkali, as reported earlier.²⁶ Briefly, 0.32 M $\text{FeSO}_4 \cdot 7\text{H}_2\text{O}$ and 0.64 M FeCl_3 are added to 10 mL of deoxygenated water (containing 12.1 N HCl) with continuous stirring at 30°C . The solution containing iron salts is dropwise added to 100 mL of NaOH solution (1.5 M) with vigorous stirring at 30°C . The mixture is then stirred for an additional 30 min, resulting in the appearance of a black precipitate. The particles are washed by centrifugation at 3500 rpm for 30 min and the supernatant is removed by decantation. The particles are then redispersed in 200 mL of deoxygenated water and are stabilized by making the pH of the sol 3.5 using HCl.

Furthermore, the Fe_3O_4 NPs are subjected to high temperature and pressure using autoclaves. 30 mL of the above synthesized NPs are autoclaved at 180°C for 4 h.²⁷

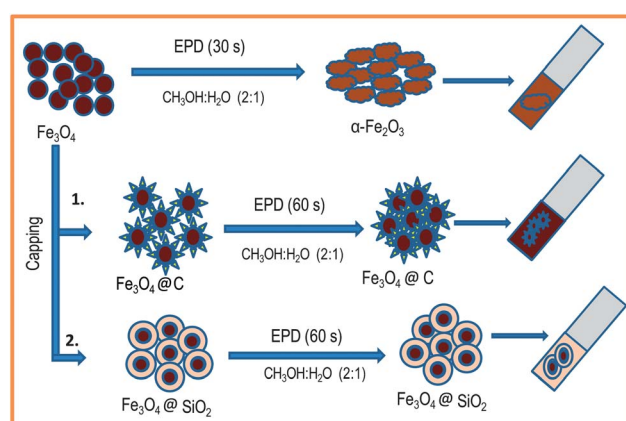
(ii) Fe_3O_4 @C NPs. Carbon capped Fe_3O_4 NPs have been prepared *via* hydrothermal carbonization reaction. For this

purpose, 10 mmol of fructose powder is added to 30 mL of Fe_3O_4 NPs sol^{23,28,29} and the mixture is autoclaved at 180°C for 4 h. At this temperature, fructose melts and carbonization of fructose occurs, resulting in a carbon shell over the Fe_3O_4 NPs.³⁰ The reaction mixture is cooled under ambient conditions. The synthesized product is washed by centrifugation at 3500 min^{-1} and the supernatant is removed by decantation. No change in color of the sol is observed and the pH of the NPs redispersed in water is recorded as 8.0.

(iii) Fe_3O_4 @ SiO_2 NPs. To 10 mL of Fe_3O_4 NPs sol (diluted with 40 mL of iso-propanol) are added 1 mL of ammonia and 1 mL of tetraethyl orthosilicate (TEOS).³¹ The mixture is stirred at 30°C for 4 h and a change in colour from dark brown to light brown is observed upon completion of the reaction. The synthesized NPs are collected by centrifugation at 3500 min^{-1} and the pH of the NPs redispersed in water is recorded as 9.6.

(b) Preparation of nanostructured iron oxide films

The nanocrystalline films of iron oxide are deposited onto ITO coated glass plates using a two-electrode system with platinum as the auxiliary electrode and an ITO-coated glass plate as the deposition electrode. The electrophoretic deposition involves charged particles in a suspension being deposited onto an electrode under the influence of an applied electric field. Thus, the use of surfactant is avoided and the charge on the surface of the NPs is introduced by adjusting the pH of the suspension to obtain a stable sol. The Fe_3O_4 NPs carry a positive charge at pH 3.5 since the isoelectric point of Fe_3O_4 is 6–7.^{32–34} Cationic NPs are deposited onto the ITO-coated glass plate at the cathode terminal. Application of even a small voltage leads to electrolysis of water, producing hydrogen and oxygen gas, which hinder continuous flow of the NPs and affect the film uniformity.²⁵ Thus, a mixture of methanol–water (2 : 1) is utilized for deposition of the desired nanocrystalline film. The conditions for obtaining uniform films have been optimized for various parameters such as applied potential, concentration, deposition time, *etc.*, and uniform films of Fe_3O_4 NPs and Fe_3O_4 NPs (autoclaved) are obtained upon application of a 5 V potential for 30 s (Scheme 1).



Scheme 1

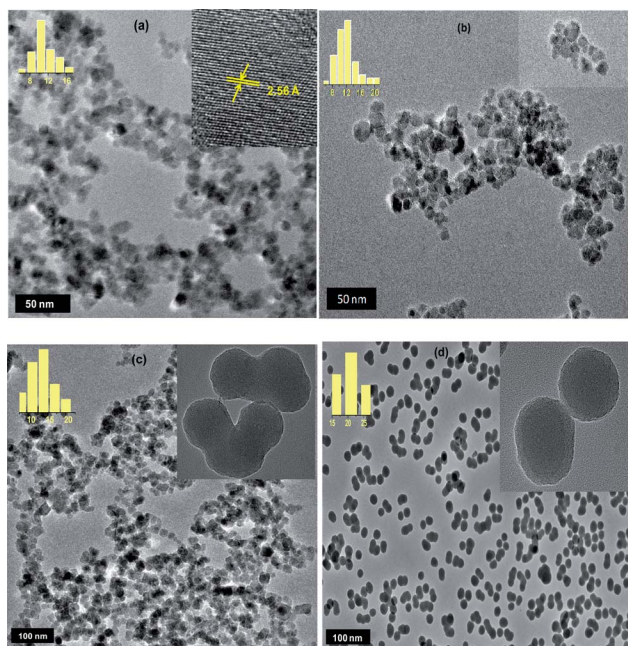


Fig. 1 TEM micrographs of: (a) Fe_3O_4 NPs (inset: high-resolution image of a single particle); (b) Fe_3O_4 NPs (autoclaved); (c) $\text{Fe}_3\text{O}_4@\text{C}$ NPs; (d) $\text{Fe}_3\text{O}_4@\text{SiO}_2$ NPs.

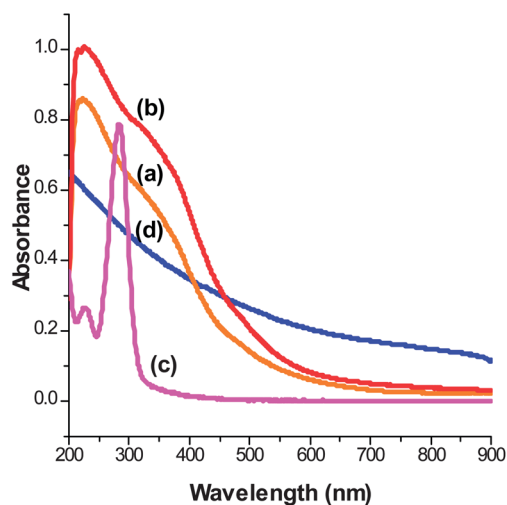


Fig. 2 UV-vis absorption spectra of: (a) Fe_3O_4 NPs; (b) Fe_3O_4 NPs (autoclaved); (c) $\text{Fe}_3\text{O}_4@\text{C}$ NPs; (d) $\text{Fe}_3\text{O}_4@\text{SiO}_2$ NPs.

The $\text{Fe}_3\text{O}_4@\text{C}$ and $\text{Fe}_3\text{O}_4@\text{SiO}_2$ NPs have been deposited in a methanol-water (2 : 1) mixture. Although the Fe_3O_4 NPs are stable at 8.0 pH, no deposition occurs, indicating that the NPs carry negligible charge. A positive charge on the NPs is then introduced by adjusting the pH to 3.5 and a nanocrystalline film is deposited onto the ITO-coated glass plate at the cathode terminal by applying an optimized potential of 10 V for 60 s. Interestingly, the $\text{Fe}_3\text{O}_4@\text{SiO}_2$ NPs carry negative charge at pH 9.6 (as the iso-electric point of SiO_2 NPs is ~ 2),³⁵ thus a nanocrystalline film is deposited onto the ITO-coated glass plates at the anode terminal upon application of a 10 V potential for 60 s.

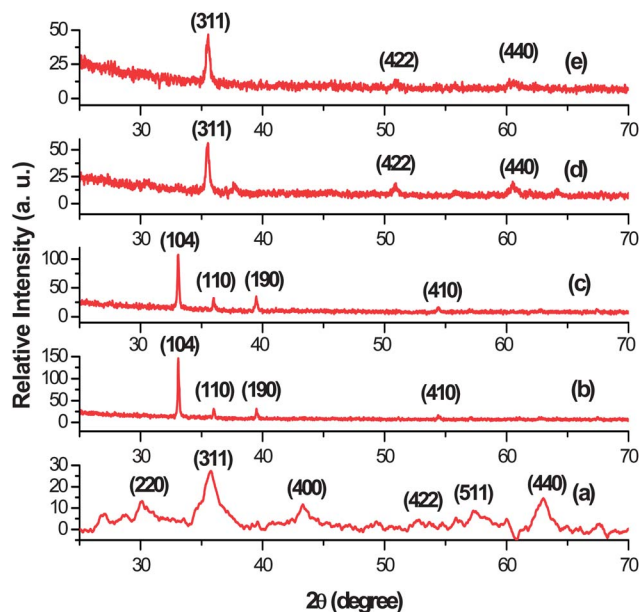


Fig. 3 XRD spectra of: (a) Fe_3O_4 NPs; (b) film obtained from Fe_3O_4 NPs; (c) film obtained from Fe_3O_4 NPs (autoclaved); (d) film obtained from $\text{Fe}_3\text{O}_4@\text{C}$ NPs; (e) film obtained from $\text{Fe}_3\text{O}_4@\text{SiO}_2$ NPs.

(c) Fabrication of nanostructured iron oxide film based bioelectrodes

ChOx is physisorbed onto the nanostructured iron oxide films. For this purpose, 20 μL of freshly prepared ChOx solution (1 mg mL^{-1}) is spread onto the $\alpha\text{-Fe}_2\text{O}_3$ and $\text{Fe}_3\text{O}_4@\text{C}$ nanocrystalline films. ChOx immobilized iron oxide films are incubated at 27 $^\circ\text{C}$ for 2 h and at 4 $^\circ\text{C}$ for 12 h.³⁶ Later, weakly bound ChOx are removed by washing these films with 100 mM PBS buffer containing 0.05% Tween-20.³⁷ These films are stored at 4 $^\circ\text{C}$ when not in use. The fabricated ChOx/ $\text{Fe}_3\text{O}_4@\text{C}$ film/ITO and ChOx/ $\alpha\text{-Fe}_2\text{O}_3$ film/ITO bioelectrodes have been characterized *via* SEM, CV and EIS studies and the enzyme activity measurements for the fabricated bioelectrodes have been carried out using CV and EIS techniques.

(d) Characterization

TEM micrographs have been recorded using a high-resolution transmission electron microscope (HR-TEM, Tecnai-G2F30 STWIN). Samples for TEM are prepared on 200 mesh carbon coated copper grids. A drop of iron oxide NPs sol is carefully placed on the copper grid surface and is then dried under ambient conditions. The structure of the powder samples and nanostructured iron oxide films have been analyzed using X-ray powder diffraction (XRD, Cu-K α radiation, Rigaku) over the 2θ range from 25–70 $^\circ$ using a monochromatized X-ray beam with Cu-K α radiation ($\lambda = 1.54 \text{ \AA}$). XPS measurements have been carried out in a Perkin Elmer XPS chamber (PHI 1257) with a base pressure of 5×10^{-9} torr. The chamber is equipped with a dual anode Mg-K α (energy 1253.6 eV) and Al-K α (energy 1486.6 eV) X-ray source and a high-resolution hemispherical energy analyzer for energy resolved electron detection. An Mg-K α X-ray source has been used for this study. The samples are

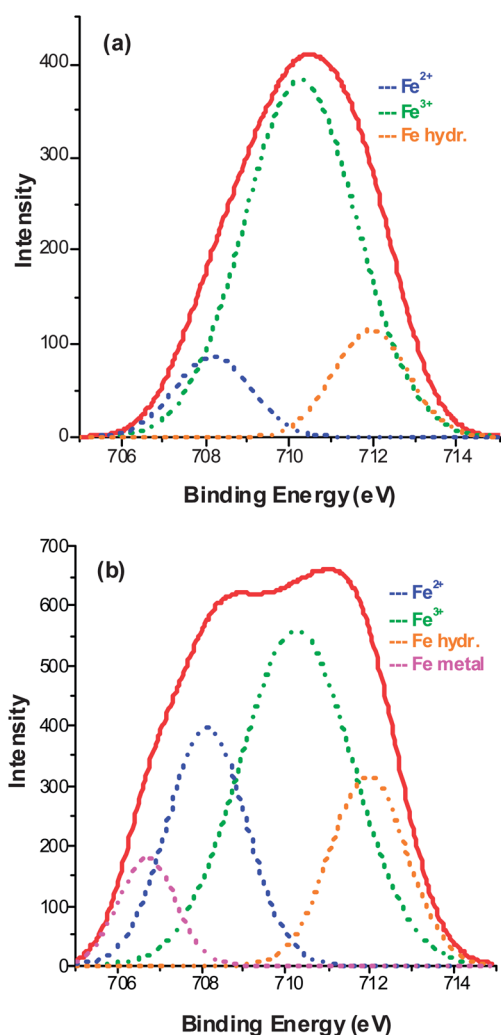


Fig. 4 Deconvoluted XPS spectra of Fe 2p_{3/2} acquired for: (a) α -Fe₂O₃ film, and (b) Fe₃O₄@C film.

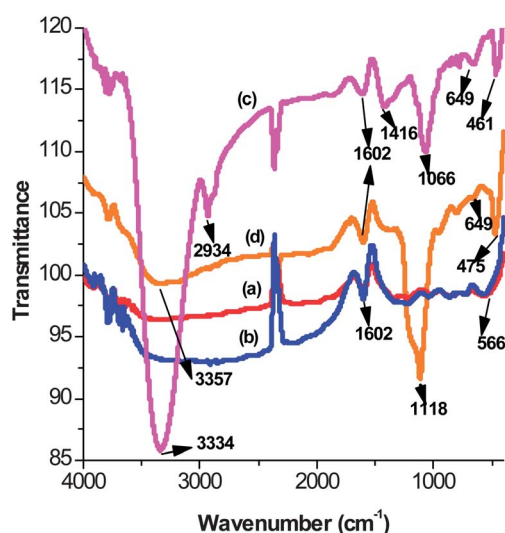


Fig. 5 FTIR spectra of: (a) α -Fe₂O₃ NPs film obtained from Fe₃O₄ NPs; (b) α -Fe₂O₃ NPs film obtained from Fe₃O₄ NPs (autoclaved); (c) film of Fe₃O₄@C NPs; (d) film of Fe₃O₄@SiO₂ NPs.

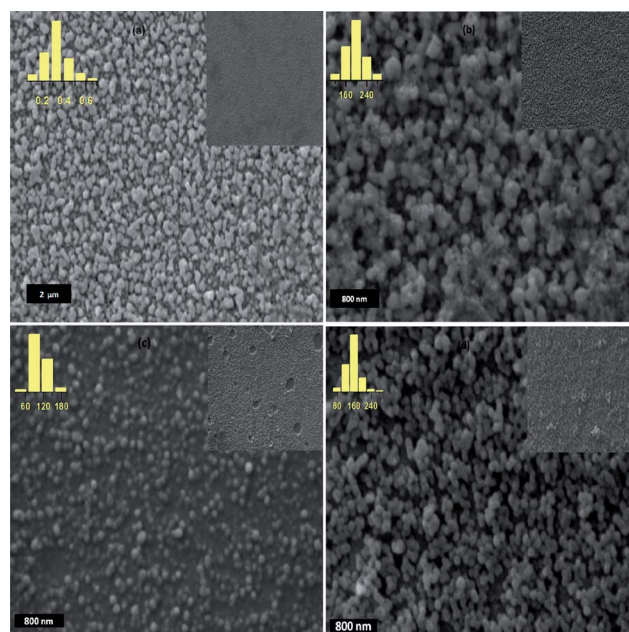


Fig. 6 SEM micrograph of: (a) α -Fe₂O₃ NPs film obtained from Fe₃O₄ NPs; (b) α -Fe₂O₃ NPs film obtained from Fe₃O₄ NPs (autoclaved); (c) film of Fe₃O₄@C NPs; (d) film of Fe₃O₄@SiO₂ NPs.

sputtered with 4 keV argon ions to remove surface contamination prior to XPS studies. The absorption studies of the bare and encapsulated NPs have been conducted on a Phoenix-2200 DPCV UV-Vis spectrophotometer in the wavelength range 200–900 nm. The transmission studies of the nanostructured iron oxide films in the infrared region have been carried out on a Perkin Elmer, Spectrum BX II spectrophotometer in the wavenumber range of 400–4000 cm⁻¹. The morphological changes of the nanocrystalline films upon enzyme immobilization have been studied using SEM (LEO 440 scanning electron microscope).

The electrochemical experiments have been conducted on an Autolab PGSTAT 302N System (Ecochemie, The Netherlands) in a three electrode system. All electrochemical experiments have been carried out in a cell containing 15 mL of 100 mM phosphate buffer solution (PBS) containing 0.9% NaCl and 5 mM K₃/K₄[Fe(CN)₆] as a redox probe and using a platinum wire as auxiliary, a Ag/AgCl wire as reference, and the nanostructured iron oxide films on ITO as the working electrode.

Results and discussion

(a) TEM studies of iron oxide NPs

Fig. 1(a) shows a TEM micrograph of the Fe₃O₄ NPs, indicating formation of nearly monodispersed nanocrystals with an average diameter of 10 nm. The lattice spacing of ~ 2.56 Å obtained from the fringe pattern (Inset Fig. 1(a)), matches with the *d*-value (2.56 Å), corresponding to the (311) *hkl* plane of the Fe₃O₄ nanocrystals (JCPDS file: 890951). However, after hydrothermal treatment, the average size of the NPs increases by about two nm (Fig. 1(b)). The increase in the average particle size of autoclaved NPs and the decrease in the number of

Table 1 Optical density of Gram positive (*Providencia* sp.) and Gram negative (*Bacillus* sp.) bacteria as a function of time in the presence of $\text{Fe}_3\text{O}_4\text{@C}$ and $\alpha\text{-Fe}_2\text{O}_3$ films

Nanostructured film	Bacteria	Optical density						
		0 h	2 h	4 h	6 h	8 h	10 h	12 h
$\text{Fe}_3\text{O}_4\text{@C}$ film	<i>Providencia</i> sp.	0.01	0.03	0.07	0.15	0.28	0.43	0.56
$\text{Fe}_3\text{O}_4\text{@C}$ film	<i>Bacillus</i> sp.	0.02	0.09	0.24	0.57	0.68	0.73	0.89
$\alpha\text{-Fe}_2\text{O}_3$ film	<i>Providencia</i> sp.	0.03	0.06	0.09	0.14	0.19	0.54	0.63
$\alpha\text{-Fe}_2\text{O}_3$ film	<i>Bacillus</i> sp.	0.02	0.08	0.26	0.58	0.65	0.82	0.85

smaller NPs indicates the growth of NPs at the expense of smaller NPs, suggesting Ostwald ripening³⁸ of NPs. Also, the edges and roughness observed on the NPs' surfaces are reduced upon hydrothermal treatment, and the NPs assume a spherical shape. Thus, the size and smoothness of the NPs can be tailored using hydrothermal treatment.

Upon capping the Fe_3O_4 NPs with carbon and silica, the average particle size of the Fe_3O_4 NPs increased to 14 nm and 20 nm (Fig. 1(c) and (d)) suggesting the formation of a carbon and silica shell, respectively, over the Fe_3O_4 NPs. Due to the formation of the thick shell of silica, the Fe_3O_4 NPs are well separated and uniform (inset Fig. 1(d)) while some agglomeration has been observed in the case of the $\text{Fe}_3\text{O}_4\text{@C}$ NPs (inset Fig. 1(c)).

(b) UV-visible studies of Fe_3O_4 , Fe_3O_4 (autoclaved), $\text{Fe}_3\text{O}_4\text{@C}$ and $\text{Fe}_3\text{O}_4\text{@SiO}_2$ NPs

Fig. 2 shows absorption spectra of the Fe_3O_4 NPs, Fe_3O_4 NPs (autoclaved), Fe_3O_4 NPs capped with carbon and Fe_3O_4 NPs capped with silica in the UV-Vis wavelength range. The absorption onset of the Fe_3O_4 NPs is at ~ 600 nm (Fig. 2(a)). Because of the quantum size effect, this onset value is blue-shifted by 100 nm as compared to that of the bulk Fe_3O_4 .³⁹ The band near 300 nm corresponds to ligand field transitions of Fe^{3+} and the shoulder peak around 480 nm corresponds to excitation of the Fe-Fe pair.⁴⁰ A similar spectrum is observed for the autoclaved Fe_3O_4 NPs (Fig. 2(b)). The higher absorption for the autoclaved NPs for the same concentration may be due to an increase in particle size of the NPs upon hydrothermal treatment.

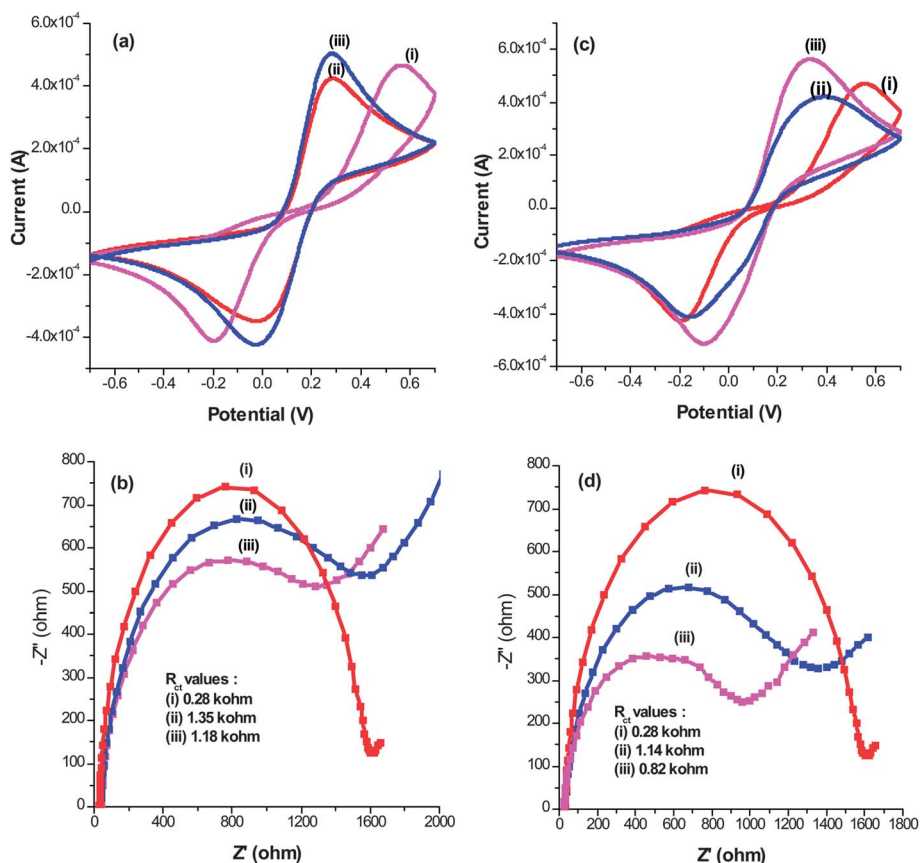


Fig. 7 (a) CV curves for the ITO electrode (i), $\text{Fe}_3\text{O}_4\text{@C}$ film/ITO electrode (ii), and $\text{ChOx}/\text{Fe}_3\text{O}_4\text{@C}$ film/ITO bioelectrode (iii); (b) Nyquist plots for the ITO electrode (i), $\text{Fe}_3\text{O}_4\text{@C}$ film/ITO electrode (ii), and $\text{ChOx}/\text{Fe}_3\text{O}_4\text{@C}$ film/ITO bioelectrode (iii); (c) CV curves for the ITO electrode (i), $\alpha\text{-Fe}_2\text{O}_3$ film/ITO electrode (ii), and $\text{ChOx}/\alpha\text{-Fe}_2\text{O}_3$ film/ITO bioelectrode (iii); (d) Nyquist plots for the ITO electrode (i), $\alpha\text{-Fe}_2\text{O}_3$ film/ITO electrode (ii), and $\text{ChOx}/\alpha\text{-Fe}_2\text{O}_3$ film/ITO bioelectrode (iii).

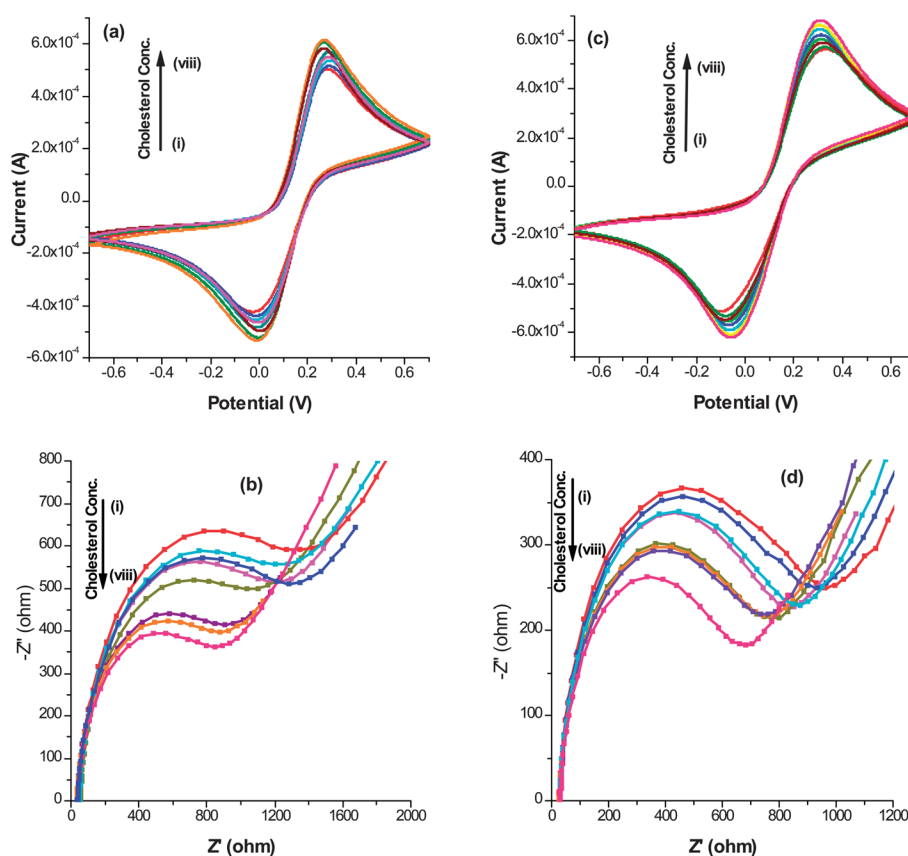


Fig. 8 (a) CV response studies of ChOx/Fe₃O₄@C film/ITO bioelectrode; (b) EIS response studies of ChOx/Fe₃O₄@C film/ITO bioelectrode; (c) CV response studies of ChOx/α-Fe₂O₃ film/ITO bioelectrode and (d) EIS response studies of ChOx/α-Fe₂O₃ film/ITO bioelectrode with different cholesterol concentrations (mg dl⁻¹): (i) 10; (ii) 25; (iii) 50; (iv) 100; (v) 200; (vi) 300; (vii) 400 and (viii) 500.

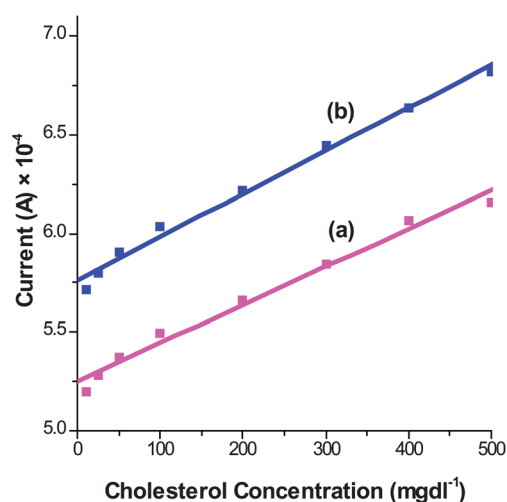


Fig. 9 Linear calibration plots obtained using CV data for: (a) ChOx/Fe₃O₄@C film/ITO bioelectrode and (b) ChOx/α-Fe₂O₃ film/ITO bioelectrode.

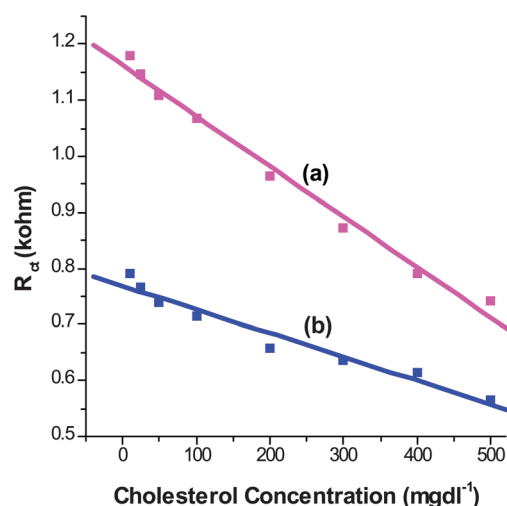


Fig. 10 Linear calibration plots obtained using EIS data for: (a) ChOx/Fe₃O₄@C film/ITO bioelectrode and (b) ChOx/α-Fe₂O₃ film/ITO bioelectrode.

Upon encapsulation of the Fe₃O₄ NPs with carbon and silica shells, the scattering from the NPs increases due to an increase in particle size.⁴¹ Importantly, this increase in scattering is specific to the wavelength range of 500–900 nm. On the contrary, the absorption at lower wavelengths is suppressed due

to capping of the Fe₃O₄ NPs. Such crossover in absorption spectra for the same concentration suggests surface modification of the Fe₃O₄ NPs. For the carbon capped Fe₃O₄ NPs, the characteristic spectrum from the Fe₃O₄ NPs is retained (Fig. 2(c)), but the partial suppression of the absorption

Table 2 Comparison table summarizing the characteristics of cholesterol biosensors based on nanostructured metal oxide films

Electrode	Transducer	Linear range (mg dL ⁻¹)	Sensitivity	K _m value	Response time (s)	Reproducibility	Shelf life (days)	Ref.
CeO ₂ /ITO	Cyclic voltammetry	10–400	—	2.08 mM	15	—	—	62
Chitosan–SnO ₂ /ITO	Cyclic voltammetry	5–400	34.7 μA mg ⁻¹ dl cm ⁻²	3.8 mM	5	—	80	63
ZnO/Au	Cyclic voltammetry	25–400	45.7 nA mg ⁻¹ dl cm ⁻²	2.1 mM	15	—	70	64
ZnO/ITO	Cyclic voltammetry	5–400	59.0 nA mg ⁻¹ dl cm ⁻²	0.03 mM	10	20	85	65
Fe ₃ O ₄ NPs	Spectroscopy	50–200	—	0.45 mM	—	—	10	66
Fe ₃ O ₄ @C/ITO	Cyclic voltammetry	25–400	193 nA mg ⁻¹ dL cm ⁻²	0.03 mM	60	25	70	Present work
	Impedance spectroscopy		0.90 Ω mg ⁻¹ dL cm ⁻²					
α-Fe ₂ O ₃ /ITO	Cyclic voltammetry	50–400	218 nA mg ⁻¹ dL cm ⁻²	0.04 mM	60	20	56	
	Impedance spectroscopy		0.42 Ω mg ⁻¹ dL cm ⁻²					

intensity suggests the capping of the Fe₃O₄ NPs with a thin layer of carbon. Upon capping the Fe₃O₄ NPs with silica, an absence of the characteristic absorption from Fe₃O₄ NPs (200–450 nm) can be seen^{42,43} (Fig. 2(d)). This suggests complete coverage of the Fe₃O₄ NPs with a thick shell of silica, which increases the overall scattering from the NPs, while on the contrary, it completely suppresses the absorption from the Fe₃O₄ NPs.

(c) X-Ray diffraction studies of Fe₃O₄ NPs and nanostructured iron oxide films

Fig. 3(a) shows an XRD pattern of the bare Fe₃O₄ NPs. The diffraction peaks obtained correspond to the cubic spinel structure of Fe₃O₄.^{44,45} The average particle diameter of 10.6 nm calculated using the Debye–Scherrer formula (from the most intense peak at $2\theta = 35.57^\circ$) is in agreement with the particle size determined by statistical analysis of the TEM images, indicating that each individual particle is a single crystal.⁴⁶

Fig. 3(b) and (c) show XRD spectra of the iron oxide films prepared from the Fe₃O₄ NPs and Fe₃O₄ NPs (autoclaved), respectively. The diffraction peaks of the films match α-Fe₂O₃ (JCPDS file: 890599-96). In spite of the Fe₃O₄ NPs being the starting material for the film deposition, the XRD spectra obtained from the deposited film corresponds to that of α-Fe₂O₃. This change of phase can be ascribed to the oxidation of NPs during electrophoretic deposition in the water–methanol mixture. The hydroxyl (OH) groups resulting from the dissociation of water and methanol molecules get adsorbed on the surface of magnetite NPs and catalyze their oxidation process.⁴⁷ In addition, the application of a potential above the oxidation potential of Fe²⁺ (*i.e.* 0.77 V) results in the modified nucleation rate (kinetics), enhanced diffusion of species and gradient of the lattice constant, which drives the nucleation of α-Fe₂O₃ NPs.^{47,48} Also, uncapped Fe₃O₄ NPs undergo rapid agglomeration during deposition, their large size favors the oxidation to hematite over magnetite.⁴⁹ To the best of our knowledge, a change in phase of Fe₃O₄ NPs obtained during electrophoretic deposition occurring in such a short span of time (30 s) has not been reported in the literature.

To control this oxidation step, the Fe₃O₄ NPs have been encapsulated with an organic carbon shell and an inorganic silica shell, as mentioned in the preceding section. Fig. 3(d) and (e) show XRD spectra of the films obtained from the Fe₃O₄@C

NPs and Fe₃O₄@SiO₂ NPs, respectively. The diffraction peaks obtained from the films of the encapsulated NPs match those of Fe₃O₄ (with a slight shift), indicating that no oxidation occurs during the deposition of films upon capping the Fe₃O₄ NPs with organic and inorganic shells. After capping, the surface of the Fe₃O₄ NPs has been passivated, which circumvents the adsorption of hydroxyl groups onto their surface and thus prevents their phase change. Thus, an additional oxidation step during electrophoretic deposition of Fe₃O₄ NPs can be circumvented using surface passivation.

(d) X-Ray photoelectron studies of α-Fe₂O₃ and Fe₃O₄@C films

To further confirm the phase of the NPs before and after electrophoretic deposition, XPS core level spectra of α-Fe₂O₃ and Fe₃O₄@C films have been acquired for Fe 2p and the deconvoluted Fe 2p_{3/2} spectra are shown in Fig. 4. Background subtraction and peak fitting of the spectra have been done using the Shirley function and Gaussian function, respectively, and the spectra have been referenced to the C 1s main peak at 284.6 eV. A considerable difference can be seen in the two spectra for the α-Fe₂O₃ and Fe₃O₄@C films.

Fig. 4(a) shows the deconvoluted XPS Fe 2p_{3/2} spectra of the α-Fe₂O₃ film. The peak fitting of the spectra reveals that Fe²⁺ and Fe³⁺ ions are present in the ratio of 1 : 6.7. This shows that the film mostly contains Fe₂O₃ with traces of Fe₃O₄, which suggests the *in situ* oxidation of uncapped Fe₃O₄ NPs during electrophoretic deposition. However, the deconvolution and peak fitting of the Fe 2p_{3/2} spectra obtained for the Fe₃O₄@C film reveals that the ratio of Fe²⁺ and Fe³⁺ ions is 1 : 2 (Fig. 4(b)). This shows that the Fe₃O₄ NPs retain their phase upon encapsulation with carbon and the film consists of Fe₃O₄ NPs. Thus, surface passivation restricts the *in situ* oxidation of Fe₃O₄ NPs during electrophoretic deposition. The presence of metal Fe has also been noticed in Fe₃O₄@C film, while hydrated Fe is present in both the films, as expected.^{50,51}

(e) FTIR studies of nanostructured iron oxide films

Fig. 5 shows the transmittance spectra of the nanostructured iron oxide films. In the case of the α-Fe₂O₃ NPs film (Fig. 5(a) and (b)) (obtained from Fe₃O₄ NPs and Fe₃O₄ NPs (autoclaved),

respectively), the peak seen at 566 cm^{-1} corresponds to the vibrations of Fe–O.¹⁹ However, upon capping of the Fe_3O_4 NPs with carbon and silica, the Fe–O vibration peak at 566 cm^{-1} disappears and two additional peaks at 649 cm^{-1} and 465 cm^{-1} (Fig. 5(c) and (d)) have been obtained.

In the case of the carbon capped Fe_3O_4 NPs (Fig. 5(c)), the peak at 2934 cm^{-1} refers to the C–H stretching vibrations, the peak at 1416 cm^{-1} refers to the C–H bending vibrations and the peak at 1066 cm^{-1} refers to the C–O stretching vibrations. All these peaks indicate the presence of aliquots of fructose, since fructose molecules present in the hydrated state are unlikely to decompose completely,^{52–54} but as a convention adopted by previous reports, we label these nanoparticles as carbon capped Fe_3O_4 NPs.^{23,29}

In the case of silica capped Fe_3O_4 NPs (Fig. 5(d)), a sharp peak at 1118 cm^{-1} corresponds to characteristic Si–O vibrations, revealing the capping of the Fe_3O_4 NPs with silica.^{55,56} The broad band found at $3300\text{--}3400\text{ cm}^{-1}$ and the peak at 1602 cm^{-1} present in all the films correspond to the O–H stretching mode and the H–O–H bending mode, respectively, indicating the presence of interstitial water molecules in the films.⁴⁴

(f) Morphological studies of nanostructured iron oxide films and bioelectrodes

Fig. 6 shows the SEM micrographs of the nanostructured iron oxide films. It can be seen that the $\alpha\text{-Fe}_2\text{O}_3$ films obtained from Fe_3O_4 NPs and Fe_3O_4 NPs (autoclaved) have an average particle size of 300 nm and 200 nm, respectively (Fig. 6(a) and (b)). The observed increase in particle size and deformation in shape indicate agglomeration of the uncapped NPs upon deposition. The agglomeration is more prominent for the as-prepared Fe_3O_4 NPs owing to their surface roughness. The electrical double layer gradient is maximum at the edges of the NPs, which results in the electrostatic attraction of the NPs and the growth in their size.⁵⁷ However, due to the removal of edges and surface smoothing of the NPs upon hydrothermal treatment, the autoclaved NPs undergo reduced agglomeration.

Upon capping of the Fe_3O_4 NPs with carbon and silica, the agglomeration has been further restricted. A radical decrease of the average particle size to 100 nm (Fig. 6(c)) and 160 nm (Fig. 6(d)) is observed in the case of the carbon capped NPs and silica capped NPs, respectively. Also, the capped NPs retain their initial spherical shape upon deposition, as compared to the film of uncapped NPs. The reduction in size and retention of spherical shape indicate a considerable decrease in the agglomeration of NPs upon capping. Further, the immobilization of cholesterol oxidase onto the nanostructured iron oxide films has been confirmed using SEM (Fig. S1, ESI†). The change in morphology from a dense uniform distribution of NPs in the nanoscale to the globular structure of ChOx at the micron scale is attributed to the physical adsorption of ChOx molecules onto nanostructured iron oxide films.⁵⁸

(g) Biocompatibility of $\text{Fe}_3\text{O}_4\text{@C}$ and $\alpha\text{-Fe}_2\text{O}_3$ films

The biocompatibility of the $\text{Fe}_3\text{O}_4\text{@C}$ and $\alpha\text{-Fe}_2\text{O}_3$ films has been investigated using bacterial systems *i.e.* Gram positive

(*Bacillus* sp.) and Gram negative (*Providencia* sp.) bacteria. Two methods have been utilized to examine the biocompatibility of nanostructured iron oxide films. Firstly, cultures of Gram positive and Gram negative bacteria are spread on nutrient agar plates and $\text{Fe}_3\text{O}_4\text{@C}$ and $\alpha\text{-Fe}_2\text{O}_3$ films are kept on these plates under optimum growth conditions (28°C and 150 rpm). No zone of inhibition is observed for the nanostructured iron oxide films. Secondly, side arm flasks are prepared with nutrient broth and both the bacteria are inoculated. Films are kept in the nutrient broth and grown under optimum conditions (28°C and 150 rpm). Colorimetric readings recorded at intervals of 2 h are summarized in Table 1, which clearly indicates the biocompatibility of the $\text{Fe}_3\text{O}_4\text{@C}$ and $\alpha\text{-Fe}_2\text{O}_3$ films as the optical density of Gram positive and Gram negative bacteria increases with time in the presence of nanostructured iron oxide films.

(h) Electrochemical characterization of ChOx immobilized iron oxide electrodes

(i) $\text{ChOx/Fe}_3\text{O}_4\text{@C}$ FILM/ITO BIOELECTRODE. Fig. 7(a) shows the cyclic voltammograms of the ITO electrode, $\text{Fe}_3\text{O}_4\text{@C}$ film/ITO electrode and $\text{ChOx/Fe}_3\text{O}_4\text{@C}$ film/ITO bioelectrode in the potential range of -0.7 V to $+0.7\text{ V}$ at a scan rate of 30 mV s^{-1} . The decrease in anodic peak current obtained for the $\text{Fe}_3\text{O}_4\text{@C}$ film/ITO electrode (Fig. 7(a), (ii)) compared to that of the ITO electrode (Fig. 7(a), (i)) reveals the formation of a layer of $\text{Fe}_3\text{O}_4\text{@C}$ NPs on the ITO surface. Furthermore, the increase in oxidation current obtained for the $\text{ChOx/Fe}_3\text{O}_4\text{@C}$ film/ITO bioelectrode (Fig. 7(a), (iii)) compared to that of the $\text{Fe}_3\text{O}_4\text{@C}$ film/ITO electrode (Fig. 7(a), (ii)) is attributed to electron transfer facilitated by redox moieties at the active sites (FAD centres) of the enzyme at the electrode surface.

Fig. 7(b) shows the Nyquist plots obtained for the ITO electrode, $\text{Fe}_3\text{O}_4\text{@C}$ film/ITO electrode and $\text{ChOx/Fe}_3\text{O}_4\text{@C}$ film/ITO bioelectrode. The increased R_{ct} value of $1.35\text{ k}\Omega$ for the $\text{Fe}_3\text{O}_4\text{@C}$ film/ITO electrode (Fig. 7(b), (ii)) compared to the R_{ct} value of $0.28\text{ k}\Omega$ for the ITO electrode (Fig. 7(b), (i)) indicates formation of a $\text{Fe}_3\text{O}_4\text{@C}$ NPs layer on the ITO surface. The presence of the $\text{Fe}_3\text{O}_4\text{@C}$ NPs layer impedes the flow of electrons, resulting in an increased value of R_{ct} . Furthermore, a decrease in R_{ct} value from $1.35\text{ k}\Omega$ for the $\text{Fe}_3\text{O}_4\text{@C}$ film/ITO electrode to $1.18\text{ k}\Omega$ for the $\text{ChOx/Fe}_3\text{O}_4\text{@C}$ film/ITO bioelectrode (Fig. 7(b), (iii)) reveals the ChOx immobilization onto the $\text{Fe}_3\text{O}_4\text{@C}$ film/ITO electrode. This decrease in R_{ct} value is ascribed to the facile electron transfer aided by the redox moieties of the enzyme at the electrode surface.

According to Laviron's theory, the slope of the linear curve between the anodic peak potential and the logarithm of scan rate represents $RT/\alpha nF$ (α : transfer coefficient). This can be used to calculate the surface concentration of the ionic species of the bioelectrodes using the following equation:

$$i_p = n^2 F^2 \nu C A (4RT)^{-1} \quad (1)$$

where, i_p/ν can be calculated from the i_p vs. ν plot⁵⁸ (i_p : anodic peak current; ν : scan rate).

The slope of the linear plot of anodic peak potential vs. logarithm of scan rate for the $\text{ChOx/Fe}_3\text{O}_4\text{@C}$ film/ITO

bioelectrode gives $RT/\alpha nF = 0.23$. Using eqn (1), the surface concentration on the ChOx/Fe₃O₄@C film/ITO bioelectrode has been found to be $2.52 \times 10^{-11} \text{ mol cm}^{-2}$.

(ii) CHOX/ α -Fe₂O₃ FILM/ITO BIOELECTRODE. Fig. 7(c) shows the cyclic voltammograms obtained for the ITO electrode, α -Fe₂O₃ film/ITO electrode and ChOx/ α -Fe₂O₃ film/ITO bioelectrode in the potential range of -0.7 V to $+0.7 \text{ V}$ at a scan rate of 30 mV s^{-1} . The oxidation peak seen at 0.38 V is attributed to the oxidation of the redox couple $\text{K}_3/\text{K}_4[\text{Fe}(\text{CN})_6]$, present in the buffer.⁵⁸ The decrease in the oxidation current obtained for the α -Fe₂O₃ film/ITO electrode (Fig. 7(c), (ii)) compared to that of the ITO electrode (Fig. 7(c), (i)) indicates formation of a layer of α -Fe₂O₃ NPs on the ITO surface. Furthermore, the increase in oxidation current obtained for the ChOx/ α -Fe₂O₃ film/ITO bioelectrode (Fig. 7(c), (iii)) compared to that of the α -Fe₂O₃ film/ITO electrode (Fig. 7(c), (ii)) is attributed to the presence of redox moieties at active sites (FAD centres) of the enzyme, leading to fast electron transfer between the enzyme and the electrode surface.³⁷

Fig. 7(d) shows the Nyquist plots obtained for the ITO electrode, α -Fe₂O₃ film/ITO electrode and ChOx/ α -Fe₂O₃ film/ITO bioelectrode. The increased R_{ct} (charge transfer resistance) value of $1.14 \text{ k}\Omega$ obtained for the α -Fe₂O₃ film/ITO electrode (Fig. 7(d), (ii)) compared to the R_{ct} value of $0.28 \text{ k}\Omega$ for the ITO electrode (Fig. 7(d), (i)) is attributed to the formation of a layer of α -Fe₂O₃ NPs on the ITO surface. Formation of an α -Fe₂O₃ NPs layer results in decreased interfacial electron transfer, thereby causing an increase in the R_{ct} value. Furthermore, the observed decrease in R_{ct} value from $1.14 \text{ k}\Omega$ for the α -Fe₂O₃ film/ITO electrode (Fig. 7(d), (ii)) to $0.82 \text{ k}\Omega$ for the ChOx/ α -Fe₂O₃ film/ITO bioelectrode (Fig. 7(d), (iii)) is attributed to facile electron transfer mediated by the redox centres of the enzyme.

The surface concentration of ionic species on the ChOx/ α -Fe₂O₃ film/ITO bioelectrode has been found to be $1.81 \times 10^{-11} \text{ mol cm}^{-2}$ (using $RT/\alpha nF = 0.16$). The higher concentration of ionic species on the ChOx/Fe₃O₄@C film/ITO bioelectrode compared to the ChOx/ α -Fe₂O₃ film/ITO bioelectrode is attributed to the larger surface area provided by the Fe₃O₄@C nanocrystalline film owing to the smaller particle size of the NPs as compared to the α -Fe₂O₃ nanocrystalline film for enzyme immobilization.

(i) Electrochemical response of ChOx immobilized iron oxide electrodes

(i) CHOX/Fe₃O₄@C FILM/ITO BIOELECTRODE. Fig. 8(a) shows the response of the ChOx/Fe₃O₄@C film/ITO bioelectrode obtained as a function of cholesterol concentration using cyclic voltammetry. The bioelectrode exhibits a response time of 60 s (Fig. S4(a)†). The anodic peak current of the ChOx/Fe₃O₄@C film/ITO bioelectrode plotted as a function of cholesterol concentration (Fig. 9(a)) reveals the linearity range as $25\text{--}500 \text{ mg dl}^{-1}$ with a standard deviation and correlation coefficient of $4.82 \mu\text{A}$ and 0.99 , respectively. The sensitivity of the ChOx/Fe₃O₄@C film/ITO bioelectrode exhibited by the slope of the linear regression curve is $193 \text{ nA mg}^{-1} \text{ dl cm}^{-2}$. The value of the

Michaelis–Menten constant of the ChOx immobilized Fe₃O₄@C film has been found to be 1.44 mg dl^{-1} .

The Nyquist plots for the ChOx/Fe₃O₄@C film/ITO bioelectrode as a function of cholesterol concentration have been investigated to obtain the impedimetric response of the biosensor (Fig. 8(b)). The linear calibration curve obtained by plotting the R_{ct} value for the ChOx/Fe₃O₄@C film/ITO bioelectrode as a function of cholesterol concentration (Fig. 10(a)) reveals a linearity range of $25\text{--}500 \text{ mg dl}^{-1}$ with standard deviation and regression coefficient of $0.02 \text{ k}\Omega$ and 0.99 , respectively. The sensitivity of $0.90 \Omega \text{ mg}^{-1} \text{ dl cm}^{-2}$ is obtained from the slope of the linear regression curve of the ChOx/Fe₃O₄@C film/ITO bioelectrode.

The shelf life and reproducibility of the ChOx/Fe₃O₄@C film/ITO bioelectrode have been investigated using cyclic voltammetry. The activity of the bioelectrode is monitored at regular intervals of seven days. The bioelectrode exhibits only 6% reduction in peak current after 10 weeks for 100 mg dl^{-1} cholesterol concentration when stored at 4°C (Fig. S2(a)†). The reproducibility of the sensing parameters of the bioelectrode has been studied with a cholesterol concentration of 25 mg dl^{-1} and it has been found that the bioelectrode can be used up to 25 times without significant decrease ($40 \mu\text{A}$) of the response signal (Fig. S3(a)†).

(ii) CHOX/ α -Fe₂O₃ FILM/ITO BIOELECTRODE. Fig. 8(c) shows the response of the ChOx/ α -Fe₂O₃ film/ITO bioelectrode obtained as a function of cholesterol concentration using the cyclic voltammetric technique. The response time of this electrode is found to be 60 s (Fig. S4(b)†). The magnitude of the amperometric current of the ChOx/ α -Fe₂O₃ film/ITO bioelectrode plotted as a function of cholesterol concentration (Fig. 9(b)) shows linearity in the range $25\text{--}500 \text{ mg dl}^{-1}$ with standard deviation and correlation coefficient of $4.52 \mu\text{A}$ and 0.99 , respectively. The sensitivity of the ChOx/ α -Fe₂O₃ film/ITO bioelectrode exhibited by the slope of linear calibration curve is found to be $218 \text{ nA mg}^{-1} \text{ dl cm}^{-2}$. The value of the Michaelis–Menten constant of the ChOx immobilized α -Fe₂O₃ film has been found to be 1.46 mg dl^{-1} .

The electrochemical impedimetric response of the ChOx/ α -Fe₂O₃ film/ITO bioelectrode has been investigated as a function of cholesterol concentration using Nyquist plots (Fig. 8(d)). The linear calibration curve obtained by plotting the R_{ct} values for the ChOx/ α -Fe₂O₃ film/ITO bioelectrode as a function of cholesterol concentration (Fig. 10(b)) reveals a linearity range of $50\text{--}500 \text{ mg dl}^{-1}$ with standard deviation and regression coefficient of $0.02 \text{ k}\Omega$ and 0.97 , respectively. The value of sensitivity exhibited by the slope of the linear regression curve for the ChOx/ α -Fe₂O₃ film/ITO bioelectrode is $0.42 \Omega \text{ mg}^{-1} \text{ dl cm}^{-2}$ (Table 2).

The shelf-life of the ChOx/ α -Fe₂O₃ film/ITO bioelectrode has been investigated for a 100 mg dl^{-1} cholesterol concentration using cyclic voltammetry. The bioelectrode exhibits a 6% decrease in the peak current for the first 8 weeks, but a sudden decrease in the signal has been observed afterwards and the current reduced by 11.5% after 10 weeks (Fig. S2(b)†). The ChOx/ α -Fe₂O₃ film/ITO bioelectrode can be used up to 20 times with insignificant loss ($66 \mu\text{A}$) of the signal (Fig. S3(b)†).

Conclusions

Nanocrystals of Fe_3O_4 with an average particle diameter of 10 nm have been synthesized. The electrophoretic deposition of bare Fe_3O_4 NPs in a methanol–water mixture results in oxidation and phase transformation of NPs and a film of $\alpha\text{-Fe}_2\text{O}_3$ NPs has been obtained. The phase transformation of the Fe_3O_4 NPs can be circumvented using surface passivation of Fe_3O_4 NPs with an organic carbon shell and an inorganic silica shell. Encapsulation of the Fe_3O_4 NPs restricts agglomeration of NPs during film deposition and retains a high surface to volume ratio for enzyme loading. Due to the non-conducting nature of silica, $\text{Fe}_3\text{O}_4@\text{SiO}_2$ NPs show poor electrochemical response. However, these can be utilized for applications in drug delivery,²¹ biocatalysis and bioseparation,^{20,59} magnetic resonance imaging,⁶⁰ determination of metal ion concentration,⁶¹ etc. Growth of Gram positive and Gram negative bacteria in contact with the $\text{Fe}_3\text{O}_4@\text{C}$ and $\alpha\text{-Fe}_2\text{O}_3$ films reveals the biocompatible nature of the nanostructures, which is suitable for prolonged activity of enzymes and thus, stability of biosensors. The fabricated cholesterol biosensors employing $\text{Fe}_3\text{O}_4@\text{C}$ and $\alpha\text{-Fe}_2\text{O}_3$ nanocrystalline films show sensitivities of $193 \text{ nA mg}^{-1} \text{ dl cm}^{-2}$ and $218 \text{ nA mg}^{-1} \text{ dl cm}^{-2}$, respectively, from cyclic voltammetric studies and sensitivities of $0.42 \Omega \text{ mg}^{-1} \text{ dl cm}^{-2}$ and $0.90 \Omega \text{ mg}^{-1} \text{ dl cm}^{-2}$, respectively, from electrochemical impedance spectroscopic studies. The low values of the Michaelis–Menten constant reveals the enhanced enzymatic activity of ChOx on nanostructured iron oxide films. The comparable sensitivities for biosensors obtained using $\text{Fe}_3\text{O}_4@\text{C}$ and $\alpha\text{-Fe}_2\text{O}_3$ NPs suggests that encapsulation of Fe_3O_4 NPs with carbon does not significantly affect the electrocatalytic activity of Fe_3O_4 NPs, while it adds to the stability of the NPs. However, the encapsulation of Fe_3O_4 NPs with conjugated carbon molecules, conducting polymers like polypyrrole, polyaniline, etc., may result in improved sensitivity of the biosensor.

Acknowledgements

We thank Prof. R. C. Budhani, Director, National Physical Laboratory, New Delhi, India for providing facilities. R. S. is thankful to the UGC-CSIR for the award of a Junior Research Fellowship. The authors thank Dr K. N. Sood, NPL for SEM measurements, Dr S. M. Shivprasad, JNCASR for XPS measurements and Dr Kavita Arora, JNU for TEM studies. Financial support received from the Department of Science and Technology (DST) centre on biomolecular electronics and CSIR Empower projects is sincerely acknowledged. Thanks are due to Dr Pratima Solanki, C. M. Pandey, Manoj Patel and all the members of the Biomedical Instrumentation Section, NPL, for discussions.

References

- S. Chou, *J. Appl. Phys.*, 1994, **76**, 6673.
- D. Schaadt, *J. Vac. Sci. Technol.*, A, 2000, **18**, 1834.
- K. Mosbach and L. Andersson, *Nature*, 1977, **270**, 259–261.
- D. K. Yi, S. S. Lee and J. Y. Ying, *Chem. Mater.*, 2006, **18**, 2459–2461.
- C. B. Catherine and S. G. C. Adam, *J. Phys. D: Appl. Phys.*, 2003, **36**, R198.
- E. Amstad, M. Textor and E. Reimhult, *Nanoscale*, 2011, **3**, 2819–2843.
- S. Laurent, D. Forge, M. Port, A. Roch, C. Robic, L. Vander Elst and R. N. Muller, *Chem. Rev.*, 2008, **108**, 2064–2110.
- T. Osaka, T. Matsunaga, T. Nakanishi, A. Arakaki, D. Niwa and H. Iida, *Anal. Bioanal. Chem.*, 2006, **384**, 593–600.
- R. Weissleder, H.-C. Cheng, A. Bogdanova and A. Bogdanov, *J. Magn. Reson. Imaging*, 1997, **7**, 258–263.
- F. Cengelli, D. Maysinger, F. Tschudi-Monnet, X. Montet, C. Corot, A. Petri-Fink, H. Hofmann and L. Juillerat-Jeanneret, *J. Pharmacol. Exp. Ther.*, 2006, **318**, 108–116.
- F. Sonvico, S. p. Mornet, S. b. Vasseur, C. Dubernet, D. Jaillard, J. Degrouard, J. Hoebeke, E. Duguet, P. Colombo and P. Couvreur, *Bioconjugate Chem.*, 2005, **16**, 1181–1188.
- M. Mahmoudi, A. Simchi, M. Imani and U. O. Halfeli, *J. Phys. Chem. C*, 2009, **113**, 8124–8131.
- A. Petri-Fink, M. Chastellain, L. Juillerat-Jeanneret, A. Ferrari and H. Hofmann, *Biomaterials*, 2005, **26**, 2685–2694.
- A. K. Gupta and S. Wells, *IEEE Trans. NanoBiosci.*, 2004, **3**, 66.
- J. Li, R. Yuan and Y. Chai, *Microchim. Acta*, 2011, **173**, 369–374.
- J. Wang, Z. Zhu, A. Munir and H. S. Zhou, *Talanta*, 2011, **84**, 783–788.
- H. Li, Q. Wei, J. He, T. Li, Y. Zhao, Y. Cai, B. Du, Z. Qian and M. Yang, *Biosens. Bioelectron.*, 2011, **26**, 3590–3595.
- I. M. Hsing, Y. Xu and W. Zhao, *Electroanalysis*, 2007, **19**, 755–768.
- G. Zhao, J. J. Feng, Q. L. Zhang, S. P. Li and H. Y. Chen, *Chem. Mater.*, 2005, **17**, 3154–3159.
- H.-H. Yang, S.-Q. Zhang, X.-L. Chen, Z.-X. Zhuang, J.-G. Xu and X.-R. Wang, *Anal. Chem.*, 2004, **76**, 1316–1321.
- K. Souza, J. Ardisson and E. Sousa, *J. Mater. Sci.: Mater. Med.*, 2009, **20**, 507–512.
- T. Sen, A. Sebastianelli and I. J. Bruce, *J. Am. Chem. Soc.*, 2006, **128**, 7130–7131.
- W. Xian-Wen, Z. Guo-Xing, X. Chuan-Jun and Y. Yin, *Nanotechnology*, 2006, **17**, 4307.
- I. Zhitomirsky, *J. Mater. Sci.*, 2006, **41**, 8186–8195.
- L. Besra and M. Liu, *Prog. Mater. Sci.*, 2007, **52**, 1–61.
- Y. S. Kang, S. Risbud, J. F. Rabolt and P. Stroeve, *Chem. Mater.*, 1996, **8**, 2209–2211.
- T. J. Daou, G. Pourroy, S. Begin-Colin, J. M. Greneche, C. Ulhaq-Bouillet, P. Legare, P. Bernhardt, C. Leuvrey and G. Rogez, *Chem. Mater.*, 2006, **18**, 4399–4404.
- Y. Li, T. Leng, H. Lin, C. Deng, X. Xu, N. Yao, P. Yang and X. Zhang, *J. Proteome Res.*, 2007, **6**, 4498–4510.
- X. Shouhu, H. Lingyun, J. Wanquan, G. Xinglong, H. Yuan and C. Zuyao, *Nanotechnology*, 2007, **18**, 035602.
- J. Li and C.-Y. Liu, *New J. Chem.*, 2009, **33**, 1474–1477.
- Y. Lu, Y. Yin, B. T. Mayers and Y. Xia, *Nano Lett.*, 2002, **2**, 183–186.

- 32 Z. X. Sun, F. W. Su, W. Forsling and P. O. Samskog, *J. Colloid Interface Sci.*, 1998, **197**, 151–159.
- 33 M. Jarlbring, L. Gunneriusson, B. Hussmann and W. Forsling, *J. Colloid Interface Sci.*, 2005, **285**, 212–217.
- 34 T. J. Daou, G. Pourroy, J. M. Greneche, A. Bertin, D. Felder-Flesch and S. Begin-Colin, *Dalton Trans.*, 2009, 4442–4449.
- 35 M. L. Fisher, M. Colic, M. P. Rao and F. F. Lange, *J. Am. Ceram. Soc.*, 2001, **84**, 713–718.
- 36 P. R. Solanki, S. K. Arya, S. P. Singh, M. K. Pandey and B. D. Malhotra, *Sens. Actuators, B*, 2007, **123**, 829–839.
- 37 Z. Matharu, G. Sumana, S. K. Arya, S. P. Singh, V. Gupta and B. D. Malhotra, *Langmuir*, 2007, **23**, 13188–13192.
- 38 L. Yonglan, *Mater. Lett.*, 2007, **61**, 1039–1041.
- 39 L. Huo, W. Li, L. Lu, H. Cui, S. Xi, J. Wang, B. Zhao, Y. Shen and Z. Lu, *Chem. Mater.*, 2000, **12**, 790–794.
- 40 T. D. Waite and D. M. Sherman, *Am. Mineral.*, 1985, **70**, 1262–1269.
- 41 T. A. Egerton and I. R. Tooley, *Int. J. Cosmet. Sci.*, 2012, **34**, 117–122.
- 42 S. L. Westcott, S. J. Oldenburg, T. R. Lee and N. J. Halas, *Langmuir*, 1998, **14**, 5396–5401.
- 43 Y. Kobayashi, V. Salgueirino-Maceira and L. M. Liz-Marzan, *Chem. Mater.*, 2001, **13**, 1630–1633.
- 44 K. Tao, H. Dou and K. Sun, *Chem. Mater.*, 2006, **18**, 5273–5278.
- 45 W. Cai and J. Wan, *J. Colloid Interface Sci.*, 2007, **305**, 366–370.
- 46 J. Sun, S. Zhou, P. Hou, Y. Yang, J. Weng, X. Li and M. Li, *J. Biomed. Mater. Res., Part A*, 2007, **80**, 333–341.
- 47 O. N. Shebanova and P. Lazor, *J. Raman Spectrosc.*, 2003, **34**, 845–852.
- 48 J. Tang, M. Myers, K. A. Bosnick and L. E. Brus, *J. Phys. Chem. B*, 2003, **107**, 7501–7506.
- 49 W. Feitknecht and K. J. Gallagher, *Nature*, 1970, **228**, 548–549.
- 50 J. Morales, L. Sanchez, F. Martin, F. Berry and X. L. Ren, *J. Electrochem. Soc.*, 2005, **152**, A1748–A1754.
- 51 P. Guardia, J. Perez-Juste, A. Labarta, X. Batlle and L. M. Liz-Marzan, *Chem. Commun.*, 2011, **46**, 6108–6110.
- 52 B. M. Kabyemela, T. Adschiri, R. M. Malaluan and K. Arai, *Ind. Eng. Chem. Res.*, 1999, **38**, 2888–2895.
- 53 Q. Wang, H. Li, L. Chen and X. Huang, *Carbon*, 2001, **39**, 2211–2214.
- 54 C. Adina, F. Florinela, T. Abdelmoumen and S. Carmen, *Rom. Biotechnol. Lett.*, 2010, **15**, 5738–5744.
- 55 A. Azione, A. Ben Slimane, L. Ait Hamou, A. Pleuvy, M. M. Chehimi, C. Perruchot and S. P. Armes, *Langmuir*, 2004, **20**, 3350–3356.
- 56 D. Kandpal, S. Kalele and S. Kulkarni, *Pramana*, 2007, **69**, 277–283.
- 57 P. Pramod, S. T. S. Joseph and K. G. Thomas, *J. Am. Chem. Soc.*, 2007, **129**, 6712–6713.
- 58 Z. Matharu, P. Pandey, M. K. Pandey, V. Gupta and B. D. Malhotra, *Electroanalysis*, 2009, **21**, 1587–1596.
- 59 T. Sen, A. Sebastianelli and I. J. Bruce, *J. Am. Chem. Soc.*, 2006, **128**, 7130–7131.
- 60 J. L. Campbell, J. Arora, S. F. Cowell, A. Garg, P. Eu, S. K. Bhargava and V. Bansal, *PLoS One*, 2011, **6**, e21857.
- 61 L. L. Vatta, J. Kramer and K. R. Koch, *Sep. Sci. Technol.*, 2007, **42**, 1985–2002.
- 62 A. A. Ansari, A. Kaushik, P. R. Solanki and B. D. Malhotra, *Electrochem. Commun.*, 2008, **10**, 1246–1249.
- 63 A. A. Ansari, A. Kaushik, P. R. Solanki and B. D. Malhotra, *Electroanalysis*, 2009, **21**, 965–972.
- 64 S. P. Singh, S. K. Arya, P. Pandey, B. D. Malhotra, S. Saha, K. Sreenivas and V. Gupta, *Appl. Phys. Lett.*, 2007, **91**, 063901–063903.
- 65 P. R. Solanki, A. Kaushik, A. A. Ansari and B. D. Malhotra, *Appl. Phys. Lett.*, 2009, **94**, 143901–143903.
- 66 G. Kouassi, J. Irudayaraj and G. McCarty, *J. Nanobiotechnol.*, 2005, **3**, 1.

Planning, Designing, Monitoring and Inspection of Wastewater Treatment Systems of Industries

Sameer Kumar* and Gaurav Singh**

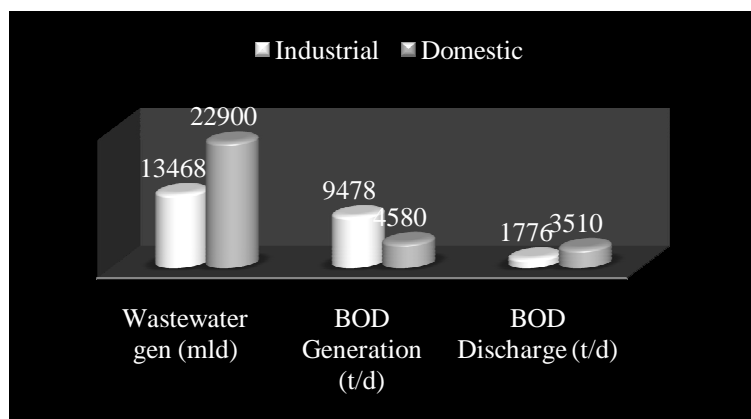
**Pursuing B-tech in Environmental Engineering from Delhi Technological University*

***Pursuing B-tech in Environmental Engineering from Delhi Technological University.*

Abstract

The fast growing economy, rapid industrialisation and growing urban population in India along with increasing wastewater generation are reasons for concern and reiterate the need for appropriate water management practices. So there are various methods for estimating the amount of wastewater generated through industries. Given below are the estimated of the percentages of water that get consumed in industries and domestic purposes. In this paper we have researched on the topic of various sub heading and we have come up on some statistical data. We have also consider various topics and researched on all of these topics which are Introduction with the wastewater treatment and management such as construction and industrial projects (textile, refinery, power plant etc)., Treatment technologies of wastewater including advanced treatment options, Decentralized methods in treating urban wastewater (existing and emerging), Affair and consult with Common Effluent Treatment Plants, State of art practices for wastewater management. This paper mainly depend on the various Industrial Exposure and research done by us.

Keywords: Author details; example; headings; layout; title page.



Comparison of pollution load generation from domestic and industrial sources

Mean Hydraulic retention time

$Q_s = \frac{V_t}{t}$ Where V_t = volume of reactor + volume of s.s. tank, V_r = volume of reactor (aeration tank), V_s = volume of s.s tank, Q = influent flow rate
Mean hydraulics retention time

—Mean Cell residence time

————— where Q_w = Cell wasting rate from reactor, Q_e = Flow rate from S.S, X_e = Cell concentration in S.S effluent

Water Demand in 2025 for Industrial purposes

Category	1990 (BCM)	2025(BCM)
Irrigation	460	688
Domestic	25	52
Industry+energy	34	80
Total	519	942

Water demand



1. Industries Treatment

Steel industries Contaminants include hydraulic oils, tallow and particulate solids. Final treatment of iron and steel products before onward sale into manufacturing includes pickling in strong mineral acid to remove rust and prepare the surface for tin or chromium plating or for other surface treatments such as galvanisation or painting. The two acids commonly used are hydrochloric acid and sulfuric acid. Wastewaters include acidic rinse waters together with waste acid. Although many plants operate acid recovery plants, (particularly those using Hydrochloric acid), where the mineral acid is boiled away from the iron salts, there remains a large volume of highly acid ferrous sulfate or ferrous chloride to be disposed of. Many steel industry wastewaters are contaminated by hydraulic oil also known as soluble oil.

Iron industries The iron production from its ores involves powerful reduction reactions in blast furnaces. Cooling waters are inevitably contaminated with products especially ammonia and cyanide. Production of coke from coal in coking plants also requires water cooling and the use of water in by-products separation.

Food industry Wastewater generated from agricultural and food operations has distinctive characteristics that set it apart from common municipal wastewater managed by public or private sewage treatment plants throughout the world: it is biodegradable and nontoxic, but that has high concentrations of biochemical oxygen demand (BOD) and suspended solids (SS).^[1] The constituents of food and agriculture wastewater are often complex to predict due to the differences in BOD and pH in effluents from vegetable, fruit, and meat products and due to the seasonal nature of food processing and postharvesting.

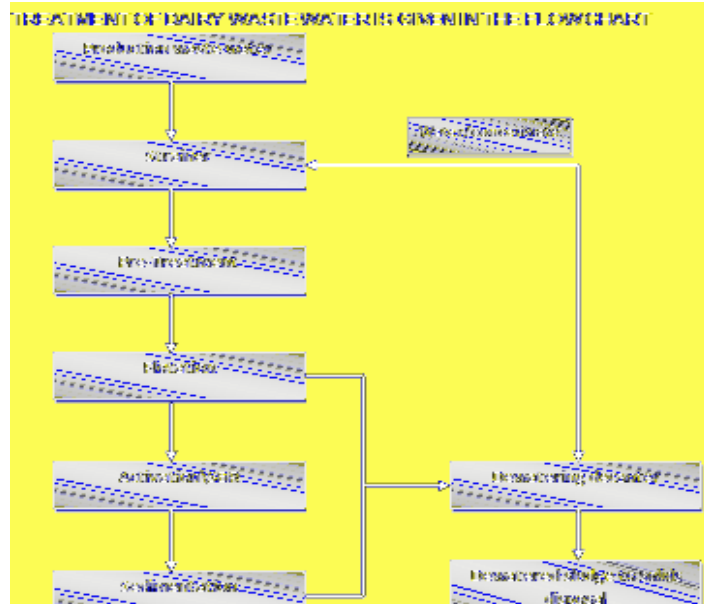
Thermal power plant Waste water from thermal power plants includes waste water from water purifiers, waste water from fuel oil pump rooms which is likely to contain oil, water from flue gas desulfurizing facility, domestic waste water from kitchen and sanitation. The major ingredients of such waste water range from acidic and alkaline substances to suspended solids, oil, and soluble iron. It is very rare that waste water contains harmful substances. In thermal power plants, waste water from all equipment is collected at one place and subjected to treatment by high-performance oil separator and coagulating sedimentation. Waste water treatment system in thermal power plants is thus integrated.

2. Introduction with the Wastewater Treatment and Management Such as Construction and Industrial Projects (Textile, Refinery, Power Plant etc).

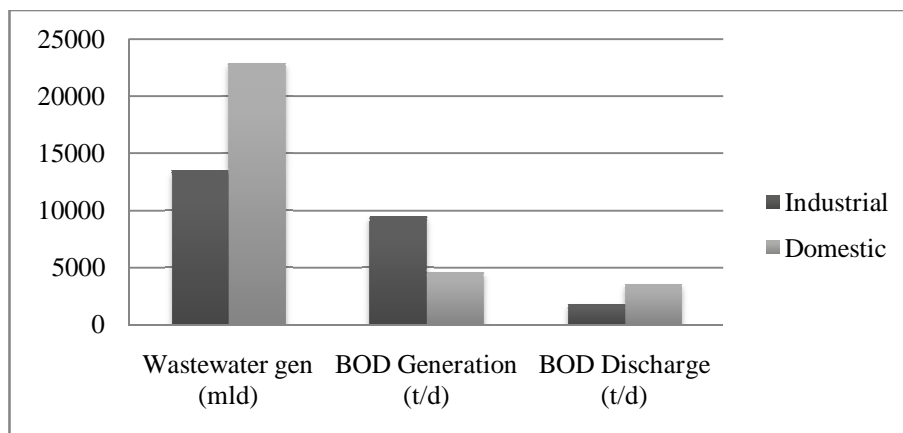
2.1 Treatment technologies of wastewater including advanced treatment options

1. Thermal powerplant

4. Diary Industry



ZERO discharge with case studies in wastewater




5. Affair and Consult with Common Effluent Treatment Plants

Small-scale industries (SSIs) have a very important role in overall industrial development in India and growth of SSI units has been actively promoted by Government of India to induce balanced economic growth and to distribute the benefits of industrial development in an equitable manner.

References

- [1] European Environment Agency. Copenhagen, Denmark. "Indicator: Biochemical oxygen demand in rivers (2001)."
- [2] Tannery Wastewater Treatment by the Oxygen Activated Sludge Process Mamoru Kashiwaya and Kameo Yoshimoto Journal (Water Pollution Control Federation), Vol. 52, No. 5 (May, 1980), pp. 999-1007 (article consists of 9 pages) Published by: Water Environment Federation
- [3] Tchobanoglous, G., Burton, F.L., and Stensel, H.D. (2003). *Wastewater Engineering (Treatment Disposal Reuse) / Metcalf & Eddy, Inc.* (4th ed.). McGraw-Hill Book Company. ISBN 0-07-041878-0.
- [4] Beychok, Milton R. (1967). *Aqueous Wastes from Petroleum and Petrochemical Plants* (1st ed.). John Wiley & Sons. LCCN 67019834.
- [5] Water and Wastewater News, May 2004 <<http://wwn-online.com/articles/50898/>>
- [6] American Petroleum Institute (API) (February 1990). *Management of Water Discharges: Design and Operations of Oil-Water Separators* (1st ed.). American Petroleum Institute.

AUTHOR QUERY FORM

 ELSEVIER	Journal: CERI Article Number: 7670	Please e-mail or fax your responses and any corrections to: E-mail: corrections.eseo@elsevier.micipd.com Fax: +44 1392 285878
---	---	--

Dear Author,

Please check your proof carefully and mark all corrections at the appropriate place in the proof (e.g., by using on-screen annotation in the PDF file) or compile them in a separate list. Note: if you opt to annotate the file with software other than Adobe Reader then please also highlight the appropriate place in the PDF file. To ensure fast publication of your paper please return your corrections within 48 hours.

For correction or revision of any artwork, please consult <http://www.elsevier.com/artworkinstructions>.

Any queries or remarks that have arisen during the processing of your manuscript are listed below and highlighted by flags in the proof. Click on the [Q](#) link to go to the location in the proof.

Location in article	Query / Remark: click on the Q link to go Please insert your reply or correction at the corresponding line in the proof
Q1	Please confirm that given names and surnames have been identified correctly and are presented in the desired order.
Q2	Corresponding author has not been indicated in the author group. Kindly provide the corresponding author's footnote.
Q3	Please check the keywords that have been added here from the transmittal form and correct if necessary.
Q4	Please check the edits made in the display equation given below and correct if necessary.
Q5	Please check the edits made in the sentence "The radiative parameters thus..." and correct if necessary.
Q6	Please provide a definition for the significance of asterisk in Table 4.
Q7	A corresponding author footnote is to be provided for atleast one author, please indicate the corresponding author.

Thank you for your assistance.

Please check this box or indicate your approval
if you have no corrections to make to the PDF file



ScienceDirect

Ceramics International ■ (■■■■) ■■■–■■■

CERAMICS
INTERNATIONALwww.elsevier.com/locate/ceramint

Pr³⁺ doped lead tungsten tellurite glasses for visible red lasers ☆

M. Venkateswarlu^a, M.V.V.K.S. Prasad^a, K. Swapna^a, Sk. Mahamuda^a,
A. Srinivasa Rao^{a,b}, A. Mohan Babu^c, D. Haranath^d

^aDepartment of Physics, KL University, Green Fields, Vaddeswaram 522502, AP, India

^bDepartment of Applied Physics, Delhi Technological University, New Delhi 110042, India

^cDepartment of Physics, Krishna Teja Technical Campus, Tirupati 517502, India

^dCSIR – National Physical Laboratory, Dr. K.S. Krishnan Road, New Delhi 110012, India

Received 6 September 2013; received in revised form 31 October 2013; accepted 15 November 2013

Abstract

Lead tungsten tellurite (LTT) glasses doped with Pr³⁺ (0.01, 0.1, 0.5, 1.0 and 1.5 mol%) ions were prepared by the conventional melt quenching technique. The glasses were characterized by X-ray diffraction, optical absorption and photoluminescence spectra. The glassy nature of LTT host glass has been confirmed through XRD measurements. From the measured intensities of various absorption bands of these glasses, the three phenomenological Judd–Ofelt (J–O) intensity parameters (Ω_2 , Ω_4 and Ω_6) have been evaluated by using the standard as well as modified J–O theory. The J–O parameters measured from the modified J–O theory were used to characterize the absorption and luminescence spectra of these glasses. From this theory, various radiative properties like radiative transition probability (A_R), total transition probability (A_T), branching ratio (β_R) and radiative lifetime (τ_R) have been evaluated for the fluorescent levels of Pr³⁺ in these glasses. The emission spectra show five emission bands in visible region for which the effective band widths ($\Delta\lambda_p$) and emission cross-sections (σ_{se}) have been evaluated. Among all the five emission transitions, a transition $^3P_0 \rightarrow ^3F_2$ is more intense and falls in red region. The visible emission spectra, stimulated emission cross-sections and branching ratios observed for all these glasses suggest the feasibility of using these glasses as lasers in red region. The CIE chromaticity co-ordinates were also evaluated from the emission spectra to understand the suitability of these materials for red emission. From the absorption, emission and CIE chromaticity measurements, it was found that 1 mol% of Pr³⁺ ion concentration is quite suitable for LTT glasses to develop bright red lasers from these glasses.

© 2013 The Authors. Published by Elsevier Ltd. All rights reserved.

Keywords: Glasses; Optical absorption; JO parameters; Photoluminescence

1. Introduction

In recent years rare-earth doped glasses have fascinated several researchers because of their potential applications in the development of several optical devices like optical amplifiers, solid state lasers, laser wave guides, light converters, sensors, three dimensional displays, color display devices, biomedical diagnostics and up conversion lasers [1–9]. The spectral characteristics of rare-earth ions are reliant on host glass composition, concentration of dopant ion and ambient temperatures [10]. Heavy metal oxide glasses are suitable candidates for

the development of non-linear optical devices, electro-optic modulators, electro-optic switches, solid state laser materials and IR technologies because of their high density, refractive index and low phonon energy [11–14]. Tellurium oxide being a conditional glass former can form a stable glass in presence of certain glass modifiers like tungsten trioxide (WO₃). Tellurium based glasses can be prepared at relatively low temperatures with phonon energies as low as $\sim 800 \text{ cm}^{-1}$ in comparison to phosphate, borate and silicate glasses. Glasses with low phonon energies offer less non-radiative relaxation rates and high fluorescence quantum efficiencies. Tellurium based glasses have slow crystallization rate, owing to good transparency in a wide spectral region from visible to NIR region. Relatively good mechanical strength, chemical stability and high refractive indices make them as the best host materials for obtaining efficient luminescence from trivalent rare-earth ions [15,16].

^{*}This is an open-access article distributed under the terms of the Creative Commons Attribution-NonCommercial-No Derivative Works License, which permits non-commercial use, distribution, and reproduction in any medium, provided the original author and source are credited.

Tungsten trioxide (WO_3) besides being a transition-metal oxide, is a very good **semi-conducting** oxide that has attracted attention for several years. It is the most investigated and used material for electro-chromic and **photochromic** devices in which coloration and bleaching can be reversibly obtained by an electro-chemical process [17] and has wide applications in smart windows, display devices and sensors. The TeO_2 – WO_3 glasses have low transition temperature, low crystallization ability, chemically inactive, high refractive index and also are transparent in the visible and near infrared region [18,19]. Addition of fluoride compounds to tellurite based glasses can reduce phonon energies, since the maximum phonon energies of the additives are 340 cm^{-1} , which are less than the phonon energies of tellurite based glasses $\sim 800\text{ cm}^{-1}$. Addition of fluoride compounds can help to remove OH group from glasses by reacting with OH group to form HF group [20,21]. This reduces the phonon energies of glasses to relatively lower values (200 – 400 cm^{-1}). Hence addition of PbF_2 to a tellurite based glass can decrease the phonon energy and thereby reduces the non-radiative decay process.

Pr^{3+} doped glasses with low phonon energy are used very much for compact solid state lasers emitting in visible region. Pr^{3+} ions in glasses have relatively good number of absorption bands in the **vis–NIR** regions due to which **they have** various technological applications as functional photonic materials like optical **fiber** amplifiers, lasers and wavelength converting devices. Pr^{3+} is a significant optical activator with its several meta-stable states that **offer** stimulated emissions in blue, green, orange, red and infrared regions [22]. In the present work, lead tungsten tellurite (LTT) glasses were prepared by varying Pr^{3+} concentration to study the optical and luminescent properties to identify the better glass for visible solid state laser devices.

2. Experimental

2.1. Glass preparation

Lead tungsten tellurite glasses doped with different concentrations of Pr^{3+} ions were prepared by the melt quenching technique. All **chemicals** used to prepare the LTT glasses were analar grade with 99.9% purity. The glass composition of LTT glasses and their **labeling** are given in Table 1. All the reagents are thoroughly mixed in an agate mortar for 2 h to get uniform mixing and then melted using a silica crucible at $735\text{ }^\circ\text{C}$ in a **programmable** furnace for about 25 min. The resultant melts were rotated 3–4 times before quenching to achieve homogeneous mixture. Such melts were then poured on a preheated brass **mold** and pressed quickly with another brass plate. The samples were annealed in another furnace for about 1 h to remove thermal strains that are produced due to sudden quenching. The glasses thus obtained were highly grounded to achieve a uniform thickness of 0.2 cm.

2.2. Physical and optical measurements

The densities for the prepared glasses were measured by using **Archimedes's** principle with xylene as an immersion

liquid. The refractive indices of all glasses were measured by using **Brewster's** angle method with **He–Ne** laser operating at 632 nm. Using density and refractive indices, some other physical properties were also measured using suitable formulae [23] and are given in Table 2. In the present study the physical properties are changing from glass to glass with increase in the concentration of Pr^{3+} ions, indicating the change in environment around the doped Pr^{3+} ions. The optical absorption spectra were measured for all the glass samples from 440 to 2400 nm at room temperature with a spectral resolution of 0.1 nm using a Jasco V-670 **UV–vis–NIR** spectrometer. The luminescence spectra were measured by using a PL spectrometer **Perkin-Elmer** LS55 with a xenon arc lamp as radiation source. In order to check the amorphous nature of the prepared glasses, the XRD spectral measurement **was** taken for undoped glasses using a Bruker X-ray diffractometer (model D8Advance) which operates at 40 KV and 40 mA current and is shown in Fig. 1. The broad hump observed in the XRD spectrum, characteristic of an amorphous material confirms the glassy nature of the prepared glasses.

3. Results and discussion

3.1. Optical absorption spectra

Optical absorption spectra of Pr^{3+} ions doped LTT glasses were recorded at room temperature in vis–NIR region. Fig. 2 shows the optical absorption spectra recorded for glass D along with the assignment of the absorption bands. The spectra for other glasses are alike with slight difference in intensity of various absorption bands and hence spectra of the remaining glasses were not shown. The band assignments are in good agreement with earlier reports [24,25]. Pr^{3+} ion doped LTT glasses contain nine absorption bands (except glass A) corresponding to the transitions between the $^3\text{H}_4$ ground level and the excited states $^3\text{P}_2$, $^3\text{P}_1$, $^3\text{P}_0$, $^1\text{D}_2$, $^1\text{G}_4$, $^3\text{F}_4$, $^3\text{F}_3$, $^3\text{F}_2$ and $^3\text{H}_6$ belonging to the $4f^2$ configuration of the Pr^{3+} ions. The absorption bands are assigned to different transitions according to the Carnal report [26] on Pr^{3+} ion and the corresponding peak wavelength is given in Table 3. In glass A, six absorption bands are only observed in vis–NIR regions which may be due to very low concentration of Pr^{3+} ions (0.01 mol%) in that glass. The experimental oscillator strengths (f_{exp}) for the electric dipole transitions were calculated from [27].

$$f_{\text{exp}} = 4.32 \times 10^{-9} \int \epsilon(\nu) d\nu$$

here $\epsilon(\nu)$ is the molar extinction coefficient corresponding to the energy ($\nu\text{ cm}^{-1}$) and $d\nu$ is the half-band width of the absorption band. Quite often in glasses the absorption bands need not show a Gaussian shape. In such cases the value of $\int \epsilon(\nu) d\nu$ is evaluated by using the area method. In the present work, for all the absorption bands, the intensities were measured by the area method. Of all the transitions, the transitions $^3\text{H}_4 \rightarrow ^3\text{P}_2$ and $^3\text{H}_4 \rightarrow ^3\text{F}_3$ are known as hypersensitive transitions whose intensities strongly depends on the

Q4

Table 1
LTT glass composition with different concentrations of Pr^{3+} ions (in mol%).

Name of the glass	TeO_2	WO_3	PbF_2	Pr_6O_{11}
Base glass	60	25	15	–
Glass A	59.99	25	15	0.01
Glass B	59.9	25	15	0.1
Glass C	59.5	25	15	0.5
Glass D	59	25	15	1
Glass E	58.5	25	15	1.5

Table 2
Various physical properties of Pr^{3+} doped LTT glasses.

Physical properties	Glass A	Glass B	Glass C	Glass D	Glass E
Density ρ (g cm^{-3})	6.606	6.607	6.612	6.616	6.622
Refractive index (n_d)	2.305	2.306	2.307	2.308	2.309
Average molecular weight \bar{M} (g)	135.1	135.2	135.9	136.8	137.6
Pr^{3+} ion contribution N (10^{21} ions/ cm^3)	0.294	2.941	14.643	29.122	43.451
Mean atomic volume ($\text{g}/\text{cm}^3/\text{atom}$)	6.629	6.296	6.308	6.324	6.338
Dielectric constant (ϵ)	5.315	5.320	5.325	5.329	5.334
Optical dielectric constant (ϵ^{-1})	4.315	4.320	4.325	4.330	4.334
Reflections loss (R) (%)	0.155	0.156	0.156	0.156	0.156
Molar refraction (R_m) (cm^{-3})	13.97	13.99	14.06	14.14	14.22
Polaron radius (\AA)	0.210	0.066	0.029	0.021	0.017
Inter ionic distance (\AA)	15.034	6.981	4.088	3.251	2.845
Molecular electronic polarizability, α (10^{-23} cm^3)	137.5	13.76	2.762	1.388	0.930
Field strength (10^{22})	0.675	6.744	33.57	66.77	99.63
Optical basicity (A_{th})	0.540	0.541	0.542	0.544	0.545

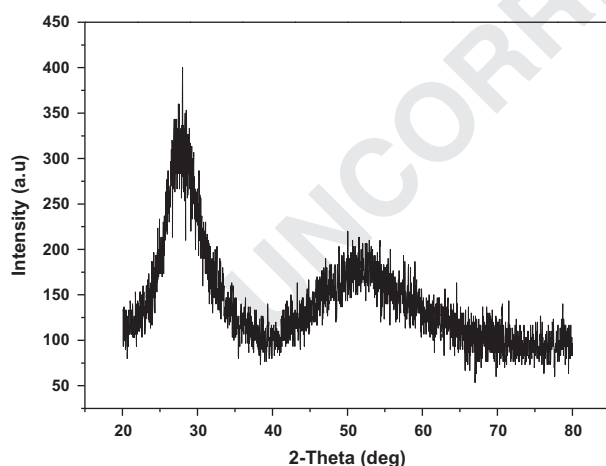


Fig. 1. XRD spectrum of undoped LTT glass.

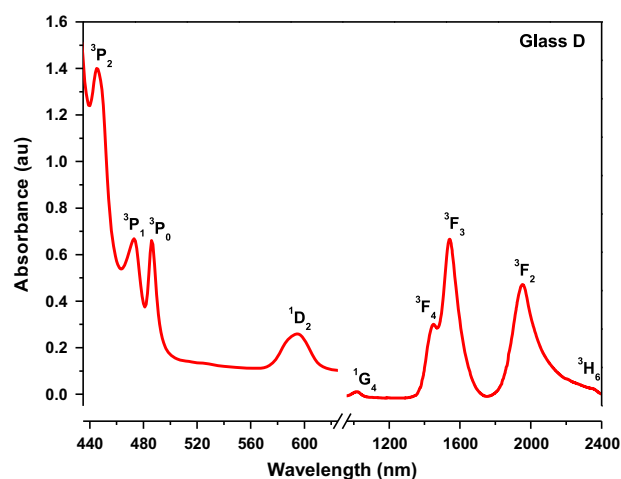


Fig. 2. Absorption spectrum of 1 mol% of Pr^{3+} ions in LTT glass (glass D) with strong absorption bands in the NIR region.

neighboring ligands [28]. The hypersensitive transitions are observed in other RE ions and exhibit anomalous nature irrespective of matrix elements and follows selection rules $\Delta S=0$, $\Delta L \leq 2$ and $\Delta J \leq 2$. Judd and Ofelt independently derived expressions for the oscillator strengths of induced electric dipole transitions for the f^N configurations [29,30]. The basic idea of the Judd–Ofelt (J–O) theory is that the intensity

of the forbidden f–f electric dipole transitions can arise from the admixture of the $4f^N$ configurations with the excited configurations of opposite parity. The calculated oscillator strengths (f_{cal}) of the $\psi_J \rightarrow \psi'_J$ transition are determined by using the expression given in the J–O theory [29,30].

It is well known that, the application of the J–O theory to the 4f transitions of Pr^{3+} ion gives poor agreement between the

Table 3
Assignment of absorption bands, experimental (f_{exp}) (10^{-6}), calculated oscillator strengths (f_{cal}) (10^{-6}) and r.m.s. deviation (δ_{rms}) (10^{-6}) of Pr^{3+} ions doped LTT glasses using standard and modified J–O theories.

Transition from	λ (nm)	Glass A			Glass B			Glass C			Glass D			Glass E		
		f_{exp}	f_{cal}	f_{cal}^*	f_{exp}	f_{cal}	f_{cal}^*	f_{exp}	f_{cal}	f_{cal}^*	f_{exp}	f_{cal}	f_{cal}^*	f_{exp}	f_{cal}	f_{cal}^*
$^3\text{H}_4 \rightarrow$																
$^3\text{P}_2$	445	–	–	–	–	–	–	6.49	5.61	7.45	8.87	6.06	8.80	6.33	4.70	6.26
$^3\text{P}_1$	473	–	–	–	5.37	8.03	7.66	4.59	6.34	6.33	7.31	7.54	7.67	5.11	6.19	6.27
$^3\text{P}_0$	486	–	–	–	2.02	7.91	7.47	3.79	6.25	6.18	4.32	7.42	7.49	4.13	6.10	6.12
$^1\text{D}_2$	596	1.26	1.20	1.47	2.30	1.56	1.91	3.62	1.88	2.27	3.92	2.04	2.47	3.09	1.55	1.88
$^1\text{G}_4$	1024	0.62	0.33	0.35	1.12	0.43	0.47	1.02	0.53	0.57	1.25	0.57	0.62	1.04	0.43	0.47
$^3\text{F}_4$	1453	3.16	3.17	3.17	1.37	4.21	4.70	4.16	5.76	6.05	4.69	6.12	6.46	3.31	4.59	4.87
$^3\text{F}_3$	1541	8.05	8.05	8.05	12.4	10.5	10.1	12.7	11.9	11.5	13.6	13.0	12.7	10.4	9.89	9.61
$^3\text{F}_2$	1956	8.36	8.35	8.35	14.2	14.3	14.3	15.1	15.1	15.1	16.7	16.7	16.7	11.1	11.1	11.1
$^3\text{H}_6$	2357	0.73	0.71	0.67	0.70	0.88	0.86	1.62	1.12	1.07	1.82	1.21	1.16	1.58	0.93	0.89
δ_{rms}		± 0.11		± 0.13	± 2.61		± 2.54	± 1.35		± 1.36	± 1.64		± 1.40	± 1.19		± 1.08

f_{cal} – calculated oscillator strengths from the standard J–O theory and f_{cal}^* – calculated oscillator strengths from the modified J–O theory.

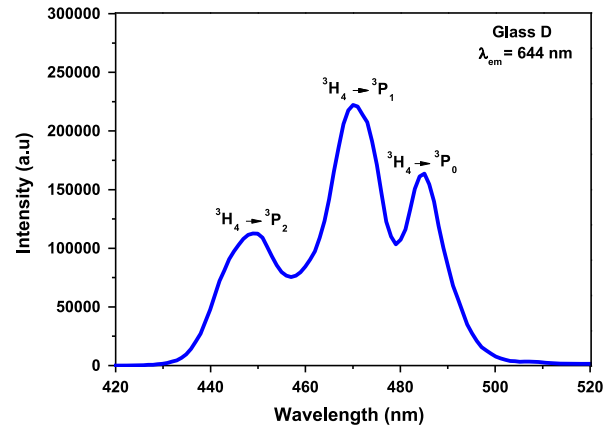


Fig. 3. Excitation spectrum of 1 mol% of Pr^{3+} ions in LTT glass (glass D).

theoretical and experimental oscillator strengths [31–34]. This poor agreement between experimental and calculated oscillator strengths is expected because of small energy difference between $4f^2$ and $4f5d$ levels. By applying the modified J–O theory, it is possible to get reasonably good agreement between theoretical and experimental oscillator strengths with less r.m.s. deviation including hypersensitive transition [35]. According to the modified J–O theory, the experimental oscillator strengths (f_{exp}) for electric dipole transitions were calculated using the following expression:

$$f_{\text{exp}} = \frac{8\pi^2 mc \theta}{3h(2J+1)} \frac{(n^2+2)^2}{9n} \times \sum_{\lambda=2,4,6} \Omega_{\lambda} [1 + 2\alpha(E_J + E_{J'} - 2E_{f_0})] (\psi_J \| U^{\lambda} \| \psi_{J'})^2$$

Here E_J is the energy of the ground state, $E_{J'}$ is the energy of excited state, E_{f_0} is the energy of the center of gravity of the $4f^2$ configuration ($\sim 10,000 \text{ cm}^{-1}$) and $\alpha = \frac{1}{2}[E(4f5d) - E(4f)]$. The parameter α has a value of 10^{-5} cm^{-1} , but in practice it is treated as an additional fitting parameter. The calculated oscillator strengths measured by using standard as well as modified J–O theories including $^3\text{H}_4 \rightarrow ^3\text{P}_2$ hypersensitive transition are tabulated in Table 3 along with the experimental oscillator strengths. From Table 3 it is observed that, for most of the LTT glasses, the modified J–O theory gives good approximation between experimental and calculated oscillator strengths with less r.m.s. deviation than the standard J–O theory. Table 4 gives the J–O parameters measured for all the LTT glasses using the standard and modified J–O theories along with their trend. Significant improvement in the J–O intensity parameters can be observed after applying the modified J–O theory. Except for glass A, the trend followed by the J–O intensity parameters is the same ($\Omega_2 > \Omega_4 > \Omega_6$) for all LTT glasses in both standard as well as modified J–O theories. From both the J–O theories, the Ω_2 parameter is found to be maximum for all the LTT glasses.

It is well known fact that the magnitude of the J–O intensity parameters is related to the physical and chemical properties such as viscosity and covalent character of the chemical bonds. In general, Ω_2 values for the rare earth ions in glasses are intermediate between crystalline oxides and chelating ligands [36–38]. In glasses, the rare earth ions are randomly distributed

Table 4
Judd–Ofelt intensity parameters Ω_2 , Ω_4 and Ω_6 (10^{-20} cm²) and their trend for Pr³⁺ doped LTT glasses with standard and modified J–O theories.

Name of the glass sample	Standard J–O theory			Trend followed in the standard J–O theory	Modified J–O theory*			Trend followed in the modified J–O theory
	Ω_2	Ω_4	Ω_6		Ω_2^*	Ω_4^*	Ω_6^*	
Glass A	4.782	6.148	2.208	$\Omega_4 > \Omega_2 > \Omega_6$	5.402*	6.609*	2.318*	$\Omega_4 > \Omega_2 > \Omega_6$
Glass B	11.06	7.156	2.854	$\Omega_2 > \Omega_4 > \Omega_6$	13.90*	5.557*	3.641*	$\Omega_2 > \Omega_4 > \Omega_6$
Glass C	12.88	5.648	4.412	$\Omega_2 > \Omega_4 > \Omega_6$	15.43*	4.590*	5.041*	$\Omega_2 > \Omega_6 > \Omega_4$
Glass D	13.89	6.70	4.606	$\Omega_2 > \Omega_4 > \Omega_6$	16.69*	5.559*	5.305*	$\Omega_2 > \Omega_4 > \Omega_6$
Glass E	8.309	5.503	3.481	$\Omega_2 > \Omega_4 > \Omega_6$	10.30*	4.542*	4.045*	$\Omega_2 > \Omega_4 > \Omega_6$

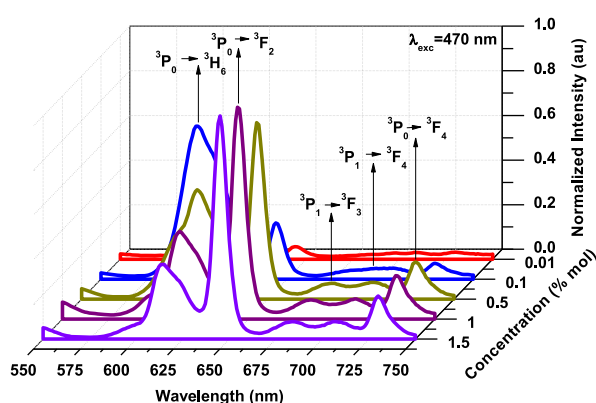


Fig. 4. Emission spectra of Pr³⁺ ions in LTT glasses.

over non-equivalent sites with a wide distribution of crystal fields. In such cases, a distribution of large number of rare earth ions occupying sites with non-centrometric potential will contribute significantly to the changes in the Ω_2 value [39]. The large Ω_2 parameter values are indicators of the covalent character of the chemical bonds among the glass matrix and rare earth ions. The Ω_2 parameter depends mainly on the asymmetry of the sites in the neighborhood of rare earth ion. The higher the Ω_2 parameter, the higher is the degree of asymmetry around the rare earth ion and stronger the covalence of rare earth ion–oxygen bond. The intensity parameters Ω_4 and Ω_6 are related to the bulk properties such as viscosity and dielectric of the media and are also affected by the vibronic transitions of the rare earth ions bound to the ligand atoms [40,41] and less sensitive to the medium in which the ions are situated. From Table 4, it is observed that, the J–O intensity parameters are found to be high for glass D, indicating that it is more asymmetric, more covalent and more rigid than the other LTT glasses.

3.2. Photoluminescence properties

To analyze the photoluminescence properties of the LTT glasses doped with Pr³⁺ ion, it is necessary to know the excitation wavelength of Pr³⁺ ion. The excitation wavelength plays an important role in recording the emission spectra of rare-earth ions doped luminescent materials. Fig. 3 shows the excitation spectra of glass D when emission is monitored at

644 nm. The excitation spectra consist of three bands corresponding to the transitions $^3\text{H}_4 \rightarrow ^3\text{P}_2$, $^3\text{H}_4 \rightarrow ^3\text{P}_1$ and $^3\text{H}_4 \rightarrow ^3\text{P}_0$. Among all these transitions, a transition $^3\text{H}_4 \rightarrow ^3\text{P}_1$ corresponding to 470 nm is more intense and is used as an excitation wavelength to record the emission spectra. The emission spectra recorded at room temperature for LTT glasses doped with different concentrations of Pr³⁺ ions in the spectral range 550–750 nm are shown in Fig. 4. The emission spectra consist of five emission bands at 613, 644, 683, 707 and 730 nm corresponding transitions to $^3\text{P}_0 \rightarrow ^3\text{H}_6$, $^3\text{P}_0 \rightarrow ^3\text{F}_2$, $^3\text{P}_1 \rightarrow ^3\text{F}_3$, $^3\text{P}_1 \rightarrow ^3\text{F}_4$ and $^3\text{P}_0 \rightarrow ^3\text{F}_4$ respectively.

Fluorescence quenching is observed in all the emission transitions with increase in the concentration of Pr³⁺ ions. The quenching of intensity is the same for all the emission transitions except for $^3\text{P}_0 \rightarrow ^3\text{H}_6$ transition. Fluorescence quenching for all the emission transitions begins at 1.0 mol% but for $^3\text{P}_0 \rightarrow ^3\text{H}_6$ transition, the quenching began at 0.1 mol% of Pr³⁺ ion concentration itself. This may be due to the energy transfer through cross-relaxation between Pr³⁺ ions. Fig. 4 also shows that, with increase in Pr³⁺ ion concentration, a significant red shift has been observed for $^3\text{P}_0 \rightarrow ^3\text{H}_6$ emission transition. The peak position of $^3\text{P}_0 \rightarrow ^3\text{H}_6$ transition in LTT glasses observed at 600, 602, 611, 613 and 614 nm for 0.01, 0.1, 0.5, 1.0 and 1.5 mol% of Pr³⁺ ion concentration respectively indicates a red shift of that peak. This red shift may be attributed to the site distribution of Pr³⁺ ions in the vicinity of ligand fields [42]. However, for the other transitions namely $^3\text{P}_0 \rightarrow ^3\text{F}_2$, $^3\text{P}_1 \rightarrow ^3\text{F}_3$, $^3\text{P}_0 \rightarrow ^3\text{F}_3$ and $^3\text{P}_0 \rightarrow ^3\text{F}_4$ no red shift has been observed because of negligible emission intensities of the respective emission bands. Fig. 5 represents the energy level diagram depicting the various lasing transitions for 1 mol% of Pr³⁺ ions in LTT glass (glass D). From Fig. 5, it is observed that the emission occurs only from $^3\text{P}_0$, which indicates that $^3\text{P}_1$ state is thermally populated.

In order to predict the emission performance of LTT glasses doped with Pr³⁺ ions, the radiative parameters such as radiative transition probability (A_R), total radiative transition probability (A_T), radiative lifetime (τ_R), branching ratio (β_R) and stimulated emission cross-section (σ_{se}) were measured for the observed fluorescent levels using the J–O parameters derived from the modified J–O theory. The necessary mathematical expressions needed to measure the above radiative parameters were collected from our previous paper [43]. The radiative parameters thus evaluated are given in Tables 5–7. In addition to these

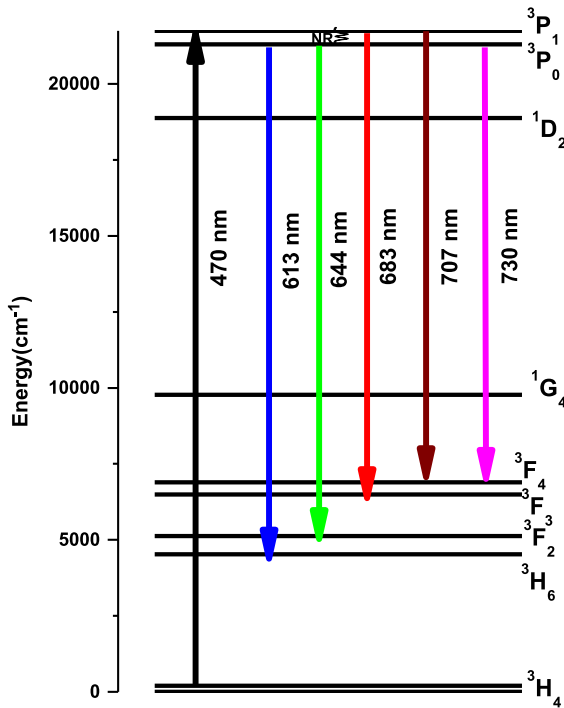


Fig. 5. Energy level scheme for emission process of 1 mol% Pr^{3+} ions in LTT glass (glass D).

parameters, the other radiative parameters like gain band width ($\sigma_{se} \times \Delta\lambda_p$) and optical gain parameters ($\sigma_{se} \times \tau_R$), which are also important to identify a laser active medium, are evaluated and included in Table 7.

Table 5 gives the transition probability (A_R), total transition probability (A_T) and radiative lifetimes (τ_R) for the observed emission transitions of Pr^{3+} ions doped LTT glasses. Large transition probability value obtained for glass D for $^3P_1 \rightarrow ^3F_3$ fluorescent level gives the potentiality of glass D over the other LTT glasses. Table 6 represents the measured and experimental branching ratios (β_R) observed for all the emission transitions of Pr^{3+} doped LTT glasses. The emission transitions with higher magnitude of β_R are more competent for laser action than the other transitions originating from a given excited state. From Table 6, it can be observed that β_R value for $^3P_0 \rightarrow ^3F_2$ transition is more than the other transitions in all LTT glasses. This gives the potentiality of this energy level for laser emission at 644 nm in these LTT glasses. From Table 6, it can also be observed that the β_R and β_{exp} are in good agreements with each other for all the transitions in LTT glasses. Table 7 gives the emission peak wavelength (λ_p), effective band widths ($\Delta\lambda_p$), stimulated emission cross-sections (σ_{se}), gain band width ($\sigma_{se} \times \Delta\lambda_p$) and optical gain parameter ($\sigma_{se} \times \tau_R$) for the emission transitions of Pr^{3+} ions doped LTT glasses. Stimulated emission cross-section which signifies the energy extraction for the material is an important parameter to estimate laser performance of a material. From Table 7, it is observed that among all the emission transitions, $^3P_0 \rightarrow ^3F_2$ (644 nm) and $^3P_0 \rightarrow ^3H_6$ (602 nm) transitions possess highest and least stimulated emission cross-sections respectively. This may be due to the variation of in-homogenous line

Table 5
Transition probabilities (A_R) (s^{-1}), total transition probability (A_T) (s^{-1}) and radiative lifetimes (τ_R) (μs) for the observed prominent emission transitions of Pr^{3+} doped LTT glasses.

Transition	Glass A			Glass B			Glass C			Glass D			Glass E		
	A_R	A_T	τ_R	A_R	A_T	τ_R	A_R	A_T	τ_R	A_R	A_T	τ_R	A_R	A_T	τ_R
$^3P_1 \rightarrow ^3F_4$	16,914	175,196	5	14,294	245,767	4	11,787	249,880	4	14,300	280,367	3	11,703	195,693	5
$^3P_1 \rightarrow ^3F_3$	45,984	175,196	5	94,941	245,767	4	102,262	249,880	4	112,030	280,367	3	71,559	195,693	5
$^3P_0 \rightarrow ^3F_4$	18,598	190,419	5	15,720	26,9284	3	12,960	27,2646	3	15,723	306,094	3	12,868	212,646	4
$^3P_0 \rightarrow ^3F_2$	59,343	190,419	5	152,956	269,284	3	170,080	272,646	3	184,281	306,094	3	113,919	212,646	4
$^3P_0 \rightarrow ^3H_6$	7492	19,0419	5	11,788	269,284	3	16,348	272,646	3	17,234	306,094	3	13,163	212,646	4

Table 6
Measured (β_R) and experimental (β_{exp}) branching ratios of different concentrations of Pr^{3+} ions doped LTT glasses.

Transition	Glass A		Glass B		Glass C		Glass D		Glass E	
	β_R	β_{exp}	β_R	β_{exp}	β_R	β_{exp}	β_R	β_{exp}	β_R	β_{exp}
$^3P_1 \rightarrow ^3F_4$	0.096	0.050	0.058	0.283	0.047	0.315	0.051	0.050	0.059	0.032
$^3P_1 \rightarrow ^3F_3$	0.262	0.191	0.386	0.109	0.409	0.304	0.399	0.409	0.365	0.456
$^3P_0 \rightarrow ^3F_4$	0.097	0.044	0.058	0.034	0.047	0.052	0.051	0.062	0.060	0.067
$^3P_0 \rightarrow ^3F_2$	0.311	0.146	0.568	0.231	0.623	0.248	0.602	0.166	0.535	0.103
$^3P_0 \rightarrow ^3H_6$	0.039	0.067	0.043	0.042	0.060	0.080	0.056	0.112	0.061	0.012

Table 7
Emission peak wavelength (λ_p) (nm), effective band widths ($\Delta\lambda_p$) (nm), stimulated emission cross-sections (σ_{se}) (10^{-20}) (cm^2), gain band width ($\sigma_{se} \times \Delta\lambda_p$) (10^{-25}) (cm^3) and optical gain parameters ($\sigma_{se} \times \tau_R$) (10^{-25}) ($cm^2 s$) for the emission transitions of Pr^{3+} doped LTT glasses.

Spectral parameters	Glass A		Glass B		Glass C		Glass D		Glass E	
$^3P_0 \rightarrow ^3H_6$										
λ_p	600		602		611		613		614	
$\Delta\lambda_p$	16.3		8.11		12.0		13.0		16.3	
σ_{se}	1.49		4.76		4.73		4.66		2.83	
$\sigma_{se} \times \Delta\lambda_p$	0.24		0.38		0.56		0.60		0.46	
$\sigma_{se} \times \tau_R$	0.74		1.43		1.42		1.40		1.14	
$^3P_0 \rightarrow ^3F_2$										
λ_p	644		644		644		644		644	
$\Delta\lambda_p$	7.61		6.52		5.43		4.89		5.43	
σ_{se}	33.5		101.0		134.0		161.0		89.8	
$\sigma_{se} \times \Delta\lambda_p$	2.55		6.57		7.29		7.90		4.88	
$\sigma_{se} \times \tau_R$	16.8		30.2		40.3		48.4		35.9	
$^3P_1 \rightarrow ^3F_3$										
λ_p	683		683		683		683		683	
$\Delta\lambda_p$	8.11		6.76		9.46		4.05		9.46	
σ_{se}	30.8		76.3		58.7		150.0		41.0	
$\sigma_{se} \times \Delta\lambda_p$	2.50		5.16		5.55		6.07		3.88	
$\sigma_{se} \times \tau_R$	15.4		30.5		23.5		45.0		20.5	
$^3P_1 \rightarrow ^3F_4$										
λ_p	707		707		707		707		707	
$\Delta\lambda_p$	14.9		13.5		12.5		12.2		13.5	
σ_{se}	7.08		6.60		5.87		7.30		5.39	
$\sigma_{se} \times \Delta\lambda_p$	1.06		0.89		0.73		0.89		0.72	
$\sigma_{se} \times \tau_R$	3.54		2.64		2.35		2.19		2.70	
$^3P_0 \rightarrow ^3F_4$										
λ_p	730		730		730		730		730	
$\Delta\lambda_p$	9.46		10.8		8.11		6.76		8.11	
σ_{se}	13.9		10.3		11.3		16.5		11.2	
$\sigma_{se} \times \Delta\lambda_p$	1.32		1.11		0.91		1.11		0.91	
$\sigma_{se} \times \tau_R$	6.97		3.09		3.39		4.94		4.49	

widths of the two transitions. In the present LTT glasses, the glass D with 1 mol% of Pr^{3+} ions possesses highest stimulated emission cross-section for all the transitions. In glass D, $^3P_0 \rightarrow ^3F_2$ transition (644 nm) possesses highest stimulated emission cross-section over the other transitions in the same glass. Hence glass D is said to be having enough competency to emit bright red laser at 644 nm. The gain parameters

($\sigma_e \times \tau_m$) and gain band width ($\sigma_e \times \Delta\lambda_p$) are used to obtain a laser host material with highest stability [44]. In the present work, the gain properties of $^3P_0 \rightarrow ^3F_2$ level are found to be maximum for all the LTT glasses. Among all the glasses, glass D possesses higher values of these parameters. Based on the measured radiative parameters, it is suggested that glass D doped with 1 mol% of Pr^{3+} ions can be used for red laser

Table 8
CIE chromaticity co-ordinates of Pr^{3+} ions doped LTT glasses

Name of the glass	Color co-ordinates	
	X-co-ordinates	Y-co-ordinates
Glass A	0.6343	0.3564
Glass B	0.6423	0.3523
Glass C	0.6646	0.3345
Glass D	0.6512	0.2785
Glass E	0.6435	0.2764

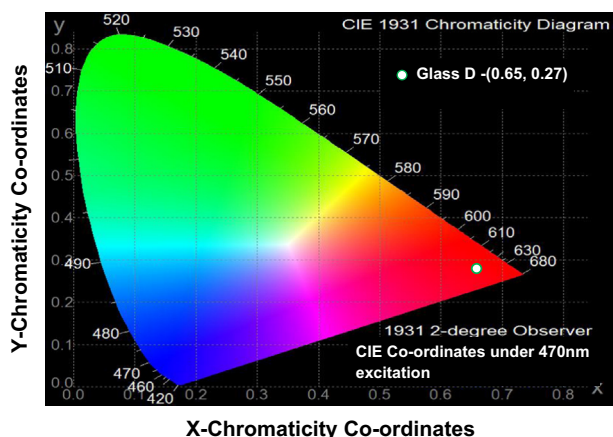


Fig. 6. CIE 1931 chromaticity diagram for 1 mol% of Pr^{3+} ions in LTT glass (glass D).

emission at 644 nm corresponding to the transitions $^3\text{P}_0 \rightarrow ^3\text{F}_2$ and it is also for optical amplification.

3.3. CIE chromaticity co-ordinates

The CIE co-ordinates are used to find the color of the light emitted by the material under excitation. They are measured from the emission spectra given by the materials under investigation. Such CIE co-ordinates measured from the emission spectra of LTT glasses doped with Pr^{3+} ions using the CIE system are presented in Table 8. The emission spectra contain three parts. The first part is orange to red, second part is red and the third part is NIR. The CIE color co-ordinates for all the samples were found to be in the bright red region. Among all the glass samples, particularly glass D color co-ordinates ($x=0.65$, $y=0.27$) are falling in the bright red region corresponding to $^3\text{P}_0 \rightarrow ^3\text{F}_2$ (644 nm) transition. Fig. 6 represents the CIE plot with color co-ordinates for 1 mol% of Pr^{3+} in LTT glass (glass D) excited at 470 nm wavelength. Hence glass D with 1 mol% of Pr^{3+} ions is quite suitable to give bright red color laser at 644 nm.

4. Conclusion

Lead tungsten tellurite (LTT) glasses doped with different concentrations of Pr^{3+} ions were prepared by using the

conventional melt quenching technique. The amorphous nature of the prepared LTT glasses was confirmed by XRD spectrum recorded for an undoped LTT glass. The modified J–O theory has been applied to analyze the absorption spectra of Pr^{3+} ions doped LTT glasses. The J–O intensity parameters calculated by using the modified J–O theory give less r.m.s. deviation between experimental and calculated oscillator strengths. In the present work, the J–O intensity parameters (Ω_2 , Ω_4 and Ω_6) are found to be high for glass D indicating that it is more asymmetric, more covalent and more rigid than the other glasses. Using the J–O parameters obtained from the modified J–O theory, the radiative properties such as transition probability (A_R), radiative lifetime (τ_R) and branching ratios (β_R) are evaluated. The emission spectra recorded at different concentrations of Pr^{3+} ions show five emission bands at 613, 644, 683, 707 and 730 nm corresponding transitions to $^3\text{P}_0 \rightarrow ^3\text{H}_6$, $^3\text{P}_0 \rightarrow ^3\text{F}_2$, $^3\text{P}_1 \rightarrow ^3\text{F}_3$, $^3\text{P}_1 \rightarrow ^3\text{F}_4$ and $^3\text{P}_0 \rightarrow ^3\text{F}_4$. Among these five emission transitions observed, $^3\text{P}_0 \rightarrow ^3\text{F}_2$ is more intense and is falling in red region. Based on visible emission spectra, the high stimulated emission cross-section and branching ratios observed for $^3\text{P}_0 \rightarrow ^3\text{F}_2$ transition for all these glasses suggest the feasibility of using these materials as lasers in red region. The CIE chromaticity co-ordinates evaluated from the emission spectra recorded at 470 nm excitation for all LTT glasses confirm the suitability of these glassy materials for red emission. From the measured emission cross-sections and CIE chromaticity co-ordinates, it was found that 1 mol% of Pr^{3+} ions in LTT glasses (glass D) is aptly suitable for the development of bright visible red lasers to operate at 644 nm from these LTT glasses.

Acknowledgments

One of the authors M. Venkateswarlu is very much thankful to Koneru Satyanarayana (President, KL University) for his motivation and support. Two of the authors, Swapna Koneru (File no.: SR/WOS-A/PS-35/2011) and Mahamuda Shaik (File no.: SR/WOS-A/PS-53/2011) are very much thankful to the Department of Science and Technology (DST), Government of India, New Delhi, for awarding them with a Women Scientist's scheme under DST-WOS(A) Program.

References

- [1] T. Som, B. Karmakar, Optical properties of Eu^{3+} doped antimony oxide based low phonon disordered matrices, J. Phys. Condens. Matter 22 (2010) 035603.
- [2] B. Lai, J. Wang, Q. Su, Ultraviolet and visible up-conversion emission in $\text{Tb}^{3+}/\text{Yb}^{3+}$ co-doped fluorophosphate glasses, Appl. Phys. B 98 (2010) 41–47.
- [3] R.S. Chaliha, K. Annapurna, A. Tarafder, V.S. Tiwari, P.K. Gupta, B. Karmakar, Luminescence and dielectric properties of nano-structured $\text{Eu}^{3+}:\text{K}_2\text{O}-\text{Nb}_2\text{O}_5-\text{SiO}_2$ glass ceramics, Solid State Sci. 11 (2009) 1325–1332.
- [4] B.J. Chen, E.Y.B. Pun, H. Lin, Photoluminescence and spectral parameters of Eu^{3+} in sodium–aluminum–tellurite ceramics, J. Alloys Compd. 479 (2009) 352–356.

- [5] Y.N. Savvin, N.V. Babayevskaya, S.S. Oleinik, O.N. Bezkravnaya, A.V. Tolmachev, **Luminescent** properties of europium-activated yttrium gadolinium phosphates, *Inorg. Mater.* 45 (2009) 423–427.
- [6] M. Mattarelli, M. Montagna, L. Zampedri, M. Bouazaoui, B. Capoen, S. Turrell, M. Ferrari, G.C. Righini, Effect of Eu^{3+} and Ce^{3+} codoping on the relaxation of Er^{3+} in **silica-hafnia** and tellurite glasses, *Phys. Status Solidi* 4 (3) (2007) 793–796.
- [7] A. Ivankov, J. Seekamp, W. Bauhofer, Optical **properties** of Eu^{3+} -doped **zinc borate glasses**, *J. Lumin.* 121 (2006) 123–131.
- [8] R. Balda, J. Fernandez, L.M. Lacha, M.A. Arriandiga, J.M. Fernandez-Navarro, Energy transfer studies in Eu^{3+} -doped **lead-niobium** germanate glasses, *Opt. Mater.* 27 (2005) 1776–1780.
- [9] C. Cascales, R. Balda, J. Fernandez, M.A. Arriandiga, J.M. Fdez-Navarro, Site selective spectroscopy of Eu^{3+} in heavy-metal oxide glasses, *J. Non-Cryst. Solids* 352 (2006) 2448–2451.
- [10] H.J. Lozykowski, W.M. Jadwisieniczak, I. Brown, Photoluminescence and cathodoluminescence of GaN doped with Pr, *J. Appl. Phys.* 88 (2000) 210–222.
- [11] Poulain Marcel, Advanced glasses, *Ann. Chim. Sci. Mater.* 28 (2003) 87–94.
- [12] J. Yang, S. Dai, Y. Zhou, L. Wen, L. Hu, Z.H. Jiang, Spectroscopic properties and thermal stability of erbium-doped bismuth-based glass for optical amplifier, *J. Appl. Phys.* 93 (2) (2003) 977–983.
- [13] E. Culea, L. Pop, S. Simon, Spectroscopic and magnetic behaviour of $x\text{Gd}_2\text{O}_3-(1-x)(\text{Bi}_2\text{O}_3 \cdot \text{PbO})$ glasses, *Mater. Sci. Eng. B* 112 (2004) 59–63.
- [14] R. Balda, I. Saez de Ocariz, J. Fernandez, J.M. Fdez. Navarro, M. A. Arriandiga, Spectroscopy and orange-blue frequency upconversion in Pr^{3+} -doped $\text{GeO}_2\text{-PbO-Nb}_2\text{O}_5$ glass, *J. Phys.: Condens. Matter* 12 (2000) 10623–10632.
- [15] H. Nii, K. Ozaki, M. Herren, M. Morita, Up-conversion fluorescence of Er^{3+} and Yb^{3+} -doped **TeO_2 -based** oxide glass and single crystals, *J. Lumin.* 76–77 (1998) 116–119.
- [16] A. Mori, Y. Ohishi, S. Sudo, Erbium-doped tellurite glass fibre laser and amplifier, *Electron. Lett.* 33 (1997) 863–864.
- [17] D. Barreca, S. Bozza, G. Carta, G. Rossetto, E. Tondello, P. Zanella, Structural and morphological analyses of tungsten oxide nanophase thin films obtained by MOCVD, *Surf. Sci.* 532 (2003) 439–443.
- [18] T. Kosuge, Y. Benino, V. Dimitrov, R. Sato, T. Komatsu, Thermal stability and heat capacity changes at the glass transition in $\text{K}_2\text{O-WO}_3\text{-TeO}_2$ glasses, *J. Non-Cryst. Solids* 242 (1998) 154–164.
- [19] I. Shaltout, Y. Tang, R. Braunstein, E.E. Shaisha, FTIR spectra and some optical properties of tungstate tellurite glasses, *J. Phys. Chem. Solids* 57 (1996) 1223–1230.
- [20] M.R. Sahar, A.K. Jehnu, M.M. Karim, **$\text{TeO}_2\text{-ZnO-ZnCl}_2$** glasses for IR transmission, *J. Non-Cryst. Solids* 213–214 (1997) 164–167.
- [21] B. Bridge, T.E. Bavins, D. Woods, T. Woolven, on the preparation and composition of the glass formation range of the system **$\text{TeO}_2\text{-ZnCl}_2$** , *J. Non-Cryst. Solids* 88 (1986) 262–270.
- [22] A.A. Kaminskii, in: *Laser Crystals*, second ed., Springer-Verlag, Berlin, 1990.
- [23] A. Srinivasa Rao, B. Rupa Venkateswara Rao, M.V.V.K.S. Prasad, J.V. Shanmukha Kumar, M. Jayasimhadri, J.L. Rao, R.P.S. Chakradhar, **Spectroscopic** and optical properties of Nd^{3+} doped fluorine containing alkali and alkaline earth **zinc** aluminophosphate optical glasses, *Physica B* 404 (2009) 3717–3721.
- [24] D.V.R. Murthy, B.C. Jamalaliah, T. Sasikala, L. Rama Moorthy, M. Jayasimhadri, Kiwan Jang, H.O. Sueb Lee, Soung Soo Yi, Jung Hyun Jeong, Optical absorption and emission characteristics of Pr^{3+} -doped RTP glasses, *Physica B* 405 (2010) 1095–1100.
- [25] A.Mendioroz Balda, J. Fernandez, M.A. arriandiga, L.S. Grisom, J.L. Adam, Laser spectroscopy and up-conversion studies of Pr^{3+} -doped halide modified sulfide glasses, *Opt. Mater.* 16 (2001) 249–254.
- [26] W.T. Carnall, P.R. Fields, K. Rajnak, Electronic energy levels in the trivalent lanthanide aquo-ions. I. Pr^{3+} , Nd^{3+} , Pm^{3+} , Sm^{3+} , Dy^{3+} , Ho^{3+} , Er^{3+} , and Tm^{3+} , *J. Chem. Phys.* 49 (1968) 4424–4442.
- [27] W.T. Carnall, J.P. Hessler, F. Wagner Jr., Transition probabilities in the absorption and fluorescence spectra of lanthanides in molten lithium nitrate–potassium nitrate eutectic, *J. Phys. Chem.* 82 (1978) 2152–2158.
- [28] C.K. Jorgensen, B.R. Judd, Hypersensitive pseudo-quadrupole transitions in lanthanides, *Mol. Phys.* 8 (1964) 281–290.
- [29] B.R. Judd, Optical absorption intensities of rare-earth ions, *Phys. Rev.* 127 (1962) 750–761.
- [30] G.S. Ofelt, Intensities of crystal spectra of rare-earth ions, *J. Chem. Phys.* 37 (1962) 511–520.
- [31] J. Hormadaly, R.J. Reisfeld, Intensity parameters and laser analysis of Pr^{3+} and Dy^{3+} in oxide glasses, *J. Non-Cryst. Solids* 30 (1979) 337–348.
- [32] S.V.J. Lakshman, L. Ramamoorthy, Optical absorption spectrum of Pr^{3+} in aprotic $\text{POCl}_3\text{-SnCl}_4$ laser liquid, *J. Quant. Spectrosc. Radiat. Transfer* 29 (1983) 439–444.
- [33] G. Amamath, S. Buddhudu, Optical properties of rare-earth doped HMF glasses, *J. Non-Cryst. Solids* 143 (1992) 252–256.
- [34] M.A. Bunuel, R. Cases, M.A. Chamarro, J. Alcalá, **Optical** properties of Pr^{3+} in **$\text{ZnF}_2\text{-CdF}_2$** , *Phys. Chem. Glasses* 33 (1992) 16.
- [35] A.A. Kornienko, A.A. Kaminskii, E.B. Dunina, Dependence of the **line strength** of f–f transitions on the **manifold energy**. II. Analysis of Pr^{3+} in $\text{KPrP}_4\text{O}_{12}$, *J. Phys. Status Solidi A* 157 (1990) 267–273.
- [36] A.F. Kirby, R.A. Palmer, Hypersensitive transition probability in tris (1,3-diphenyl-1, 3-propanedionato) aquo lanthanides(III), *Inorg. Chem.* 20 (1981) 4219–4222.
- [37] A.F. Kirby, R.A. Palmer, Single-crystal electronic absorption of tris (1,3-diphenyl-1, 3-propanedionato) aquoneodymium (III): oscillator strength of the $^4I_{9/2} \rightarrow ^4G_{5/2}$ **hyper-sensitive transition**, *Inorg. Chem.* 20 (1981) 1030–1033.
- [38] R. Reisfeld, C.K. Jorgenson, in: *Lasers and Excited States of Rare Earths*, Springer, New York, 1977.
- [39] K.B. Yatsimirskii, N.K. Davidenko, Absorption spectra and structure of lanthanide **co-ordination** compounds in solution, *Coord. Chem. Rev.* 27 (1979) 223–273.
- [40] W.F. Krupkee, Optical absorption and fluorescence intensities in several **rare-earth** doped Y_2O_3 and LaF_3 single crystals, *Phys. Rev.* 145 (1966) 325–337.
- [41] C. GorllerWalrand, K. Binnemas, Spectral intensities of f–f transitions, in: K.A. Gschneidner Jr., L. Eyring (Eds.), *Hand Book of Physics and Chemistry of Rare Earths*, vol. 25, Elsevier, Netherlands, 1998, p. 101.
- [42] X.J. Wang, H.R. Zheng, D. Jia, S.H. Huang, R.S. Meltzer, M.J. Dejneka, W.M. Yen, Spectroscopy of different sites in Pr^{3+} doped oxy-fluoride glass ceramics, *Microelectron. J.* 34 (2003) 549–551.
- [43] S.k. Mahamuda, K. Swapna, A. Srinivasa Rao, T. Sasikala, L. Rama Moorthy, **Reddish-orange** emission from Pr^{3+} doped zinc aluminobismuth borate glasses, *Physica B* 428 (2013) 36–42.
- [44] M. Liao, Z. Duan, L. Hu, Y. Fang, L. Wen, Spectroscopic properties of $\text{Er}^{3+}/\text{Yb}^{3+}$ co-doped fluorophosphate glasses, *J. Lumin.* 126 (2007) 139–144.

Sensitivity Analysis of Characteristic Parameters of Railway Electric Traction System

Rachana Garg and Priya Mahajan

Deptt. of Electrical Engg., Delhi Technological University, Delhi, India

Email: rachnagarg@dce.ac.in, priyamahajan.eed@gmail.com

Parmod Kumar

(IRD), Maharaja Agrasen Institute of Technology, Delhi, India

Email: pramodk2003@yahoo.co.in

Abstract—The modal analysis, which decouples the contact wire and rail track conductors, is used to develop an integrated model of single rail track and contact wire. The characteristic impedance and propagation constant matrices of integrated model have been computed. The authors have studied effects of various parameters of interest on characteristic impedance and propagation constant using sensitivity analysis. The sensitivity functions of series impedance and shunt admittance related to contact wire and catenary have been developed and validated in this paper.

Index Terms—railway traction lines, characteristic parameters, sensitivity analysis, parameter sensitivity

I. INTRODUCTION

Railway electric traction system is a fast and green transportation system with enhanced load carrying capacity. The analysis and design of power and signaling system of railway electric traction system needs mathematical model of the system. The authors in this paper have used the multi-conductor transmission line theory to develop the mathematical model of the electric traction system and to compute the characteristic impedance and propagation constant of this system. This approach can then be extended to find the voltage and current distribution of the system. The characteristic impedance and propagation constant are the functions of line parameters i.e. self and mutual impedances and admittances of contact wire and rail track. The numerical values of these parameters are not accurately known under practical conditions as they are dependent on varying/uncertain parameters like permeability, supply frequency and shape of the conductor. In order to study the effect of these uncertain parameters on the characteristic parameters of the railway electric traction system, the authors have carried out the sensitivity analysis of characteristic impedance and propagation constant with respect to the above mentioned parameters of interest for the first time in the literature. In a rail track ferromagnetic material, both saturation and hysteresis are

observed. This affects the permeability of rail track. The permeability also depends upon the composition of rail track material which may not remain constant throughout the length of the track. Further, to enhance the performance of the traction system, it is desirable to consider a conductor with a cross-section that will produce uniform magnetic field on its surface. Also, the supply side contains the harmonic frequency components due to the power electronic devices which are inherent to the modern electric traction drives. The variations in these parameters of interest motivated the authors to carry out the sensitivity analysis of characteristic parameters of the system wrt these parameters.

The complete mathematical model of railway electric traction lines, which include the contact wire and rail track, has received little attention in the literature. Most of the traction studies are limited to railway track modeling. R.J. Hill *et al.* [1] has computed frequency dependent self and mutual admittance for a single track power-rail, considering it as a distributed transmission line. They have computed the impedance by numerical calculations and compared with analytic impedance models based on the Carson eqns. for a stratified weakly conducting ground. A. Mariscotti has applied multi conductor transmission lines theory to railway traction system to find the distribution of the traction return current in AC and DC electric railway systems and carried out sensitivity analysis of rail current and rail to rail voltage wrt parameters of interest [2]. He has also carried out modeling of track circuit signaling system which may be helpful in automatic train control [3]. Measurement of currents at power-supply frequency and validation of a multi-conductor transmission-line model is done for (2x25kV) electric railway system with autotransformer [4]. An electromagnetic field model for identification of distributed self and mutual shunt admittances using multi-conductor transmission lines (MTL) is formulated and used to study the parametric behavior of single track admittance [5]. Andrea Mariscotti *et al.* [6] have analyzed the published experimental data and formulae for the determination of the electric parameters of railway traction lines. He observed that the experimental results conform with the

calculated results in frequency range of 50Hz-50 kHz. He also focused on the CCITT simplified method for the evaluation of induced voltages in electric traction system [7].

II. CONFIGURATION OF RAILWAY ELECTRIC TRACTION LINES

In modern overhead electric traction system, the catenary is fed at 25kV, 1-phase ac through the feeding posts which are positioned at frequent intervals alongside the track. The catenary energizes the contact wire which is kept at constant height and in the right position with the help of droppers. The pantograph, a high-strength tubular steel structure which can be raised or lowered, is used to make contact with the overhead contact wire to draw energy to feed the drives of the locomotive. Fig. 1 shows the physical model of railway electric traction system.

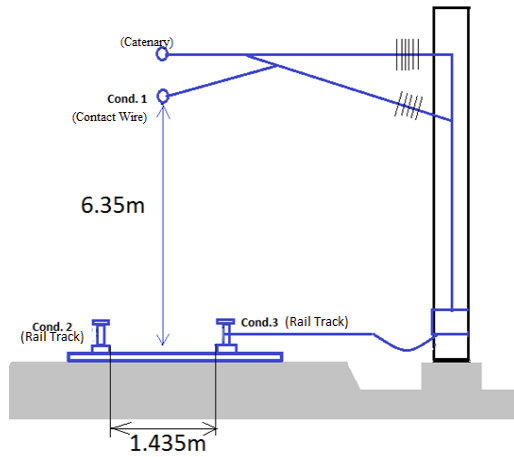


Figure 1. Physical model of railway electric traction system

III. MATHEMATICAL MODEL

A mathematical model based on the electromagnetic properties of rail track is necessary for the analysis and design of railway electric power and signaling systems. The studies related to propagation of voltages and currents signals over the railway electric traction lines need the series impedance and shunt admittance matrices per unit length. These matrices state the electrostatic and electromagnetic performance of the system and depend on the physical and electrical characteristics of the rail track conductor, the geometric arrangement of the conductors and rail track, height above the earth level, permeability and the earth resistivity [8]. The accuracy of the result depends, therefore, on accuracy with which the basic series impedance and shunt admittance matrices of railway electric traction system have been formed.

A. Series Impedance Matrix

The series impedance matrix, Z can be given by (1)

$$Z = R_c + R_e + j(X_c + X_e + X_g) \quad (1)$$

where suffix 'c' denotes the quantities relating to conductor, 'e' denotes the quantities relating to earth and 'g' denotes the quantities relating to geometric arrangement of the conductors. The resistance matrix R_c is

a diagonal matrix whose off diagonal elements are zero. The resistance of the catenary conductor, R_{c11} , is given by (2),

$$R_{c11} = S \times R_o \quad (2)$$

where R_o is dc resistance of the conductor, S is skin effect ratio and is given by (3):

$$S = \frac{1 + \sqrt{1 + \frac{x^4}{48}}}{2}, \quad x = \pi d \sqrt{\frac{2f\mu \times 10^{-5}}{\rho}} \quad (3)$$

where d is the diameter of catenary in mm, f is frequency of supply in Hz, μ is permeability of conductor material and ρ is the resistivity of material in micro-ohm cm.

The resistance of rail track conductors, R_{c22} and R_{c33} is given by (4)[9]:

$$R_{c22} = R_{c33} = \frac{1}{\pi a^2 \sigma_r} \left[\frac{1}{4} + \sqrt{2} \cos\left(\frac{\pi}{4} - \frac{\theta}{2}\right) \right] \left[\frac{a}{2\delta_r} + \frac{3\delta_r}{32a} \right] \quad (4)$$

where, σ_r is the conductivity of rail track, θ is the hysteresis angle, δ_r is skin depth and 'a' is the equivalent radius of rail track and may be calculated considering the rail track as an equivalent I structure[9].

$$X_{c11} = \omega \frac{\mu_0}{8\pi} \quad (5)$$

The reactance of track conductors X_{c22} and X_{c33} is given by (6)[9].

$$X_{c22} = X_{c33} = \frac{1}{\pi a^2 \sigma_r} \left[\sqrt{2} \sin\left(\frac{\pi}{4} - \frac{\theta}{2}\right) \right] \left[\frac{a}{2\delta_r} - \frac{3\delta_r}{32a} \right] \quad (6)$$

The resistance and reactance due to earth path, R_e and X_e , are computed using Carson's formula [10] given by (7.1) and (7.2) respectively.

$$R_e = [10^{-4}] (8 \pi P f) \quad (7.1)$$

$$X_e = [10^{-4}] (8 \pi Q f) \quad (7.2)$$

P and Q are calculated using Carson's series [10] in terms of two parameters c_{ij} and the angle subtended between the conductor and the image, θ_{ij} .

Inductive reactance due to geometry of conductors above the ground, X_g is given by (8.1),

$$X_g = 2\pi f (\mu_0 \mu_r) F \quad (8.1)$$

where, F is Maxwell's coefficient matrix, whose elements are given by (8.2),

$$\ln(2H_i/r_i), i=1,2,3; \ln(x_{ij}/u_{ij}), i=1,2,3, j=1,2,3, i \neq j \quad (8.2)$$

Each term in the matrix represents the distance between two conductors or the conductor and the image.

B. Shunt-Admittance Matrix

The shunt-admittance matrix, Y is a function of the physical geometry of the conductor relative to the earth plane. Further, because the rail track conductor is on the ground, it has appreciable leakage currents while the catenary conductor is located at a sufficient height from the ground and from the rail track conductors hence the leakage currents from catenary to ground and from catenary to rail conductors are assumed to be zero [8].

The admittance matrix is given by (9):

$$Y=G+j\omega C \quad (9)$$

where, G is the conductance matrix. The elements of conductance matrix corresponding to the catenary are zero and the elements corresponding to rail track are given by (10) [5].

$$g_{22} = g_{33} = \frac{\pi\sigma_r}{\ln 2b/a}; g_{23} = g_{32} = \frac{\pi\sigma_r}{\ln 2} \quad (10)$$

where, σ_r is conductivity of rail track, b is distance between two rail track.

The capacitance matrix $[C]$ is given by (11),

$$[C] = 2\pi\epsilon_0 [F]^{-1} \quad (11)$$

IV. MODAL THEORY

In order to compute the characteristic parameters of railway electric traction lines, modal theory has been applied to decouple the phase quantities to modal quantities using the transformation given by(12)[11]-[12].

$$Pq=\lambda q \quad (12)$$

where, P is the product matrix and is given by (13)

$$P=[Z][Y] \quad (13)$$

λ is the eigen value of P and q is the corresponding eigen vector.

Thus, as given by (14), phase voltage and currents can be transformed into modal quantities which make the product matrix $[Z][Y]$ diagonal.

$$[Q]^{-1}[Z][Y][Q]=[\lambda] \quad (14)$$

where $[Q]$ is the transformation matrix of phase voltages, constituted by the eigenvectors associated with each of the eigen values, λ_i , of $[P]=[Z][Y]$. The eigen value matrix, λ can be given by (15),

$$[\lambda_i]=\text{diag}(\lambda_1, \dots, \lambda_n) \quad (15)$$

The propagation constant $\gamma^{(k)}$ of the k^{th} mode is equal to the square root of the k^{th} eigen value of $[Z][Y]$ and is given by (16),

$$\gamma^{(k)}=\lambda_k^{1/2}=\alpha^{(k)}+j\beta^{(k)} \quad (16)$$

where, $\alpha^{(k)}$ is the attenuation constant and $\beta^{(k)}$ is the phase coefficient. The phase velocity $v^{(k)}$ is obtained from (17)

$$v^{(k)}=\omega/\beta^{(k)} \quad (17)$$

where ω is the angular velocity of phase voltages.

The characteristic impedance Z_0 , is given by (18)

$$Z_0=\sqrt{Z/Y}=Q\lambda^{-1/2}Q^{-1}Z \quad (18)$$

V. PARAMETER SENSITIVITY

Sensitivity analysis is an effective method to predict the effect of a parameter on the response of the system. Mathematically, it is given by (19) [13]:

$$\hat{S}_p^F = \frac{\partial F/F}{\partial p/p} = \left(\frac{p}{F}\right) \left(\frac{\partial F}{\partial p}\right) = \frac{\partial(\log F)}{\partial(\log p)} \quad (19)$$

The (19) is applicable for small parameter variations; however, for large parameter variations the same equation can be used in steps, assigning small variations to the parameters until the values corresponding to the system are reached. In any physical system, generally more than one parameter changes simultaneously, for eg., in railway traction system the permeability of the rail track, the earth resistivity, the supply frequency and height of the catenary conductor etc. change simultaneously. Therefore, in order to carry out the complete sensitivity, the Jacobian matrix can be developed as given by (20).

$$J_{0P_i}^F = \begin{Bmatrix} \partial F_1/\partial P_1 \partial F_1/\partial P_2 \dots \partial F_1/\partial P_N \\ \vdots \\ \partial F_A/\partial P_1 \partial F_A/\partial P_2 \dots \partial F_A/\partial P_N \end{Bmatrix} \quad (20)$$

A. Sensitivity Functions

The normalised sensitivity of characteristic impedance, Z_0 , and propagation constant, γ with respect to the generic parameter x_i is given by (21) – (24),

$$\hat{S}_{x_i}^{Z_0} = \frac{x_i}{Z_0} \hat{S}_{x_i}^{Z_0} \quad (21)$$

$$\hat{S}_{x_i}^{\gamma} = \frac{x_i}{\gamma} \hat{S}_{x_i}^{\gamma} \quad (22)$$

where,

$$\hat{S}_{x_i}^{Z_0} = \frac{\partial[Z_0]}{\partial x_i} = \frac{1}{2} (Z^{-1/2} \frac{\partial[Z]}{\partial x_i} Y^{1/2} - Z^{1/2} Y^{-3/2} \frac{\partial[Y]}{\partial x_i}) \quad (23)$$

$$\hat{S}_{x_i}^{\gamma} = \frac{\partial[\gamma]}{\partial x_i} = \frac{1}{2} (Z^{-1/2} \frac{\partial[Z]}{\partial x_i} Y^{1/2} + Z^{1/2} Y^{-1/2} \frac{\partial[Y]}{\partial x_i}) \quad (24)$$

In order to determine the normalised sensitivity of Z_0 and γ , the sensitivity functions of $[Z]$ and $[Y]$ are calculated as given by (25) and (26) respectively,[11]

$$[S_{x_i}^Z] = \frac{\partial[Z]}{\partial x_i} = \frac{\partial R_e}{\partial x_i} + \frac{\partial R_c}{\partial x_i} + \left(\frac{\partial X_e}{\partial x_i} + \frac{\partial X_c}{\partial x_i} + \frac{\partial X_g}{\partial x_i} \right) \quad (25)$$

$$[S_{x_i}^Y] = \frac{\partial[Y]}{\partial x_i} = \frac{\partial G}{\partial x_i} + \left(\frac{\partial C}{\partial x_i} \right); i=1,2, \dots, N_p \quad (26)$$

where N_p represents the number of parameters of interest. From (13), the sensitivity functions of the matrix $[P]$ are obtained as given by (27):

$$[S_{x_i}^P]=[S_{x_i}^Z][Y]+[Z][S_{x_i}^Y] \quad (27)$$

The sensitivity matrix of $[P]$ is used to find the sensitivities of all the eigen values λ_k of $[P]$, as given by (28) [14],

$$[S_{x_i}^{\lambda}] = \frac{\{[S_{x_i}^P][Q_k]\}*[S_k]}{[Q_k]*[S_k]} \quad (28)$$

where $[Q_k]$, $[S_k]$ are the eigenvectors of $[P]$ and $[P_i]$ respectively, associated with the eigen value λ_k , and the asterisk indicates the scalar product of two vectors.

From (16), the sensitivity functions of the modal propagation constants $\gamma^{(k)}$ are given by (29)-(32),

$$S_{x_i}^{\gamma^{(k)}} = S_{x_i}^{\alpha^{(k)}} + j S_{x_i}^{\beta^{(k)}} = (2\gamma^{(k)})^{-1} S_{x_i}^{\lambda^{(k)}} \quad (29)$$

$$S_{x_i}^{\alpha^{(k)}} = R_e\{(2\gamma^{(k)})^{-1} S_{x_i}^{\lambda^{(k)}}\} \quad (30)$$

$$S_{x_i}^{\beta(k)} = I_m \{ (2\gamma^{(k)})^{-1} S_{x_i}^{\lambda(k)} \} \quad (31)$$

$$S_{x_i}^{v(k)} = \frac{v^{(k)}}{\beta^{(k)}} S_{x_i}^{\beta(k)} \quad (32)$$

Finally, the normalised sensitivity functions are obtained as given by (33) - (35):

$$\hat{S}_{x_i}^{\alpha(k)} = \frac{x_i}{\alpha^{(k)}} S_{x_i}^{\alpha(k)} \quad (33)$$

$$\hat{S}_{x_i}^{\beta(k)} = \frac{x_i}{\beta^{(k)}} S_{x_i}^{\beta(k)} \quad (34)$$

$$\hat{S}_{x_i}^{v(k)} = \frac{x_i}{v^{(k)}} S_{x_i}^{v(k)} = \hat{S}_{x_i}^{\beta(k)} \quad (35)$$

VI. NUMERICAL RESULTS

The characteristic parameters of the system are computed using the specifications for catenary and rail track as given in Appendix A. Using (12)- (18), the characteristic impedance, Z_o , propagation constant, γ , and modes of propagation are computed and presented in Table I, II and III.

TABLE I. CHARACTERISTIC IMPEDANCE MATRIX

Characteristic Impedance, Z_o in ohms		
$545.99 - 57.47j$	$0.65 + 0.50j$	$0.65 + 0.50j$
$0.65 + 0.50j$	$7.13 + 6.92j$	$0.49 - 0.55j$
$0.65 + 0.50j$	$0.49 - 0.55j$	$7.13 + 6.92j$

TABLE II. PROPAGATION CONSTANT

γ_{11} (/m)	$(10)^{-3}[0.0001 + 0.0013j]$
$\gamma_{22} = \gamma_{33}$ (/m)	$(10)^{-3}[0.2497 + 0.2413j]$

TABLE III. MODES OF PROPAGATION

Ground Mode	Aerial Mode I	Aerial Mode II
$0.124 - 0.013j$	$-0.000 - 0.000j$	$1.000 + 0.000j$
$0.706 + 0.000j$	$0.707 + 0.000j$	$-0.0005 - 0.003j$
$0.706 + 0.000j$	$-0.707 + 0.000j$	$-0.0005 - 0.003j$

From the Table III, it is observed that there are three modes of propagation for a catenary and rail track lines as shown in Fig. 2. The three modes are independent to each other. The mode related to maximum attenuation and lowest velocity of attenuation is called ground mode whereas the mode having minimum attenuation and maximum velocity is called aerial mode 1 and the other is called aerial mode 2. For ground mode, current is flowing in all of the three conductors. In aerial mode 1, only two outer conductors take part in signal propagation. Here current is entering the rail track conductor 2 and leaving through rail track conductor 3. As the resistivity of catenary conductor is much smaller as compared to rail track, current coming out from catenary is much higher compared to current flowing through track conductors for aerial mode 2.

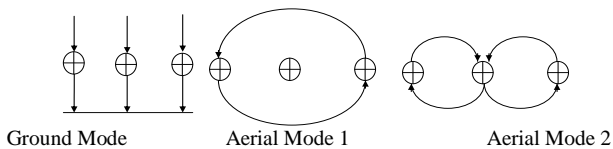


Figure 2. Modes of propagation

Fig. 3-Fig. 6 shows the variation of characteristic impedance of contact wire and rail track conductor respectively with respect to frequency for two frequency ranges. It is noted that characteristic impedance of contact wire decreases wrt the frequency up to around 170 kHz and then starts increasing at higher frequencies whereas the characteristic impedance of rail track conductor increases exponentially with the frequency up to nearly 400 kHz and then it becomes approximately constant at around 620 ohms. It is also observed that propagation constant of both contact wire and rail track conductor increases linearly with the frequency as shown in Fig. 7 and Fig. 8. Fig. 9 and Fig. 10 show that characteristic impedance and propagation constant of rail track conductor varies linearly with the permeability of rail track conductor.

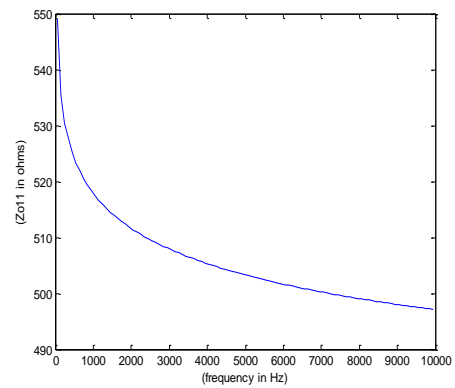


Figure 3. Variation of Z_{o11} with frequency(0-10k Hz.)

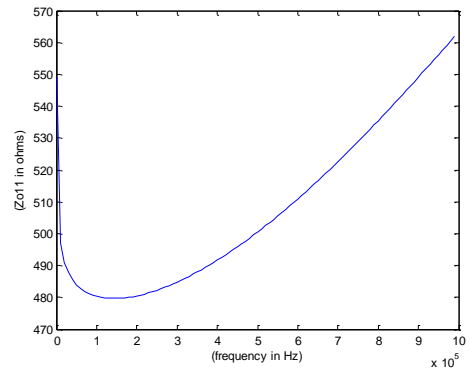


Figure 4. Variation of Z_{o11} with frequency(0-1M Hz.)

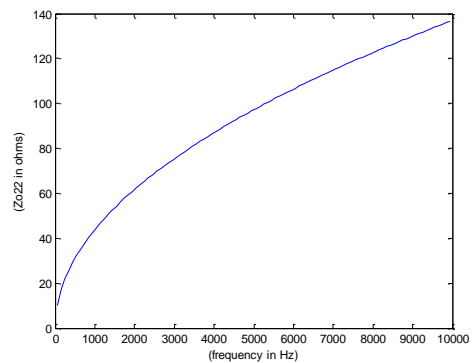
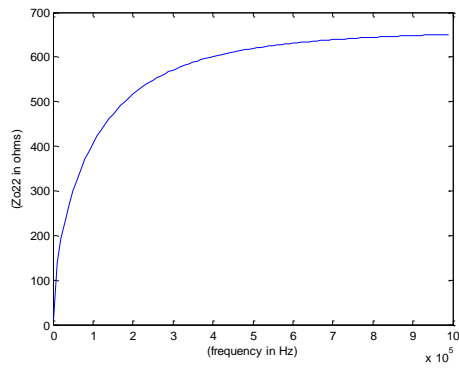
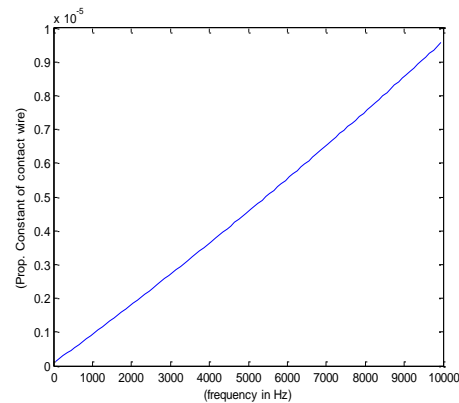
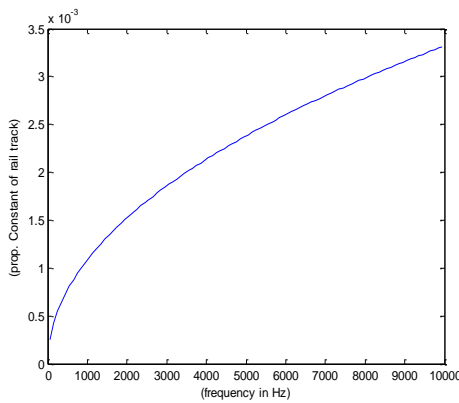
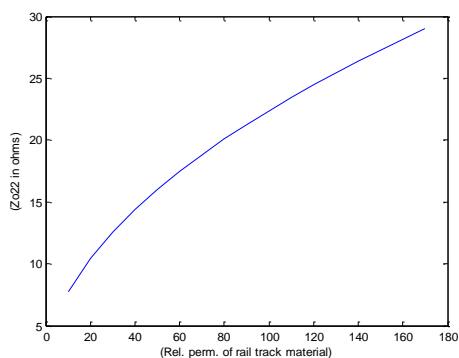
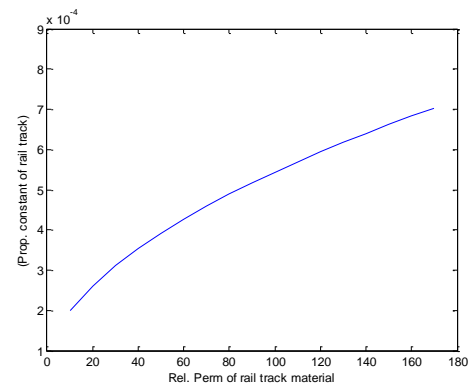


Figure 5. Variation of Z_{o22} with frequency(0-10k Hz.)


 Figure 6. Variation of Z_{022} with frequency(0-1M Hz.)

 Figure 7. Variation of γ_{11} with frequency(0-10 kHz.)

 Figure 8. Variation of γ_{22} with frequency(0-10kHz.)

 Figure 9. Variation of Z_{022} with μ_{tr}

 Figure 10. Variation of γ_{22} with μ_{tr}

Further, the effect of catenary parameters and rail track parameters on characteristic impedance and propagation constant are studied using sensitivity model. The sensitivity analysis of the series impedance and the shunt admittance, on which the characteristic impedance, propagation constant matrix, velocity of propagation and attenuation depend, has been carried out for the system under consideration. The sensitivity functions for series impedance and shunt admittance have been developed, with respect to radius of rail track, supply frequency and permeability of rail track material, first time in the literature and are presented in Appendix B. The results for normalized sensitivity are presented in Table IV. In order to validate the results of Table IV, normalized sensitivity has also been computed using difference equations. The results are presented in Table V and it is observed that the sensitivity computed by two methods conform to each other.

TABLE IV. COMPUTED VALUES OF NORMALIZED SENSITIVITY FROM SENSITIVITY FUNCTIONS DEVELOPED

Parameter \rightarrow Normalised sensitivity	Equivalent Radius of Rail Track	Supply Frequency	Permeability Of Rail Track
$\hat{S}_p^{Rc22} = \hat{S}_p^{Rc33}$	-1.0266	0.5	0.5
$\hat{S}_p^{Xc22} = \hat{S}_p^{Xc33}$	-0.974	0.5	0.5
$\hat{S}_p^{Xg22} = \hat{S}_p^{Xg33}$	-0.389	1	1
\hat{S}_p^{Xg11}	0	1	0
$\hat{S}_p^{Xg12} = \hat{S}_p^{Xg13}$ $= \hat{S}_p^{Xg21} = \hat{S}_p^{Xg31}$	0	1	0
$\hat{S}_p^{Xg23} = \hat{S}_p^{Xg32}$	0	1	1
\hat{S}_p^{Xyc11}	0	1	0
$\hat{S}_p^{Xyc22} = \hat{S}_p^{Xyc23}$	0.409	1	0
$\hat{S}_p^{Xyc13} = \hat{S}_p^{Xyc12}$ $= \hat{S}_p^{Xyc31} = \hat{S}_p^{Xyc21}$	0	1	0
$\hat{S}_p^{Xyc23} = \hat{S}_p^{Xyc32}$	0	1	0
$\hat{S}_p^{G22} = \hat{S}_p^{G33}$	0	0	0
$\hat{S}_p^{G23} = \hat{S}_p^{G32}$	0.310	0	0

TABLE V. COMPUTED VALUES OF NORMALIZED SENSITIVITY FROM DIFFERENCE EQUATIONS

Parameter → Normalised sensitivity	Equivalent Radius of Rail Track	Supply Frequency	Permeability of Rail Track
$\hat{S}_p^{Rc22} = \hat{S}_p^{Rc33}$	-1.057	0.516	0.528
$\hat{S}_p^{Xc22} = \hat{S}_p^{Xc33}$	-0.980	0.581	0.5
$\hat{S}_p^{Xg22} = \hat{S}_p^{Xg33}$	-0.392	0.991	1.01
\hat{S}_p^{Xg11}	0	1.006	0
$\hat{S}_p^{Xg12} = \hat{S}_p^{Xg13}$ $= \hat{S}_p^{Xg21} = \hat{S}_p^{Xg31}$	0	1	0
$\hat{S}_p^{Xg23} = \hat{S}_p^{Xg32}$	0	0.900	1.005
\hat{S}_p^{Xyc11}	0	1	0
$\hat{S}_p^{Xyc22} = \hat{S}_p^{Xyc23}$	0.3894	0.910	0
$\hat{S}_p^{Xyc13} = \hat{S}_p^{Xyc12}$ $= \hat{S}_p^{Xyc31} = \hat{S}_p^{Xyc21}$	0	1	0
$\hat{S}_p^{Xyc23} = \hat{S}_p^{Xyc32}$	0	1	0
$\hat{S}_p^{G22} = \hat{S}_p^{G33}$	0	0	0
$\hat{S}_p^{G23} = \hat{S}_p^{G32}$	0.331	0	0

From the Table IV, it is observed that the variation in the radius of rail track affects the resistance of the rail track the most while the mutual conductance between the rail track is least affected wrt radius of rail track. The other quantities viz. catenary resistance and reactance as well as the self and mutual capacitance of both rail track and catenary are insensitive to radius of rail track. Further, the sensitivity functions and hence, sensitivity of series impedance and shunt admittance matrix elements wrt frequency and permeability are constant.

The normalized sensitivity of characteristic impedance and propagation constant wrt same parameters of interest is calculated and presented in the Table VI.

TABLE VI. NORMALIZED SENSITIVITY OF CHARACTERISTIC IMPEDANCE, Z_0 AND PROPAGATION CONSTANT, γ

Parameter → Normalised sensitivity	Equivalent Radius Of Rail Track	Supply Frequency	Permeability Of Rail Track
\hat{S}_p^{Z011}	-0.0008 + 0.0006i	-0.0715 + 0.0925i	-0.0001 - 0.0013i
$\hat{S}_p^{Z022} = \hat{S}_p^{Z033}$	-0.3088 + 0.0122i	1.4504 - 0.7840i	0.1221 - 0.2348i
\hat{S}_p^{Y11}	-0.0343 - 0.1262i	0.9769 - 0.1527i	0.0565 + 0.0148i
$\hat{S}_p^{Y22} = \hat{S}_p^{Y33}$	-0.3316 - 0.0096i	0.3953 + 0.0379i	0.1017 - 0.1820i

From the Table VI, it is noted that wrt supply frequency, the sensitivity of characteristic impedance of rail track conductors is higher than the sensitivity of characteristic impedance of contact wire whereas propagation constant of contact wire is more sensitive than propagation constant of rail track conductors. The permeability of rail track affects mainly the characteristic impedance and propagation constant of rail track conductor. The equivalent radius of rail track also has negligible effect on the characteristic parameters of contact wire conductors but appreciably effects the parameters related to rail track conductors.

VII. CONCLUSIONS

The mathematical model of integrated contact wire cum rail track has been developed using modal analysis. Characteristic impedance and the propagation constant have been computed and three modes of propagation have been identified. The normalized sensitivity functions related to characteristic impedance and propagation constant have been developed wrt parameters of interest first time in the literature. The results are validated using difference equations. It is observed that characteristic parameters are most sensitive wrt frequency whereas permeability of rail track has minimum effect on these parameters.

The variation of characteristic impedance and propagation constant has been drawn for different frequency range. Also the effect of permeability on these parameters has been studied. The studies shall be useful for the system and design engineer for the protection, signalling and automation schemes of railway electric traction lines.

APPENDIX A SPECIFICATIONS AND DATA USED.

supply frequency = 50Hz;
earth resistivity = 100Ωm;
height of catenary above ground = 6.35m;
height of rail track above ground = 0.75m;
area of catenary conductor = 157mm²;
radius of rail conductor = 115mm;
permeability of rail conductor material = 18;
hysteresis angle = 0.4675radians;
contact wire resistivity = 2.78 10⁻⁸ Ωm;
rail track resistivity = 0.225 × 10⁻⁶ Ωm;

APPENDIX B SENSITIVITY FUNCTIONS DEVELOPED

The sensitivity functions of series impedance and shunt admittance matrix are developed with respect to radius of rail track, supply frequency and permeability of rail material as under:

The sensitivity functions with respect to radius of rail track are given by B.1 – B.10:

$$\hat{S}_a^{Rc22} = \hat{S}_a^{Rc33} = \frac{a}{R_{c22}} * \frac{\partial R_{c22}}{\partial a} = - \left[1 + \frac{[6\delta_r/32a]}{[a/2\delta_r + 3\delta_r/32a]} \right] \quad (B.1)$$

$$\hat{S}_a^{Re11} = \hat{S}_a^{Re11} = \hat{S}_a^{Re22} = \hat{S}_a^{Re33} = \hat{S}_a^{Re13} = \hat{S}_a^{Re12} = \hat{S}_a^{Re21} = \hat{S}_a^{Re31} = \hat{S}_a^{Re23} = \hat{S}_a^{Re32} = 0 \quad (B.2)$$

$$\hat{S}_a^{Xc22} = \hat{S}_a^{Xc33} = \frac{a}{X_{c22}} * \frac{\partial X_{c22}}{\partial a} = - \left[1 - \frac{[6\delta_r/32a]}{[a/2\delta_r + 3\delta_r/32a]} \right] \quad (B.3)$$

$$\hat{S}_a^{Xc12} = \hat{S}_a^{Xc13} = \hat{S}_a^{Xc11} = \hat{S}_a^{Xc21} = \hat{S}_a^{Xc23} = \hat{S}_a^{Xc31} = \hat{S}_a^{Xc32} = 0 \quad (B.4)$$

$$\hat{S}_a^{Xe11} = \hat{S}_a^{Xe22} = \hat{S}_a^{Xe33} = \hat{S}_a^{Xe13} = \hat{S}_a^{Xe12} = \hat{S}_a^{Xe21} = \hat{S}_a^{Xe31} = \hat{S}_a^{Xe23} = \hat{S}_a^{Xe32} = 0 \quad (B.5)$$

$$\hat{S}_a^{Xg22} = \hat{S}_a^{Xg33} = \frac{a}{X_{g22}} * \frac{\partial X_{g22}}{\partial a} = - \frac{1}{\log_n 2h/a} \quad (B.6)$$

$$\hat{S}_a^{Xg12} = \hat{S}_a^{Xg13} = \hat{S}_a^{Xg11} = \hat{S}_a^{Xg21} = \hat{S}_a^{Xg23} = \hat{S}_a^{Xg31} = \hat{S}_a^{Xg32} = \hat{S}_a^{Xg22} = \hat{S}_a^{Xg33} = 0 \quad (B.7)$$

$$\hat{S}_a^{G23} = \hat{S}_a^{G32} = \frac{a}{G_{23}} * \frac{\partial G_{23}}{\partial a} = \frac{1}{\log_n 2b/a} \quad (B.8)$$

$$\hat{S}_a^{C22} = \hat{S}_a^{C33} = \frac{a}{C_{22}} * \frac{\partial C_{22}}{\partial a} = \frac{1}{\log_n 2h/a} \quad (B.9)$$

$$\hat{S}_a^{C11} = \hat{S}_a^{C12} = \hat{S}_a^{C13} = \hat{S}_a^{C21} = \hat{S}_a^{C23} = \hat{S}_a^{C31} = \hat{S}_a^{C32} = 0 \quad (B.10)$$

Sensitivity functions wrt frequency are given by B.11 – B.17:

$$\hat{S}_{\omega}^{RC22} = \hat{S}_{\omega}^{RC33} = \frac{\omega}{R_{c22}} * \frac{\partial R_{c22}}{\partial \omega} = \frac{1}{2} - \frac{[3\delta_r/32a]}{[a/2\delta_r + 3\delta_r/32a]} \quad (B.11)$$

$$\hat{S}_{\omega}^{RC11} = \frac{x^4}{S(4S-2)} \quad (B.12)$$

$$\hat{S}_{\omega}^{Re} = \left[1 + \frac{\omega}{P} \frac{\partial P}{\partial \omega} \right] \quad (B.13)$$

$$\frac{\partial P}{\partial \omega} = \frac{-\pi}{8} \frac{\partial S_4}{\partial \omega} + \frac{1}{2} \left(\log \frac{2}{\gamma c_{ij}} \right) \frac{\partial S_2}{\partial \omega} - \frac{1}{2} \frac{S_2}{c_{ij}} \frac{\partial c_{ij}}{\partial \omega} + \frac{1}{2} \theta_{ij} \frac{\partial S'_2}{\partial \omega} - \frac{1}{2} \frac{\partial \sigma_1}{\partial \omega} + \frac{1}{2\sqrt{2}} \frac{\partial \sigma_2}{\partial \omega} \quad (B.13.1)$$

$$\frac{\partial S_4}{\partial \omega} = \frac{4n}{c_{ij}} S_4 \frac{\partial c_{ij}}{\partial \omega}; \frac{\partial S_2}{\partial \omega} = \frac{2(2n+1)S_2}{c_{ij}} \frac{\partial c_{ij}}{\partial \omega}; \frac{\partial S'_2}{\partial \omega} = \frac{2(2n+1)S'_2}{c_{ij}} \frac{\partial c_{ij}}{\partial \omega}; \quad (B.13.2)$$

$$\frac{\partial \sigma_1}{\partial \omega} = \frac{(4n-1)\sigma_1}{c_{ij}} \frac{\partial c_{ij}}{\partial \omega}; \frac{\partial \sigma_2}{\partial \omega} = \frac{2(2n+1)\sigma_2}{c_{ij}} \frac{\partial c_{ij}}{\partial \omega}; \frac{\partial c_{ij}}{\partial \omega} = \frac{c_{ij}}{2\omega} \quad (B.13.2)$$

$$\hat{S}_{\omega}^{Xe} = \left[1 + \frac{\omega}{Q} \frac{\partial Q}{\partial \omega} \right] \quad (B.14)$$

$$\frac{\partial Q}{\partial \omega} = - \left(\log \frac{2}{\gamma c_{ij}} \right) \frac{\partial S_4}{\partial \omega} - \frac{1}{2} \frac{S_4}{c_{ij}} \frac{\partial c_{ij}}{\partial \omega} - \frac{1}{2} \theta_{ij} \frac{\partial S'_4}{\partial \omega} + \frac{1}{\sqrt{2}} \frac{\partial \sigma_1}{\partial \omega} - \frac{\pi}{8} \frac{\partial S_2}{\partial \omega} + \frac{1}{\sqrt{2}} \frac{\partial \sigma_3}{\partial \omega} - \frac{1}{2} \frac{\partial \sigma_4}{\partial \omega} \quad (B.14.1)$$

$$\frac{\partial S'_4}{\partial \omega} = \frac{4n}{c_{ij}} S'_4 \frac{\partial c_{ij}}{\partial \omega}; \frac{\partial \sigma_3}{\partial \omega} = \frac{(4n-1)\sigma_3}{c_{ij}} \frac{\partial c_{ij}}{\partial \omega}; \frac{\partial \sigma_4}{\partial \omega} = \frac{(4n)\sigma_4}{c_{ij}} \frac{\partial c_{ij}}{\partial \omega} \quad (B.14.2)$$

$$\hat{S}_{\omega}^{XC22} = \hat{S}_{\omega}^{XC33} = \frac{\omega}{X_{c22}} * \frac{\partial X_{c22}}{\partial \omega} = \frac{1}{2} + \frac{[3\delta_r/32a]}{[a/2\delta_r - 3\delta_r/32a]} \quad (B.15)$$

$$\hat{S}_{\omega}^{Xg11} = \hat{S}_{\omega}^{Xg12} = \hat{S}_{\omega}^{Xg13} = \hat{S}_{\omega}^{Xg21} = \hat{S}_{\omega}^{Xg22} = \hat{S}_{\omega}^{Xg23} = \hat{S}_{\omega}^{Xg31} = \hat{S}_{\omega}^{Xg32} = \hat{S}_{\omega}^{Xg33} = 1 \quad (B.16)$$

$$\hat{S}_{\omega}^{C11} = \hat{S}_{\omega}^{C12} = \hat{S}_{\omega}^{C13} = \hat{S}_{\omega}^{C21} = \hat{S}_{\omega}^{C22} = \hat{S}_{\omega}^{C23} = \hat{S}_{\omega}^{C31} = \hat{S}_{\omega}^{C32} = \hat{S}_{\omega}^{C33} = 1 \quad (B.17)$$

Sensitivity functions with respect to permeability of rail track are given by B.18 – B.25:

$$\hat{S}_{\mu_r}^{RC22} = \hat{S}_{\mu_r}^{RC33} = \frac{\mu_r}{R_{c22}} * \frac{\partial R_{c22}}{\partial \mu_r} = \frac{1}{2} - \frac{[3\delta_r/32a]}{[a/2\delta_r + 3\delta_r/32a]} \quad (B.18)$$

$$\hat{S}_{\mu_r}^{RC11} = \hat{S}_{\mu_r}^{Xg11} = \hat{S}_{\mu_r}^{Xg12} = \hat{S}_{\mu_r}^{Xg13} = \hat{S}_{\mu_r}^{Xg21} = \hat{S}_{\mu_r}^{Xg22} = \hat{S}_{\mu_r}^{Xg23} = \hat{S}_{\mu_r}^{Xg31} = \hat{S}_{\mu_r}^{Xg32} = \hat{S}_{\mu_r}^{Xg33} = 0 \quad (B.19)$$

$$\hat{S}_{\mu_r}^{Re11} = \hat{S}_{\mu_r}^{Re22} = \hat{S}_{\mu_r}^{Re33} = \hat{S}_{\mu_r}^{Re13} = \hat{S}_{\mu_r}^{Re12} = \hat{S}_{\mu_r}^{Re21} = \hat{S}_{\mu_r}^{Re31} = \hat{S}_{\mu_r}^{Re23} = \hat{S}_{\mu_r}^{Re32} = 0 \quad (B.20)$$

$$\hat{S}_{\mu_r}^{Xe11} = \hat{S}_{\mu_r}^{Xe22} = \hat{S}_{\mu_r}^{Xe33} = \hat{S}_{\mu_r}^{Xe13} = \hat{S}_{\mu_r}^{Xe12} = \hat{S}_{\mu_r}^{Xe21} = \hat{S}_{\mu_r}^{Xe31} = \hat{S}_{\mu_r}^{Xe23} = \hat{S}_{\mu_r}^{Xe32} = 0 \quad (B.21)$$

$$\hat{S}_{\mu_r}^{XC22} = \hat{S}_{\mu_r}^{XC33} = \frac{\mu_r}{X_{c22}} * \frac{\partial X_{c22}}{\partial \mu_r} = \frac{1}{2} + \frac{[3\delta_r/32a]}{[a/2\delta_r - 3\delta_r/32a]} \quad (B.22)$$

$$\hat{S}_{\mu_r}^{Xg22} = \hat{S}_{\mu_r}^{Xg23} = \hat{S}_{\mu_r}^{Xg32} = \hat{S}_{\mu_r}^{Xg33} = 1 \quad (B.23)$$

$$\hat{S}_{\mu_r}^{C11} = \hat{S}_{\mu_r}^{C12} = \hat{S}_{\mu_r}^{C13} = \hat{S}_{\mu_r}^{C21} = \hat{S}_{\mu_r}^{C22} = \hat{S}_{\mu_r}^{C23} = \hat{S}_{\mu_r}^{C31} = \hat{S}_{\mu_r}^{C32} = \hat{S}_{\mu_r}^{C33} = 0 \quad (B.24)$$

$$\hat{S}_{\mu_r}^{G22} = \hat{S}_{\mu_r}^{G23} = \hat{S}_{\mu_r}^{G32} = \hat{S}_{\mu_r}^{G33} = 0 \quad (B.25)$$

REFERENCES

- [1] R. J. Hill and D. C. Carpenter, "Rail track distributed transmission line impedance and admittance: Theoretical modeling and experimental results," *IEEE Trans. Veh. Technol.*, vol. 42, no. 2, pp. 225-241, May 1993.
- [2] A. Mariscotti, "Distribution of the traction return current in AC and DC electric railway systems," *IEEE Trans. Power Del.*, vol. 18, no. 4, pp. 1422-1432, Oct. 2003.
- [3] A. Mariscoti, M. Rusceli, and M. Vanti, "Modeling of audiofrequency track circuits for validation, tuning, and conducted interference prediction," *IEEE Trans. Intell. Transp. Syst.*, vol. 11, no. 1, pp. 52-60, Mar. 2010.

- [4] R. Cella *et al.*, "Measurement of AT electric railway system currents at power-supply frequency and validation of a multiconductor transmission-line model," *IEEE Trans. Power Del.*, vol. 21, no. 3, pp. 1721-1726, July 2006.
- [5] R. J. Hill, S. Brillante, and P. J. Leonard, "Railway track transmission line parameters from finite element field modelling: Shunt admittance," *Proc. IEE- Electr. Power Appl.*, vol. 147, no. 3, pp. 227-238, May 2000.
- [6] A. Mariscotti and P. Pozzobon, "Determination of the electrical parameters of railway traction lines: calculation, measurement, and reference data," *IEEE Trans. Power Del.*, vol. 19, no. 4, pp. 1538-1546, Oct. 2004.
- [7] A. Mariscoti, "Induced voltage calculation in electric traction systems: Simplified methods, screening factors, and accuracy," *IEEE Trans. Intell. Transp. Syst.*, vol. 12, no. 1, pp. 52-60, Mar. 2011.
- [8] R. H. Galloway, W. Shorrock, and L. M. Wedepohl, "Calculation of electrical parameters for short and long polyphase transmission lines," *Proc. IEE*, vol. 111, pp. 2058-2059, 1969.
- [9] R. J. Hill and D. C. Carpenter, "Determination of rail internal impedance for electric railway traction system simulation," *Proc. IEE*, vol. 138, no. 6, pp. 311-321, Nov. 1991.
- [10] J. R. Carson, "Wave propagation in overhead wires with ground return," *Bell Syst. Tech. J.*, vol. 5, pp. 539-554, Oct. 1926.
- [11] P. Mahajan, R. Garg, and P. Kumar. (2011, Jan.) Sensitivity analysis of railway electric traction system. IICPE 2010. [Online]. Available: IEEE Xplore
- [12] L. M. Wedepohl, "Application of matrix methods to the solution of travelling wave phenomenon in poly phase systems," *Proc. IEE*, vol. 10, no. 13, pp. 2200-2212, Dec. 1963.
- [13] C. S. Indulkar, P. Kumar, and D. P. Kothari, "Sensitivity analysis of modal quantities for underground cables," *Proc. IEE*, vol. 128, no. 4, pp. 229-234, July 1981.
- [14] C. S. Indulkar, P. Kumar, and D. P. Kothari, "Sensitivity analysis of multi conductor transmission line," *Proc. IEEE*, vol. 70, no. 3, pp. 299-300, Mar. 1982.

Rachana Garg received the B.E. and M.E. degree in 1986 and 1989 respectively from NIT, Bhopal. She has obtained her Ph.D in Electrical Engg. from Delhi University in 2009. Presently, she is working as Associate Prof. in Delhi Technological University, Delhi. Her area of interest is modeling of transmission lines, power system operation and control.

Priya Mahajan received the B.E. and M.E. degree in 1996 and 1998 from Thapar Institute of Engg. & Tech. Patiala and Punjab Engg. College, Chandigarh respectively. Presently she is pursuing the Ph.D degree in electrical engineering from Delhi University, Delhi. She is working as Assistant Prof. in Delhi Technological University, Delhi since last 13 years. Her area of interest includes power system and railway traction system.

Parmod Kumar received the B.E., M.E., and Ph.D. degrees in 1972, 1975, and 1982, respectively. After post-graduation in measurement and instrumentation, he joined M.P. Electricity Board, M.P., India, as an Assistant Engineer and commissioned telemetry and SCADA instruments at substations, power stations, and the central control room. In 1983, he joined the Central Electricity Authority as a Dynamic System Engineer and designed and configured the load dispatch centers for electric utilities. Subsequently, he served on various capacities to Indian Railway Construction Company, ERCON, ESPL, ESTC, and then entered academic life in 1991. His area of interest is smart and intelligent system design, operation, and control.

Solid Waste Management: Its Sources, Collection, Transportation and Recycling

Gaurav K. Singh, Kunal Gupta, and Shashank Chaudhary

Abstract—Solid wastes may be defined as useless, unused, unwanted, or discarded material available in solid form. Semisolid food wastes and municipal sludge may also be included in municipal solid waste. The subject of solid wastes came to the national limelight after the passage of the solid waste disposal act of 1965. Today, solid waste is accepted as a major problem of our society. In the United States over 180 million tons of municipal solid waste (MSW) was generated in 1988. At this generation quantity, the average resident of an urban community is responsible for more than 1.8 kg (4.0 lbs.) of solid waste per day. This quantity does not include industrial, mining, agricultural, and animal wastes generated in the country each year. If these quantities are added, the solid waste production rate reaches 45 kg per capita per day (100 lb./c.d.). To introduce the reader to the solid waste management field, an overview of municipal solid waste problems, sources, collection, resource recovery, and disposal methods are presented in this paper. Greater emphasis has been given to the design and operation of municipal sanitary landfills, regulations governing land disposal, and leachate generation, containment and treatment methods.

Index Terms—Community, density, generation, landfills, population, solid waste.

I. INTRODUCTION

Municipal solid waste (MSW) includes wastes such as durable goods, nondurable goods, containers and packaging, food wastes yard wastes, and miscellaneous inorganic wastes from residential, commercial, institutional, and industrial sources. Example of waste from these categories include appliances, newspapers, clothing, food scraps, boxes, disposable tableware, office and classroom paper, wood pallets, and cafeteria wastes. MSW does not include wastes from sources such as municipal sludge, combustion ash, and industrial non-hazardous process wastes that might also be disposed of in municipal waste landfills or incinerators. Determining actual MSW generation rates is difficult. Different studies report a wide variation as they use different components. Many times industrial and demolition wastes are included in municipal solid wastes. Reference [1] has estimated that a total of over 180 million tons of MSW was generated in the United States in 1988, and that the generation is rising at a rate of slightly over 1 percent each year. This estimate is based on a material flow model utilized by [2], and is generally referred to as the EPA/Franklin model [1], [3]. Most of the increase in the MSW generation rate is

due to population growth. However, each person is also generating more waste on an average. It is estimated that, without source reduction, MSW generation will increase to 200 million tons or 1.9 kg/c.d (4.2 lb./c.d) by the year 1995, and 216 million tons or 2.0 kg/c.d (4.4 lb./c.d) by the year 2000. Based on current trends and information, EPA projects that 20 to 28 percent of MSW will be recovered annually by 1995. A successful solid waste management system utilizes many functional elements associated with generation, on-site storage, collection, transfer, transport, characterization and processing, resource recovery and final disposal [4]. All these elements are interrelated, and must be studied and evaluated carefully before any solid waste management system can be adapted. It is a multidisciplinary activity involving engineering principles, economics, and urban and regional planning.

II. SOURCES AND CHARACTERISTICS

Municipal solid waste (MSW) or urban solid waste is normally comprised of food wastes, rubbish, demolition and construction wastes, street sweepings, garden wastes, abandoned vehicles and appliances, and treatment plant residues. Quantity and composition of MSW vary greatly for different municipalities and time of the year. Factors influencing the characteristics of MSW are climate, social customs, per capita income, and degree of urbanization and industrialization. The composition of MSW as collected may vary greatly depending upon geographical region and season. The typical moisture content of MSW may vary from 15 to 40 percent depending upon the composition of the waste and the climatic conditions. The density of MSW depends upon the composition and degree of compaction. The uncompacted density of MSW is around “150 kg/m³ (250 lb./yd³).” The density of collected solid waste is “235-350 kg/m³.” The energy content of MSW as collected is “9,890 kJ/kg (4,260 BTU/lb.)”. Information of chemical composition of the organic portion of MSW is important for many processes such as incineration, composting, biodegradability, leachate generation, and others. The ultimate analysis of the organic fraction of MSW is in terms of the constituents carbon, hydrogen, oxygen, nitrogen, sulfur and ash.

III. COLLECTION AND TRANSPORT

Solid waste collection and transport involves storage at the generation and pick-up points, pick up by the crew, trucks driving around the neighborhood, and truck transport to a transfer station or disposal point. The collection is difficult, complex and costly. Collection of solid waste typically

Manuscript received October 10, 2013; revised December 3, 2013.

The authors are with the Delhi Technological University in Department of Environmental Engineering, New Delhi-110042, India (e-mail: gauravkumardce@gmail.com, guptakunal.dce@gmail.com, shshnkchaudhary73@gmail.com).

consumes 60-80 percent of the total solid waste budget of a community. Therefore, any improvement in the collection system can reduce overall cost significantly [5].

A. Onsite Storage and Handling

In single family residential areas solid waste storage is handled by residents and tenants. Commonly used containers are plastic or galvanized metal containers, and disposable paper or plastic bags. The plastic or galvanized containers are 75-150 liter size with tight covering. The single use paper or plastic bags are generally used when curb service is provided and the homeowner is responsible for placing the bags along the curb. In high-rise buildings the waste is picked up by the building maintenance personnel, or special vertical chutes are provided to deliver the waste to a central location for storage, processing, or resource recovery. A recent development is to provide underground pneumatic transport systems to move waste to a central location for onsite storage, processing, or resource recovery. Apartment districts utilize stationary container systems into which the residents drop the solid wastes. Solid wastes from commercial buildings are collected in large containers that may be stationary or transportable.

B. Collection of Solid Waste

In residential areas, the most common collection methods are curb or alley, setout-setback, and backyard carry. In curb or alley service, the residents carry the single-use plastic bags and containers to the curb or collection point, and then return the empty container after pickup. Setout service utilizes a crew that carries the containers to the collection point. A separate collection crew empties the containers and residents return the empty containers. In setout-setback service, a third crew returns the empty containers. In backyard carry service, the collection crew transfers the solid waste into a wheeled barrel, and then unloads it into the collection truck. The containers remain in the backyard. Many communities have instituted regulations for separation of solid wastes at the source by residents. Components such as newspapers and cardboard, aluminum, mixed glass, and food wastes from restaurants have been separated at the source. Although the concept is good, the participation of the public drops quickly. Also, the price of recycle material fluctuates greatly, and it is often more expensive to recycle waste material. All these factors are considered for instituting a mandatory separation and recycling program. There is, however, much interest in recycling these days due to mounting pressures of decreasing landfill sites, environmental concerns, economic incentives, and political support. The usual vehicle for residential collection of solid wastes is the manually rear or side-loaded compaction truck operating with a crew of two or three, including the driver. The typical truck is 14 to 18 m³ (15 to 20 yd³), and can carry 4 to 5 tons of wastes to the disposal site or transfer station. Reference [6] reported features of new trucks that are equipped with an electronic control system for efficient operation and information storage and retrieval. Large self-loading compactor vehicles are equipped to centers, and then replace the empty ones for reuse at the site. Other container trucks provide container exchange service. They are equipped to carry an empty storage container to a collection point, pick up a full container and transport it to a

central location or disposal site, then replace the empty container at a new location. The frequency of solid waste collection in most communities is once or twice per week. The daily truck routes are fixed and balanced to provide a fair day's work. Several methods are used to optimize the route. Reference [7] has developed heuristic routing rules.

IV. TRANSFER STATION AND TRANSFER

If the disposal site is too far from the city, the time spent by the crew of the pickup truck in unproductive travel becomes excessive. As a result, it may be uneconomical to use collection trucks for travel to the disposal site. Transfer stations are therefore established at convenient locations, and one-person trailer or large trucks, 27 to 46 m³ (35 to 60 yd³) or larger, are used to transfer wastes to the disposal site. Reference [8] reported that long-haul trailer units are more economical if average round-trip haul distance is more than 50 km (30 miles). Among the important considerations in planning and designing a transfer station are location, type of station, access, and environmental effects. At the transfer station, partial or complete solid waste processing such as sorting, shredding, compacting, baling, or composting may be provided. The objective is to reduce the volume, alter the physical form, and recover usable materials. It is important that the transfer station be located as near as possible to the generation center. Good access roads as well as secondary or supplemental means of transportation are necessary. Also, the site must be environmentally acceptable. If more than one transfer station and disposal sites are used, then optimum allocation of wastes from each transfer station to each disposal site will be necessary. This is a classical problem in the field of operations research. Several mathematical models can be used to achieve economical solid waste allocation to the transfer stations and distribution to the disposal sites. References [3], [9], [10] provided examples to optimize solid waste allocation and distribution.

V. RESOURCE RECOVERY AND RECYCLING

Many components of municipal solid wastes can be reused as secondary material. Among these are papers, cardboard, plastic, glass, ferrous metal, aluminum, and other nonferrous metals. These materials must be separated from MSW before they can be recycled. In this section, material recycling, and separation methods are first briefly presented, followed by bioconversion and refuse derived fuel (RDF) methods.

A. Material Recycling

The thrust of much state and local legislative action in mid-1980s was to encourage recycling of various components of municipal solid waste. Many have been made in the area of recycling, but not have been very successful. There are several reasons such as recycled material may contain increased levels of foreign materials that could interfere with product quality, uncertainty of supply and price variation of secondary material, methods of quality control of recycled material are not developed as for virgin materials. Many components of MSW are currently recycled. Among these are paper and paper products. These products are

recycled in manufacturing building materials such as roofing felt, insulation and wallboard, and are also used to manufacture cartons and containers. Plastic is recycled to produce insulating material, sheets, bags, and structural material. Energy is recovered from combustion of organic wastes. Other components of MSW (1990) estimate that approximately 13% of MSW is currently recycled, and a 14 percent fraction is incinerated.

B. Separation Methods

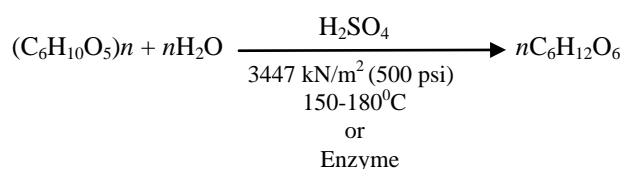
The separation of material is performed by the users at the source, or separated from mixed refuse at a central processing facility. Material separation at the source involves users separating the material into different components, followed by transporting from the point of generation to a secondary material dealer. Unfortunately, active household response for separation at the source has been very poor. As a result, effort has been directed toward separation of MSW at a central facility. Handpicking is a long-used form of separation of a few components of solid wastes. In this operation, a conveyor moves the solid waste pass by a group of workers who pick up the designated components by hand. This method of separation is costly, and only a few bulky components, such as bundled newspapers and cardboard, can be separated. A mechanized material recovery method provided by [11] utilizes shearers that break open the bags and liberate cans and bottles. Trammel screens separate cans, glass and other inorganic material. The organic material is shredded and passed through air classifiers, which separate the components desired for recovery of fibers for paper making or for producing refuse derived fuel. Magnetic and electromechanical systems separate ferrous and nonferrous metals.

C. Bioconversion

Bioconversion of the organic fraction of municipal solid waste into a number of products including sugar, ethanol, and protein compost, has been reported in the literature by [4], [10]-[13].

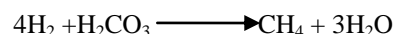
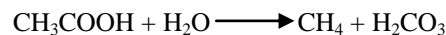
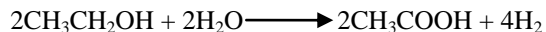
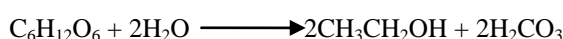
1) Sugar

The recovery of fibers from paper has cellulose as major constituent. The cellulose is hydrolyzed into sugars. The hydrolysis of cellulose produces glucose and mixtures of other sugars. Hydrolysis of paper fibers is achieved under low pH, or by enzymes. The hydrolysis reaction is given by Equation:



2) Ethanol and other fermentation products

Microorganisms can produce alcohols and short-chain organic acids. These products have commercial value in the industrial chemical market. Some of these fermentation reactions are given by equations



Many researchers have investigated the production of commercial quantities of these products using paper fibers recovered from municipal solid wastes. However, the cost of production and recovery of these products in a relatively pure state from MSW is much greater than the cost of producing the raw materials.

3) Protein

Earlier research conducted by the Denver Research Institute suggested that fibers produced from waste paper can be converted to protein using a fast-growing-hydrocarbon-cellulose digesting organism. The organism is *Candia utilis* culture, commonly called Torula yeast. The protein thus produced is usable by livestock [12]. Another concept, reported by [11], is to utilize processed organic wastes as the feedstock for a rapidly expanding population of red earthworms. This process is called annelidic recycling. The organic component is converted into a rich fertilizer in the form of worm of worm castings, the excess worms are dried into high-protein food supplement in animal food. Another similar concept is to breed flies and recover larvae as a protein source for animal feed supplement.

VI. INCINERATION AND ENERGY RECOVERY

Incineration of MSW is practiced to reduce waste volume and recover energy. The batch-fed incinerators built in the 1930s and 1940s reduced the volume but were major contributors of air pollution problems. Most of these incinerators have been shut down or replaced by newer designs. The newer incinerators utilize innovative technology to produce steam more efficiently and reduce air pollutants to greater extent. The capital and operating costs, however, are quite high. Reference [8] reported capital cost about \$120 million per 1000 tons of daily capacity, and operating cost of \$15 to \$30 per ton, for cities over 300,000 populations (1987 dollars). The unit cost of incinerators for smaller cities is even larger. The high cost of installing the air pollution control equipment forced municipalities to seek cheaper methods such as sanitary landfills for solid waste disposal. Due to stricter regulation on landfilling, and rapidly diminishing capacity, there is renewed interest in incinerator design and construction. Reference [9] reported that in 1978 there were only 56 facilities that remained active in United States. Today there are more than 100 facilities in operation, and over 100 more are in the planning and construction stages.

VII. REFUSE-DERIVED FUEL (RDF)

Solid wastes may be burned directly in incinerators (a process called mass-burning) or converted to more efficient

refuse-derived fuel (RDF). The solid waste is processed by means of size reduction and material separation techniques to obtain a product which has a substantial heat value. Physically, shredded and air classified organic fraction of solid wastes are burned along with a fossil fuel such as coal. Many boilers need only minor modifications to accept such fuel. Also, the shredded and air classified solid wastes can be made densely into cubes or pellets that are suitable for many thermal conversion processes such as incineration, gasification, and pyrolysis. Many communities have built refuse-to-energy plants that are fast replacing sanitary landfills. The steam is used for heating and for driving turbines to produce electricity. Reference [14] has reported that there are 190 municipal waste combustor plants in the USA. Of these, 142 facilities are waste-to-energy combustors. The total processing capacity exceeds 31.4 million tons of MSW per year. These facilities do not include RDF-processing plants or simple incinerators. There are also approximately 49 waste-to-energy combustors planned or under construction.

VIII. DISPOSAL BY LANDFILLING

The volume of municipal solid waste is greatly reduced by incineration, conversion processes or resource recovery. In all cases, there is a residue that must be disposed of so that it no longer creates a nuisance or hazard to the society. Engineering principles must be followed for site selection and design of ultimate-land disposal methods. An acceptable land disposal method of MSW and residues utilizes sanitary landfills. Sanitary landfilling is the most common method of solid waste disposal in the United States. It is economical, and applies to all components of MSW. Proper site selection is perhaps the most difficult part of disposal by landfilling. The operation involves compaction of solid wastes in layers, then covering with a layer of compacted soil at the end of each day's operation. In recent years, special care has been required in site selection, refuse compaction, cover application, leachate collection and treatment, and site monitoring.

IX. CONCLUSIONS

The quantity of MSW generated is increasing rapidly due to increasing population and change in lifestyle. The current MSW crisis should be approached holistically; while planning for long term solutions, focus on the solving the present problems should be maintained. The Government and local authorities should work with their partners to promote source separation, achieve higher percentages of recycling and produce high quality compost from organics. While this is being achieved and recycling is increased, provisions should be made to handle the non-recyclable wastes that are being generated and will continue to be generated in the future. Policy to include waste-pickers in the private sector must be introduced to utilize their low cost public and environmental service and to provide better working conditions to these marginalized populations.

REFERENCES

- [1] U.S. Environmental Protection Agency, "Characterization of municipal solid waste in the United States," *Solid Waste and Emergency Response*, Washington D.C., 1990.
- [2] U.S. Environmental Protection Agency, "Characterization of municipal solid waste in the United States," Final Report Prepared by Franklin Associates, Inc, 1988.
- [3] P. A. Vesilind, J. J. Pierce, and R. F. Weiner, *Environmental Engineering*, 2nd ed. Boston, MA: Butterworth's, 1988.
- [4] U.S. Environmental Protection Agency, "Decision-Makers guide in solid waste management," SW-500, Washington D.C.: U.S. Government Printing Office, 1976.
- [5] U.S. Congress, "Facing America's trash: What next for municipal solid waste," OTA-0-424, Office of Technology Assessment, Washington D.C.: U.S. Government Printing Office, 1989.
- [6] R. Woods, "Refuse vehicles of the '90s," *Waste Age*, vol. 23, no. 5, 38-44, 1992.
- [7] K. A. Shuster and D. A. Schur, "Heuristic routing for solid waste collection vehicles," *SW-11*, U.S. Environmental Protection Agency, 1974.
- [8] Matrecon, "Lining of waste impoundment and disposal facilities," SW-870, U.S. Environmental Protection Agency, Cincinnati, OH, 1980.
- [9] M. L. Davis and D. A. Cornwell, *Introduction to Environmental Engineering*, 2nd ed. New York: MacGraw-Hills, Inc, 1991.
- [10] G. Tchobanoglous, H. Theisen, and S. Vigil, "Integrated solid waste management," *Engineering Principles and Management Issues*, New York: McGraw Hill, 1993.
- [11] D. C. Wilson, *Waste Management: Planning, Evaluation Technologies*, Oxford: Clarendon Press, 1981.
- [12] N. L. Drobny, H. E. Hull, and R. F. Testin, "Recovery and utilization of municipal solid waste," EPA-SW-10C-71, U.S. Environmental Protection Agency, Office of Solid Waste Management Program, Washington D.C. (NTIS No. PB-204 922), 1971.
- [13] P. A. Vesilind and A. E. Rimer, *Unit Operations in Response Recovery Engineering*, Englewood Cliffs, NJ: Prentice Hall, Inc, 1981.
- [14] J. V. L. Kiser, "Municipal waste combustion in North America," *Waste Age*, vol. 23, no. 11, pp. 26-34, 1992.



Gaurav Kumar Singh was born in Darbhanga, Bihar, India on March 17, 1993. He passed his 10th class in 2008 and 12th class in 2010 from The Air Force School (TAFS), Delhi, India achieving 1st division with distinction. He is currently pursuing B.Tech. in environmental engineering from Delhi Technological University, Delhi, India and expected year of completion of course is 2015.

He did internship in Central Road Research Institute (CRRI) on the project of measuring the fuel consumption of vehicles at idling condition and in Delhi Metro Rail Corporation (DMRC) on energy efficiency of metro trains. He published research paper on "Spectrometric determination of NO₂ in ambient air and its control" in International Journal of Environmental Engineering and Management (IJEEM) and presented at the 2nd International Conference on "Agriculture, Food Technologies and Environment (AFTENA 2013)" held in JNU, India.

Mr. Singh was awarded scholarship of Rs. 5,000 by AFFWA (IAF) for obtaining above 80% in AISSCE and qualified prestigious All Indian Engineering Entrance Examination and stood among top 0.90% students that appeared for AIEEE 2011. Mr. Singh has also achieved expertise in AutoCAD 2D & 3D and was presented 'Grade A' in prestigious United Nation Rio+20 India Program.



Kunal Gupta was born in Ajmer, Rajasthan, India on March 30, 1993. He passed his AISSE exam in 2009 and AISSCE exam in 2011 from Aklank Public School, Kota, Rajasthan, India achieving 1st division with distinction. He is currently pursuing B.Tech. in environmental engineering from Delhi Technological University, Delhi, India and expected year of completion of course is 2015.

He did internship in DCM Shriram Consolidated Ltd. (DSCL), Kota, Rajasthan, India on the project of air quality monitoring in heavy industrial areas and in Kota Thermal power Station. He published

research paper on “Spectrometric determination of NO₂ in ambient air and its control” in International Journal of Environmental Engineering and Management (IJEEM) and presented in the 2nd International Conference on “Agriculture, Food Technologies and Environment (AFTENA 2013)” held in JNU, India.

Mr. Gupta had qualified prestigious All Indian Engineering Entrance Examination and stood among top 0.92% students that appeared for AIEEE 2011.



Shashank Chaudhary was born in Lucknow, Uttar Pradesh, India on May 20, 1991. He passed his AISSE exam in 2008 and AISSCE exam in 2010 from Delhi Public School, Lucknow, Uttar Pradesh, India achieving 1st division with distinction. He is currently pursuing B.Tech. in Polymer Science and Chemical Technology from Delhi Technological University, Delhi, India and expected year of completion of course

is 2015.

He did his internship in BASF-The Chemical Company, Delhi, India as a mentor in Indo-German Urban Mela Delhi, India and Hindustan Petroleum Corporation Limited Lucknow, India. He worked as a corporate team member of team DTU-Solaris (India's one and only Solar Car Team).

Mr. Chaudhary had qualified prestigious All Indian Engineering Entrance Examination and stood among top 0.92% students that appeared for AIEEE 2011.

Speed Control of Hybrid Electric Vehicle Using Artificial Intelligence Techniques

Japjeet Kaur, Prerna Gaur, Piyush Saxena and Vikas Kumar

Department of Instrumentation of Control Engineering, Netaji Subhas Institute of Technology, New Delhi, India

*E-mail: japjeet_shiney@yahoo.co.in, prernagaur@yahoo.com, piyushsaxena@yahoo.com
sainivika@gmail.com*

Received: 24 Aug. 2013, Revised: 28 Oct. 2013, Accepted: 30 Oct. 2013, Published: 1 Jan. 2014

Abstract: Growing concerns regarding toxic CO_x and NO_x emissions caused by the vehicles and the scarcity of over-exploited non-renewable resources that led the automobile industry to look out for a more energy efficient energy consumption is the main reason behind the development of Hybrid Electric Vehicles (HEVs). This paper comprises of artificial intelligence techniques employed to achieve smooth speed tracking performance in nonlinear HEVs. Techniques like fuzzy logic, neural network and genetic algorithm have been applied to tune and optimize the parameters of Proportional-Integral-Derivative (PID) controller.

Keywords: Hybrid Electric Vehicle; Artificial Intelligence techniques; PID controller; optimization; Fuzzy logic; Neural Networks; Genetic Algorithm.

I. INTRODUCTION

Surprisingly, the concept of a hybrid electric vehicle is almost as old as the automobile itself. The primary purpose, however, was not so much to lower the fuel consumption but rather to assist the ICE to provide an acceptable level of performance. But this highly developed automobile industry has resulted in the deterioration in air quality, global warming and decrease in non-replenishable petroleum resources. More and more stringent emissions and fuel consumption regulations have stimulated an interest in the development of safe, clean, and high-efficiency transportation. In recent decades, the research and development activities related to transportation have emphasized that the hybrid is the ideal transition from the all-petroleum vehicle to the all-electric vehicle.

The pioneering authors are actively working to improve the fuel economy and vehicle performance so as to achieve high efficiency, ruggedness, small sizes, and low costs in power converters and electric machines, as well as in associated electronics [1]. The performance of HEV depends primarily on the applied automation system but the conventional controllers designed haven't proved to be competent due to imprecise input output relation and unknown external disturbances. Many controllers such as

LQR controller, state feedback controller, observer based controller have been designed in near past [2-3].

By controlling the servo motor which in turn is controlling the throttle position to have smooth torque, the speed of the HEVs can be controlled. Some other authors have proposed different control technique for electric vehicle [5].

This work comprises the tuning of a conventional PID controller used to optimize the speed of the HEV. There are a number of tuning methods for classical controllers, such as, the Ziegler-Nichols methods, pole placement procedures, the quarter decay ratio method, performance indices (ISE, IAE, ITAE, and ITSE) based optimization. Nowadays, all these methods are usually employed to a limited class of problems as they possess some drawback. In this paper, we propose an automatic tuning method for a PID controller by means of artificial intelligence techniques: Fuzzy Logic, Artificial Neural network and Genetic Algorithm (GA).

This paper is organized as follows: in section two the details of the model undertaken are posed; section three presents the control strategy used; section four shows the results; and hence conclusions are drawn in section five.

II. SYSTEM DETAILS

Fig. 1 shows a schematic diagram of the electronic throttle control using a DC servo motor. The dynamics of the vehicle are taken as configuration of leader-follower [2], [6] given below and the hence designed Simulink model is shown in Fig. 2.

Given below are the assumptions made:

1. Gravity induced force (f_g) is 30% of weight of vehicle.
2. Engine time constant (τ_f) is taken as 0.2s that generally ranges from 0.1 to 1sec.

The value of all other parameters is shown in Table I.

A. Open Loop Stability Analysis

The transfer function is obtained from given system dynamics and hence state equation is obtained. [2]

Transfer function:

$$\frac{V(s)}{\theta(s)} = \frac{829000}{s(s+5)}$$

State space variable:

$$A = \begin{bmatrix} 0 & 1 \\ 0 & -5 \end{bmatrix}, \quad B = \begin{bmatrix} 0 \\ 829000 \end{bmatrix}$$

$$C = [1 \quad 0], \quad D = [0]$$

The characteristic equations of system is $|\lambda I - A| = 0$, whence we get the eigenvalues as $\lambda_1 = 0$, $\lambda_2 = -5$. The system is found controllable and observable, as the order of matrix M and N is equal to rank = 1; $M = 829000 \times \begin{bmatrix} 0 & 1 \\ 1 & -5 \end{bmatrix}$, $N = \begin{bmatrix} 1 & 0 \\ 0 & 1 \end{bmatrix}$.

III. CONTROL STRATEGIES

A. PID Controller

Proportional-integral-derivative control is a feedback controller involving three separate constant parameters, the proportional, the integral and derivative values, denoted P, I, and D, therefore sometimes called three-term control: The Simulink model of vehicle controlled by PID controller is shown in Fig. 3.

By combining the advantages like quicker response time (due to P-only control), along with the decreased/zero offset (due to I-only control) and prediction of disturbances to the system (due to D-control) minimizes the error between some user-defined set point and the measured process variable. The actuating signal for the PID controller and the transfer function are given in (3) and (4)

$$e_a(t) = e(t) + K_d \frac{de(t)}{dt} + K_i \int e(t) dt \quad (3)$$

$$C(s) = K_p + \frac{K_i}{s} + K_d s = K_p \left(1 + \frac{1}{T_i s} + T_d s \right) \quad (4)$$

Where: K_p = Proportional Gain, K_i = Integral Gain, T_i = ResetTime = K_p/K_i , K_d = Derivative gain, T_d = Rate time or derivative time = K_d/K_p .

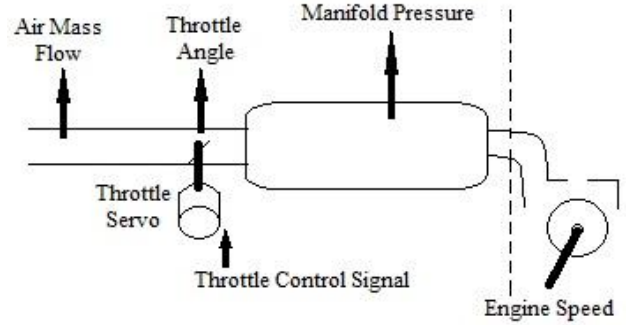


Figure 1. Schematic diagram of electronic throttle control [2]

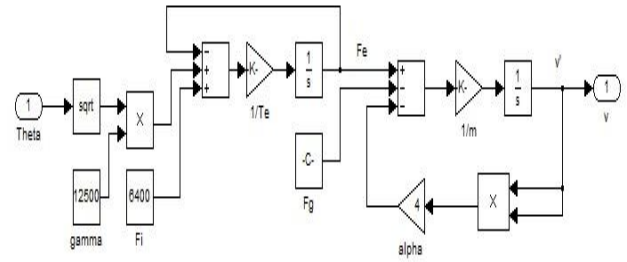


Figure 2. Simulink model of Hybrid Electric Vehicle

TABLE I. NUMERICAL VALUES OF THE PARAMETERS

Constant	Notation	Value (SI Unit)
Mass of Vehicle	M	1000 Kg
Aerodynamic Drag Coefficient	α	4 N/(m/s) ²
Engine Force Coefficient	γ	12500 N
Engine Idle Force	f_i	6400 N

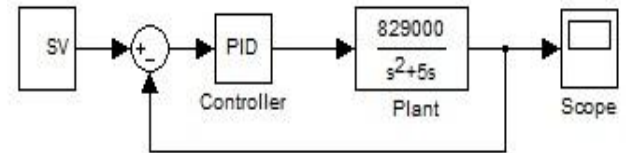


Figure 3. Model with PID Controller

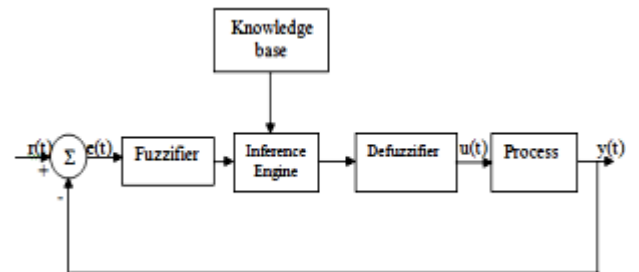


Figure 4. Block diagram of fuzzy controller

B. Fuzzy Logic

The first seminal paper of “Fuzzy Logic” was given by Prof. Lotfi Zadeh in 1965 on Sets the Foundation of the Fuzzy Set theory. Fuzzy systems are knowledge/rule based systems resembling human decision making with an ability to generate precise solutions from certain or

approximate information. While other approaches require accurate equations to model real world behaviours; fuzzy logic can accommodate the ambiguities of real-world human language and logic by providing an intuitive method for describing systems in human terms and converting it into effective models.

Being non-linear in nature, it is more difficult to set the gains in fuzzy logic controller (FLC) shown in Fig. 4, as compared to PID controllers. In this paper, two types of configurations are applied, mainly, fuzzy PD and fuzzy PD+I. The Mamdani based FLC has two-input (e, ce), divided into seven states and one-output (u). The control performance depends on the adopted rule base, so, 7 inputs & 7 output membership functions are described in 49 Fuzzy-if-then rules given in Table II.

Note that states are represented as abbreviations like “NS” for “negative small” and so on as it helps to keep the linguistic descriptions short yet precise.

Fig.5 shows Simulink model of HEV with fuzzy PD Controller and Fig.6 shows the simulink model of fuzzy PD block. Similarly, Fig. 7 and 8 shows the model with fuzzy PD+I controller and its block respectively. It gives the better performance in comparison to conventional PID controller and improves the performance index such as maximum overshoot, settling time, and steady state error.

C. Neural Network

Neural networks, with their remarkable ability to derive meaning from complicated or imprecise data, are good pattern recognition engines that comprise collections of identical mathematical models emulating the behaviour of biological nervous systems. ANN's have shown that they are capable of identifying complex nonlinear systems and are well suited for generating the complex internal mapping from inputs to control actions by detecting trends that are too complex to be noticed by either humans or other computer techniques.

Fig. 9 shows proposed neural network controller, which was trained to replace the conventional PID speed controller. The neural network controller which is static type has replaced PID controller, thus simplifying the control implementation and reducing the development time. In this paper, a 3-layer back-propagation based feed-forward artificial neural network controller is designed. All nodes of specific layer are connected by weights that represent the strength of the connection.

The designed neural network controller hence obtained is trained using the target values to find out the desired mean square error. During training, the output signal is compared to the desired output signal, and the weights are adjusted each time by the back-propagation algorithm. Fig. 10 shows the Simulink model of HEV with ANN controller.

D. Genetic Algorithm

Genetic Algorithm, formerly introduced by John Holland in the 60s, is an adaptive heuristic, stochastic global search method inspired by Darwinian evolutionary ideas. Operating on the principle of the survival of the

fittest, they intelligently exploit a population of potential solutions within a defined search space and provide alternative methods to solve real-world high-dimensional, nonlinear problems.

TABLE II. FUZZY RULE BASE

(e)\(ce)	NB	NM	NS	ZE	PS	PM	PB
NB	NB	NB	NB	NB	NB	NM	ZE
NM	NB	NB	NB	NB	NM	ZE	PM
NS	NB	NB	NB	NM	ZE	PM	PB
ZE	NB	NB	NB	ZE	PM	PB	PB
PS	NB	NM	ZE	PM	PB	PB	PB
PM	NM	ZE	PM	PB	PB	PB	PB
PB	ZE	PM	PB	PB	PB	PB	PB

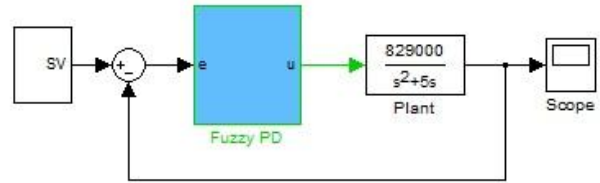


Figure 5. Simulink model of HEV with Fuzzy PD controller

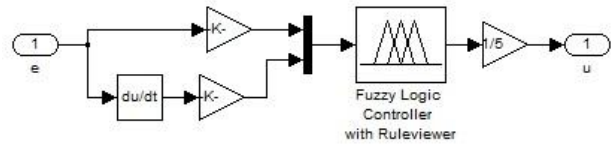


Figure 6. Fuzzy PD Block

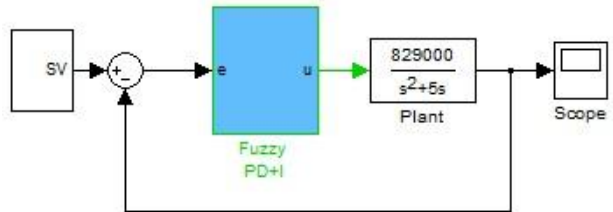


Figure 7. Simulink model of HEV with Fuzzy PD+I controller

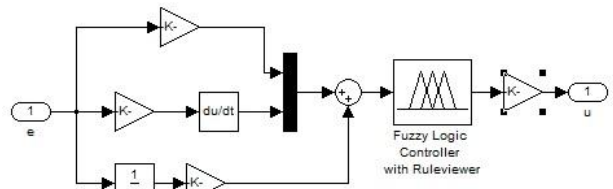


Figure 8. Fuzzy PD+I Block

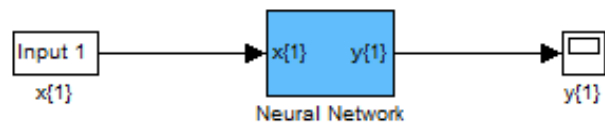


Figure 9. Generated proposed ANN model to replace PID controller

A GA based optimization process generates a random set of approximations (binary or decimal strings) termed as population by selecting individuals according to their fitness levels. Based on nature-inspired operators (reproduction, crossover, mutation etc.) new individuals (better suited) are created at each generation. The fitness is usually the value of the objective function in the optimization problem being solved. The procedure then stops when a pre-defined number of generations is reached or before that if a very good solution is found.

This parallel, global search procedure does not require any derivative information or other auxiliary knowledge other than the fitness levels and the objective. In this paper, the objective is smooth throttle movement and quickest settling time that will minimize the error of the controlled system. The fitness function provides a link to the application wherein a suitable weighted function is defined that considers each constraint to analyse the performance of each chromosome in the population. The objective function includes the way the parameters are to be minimized. This means that an optimal solution is found to satisfy a priori defined fitness function.

1) *Selection*: The selection operator primarily determines the eligibility of the solutions based on the fitness evaluation that will later generate offsprings of future populations. The chances for recombination and generation of offspring are higher for the individuals having small fitness function value, if the optimization problem is a minimization one. In this work the Uniform Selection is employed to implement the selection operator.

Reproduction cannot create new and better strings. This improvement may be achieved by Crossover and to a lesser extent by Mutation.

2) *Crossover*: This is a genetic operator that combines (mates) two individuals (parents) to produce a new one (offspring) according to a user-definable crossover probability. It selects random individuals from mating pool and the gene information between them is exchanged (according to defined crossover ratio) such that it takes the best characteristics from each of the parents.

3) *Mutation*: The mutation operator ensures that genetic diversity is maintained in the mating pool by removing or reinserting a critical feature (genetic information) from a population and so it is considered as a secondary mechanism of GA adaption. New individuals are generated by random modification of the value of a string position (gene) that will converge the search algorithm to a global solution.

The goal of the system is to design a controller that ensures optimal speed tracking performance. The code is written using Mfile in MATLAB. The integral gains of the PID controller are optimized based on the Genetic Algorithm. GA is used to calculate the optimum value of the variables based on the best dynamic performance and a domain search of the variable.

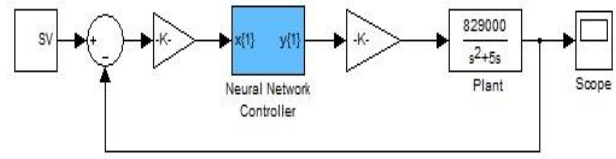


Figure 10. Simulink model of HEV with ANN controller

TABLE III. PARAMETERS OF GA

Operators	Values/Parameters Assigned
Population Size	20
Selection	Uniform
Crossover	Arithmetic
Objective Function	Mean Square Error

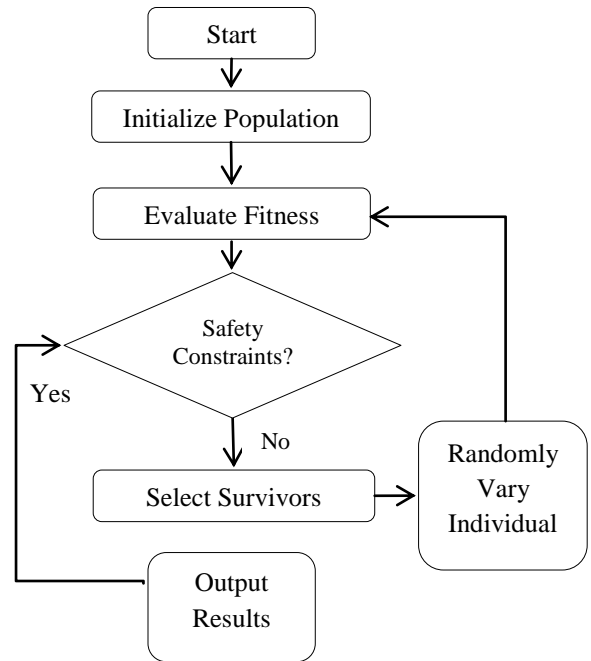


Figure 11. Flow Chart for the operation of GA control

GA finds the values of K_p , K_i and K_d of the PID controller based on chosen operators, to achieve better dynamic performance of the overall system. These values of gains lead to the optimum value of gains for which the system achieves the desired values by improving the rising time and oscillations. The main aspects of the proposed GA approach for optimizing the gains of PID controller, and the flowchart procedure for the GA optimization process is shown in Fig. 11. Parameters considered in GA are shown in Table III.

IV. SIMULATION RESULTS AND DISCUSSIONS

In this section the results obtained from the open loop system without controller and closed loop system with controller are presented. The response of the system with controllers such as PID and GA tuned PID are presented and compared. Fig. 12 shows the Open loop step response that shows the system is unstable as it is not converging.

Fig. 13 shows the response with PID Controller. Here PID controller is tuned by using both Hand-tuning rule and Ziegler-Nichols method that gives 46.7% and 15.6% Max overshoot respectively. Tuning by hand tuning rule gives better performance. Fig. 13 also shows the vehicle response for GA-tuned PID, which is an improvement over the former one.

Fig. 14 shows the response with ANN controller, where it takes longer time for controlling the vehicle. Fig. 15 and 16 shows the fuzzy PD and fuzzy PD+I controller response, where both reduces the overshoot and settling time as well.

Fig. 17 shows the combined response of all controllers for first 5 seconds to make the comparison among them and Fig. 18 shows the enlarged view of Fig. 17. The performance index shown in Table IV is made by using Fig. 18.

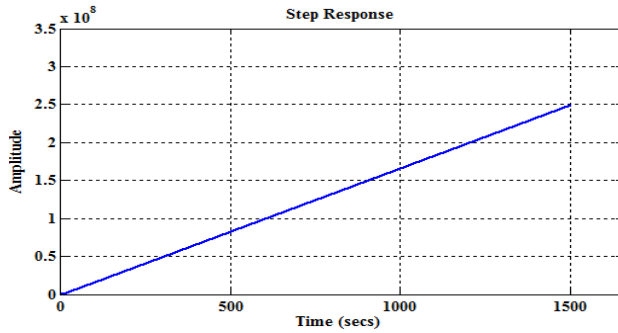


Figure 12. Open Loop Step Response

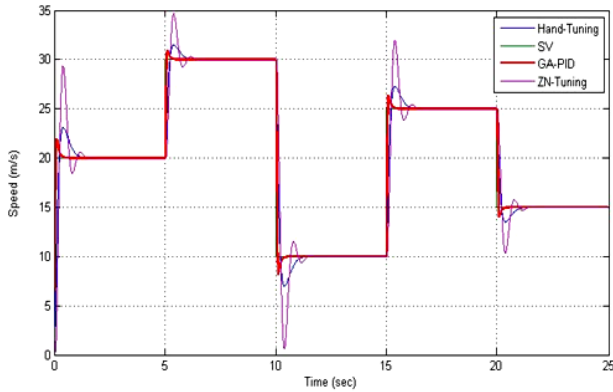


Figure 13. Vehicle response of Conventional PID and GA-tuned PID controller

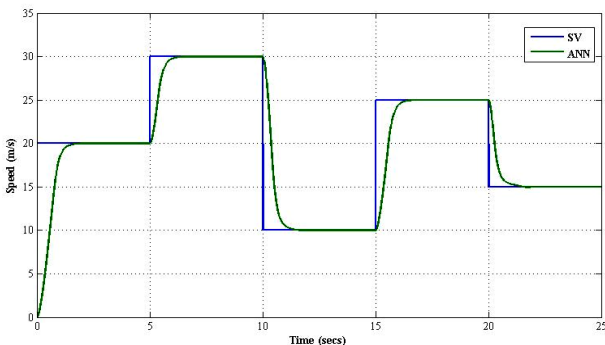


Figure 14. Vehicle response with ANN controller

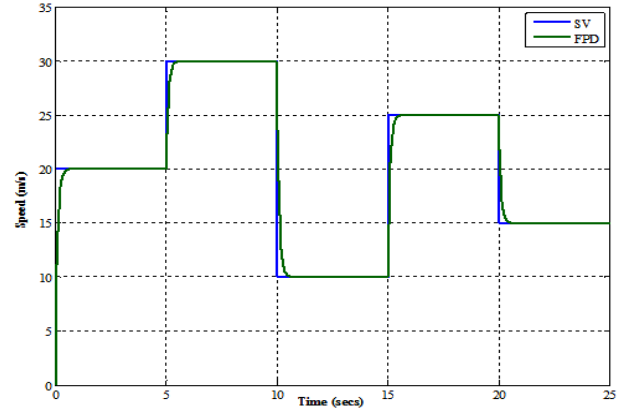


Figure 15. Vehicle response with Fuzzy PD controller

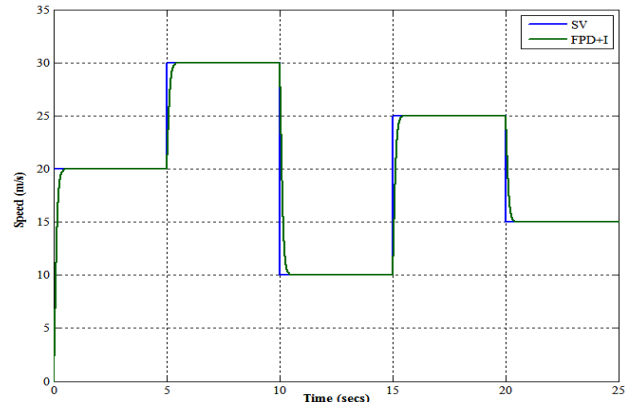


Figure 16. Vehicle response with Fuzzy PD+I controller

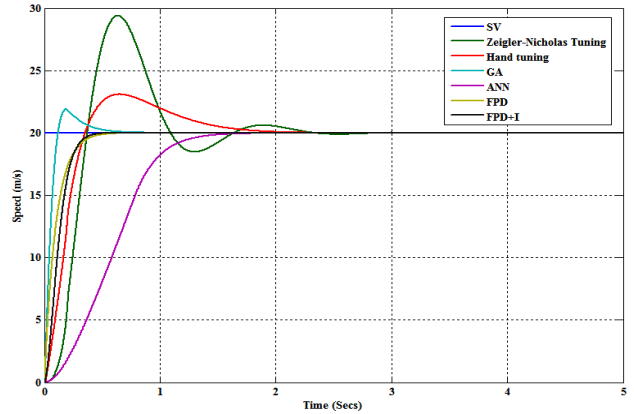


Figure 17. Combined Vehicle Response

On the basis of Fig. 18 that shows the enlarged view of Fig. 17 and Table IV, the Fuzzy PD+I controller response has got least max. overshoot, i.e. 0%. Hence fuzzy PD+I controller gives better performance index in comparison with PID.

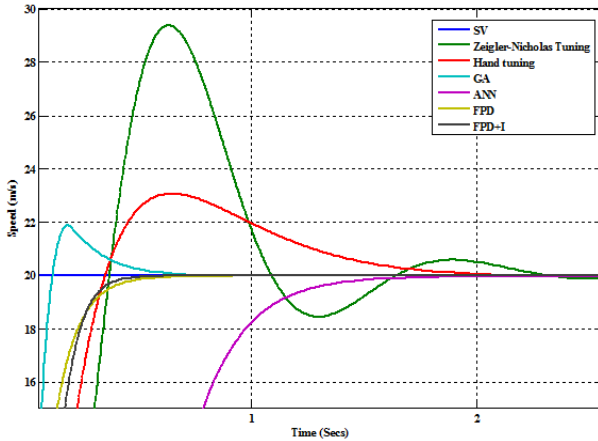


Figure 18. Combined Vehicle response (enlarged)

TABLE IV. PERFORMANCE INDICES

Controllers	% Max Overshoot	Settling Time (s)	Rise Time (s)
PID	15.6	0.79	0.19
GA-PID	9.5	0.27	0.05
ANN	~0	1.29	0.765
FPD	~0	0.392	0.218
FPD+I	~0	0.352	0.205

V. CONCLUSION

A comparative analysis of all the controllers applied to control the speed of nonlinear hybrid electrical vehicle, vividly shows that fuzzy PD+I controller gives better performance result. Although the settling time and rise time are more than that of GA but since our design objective is to have smooth throttle control so as to have reduced torque ripples that will in turn reduce the current and overall operating cost and increase battery life. Also the battery operation of such vehicles will be optimal. Vehicle drive train efficiency may be improved and the fuel efficiency of HEV may also be optimized.

REFERENCES

- [1] Ali Emadi, Young Joo Lee, and Kaushik Rajashekara, "Power Electronics and Motor Drives in Electric, Hybrid Electric, and Plug-In Hybrid Electric Vehicles", *IEEE Transactions on Industrial Electronics*, Vol. 55, No. 6, pp. 2237-2245, June. 2008
- [2] A. K.Yadav, P. Gaur, S. K. Jha, J. R. P. Gupta, and A. P. Mittal, "Optimal speed control of Hybrid Electric Vehicles", *Journal of Power Electronics*, Vol. 11, No. 4, pp. 393-400, July 2011.
- [3] Japjeet K., P. Gaur, P. Saxena, "Genetic algorithm based speed control of Hybrid Electric Vehicle", *IEEE Conference on Contemporary Computing*, pp. 65-69, August 2013.
- [4] X. Liu, Q. Huang, Y. Chen, and J. Li, "Nonlinear modelling and optimal controller design for Radar Servo System", *Third International Symposium on Intelligent Information Technology Application*, pp. 327-330, 2009.
- [5] A. Varsek, T. Urbanit & B. Fillipit, "Genetic algorithms in controller design and tuning", *IEEE Transactions Systems Man and Cybernetics*, Vol. 23, No. 5, pp. 1330-1339, 1993.
- [6] K. M. Junaid and S. Wang, "Automatic Cruise control modelling-a lattice PWL approximation approach", *Proc. of the IEEE ITSC*, pp. 1370-1375, Sep. 2006.
- [7] Karen L. Butler, Mehrdad Ehsani, Preyas Kamath, "A Matlab-Based Modeling and Simulation Package for Electric and Hybrid Electric Vehicle Design", *IEEE Transactions on Vehicular Technology*, Vol. 48, No. 6, pp. 1770-1778 Nov. 1999.
- [8] L. Feiqiang, W. Jun, L. Zhaodu, "On the vehicle stability control for Electric Vehicle based on control allocation," *IEEE Vehicle Power and Propulsion Conference (VPPC)*, pp. 1-5, 2008.
- [9] M. Namazov, "DC motor position control using Fuzzy proportional-derivative controllers with different defuzzification methods," *Turkish Journal of Fuzzy Systems*, An Official Journal of Turkish Fuzzy Systems Association, Vol. 1, No. 1, pp. 36-54, 2010.
- [10] S. Omatu, M. Yoshioka, and T. Kosaka, "PID Control of Speed and Torque of Electric Vehicle", *Third International Conference on Advanced Engineering Computing and Applications in Sciences*, pp. 157-162, 2009.
- [11] Gadoue, S.M.; Giaouris, D.; Finch, J.W., "Sensorless control of Induction Motor Drives at very low and zero speeds using Neural Network Flux Observers," *Industrial Electronics, IEEE Transactions on*, vol.56, no.8, pp.3029,3039, Aug. 2009
- [12] Atri, Amit, and Md Ilyas. "Speed control of DC motor using Neural Network configuration." *International Journal of Advanced Research in Computer Science and Software Engineering* Vol.2, No. 5, pp. 209-212, May 2012
- [13] Sumathi, S., Hamsapriya, T., & Surekha, P. "Evolutionary Intelligence: An introduction to theory and applications with Matlab", Springer, 2008
- [14] Wei Liu, "Introduction to Hybrid Vehicle system modelling and control", Wiley, 2013.



Japjeet Kaur received her B.Tech Degree in 2010 from P. D. M. College of Engineering, M. D. University, Haryana and M.Tech degree in Instrumentation and Control Engineering from Netaji Subhas Institute of Technology, Delhi University in 2013.



Prerna Gaur received her B.Tech and M.E in 1988 and 1996 from G.B. Pant College of Technology, Uttranchal, India and Delhi College of Engineering, Delhi University, respectively. She is PhD in the field of Motion Control of PMSM. She joined the industry in 1989 and Delhi College of Engineering as a Lecturer in 1994. She is an Associate Professor in the Instrument and Control Engineering Division at Netaji Subhas Institute of Technology, Delhi. She is a Life Member of the Indian Society for Technical Education (ISTE) and Senior Member of Institute of Electrical and Electronics Engineers (IEEE). Her research interests include Power Electronics, Electric Drives, Artificial Intelligence Based Control etc.

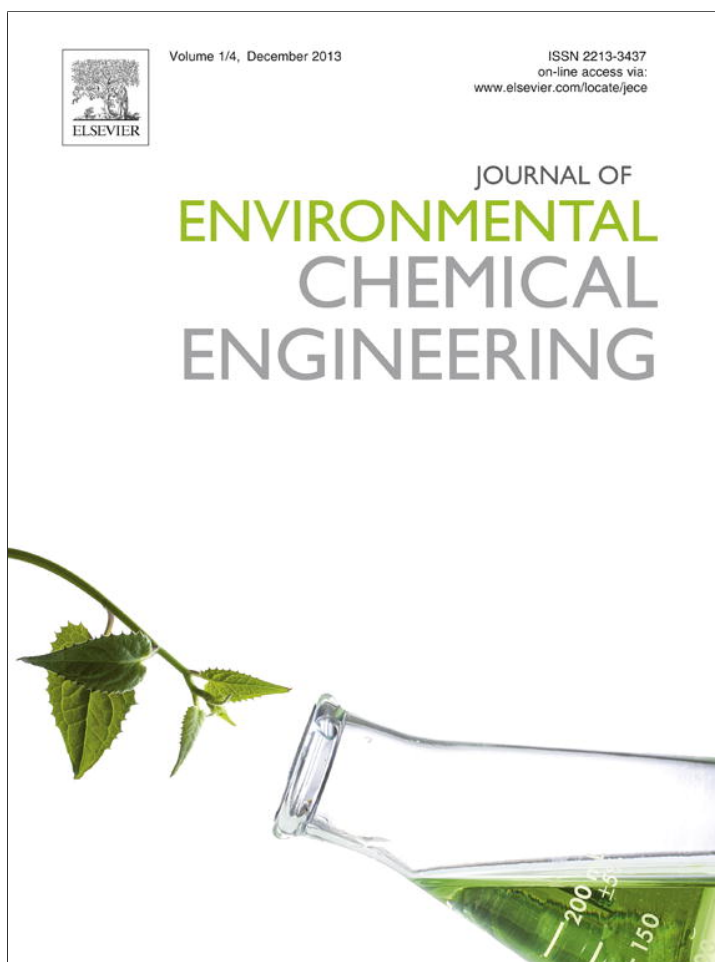


Piyush Saxena received her B.Tech degree in 1981 from B. C. E., Patna and M.Tech degree in 1986 from Delhi College of Engineering, Delhi University, respectively. She joined the industry in 1983 and served for two years. She joined Netaji Subhas Institute of Technology, Delhi in 1985. She is a Member of Institute of Electrical and Electronics Engineers (IEEE). She is an Associate Professor in Netaji Subhas Institute of Technology, Delhi and pursuing

PhD in Renewable Energy from the same.



Vikas Kumar received his B.Tech in Instrumentation Engineering from Kurukshetra University and M.Tech Instrumentation and Control Engineering from Netaji Subhas Institute of Technology, Delhi University. Currently, he is working as a Teaching cum Research Fellow in the Division of Instrumentation and Control Engineering, NSIT. His research area includes predictive control of drives and power converters, intelligent control techniques, sensorless control of servo drives and electric vehicle control.



This article appeared in a journal published by Elsevier. The attached copy is furnished to the author for internal non-commercial research and education use, including for instruction at the authors institution and sharing with colleagues.

Other uses, including reproduction and distribution, or selling or licensing copies, or posting to personal, institutional or third party websites are prohibited.

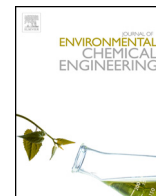
In most cases authors are permitted to post their version of the article (e.g. in Word or Tex form) to their personal website or institutional repository. Authors requiring further information regarding Elsevier's archiving and manuscript policies are encouraged to visit:

<http://www.elsevier.com/authorsrights>



Contents lists available at ScienceDirect

Journal of Environmental Chemical Engineering

journal homepage: www.elsevier.com/locate/jece

Tertiary recycling of poly(ethylene terephthalate) wastes for production of polyurethane–polyisocyanurate foams

P.K. Roy^{a,*}, R. Mathur^b, D. Kumar^b, C. Rajagopal^a^a Centre for Fire, Explosive and Environment Safety, Timarpur, Delhi 110054, India^b Department of Applied Chemistry and Polymer Technology, Delhi Technological University, Delhi 110042, India

ARTICLE INFO

Article history:

Received 28 May 2013

Received in revised form 10 August 2013

Accepted 13 August 2013

Keywords:

Microwave

Poly(ethylene terephthalate)

Polyurethane

Polyisocyanurate

Recycling

ABSTRACT

The present work aims at tertiary recycling of poly(ethylene terephthalate) (PET) wastes to derive raw materials for production of polyurethane–polyisocyanurate foams. The first step involves glycolytic depolymerization of PET in the presence of diethylene glycol (DEG), under the influence of microwave irradiation with an aim to reduce the energy intensiveness of the process. Experimental conditions like PET:DEG ratio and reaction time were optimized to maximize the extent of PET conversion. Multiple extrusion of PET led to reduction in its molecular weight, which increased its reactivity towards glycolysis. The time required for glycolytic depolymerization of PET could be significantly reduced by employing microwave irradiation instead of conventional thermal process. The glycolysate was subsequently reacted with two different diacids: adipic acid (AA) and sebacic acid (SA) to obtain aromatic oligoesters. For the purpose of comparison, analogous aliphatic oligoesters were also prepared by reacting AA and SA with DEG under similar reaction conditions. The oligoesters were subsequently employed as a raw material for the preparation of polyurethane foams by reacting with diphenylmethane diisocyanate. The hydroxyl:isocyanate ratio in the formulation was decreased to introduce isocyanurate linkages, which resulted in the formation of polyisocyanurate foams with high compressive strength. Various characterization techniques were employed to determine the effect of the aromatic phenyl group and chain length of the diacid on the mechanical and structural properties of the resultant foams.

© 2013 Elsevier Ltd. All rights reserved.

Introduction

Successful demonstration of blow moulding technique for the production of poly(ethylene terephthalate) (PET) bottles, way back in the 1970s, has led to a massive increase in the overall usage of this polymer for packaging purposes [1]. Because of its excellent barrier properties against oxygen and carbon dioxide [2], PET has become the choicest of materials for bottling beverages, particularly mineral water and carbonated soft drinks. In addition, it finds extensive application in the textile industry, which consumes more than 60% of all the PET produced worldwide [3]. Unfortunately, irresponsible usage of this nondegradable thermoplastic over the last few decades has led to its accumulation in the environment [4,5]. Of all thermoplastics, the practice of recycling PET is very common, but the cost of the recycled product is rather high [6]. It is thus highly desirable to adopt technically and

economically feasible routes towards recycling of PET into industrially important products.

Primary and secondary recycling of PET involves thermal reprocessing of the polymer which reduces its molecular weight substantially [7], thereby setting up an upper limit on the maximum number of recycling steps. There is abundant academic and practical studies on tertiary recycling of PET, whereby it is converted into basic chemicals [8], by processes like glycolysis [9], aminolysis [10], hydrolysis [11], alkalolysis [12] and alcoholysis, out of which only the former two have reached the level of commercial maturity [8,13]. Glycolysis of PET leads to formation of oligomers which have the potential to be used as a raw material for preparation of unsaturated polyesters [14], alkyd resins [15–17] and polyurethanes [18–20], etc.

At present, oligoesters used for the preparation of flexible polyurethane foams are essentially derived by reacting low molecular weight diols, e.g. diethylene glycol (DEG) with adipic acid (AA) in the presence of glycerol [21]. For rigid PU foam applications, the polyol is obtained by the reaction of AA with ethylene glycol (EG) or diethyleneglycol (DEG) in the presence of phthalic anhydride [19]. Interestingly, such polyols can also be

* Corresponding author. Tel.: +91 11 23907191; fax: +91 11 23813367.
E-mail addresses: pk_roy2000@yahoo.com, prasunroy2000@gmail.com (P.K. Roy).

derived by transesterification of PET, which in turn can be further reacted with aliphatic diacids for preparation of either type of PU foam, depending on the type of spacer employed. The polyester polyol obtained from PET is expected to render advantageous characteristics to the final product, particularly in terms of better mechanical properties, high thermal stability, resistance to major chemical solvents due to the presence of aromatic phenyl group [22]. Thus, synthesizing polyols by transesterification of PET waste is a process of preserving natural resources, and this in fact is the driving force for the present study.

It has been previously reported that the time and energy requirements for PET glycolysis can be significantly lowered by using microwave as an alternate energy source [23]. We have reported previously that the reactivity of PET is inversely proportional to the molecular weight of diol used for glycolysis. We observed that complete conversion of PET under microwave-assisted glycolytic conditions could be achieved in the presence of DEG but the polyurethane foams obtained there from are rather rigid [24]. By reacting the glycolysed polyol with suitable diacids, it is possible to introduce spacer molecules, with increased flexibility. In this context, the reaction of glycolysed PET with AA has been reported to form oligoesters, which in turn leads to flexible foams [19]. However, literature is scarce on the effect of soft segment chain length of the diacid on the final foam properties. We hypothesize that a higher molecular weight diacid, like sebacic acid (SA) can be used to increase the flexibility of the aromatic polyester polyol based foam further.

In this article, we propose a combination of microwave-assisted PET depolymerization process, which was used to prepare low molecular weight oligomers, followed by polycondensation with aliphatic diacids to prepare oligoesters with desired properties. We also hypothesize that it should be relatively easy to adopt chemical recycling for recycled PET grades, which have been subjected to a few thermal processing steps. In this regard, we have demonstrated the potential of this process for recycled PET grades. The oligoesters have been used as a raw material for production of flexible foams, where the rigidity was increased by varying the amount of isocyanate in the composition.

Experimental

Materials

Disposed off PET bottles were collected, washed, dried and cut into small pieces (6 mm × 6 mm) after removal of the polyethylene caps and the polypropylene label. Zinc acetate dihydrate [$\text{Zn}(\text{CH}_3\text{COO})_2 \cdot 2\text{H}_2\text{O}$, Merck] with a purity of 99% was employed as the trans-esterification catalyst. Adipic acid (Central Drug House (CDH)), sebacic acid (CDH), p-toluene sulfonic acid (PTSA) (CDH), potassium acetate (CDH), diethylene glycol, glycerol (CDH), diphenylmethane 4,4'-diisocyanate, a mixture of di- and triisocyanates (MDI) (Merck) and dibutyl tin dilaurate (DBTL) (Merck) were used without any further purification. Double distilled water was used throughout the course of this work.

Microwave aided glycolysis

A domestic microwave oven (LG) with a magnetron source for microwave generation (2.45 GHz, maximum power: 900 W) was used for performing glycolytic experiments. PET pieces (10 g) together with requisite amount of DEG and zinc acetate (0.5% (w/w) PET) were introduced into a loosely stoppered reaction flask which was placed in the microwave reactor. To increase the functionality of the glycolysate, a trifunctional alcohol (glycerol) was introduced in the reaction medium along with PET and DEG [21]. The effect of increasing triol concentration on the properties

of the resultant glycolysate has been discussed in our previous paper [24], and based on the previous studies, 5% (w/w) of glycerol was employed in the present investigation. Experiments were performed at different molar ratio of PET:DEG:: 1:2, 1:4 and 1:6 and was allowed to proceed at 450 W for extended time periods, leading to the formation of a viscous liquid, which did not solidify on cooling. After predetermined periods, the reaction mixture was filtered through a copper wire mesh (0.5 × 0.5 mm pore size), and the remaining unreacted PET flakes were weighed to estimate PET conversion % as follows:

$$\text{PET conversion (\%)} = \left(\frac{m_{\text{PET, initial}} - m_{\text{PET, remaining}}}{m_{\text{PET, initial}}} \right) \times 100 \quad (1)$$

where $m_{\text{PET, initial}}$ refers to the mass of PET initially taken for the experiment and $m_{\text{PET, remaining}}$ refers to the mass of solid PET flakes which remained unreacted in the reaction medium. For comparison purposes, glycolysis was also performed at 180–190 °C in an oil bath, under inert atmosphere in a four-necked round bottom flask, connected to a reflux condenser, N_2 gas inlet, thermometer and stirrer, the concentration of reactants being same. The results in terms of PET conversion were compared with those obtained under microwave irradiation.

Secondary recycling: multiple extrusions

Studies were performed to investigate the effect of multiple extrusions on the intrinsic viscosity of PET, which is expected to affect its reactivity towards glycolysis. For this purpose, approximately 15 g of dried PET flakes was loaded into the plastometer barrel of an MFI instrument (International Equipments) and extruded under a load of 2.16 kg at 260 °C and the extrudate was loaded into the plastometer barrel for re-extrusion. This process was repeated 10 times and the effect of extrusion on the intrinsic viscosity of the sample was measured, before being subjected the degraded PET to glycolytic experiments. The thermally degraded PET will be referred to as RPET in the subsequent text.

Polyesterification of glycolysed products

The DEG glycolysed product, obtained by employing a PET:DEG:: 1:4, was used without any further separation. The obtained glycolysate was reacted with two different difunctional carboxylic acids, namely AA and SA (hydroxyl:acid ratio:: 1:1). For comparison purposes, aliphatic oligoesters were also prepared by reaction of AA and SA with DEG under similar conditions. Esterification catalyst, PTSA (0.1%), based on the moles of diacid, was introduced in steps into a reaction kettle (500 mL capacity) containing the glycolysed product and the diacid. The reactor was equipped with a stirring assembly, a thermowell and a dean stark apparatus. The reaction was initially heated to 170 °C and maintained for a period of 3 h, after which the temperature was increased to 200 °C. The reaction was allowed to proceed at 200 °C till the required acid number (<30) was achieved. Water formed as a result of the esterification process was collected and quantified.

Preparation of polyurethane foams

In order to assess the effect of the aromatic phenyl group on the properties of PU foams, both aromatic as well as aliphatic oligoesters were reacted with isocyanates to prepare polyurethane foam. For this purpose, weighed amount of the oligoester, silicone oil surfactant (2% (w/w) oligoester), DBTL catalyst (1% (w/w) oligoester) and foaming agent (water) were mixed in a flat-bottom teflon beaker and stirred mechanically for 1 min. Requisite amount of MDI, calculated according to the following formula was added and stirred vigorously, which led to the formation of a viscous

liquid. This was poured into cylindrical Teflon moulds (60 mm diameter, 36 mm length) and allowed to foam within.

$$m_{iso} \cdot n_{eq,iso} = [m_{H_2O} \cdot n_{eq,H_2O} + m_{poly} \cdot n_{eq,poly}] i_{NCO} \quad (2)$$

where m_{iso} , m_{H_2O} and m_{poly} refer to the mass of polyisocyanate, water and oligoester, respectively, and $n_{eq,iso}$, n_{eq,H_2O} and $n_{eq,poly}$ are the equivalent number of polyisocyanate (7.4 mmol/g), water (111.1 mmol g⁻¹) and oligoester (estimated from the hydroxyl number) and i_{NCO} is the desired NCO index (1.05) maintained for the preparation of flexible PU foam formulation [25].

Under similar conditions, polyisocyanurate foams (PIR) were also prepared, where the NCO index was increased to 2. In addition, the PIR formulation also contained requisite amounts of potassium acetate, which reportedly catalyses the rate of trimerisation of isocyanate [19]. The process of foam formation was monitored by measuring characteristic parameters including cream time, gel time and tack-free time.

The polyurethanes and polyisocyanurates were designated as PETPU and PETPI followed by the acid used for its preparation, i.e. AA and SA for denoting adipic acid and sebacic acid, respectively. For example, the polyurethane foam derived from glycolysis of PET followed by esterification with AA will be referred to as PETPU-AA and the isocyanurate foam derived from the same will be referred to as PETPI-AA, respectively, in the subsequent text. The naming of polyurethanes and polyisocyanates derived from aliphatic oligoesters follows similar naming pattern where DEG is used instead of PET.

Characterization techniques

The viscosity-average molecular weight of PET was determined by solution viscometry. Samples were dissolved in a mixture of phenol and 1,1,2,2-tetrachloroethane (60/40, w/w) under heating, and the intrinsic viscosity $[\eta]$ was measured using Ubbelohde suspension level viscometer at 25 °C. For determination of $[\eta]$ of residual PET, the samples were washed with acetone to remove the adhering DEG and EG. The viscosity average molecular weight of PET was calculated using the following equation [26]:

$$[\eta] = 75.5 \times 10^{-3} \text{ mL/g } M_v^{0.685} \quad (3)$$

The intrinsic viscosity of the glycolysate was determined in methanol at 25 °C. The hydroxyl number (HN) was determined using acetic anhydride, as per test method A, described in ASTM D 4274–99. For the purpose of acid number determination, the solution was titrated against standard methanolic KOH solution in acetone medium, as per the procedure reported previously.

Thermal characterization was performed using Perkin Elmer Diamond STG-DTA-DSC in N₂ atmosphere in the temperature range of 50–550 °C. A heating rate of 10 °C/min and sample mass of 5.0 ± 0.5 mg were used for each experiment. Percentage crystallinity was calculated from the DSC traces as follows:

$$\% \text{ Crystallinity} = \frac{\Delta H_{f(\text{observed})}}{\Delta H_{f(100\% \text{ crystalline})}} \times 100 \quad (4)$$

where $\Delta H_{f(\text{observed})}$ is the enthalpy associated with melting of the material and $\Delta H_{f(100\% \text{ crystalline})}$ is the enthalpy of 100% crystalline PET reported in the literature to be 135.8 J/g [27].

The surface morphology of samples was studied using a Scanning Electron Microscope (Zeiss EVO MA15) under an acceleration voltage of 20 kV. Samples were mounted on metal stubs and sputter-coated with gold and palladium (10 nm) using a sputter coater (Quorum-SC7620) operating at 10–12 mA for 60 s. The average cell dimensions and standard deviations were determined by measuring the diameters of about 20 cells using inbuilt image processing software.

The density of the PU foam was determined by averaging the mass:volume ratio of five specimens per sample following ASTM D1622–98 standard. The average value along with the standard deviation has been reported in the paper. The compressive mechanical properties of the foams were determined using a Universal Testing Machine (International Equipments) as per ASTM D1621–00. Compressive load was applied at a cross-head speed of 3.6 mm/min, till the foam was compressed to ~15% of its original thickness. The compressive strength was calculated based on the “10% deformation” method as per the standard procedure. At least, three identical specimens were tested for each composition and the average results along with the standard deviation values have been reported.

FTIR spectra of samples were recorded in the wavelength range 4000–600 cm⁻¹ using Fourier transform infrared (FTIR) spectroscopy on a Thermo Fisher FTIR (NICOLET 8700) analyser with an attenuated total reflectance (ATR) crystal accessory. The isocyanurate content was estimated as the ratio of intensity of the isocyanurate absorption band at 1412 cm⁻¹ to intensity of the aromatic absorption band at 1597 cm⁻¹ [19]. Waters (1525) gel permeation chromatograph (Milford, MA) equipped with styragel (HR-3 and HR-4, 7.8 × 300 mm²) columns along with Evaporating Light Scattering Detector (ELSD-2420) was used for determination of the molecular weight and molecular weight distribution of the glycolysate. Narrow molar mass polystyrene standards were used for calibration purposes.

Results and discussion

Microwave assisted glycolysis

The TG and DSC trace of the PET used for the present study is presented in the Supplementary section (Fig. S1). It can be seen that the PET samples exhibit a sharp melting point peaking at 246 °C and undergoes a single step pyrolytic decomposition commencing at 400 °C. The DSC crystallinity as determined from the area of the endotherm is ~27.2% and the molecular weight (M_v) of PET, as determined from viscometric studies was 27,431. Glycolysis of PET with DEG leads to the formation of liquid oligomers, which do not solidify on cooling. The reaction was followed by monitoring the extent of PET conversion, the variation of which is presented in Fig. 1. It can be seen that the PET conversion reached a maxima after 30 min of irradiation, after which even traces of PET could not be detected in the medium.

It can be seen from the figure that complete conversion of PET is achievable under these conditions (PET:DEG:: 1:2). However, the

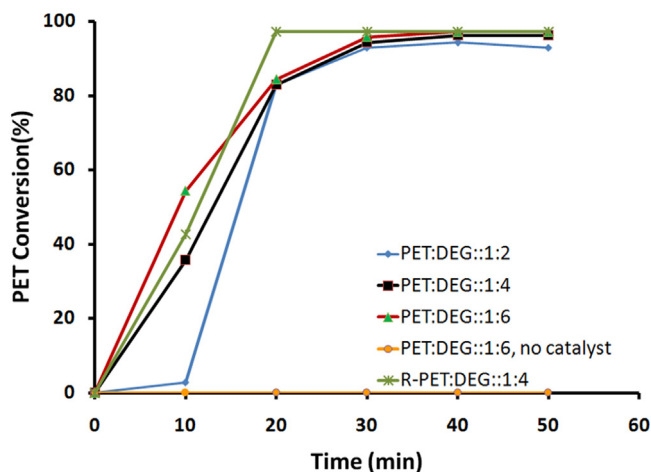


Fig. 1. Effect of glycolysis time and PET:DEG ratio on the extent of PET conversion.

effect on the PET conversion due to increasing the PET:DEG ratio is quite pronounced, especially during the initial periods of reaction (Fig. 1). Under a PET:DEG:: 1:2, PET conversion is rather low ($\sim 3\%$) in the initial periods ($t < 10$ min), which can be attributed to the reduced availability of DEG on the surface of PET.

Pardal et al. [28,29] have extensively studied the kinetics of the glycolytic depolymerization process, in which the mechanism behind the evolution of an initially heterogenous phase of liquid glycol and the solid polymer into a single homogeneous liquid phase has been discussed. It has been suggested that initially, the liquid glycol diffuses into the bulk of the solid polyester which leads to the swelling of the matrix. This followed by glycolysis of the amorphous interlamellar chains. Subsequently, the reaction products diffuse from the surface, leading to a rough texture as evident from the SEM images presented in Fig. 2. Being a two phase reaction, the susceptibility towards glycolysis is highly dependent on the availability of glycols on the surface of the solid, which increases with the increasing amount of DEG in the reaction medium, which accounts for the increase in the rate of PET conversion with increase in the PET:DEG ratio.

Although complete PET conversion could be achieved even under PET:DEG ratio of 1:2, the glycolysate obtained were comparatively viscous (intrinsic viscosity = 0.02 dL/g). With increase in the amount of glycol in the reaction medium, the intrinsic viscosity decreased to 0.016 and 0.012 dL/g for PET:DEG of 1:4 and 1:6, respectively, which was reasonably easy to handle for the subsequent polycondensation step. Since, excess of glycol (PET:DEG: 1:6) is expected to the incorporation of less amounts of aromatic moieties in the oligoester, it was decided to perform the polycondensation reaction with the glycolysate obtained using an optimized PET:DEG ratio of 1:4.

In view of the above, large scale glycolytic reactions with PET (50 g batch) were performed under the optimized ratio of PET:DEG:: 1:4. There was not much variation in the HN after ~ 30 min of reaction, which was of the order of 430 ± 15 after 30 min. Size exclusion chromatography was performed to determine the molecular weight distribution of the glycolysed product. The M_n , M_w , and M_z of the PET glycolysate were 330, 456 and 564, respectively. It is interesting to note that the glycolytic depolymerization of PET does not take place in the absence of catalyst in the time frame of reaction (60 min), as is evidenced in Fig. 1.

The viscosity-average molecular weight of PET was determined by solution viscometry, which revealed that the M_v of the PET films decreased from an initial value of $27,431\text{--}1521 \pm 130$ after glycolysis for 30 min in the presence of DEG. This was also associated with an increase in the DSC crystallinity increased from 27.2% to

37.1% after 30 min of glycolysis, which clearly indicate that the amorphous regions are preferentially eroded as compared to the crystalline regions.

Under conventional heating ($T = 180\text{--}190^\circ\text{C}$) and similar PET:glycol concentrations (PET:DEG:: 1:4); the reaction took ~ 9 h to reach the same level of de-polymerization. The effect of characteristic parameters like temperature, catalyst and polymer morphology has been discussed in detail by Pardal et al. previously [29]. It has been reported that the reactivity of PET with DEG is substantially low at 190 and 200°C that the liquid phase remains heterogeneously white even after 270 min of reaction, and our studies confirmed the same.

One of the main problems associated with the primary and secondary recycling of PET is linked with the decrease in quality of the recycled product, which occurs as a result of degradation due to the moisture content and contaminants in the feed. Exposure of PET to 10 extrusion cycles at 260°C led to a significant decrease in the molecular weight to $19,329 \pm 132$, which in turn is expected to result in its increased susceptibility towards glycolysis. As can be seen from Fig. 1, complete conversion of this thermally reprocessed grade could be achieved within 20 min.

The FTIR spectra of PET, DEG and glycolysed PET are presented in Fig. 3. The spectrum of DEG exhibits characteristic absorption bands due to ether stretching (C–O) at $\sim 1050\text{--}1150\text{ cm}^{-1}$, with maxima at 1150 cm^{-1} . Characteristic alkyl (R–CH₂) stretching at $\sim 2850\text{--}3000\text{ cm}^{-1}$ was also observed, along with hydroxyl group absorption ranging from ~ 3200 to 3600 cm^{-1} . In comparison, the glycolysed product exhibit absorption at 1715 cm^{-1} due to C=O stretching, which can be attributed to the presence of ester group, formed as a result of glycolysis of PET and this peak could also be observed in the spectra of PET. The absorption band at $\sim 3200\text{--}3600\text{ cm}^{-1}$ can be attributed to the presence of free hydroxyl groups present in glycolysed PET oligoesters.

Microwave assisted heating: role of diethylene glycol

The energy associated with the microwave frequency (2.45 GHz, 0.0016 eV) employed for the glycolytic depolymerization is too small to cleave covalent chemical bonds, which leads us to believe that the enhanced efficiency of the microwave assisted glycolytic process can be attributed to the efficient heating of the medium under the reaction conditions employed,

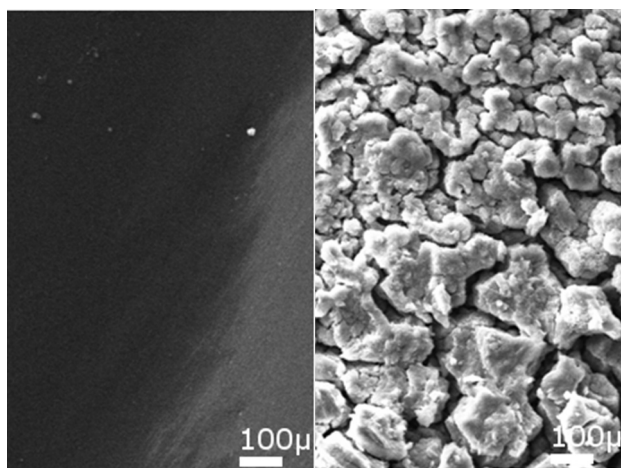


Fig. 2. SEM images of the PET surface: (a) initially and (b) after 30 min of glycolysis.

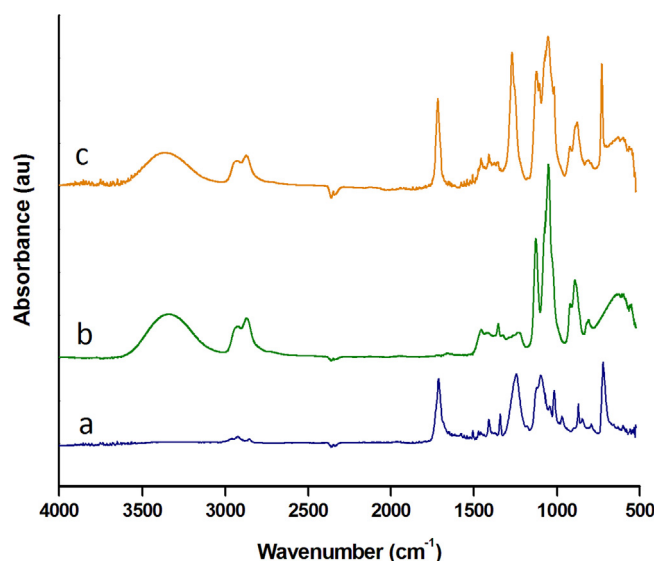


Fig. 3. FTIR spectra: (a) poly(ethylene terephthalate), (b) diethylene glycol and (c) glycolysed PET.

a feature more commonly known as the “microwave dielectric heating” effect. In the present study, DEG plays an extremely important function of an efficient microwave absorber, apart from serving its primary role as a reactant. Due to its exceptionally high loss factor ($\tan \delta_{\text{DEG}} = 1.2$, 30°C) [30] it is capable of effectively converting electromagnetic energy into heat, which leads to rapid PET depolymerization under the experimental conditions employed. However, in the conventional process, the reaction mixture in contact with the vessel wall is heated first, which is then conducted through the medium to the PET flakes. In the latter, the potential of DEG as an effective microwave absorber is not tapped, and this can be used to explain the difference between the observed rates of the two processes.

Polycondensation of glycolysed PET

The PET glycolysate was esterified with two difunctional acids (AA and SA) over extended periods and the variation in the acid number (AN) of the liquid oligoester as a function of time is presented in Fig. 4. As expected, the AN decreases as a result of the condensation reaction and the extent of decrease is higher initially, after which it tends to level off. It has been reported that the catalyst degrades over a period of time and in view of the same, it was introduced in steps, (initially and after 9 h), the total amount remaining same (0.1% mol) [31]. Interestingly, the oligoesters prepared by polyesterification of glycolysed oligomers with AA exhibit slightly lower AN, which is indicative of its higher reactivity as compared to SA. The polymerization process was also associated with an increase in the viscosity, which was quantified by viscometric techniques. On the basis of the higher reactivity of AA, the oligoesters prepared by reaction of glycolysate with AA exhibit higher viscosities (intrinsic viscosity 0.16 dL/g) as compared to sebacic acid based oligoesters (intrinsic viscosity 0.12 dL/g) after 15 h of reaction.

The FTIR spectra of the products obtained post-esterification with adipic acid is presented in Fig. 5. Characteristic hydroxyl group absorption ($\sim 3200\text{--}3600\text{ cm}^{-1}$) was observed in the spectra of DEG glycolysed PET. Due to polyesterification reaction, the hydroxyl groups are consumed as a result of which the absorption in this region decreases. In view of the similar functional groups, the FTIR spectra of both types of oligoesters is similar, irrespective of the type of diacid used for its preparation, and hence only adipic acid containing oligoester has been included as a representative in the figure. The hydroxyl number decreases from an initial value of 430 ± 15 for DEG glycolysed PET to 20 ± 2 and 28 ± 2 after reaction with AA and SA, respectively.

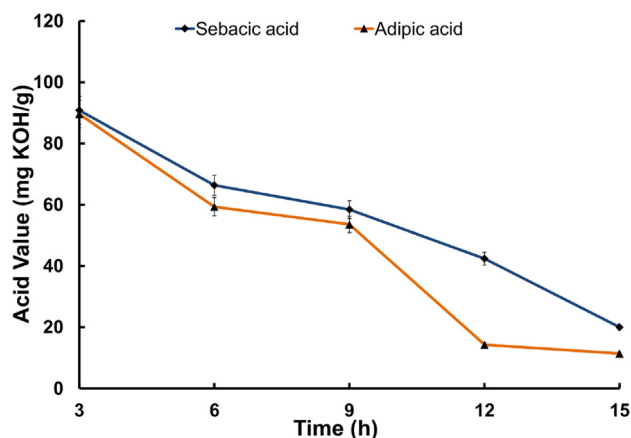


Fig. 4. Variation of acid number with progress of polyesterification reaction.

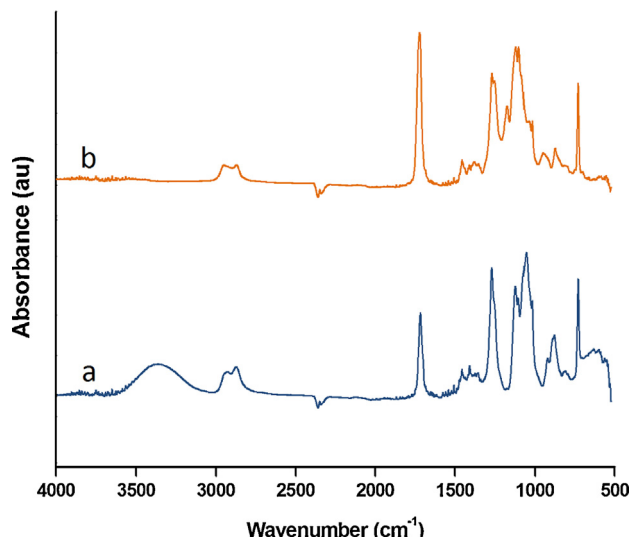


Fig. 5. FTIR spectra: (a) DEG glycolysed PET and (b) oligoester obtained after polyesterification with adipic acid.

Polyurethane foams from oligoesters

The oligoesters, obtained after reaction of glycolysate (PET:DEG:: 1:4) with diacids were further reacted with MDI in varying amounts to prepare polyurethane–polyisocyanurate foams, and the foaming process was monitored by measuring the duration of cream time, gel time and tack-free time, the results of which are presented in Table 1. The exothermic foaming process initiated almost instantaneously upon mixing of the reagents and the viscous mass continued to expand till the resulting foamed mass solidified due to progressive cross-linking. The isocyanate index for PU formulations is normally varied between 105 and 125, while for PU–PIR foams, it is increased to 180–350. In the present study, the same was maintained at 200 to obtain PIR foams, which were mechanically much stronger as compared to their PU analogues.

The entire process of foam formation is a delicate balance between two reactions. The initial blowing step involves the reaction of the isocyanate group with water to yield a thermally unstable carbamic acid, which decomposes to form amine, carbon dioxide and heat. This is followed by a gelation step, which leads to the formation of a solid cellular foam. These two steps involve several reactions, the details of which are presented in the Supplementary section. It is to be mentioned that if the rate of gelation is slow in comparison to the initial blowing step, it amounts to the collapse of the reticular structure. On the contrary, the reverse scenario leads to formation of foams with closed cells, both of which are undesirable, for practical applications. It is in this context that cream time and gel time become critical for industrial formulations. For all practical applications in injection technology, the cream time has to be more than the injection time. The foam should expand and fill the form in approximately the same time as the gel time. The cream time and gel time recommended by reactivity profiles of injection technology are 4–8 s and 30–60 s, respectively [32]. In the present study, the foam rising (cream time) begins approximately within 15 s of mixing and solidifies completely (tack-free time) within 52–62 s (Table 1).

The apparent density of foams, as determined by mass volume ratio is reported in Table 1. PIR foams exhibit higher density than PU foams, which was also evident from the smaller cell sizes, as determined from SEM images (Fig. 6). The average cell size of the foam along with the standard deviations was also determined and is reported in Table 1. As can be seen from the SEM images, all the foams possessed cells with almost uniform sizes.

Table 1
Characteristics of polyurethane foam derived from glycolysed PET.

Foam	Cream time (s)	Gel time (s)	Tack free time (s)	Density (kg/m ³)	Cell size (μ)	Compressive strength (kPa) ^a	Young's modulus (kPa)
DEGPUAA	15	36	62	225 ± 21	230 ± 21	5.27 ± 0.24	0.5 ± 0.02
DEGPUSA	15	39	60	187 ± 12	322 ± 42	1.35 ± 0.04	0.15 ± 0.01
DEGPI-AA	13	36	63	354 ± 29	198 ± 24	80.76 ± 3.41	102.7 ± 4.3
DEGPI-SA	14	40	67	312 ± 21	296 ± 22	21.4 ± 1.01	27.4 ± 1.2
PETPU-AA	14	33	52	233 ± 18	210 ± 23	18.3 ± 0.97	1.84 ± 0.04
PETPU-SA	14	34	60	198 ± 16	309 ± 31	7.39 ± 0.26	0.73 ± 0.03
PETPI-AA	15	38	61	376 ± 31	196 ± 25	158.86 ± 6.41	189.8 ± 8.34
PETPI-SA	15	36	62	348 ± 26	281 ± 32	122.7 ± 5.22	154.3 ± 7.43

^a Values at 10% strain.

The isocyanurate content was quantified in terms of the ratio of intensity of absorption band at 1412 cm⁻¹ to intensity of the aromatic absorption band at 1597 cm⁻¹, [19] the results of which are presented in Fig. 7. The representative FTIR spectra of PIR foams are also presented in the figure. As can be seen, the PIR samples exhibit increased absorption at 1412 cm⁻¹ due to the presence of isocyanurate groups.

Mechanical properties of foams

The mechanical properties of the foams were evaluated under compression mode and representative stress–strain curves are presented in Fig. 8. The compressive modulus and strength (at 10% strain) of the foams are reported in Table 1. It can be seen from the figure that all the samples exhibit similar profiles, i.e. an initial linear elastic region at low stresses, followed by an extended plateau. This feature is more pronounced in rigid foams with increased isocyanurate content. The observed elastic region arises primarily from the bending of cell struts, and stretching of the membranes in the cell walls. The subsequent broad plateau is a result of the plastic collapse or cell wall buckling of the foam, which is more commonly referred to as the collapse stress [33]. It is this extended plateau, which endows the foams with their high compressibility and enables them to exert a relatively constant stress up to high strain levels.

As expected, the use of higher molecular weight acid, i.e. SA, led to the formation of foams with lower compressive strength. The initial linear region was used to determine the modulus of the foams, the results of which are reported in Table 1. As expected,

the modulus of samples prepared using glycolysed PET was much higher, due to the introduction of aromatic phenyl ring in the main chain.

Thermal characterization of PU foams

In view of the higher stability of isocyanurates in comparison to urethanes, a considerable improvement of thermal stability is expected [34]. The TG trace of polyurethane and polyisocyanurate foams under N₂ atmosphere is presented in Fig. 9. Interestingly, the thermal degradation profiles was not affected with the type of spacer soft segment present in the polymeric chain and for the sake of brevity, only the TG traces of foams prepared from adipic acid based oligoester are presented. As can be seen, the decomposition of PU foams initiates at slightly lower temperature than PIR foams. It can also be seen that the presence of aromatic groups in the foams derived from glycolysed PET lead to higher char yields. The moisture content was highest in PU foams derived from the polycondensation of aliphatic acids and diols (DEGPU-AA), and as expected, the presence of hydrophobic phenyl rings resulted in lower moisture content in foams derived from PET glycolysates.

The thermal decomposition of polymeric materials usually initiates with the cleavage of the weakest bonds in the chain. It has been reported that the decomposition of PU foams starts with the thermal dissociation of urethane linkages, which leaves behind a char ~20% [6] while the PIR foams containing isocyanurate rings are much more stable with a char yield of ~30–50% [34]. Slightly lower char yields obtained in the present study can be attributed to

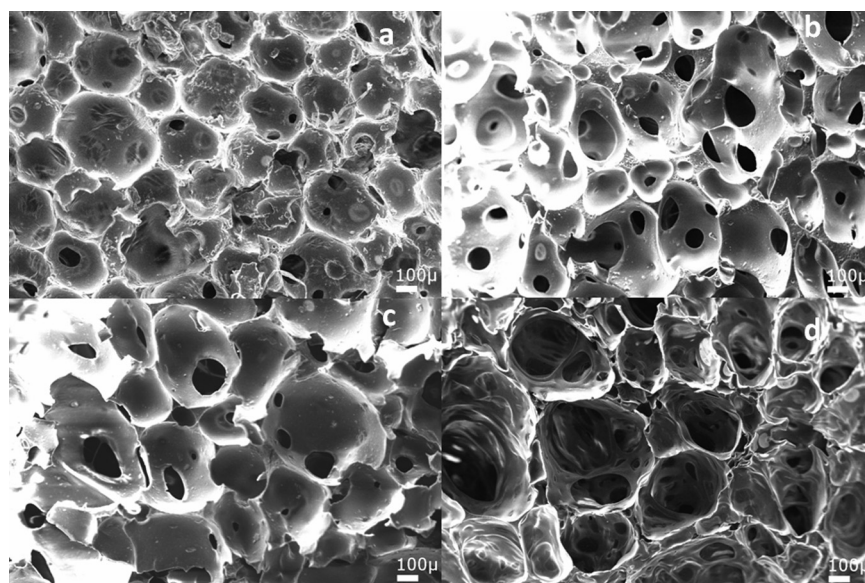


Fig. 6. Scanning electron micrograph of representative polyurethane foams: (a) DEGPU-AA, (b) DEGPI-AA, (c) PETPU-AA and (d) PETPI-AA.

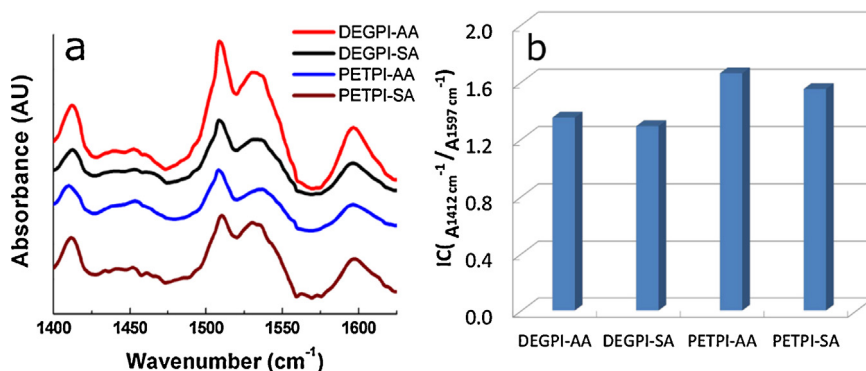


Fig. 7. (a) FTIR spectra of representative isocyanurate foams and (b) isocyanurate content of PIR and PU foams.

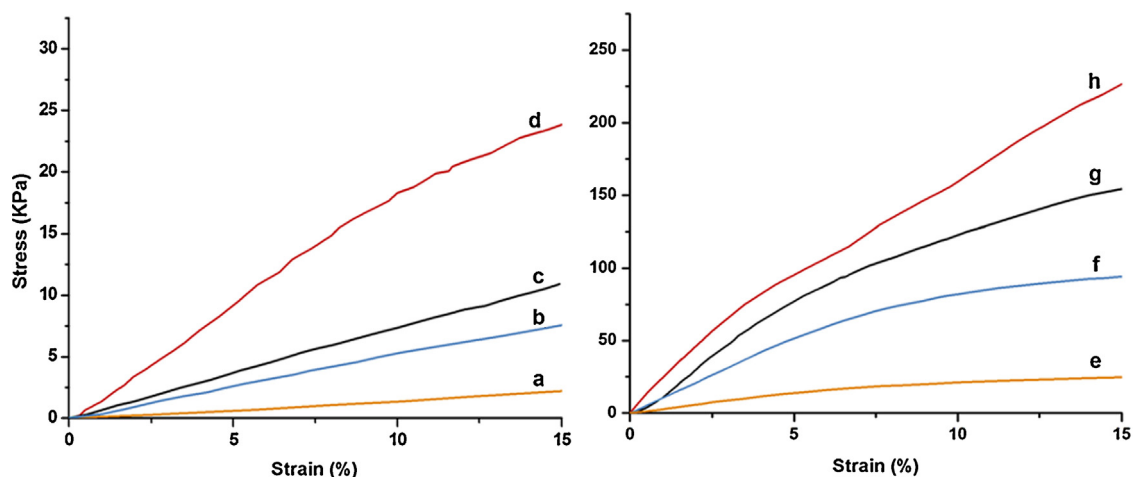


Fig. 8. Compressive stress-strain relationship for foams in compression mode: (a) DEGPU-SA, (b) DEGPU-AA, (c) PETPU-SA, (d) PETPU-AA, (e) DEGPI-SA, (f) DEGPI-AA, (g) PETPI-SA and (h) PETPI-AA.

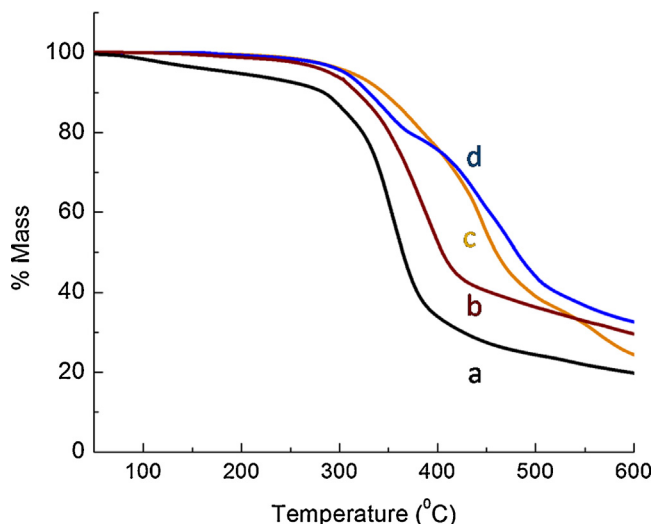


Fig. 9. Thermogravimetric traces: (a) DEGPU-AA, (b) PETPU-AA, (c) DEGPI-AA and (d) PETPI-AA.

the presence of higher amounts of aliphatic acid in the composition, which was introduced to achieve flexibility. The studies clearly indicate that all the foam samples could be safely used in service till a maximum of 270 °C, without undergoing any major thermal degradation, and the presence of aromatic rings in the chain leads to enhanced thermal stability.

Conclusion

PET bottles were glycolyzed with DEG under microwave irradiation in the presence of zinc acetate (0.5%, w/w). The reaction time required for glycolysis could be significantly reduced (~30 min) by the use of microwave as compared to the conventional thermal glycolytic process ($T = 180\text{--}190\text{ }^{\circ}\text{C}$), which requires a minimum of 9 h to reach the same level of depolymerization. The increased rate of glycolysis under microwave irradiation was attributed to efficient microwave absorption characteristics of DEG. To determine the effect of degradation resulting from 1^o and 2^o recycling on the extent of PET conversion, multiple extrusions were carried out in a plastometer, and the degraded product was found to be more susceptible to glycolytic depolymerization. The glycolysates obtained after 30 min of microwave assisted glycolysis (PET:DEG:: 1:4) were found to possess optimum viscosity, to be used for further polycondensation reaction with diacids. Oligoesters were prepared by reacting glycolysed PET with difunctional acids like sebacic acid and adipic acid with an aim to introduce soft spacer segments within the polymeric chain. The oligoesters hence obtained were used as a raw material for preparation of polyurethane–polyisocyanurate foams by varying the isocyanate index. The effect of soft segment chain length, and the aromatic phenyl group on the compressive mechanical properties of the foams was evaluated. All the foams possessed cells of uniform dimensions, and the flexibility of the foam were found to be directly proportional to the chain length of the spacer molecule used for its preparation. The use of PET glycolysate in the formulation led to an improvement in the

thermal stability of the resultant foams due to the introduction of phenyl rings within the polymeric chain.

Acknowledgement

The authors are thankful to Director, Centre for Fire, Explosive and Environment Safety, Delhi, India for his keen interest in the work and providing logistic support to perform the study.

Appendix A. Supplementary data

Supplementary data associated with this article can be found, in the online version, at [doi:10.1016/j.jece.2013.08.019](https://doi.org/10.1016/j.jece.2013.08.019).

References

- [1] L. Shen, E. Worrell, M.K. Patel, Open-loop recycling: a LCA case study of PET bottle-to-fibre recycling, *Resour. Conserv. Recycl.* 55 (2010) 34–52.
- [2] M. Frounchi, A. Dourbash, Oxygen barrier properties of poly(ethylene terephthalate) nanocomposite films, *Macromol. Mater. Eng.* 294 (2009) 68–74.
- [3] J. Scheirs, K. Walter, Feedstock Recycling and Pyrolysis of Waste Plastics: Converting Waste Plastics into Diesel and Other Fuels, John Wiley & Sons, West Sussex, 2006.
- [4] L. Bartolome, M. Imran, B.G. Cho, W.A. Al-Masry, D.H. Kim, Recent Developments in the Chemical Recycling of PET, InTech, Rijeka, Croatia, 2012.
- [5] P.K. Roy, M. Hakkarainen, I.K. Varma, A.-C. Albertsson, Degradable polyethylene: fantasy or reality, *Environ. Sci. Technol.* 45 (2011) 4217–4227.
- [6] I. Vitkauskienė, R. Makuska, U. Stirna, U. Cabulis, Thermal properties of polyurethane-polyisocyanurate foams based on poly(ethylene terephthalate) waste, *Mater. Sci. (Medziagotyra)* 17 (2011) 249–253.
- [7] D.H. Kang, R. Auras, K. Vorst, J. Singh, An exploratory model for predicting post-consumer recycled PET content in PET sheets, *Polym. Test.* 30 (2011) 60–68.
- [8] D.E. Nikles, M.S. Farahat, New motivation for the depolymerization products derived from poly(ethylene terephthalate) (PET) waste: a review, *Macromol. Mater. Eng.* 290 (2005) 13–30.
- [9] N.D. Pingale, S.R. Shukla, Microwave assisted ecofriendly recycling of poly(ethylene terephthalate) bottle waste, *Eur. Polym. J.* 44 (2008) 4151–4156.
- [10] G. Mir Mohamad Sadeghi, R. Shamsi, M. Sayaf, From aminolysis product of PET waste to novel biodegradable polyurethanes, *J. Polym. Environ.* 19 (2011) 522–534.
- [11] M.N. Siddiqui, D.S. Achilias, H.H. Redhwi, D.N. Bikiaris, K.A.G. Katsogiannis, G.P. Karayannidis, Hydrolytic depolymerization of PET in a microwave reactor, *Macromol. Mater. Eng.* 295 (2010) 575–584.
- [12] P. Manju, A. Kumar Roy, C. Ramanan, Rajagopal, Post consumer PET waste as potential feedstock for metal organic frameworks, *Mater. Lett.* 106 (2013) 390–392.
- [13] F. Awaja, D. Pavel, Recycling of PET, *Eur. Polym. J.* 41 (2005) 1453–1477.
- [14] D.R. Abu Bakar, I. Ahmad, A. Ramli, Chemical recycling of PET waste from soft drink bottles to produce a thermosetting polyester resin, *Malays. J. Chem.* 8 (2006) 022–026.
- [15] G. Güçlü, M. Orbay, Alkyd resins synthesized from postconsumer PET bottles, *Prog. Org. Coat.* 65 (2009) 362–365.
- [16] G.P. Karayannidis, D.S. Achilias, I.D. Sideridou, D.N. Bikiaris, Alkyd resins derived from glycolized waste poly(ethylene terephthalate), *Eur. Polym. J.* 41 (2005) 201–210.
- [17] G.P. Karayannidis, D.S. Achilias, Chemical recycling of poly(ethylene terephthalate), *Macromol. Mater. Eng.* 292 (2007) 128–146.
- [18] A.S. Sabnis, G. Bhave, M.S. Kathalewar, S. Mare, P.P. Raut, New polyester polyol derived from recycled poly(ethylene terephthalate) for coating application, *Appl. Sci. Res.* 4 (2012) 85–93.
- [19] I. Vitkauskienė, R. Makuska, U. Stirna, U. Cabulis, Synthesis and physical-mechanical properties of polyurethane-polyisocyanurate foams based on PET-waste-derived modified polyols, *J. Cell. Plast.* 47 (2011) 467–482.
- [20] S.M. Kakić, I.S. Ristić, M. M-Cincović, N.Č. Nikolić, O.Z. Ilić, D.T. Stojiljković, J.K. B-Simendić, Glycolized products from PET waste and their application in synthesis of polyurethane dispersions, *Prog. Org. Coat.* 74 (2012) 115–124.
- [21] D. Eaves, Handbook of Polymer Foams, iSmithers Rapra Publishing – Technology & Engineering, 2004.
- [22] O. Kadkin, K. Osajda, P. Kaszynski, T.A. Barber, Polyester polyols: synthesis and characterization of diethylene glycol terephthalate oligomers, *J. Polym. Sci. Part A: Polym. Chem.* 41 (2003) 1114–1123.
- [23] D.S. Achilias, H.H. Redhwi, M.N. Siddiqui, A.K. Nikolaidis, D.N. Bikiaris, G.P. Karayannidis, Glycolytic depolymerization of PET waste in a microwave reactor, *J. Appl. Polym. Sci.* 118 (2010) 3066–3073.
- [24] S. Chaudhary, P. Surekha, D. Kumar, C. Rajagopal, P.K. Roy, Microwave assisted glycolysis of poly(ethylene terephthalate) for preparation of polyester polyols, *J. Appl. Polym. Sci.* 129 (2013) 2779–2788.
- [25] M.S.L. Pinto, Formulation, preparation, and characterization of polyurethane foams, *J. Chem. Educ.* 87 (2010) 212–215.
- [26] H. Wang, Y. Liu, Z. Li, X. Zhang, S. Zhang, Y. Zhang, Glycolysis of poly(ethylene terephthalate) catalyzed by ionic liquids, *Eur. Polym. J.* 45 (2009) 1535–1544.
- [27] J.P. Jog, Crystallization of polyethylene terephthalate, *J. Macromol. Sci. C* 35 (1995) 531–553.
- [28] F. Pardal, G. Tersac, Kinetics of poly(ethylene terephthalate) glycolysis by diethylene glycol. I. Evolution of liquid and solid phases, *Polym. Degrad. Stab.* 91 (2006) 2840–2847.
- [29] F. Pardal, G. Tersac, Kinetics of poly(ethylene terephthalate) glycolysis by diethylene glycol. Part II: effect of temperature, catalyst and polymer morphology, *Polym. Degrad. Stab.* 92 (2007) 611–616.
- [30] R.J. Sengwa, K. Kaur, Microwave absorption in oligomers of ethylene glycol, *Indian J. Biochem. Biophys.* 36 (1999) 325–329.
- [31] M. Ionescu, Chemistry and Technology of Polyols for Polyurethanes, iSmithers Rapra, Shawbury, Srewsbury, UK, 2005.
- [32] I. Vitkauskienė, R. Makuska, U. Stirna, U. Cabulis, Synthesis and physical-mechanical properties of polyurethane-polyisocyanurate foams based on PET-waste-derived modified polyols, *J. Cell. Plast.* 47 (2011) 467–482.
- [33] S. Narine, X. Kong, L. Bouzidi, P. Sporns, Physical properties of polyurethanes produced from polyols from seed oils: II. Foams, *J. Am. Oil Chem. Soc.* 84 (2007) 65–72.
- [34] M. Modesti, A. Lorenzetti, Improvement on fire behaviour of water blown PIR–PUR foams: use of an halogen-free flame retardant, *Eur. Polym. J.* 39 (2003) 263–268.

Thermodynamic Analysis of Linde System for Liquefaction of Gases

Devender Kumar^{*}, R.S Mishra

Department of Mechanical Engineering, Delhi Technological University, Delhi, India

Article Info

Article history:

Received 15 November 2013

Received in revised form

30 November 2013

Accepted 05 December 2013

Available online 15 December 2013

Keywords

Thermodynamics Analysis

Lindesystem,

COP,

Exergy Efficiency,

Exergy Destruction

Abstract

Cryogenics systems are which are capable of producing temperature below -150 .Linde cryogenics cycle is carefully observe and various gases are liquefy by it. A comprehensive exergy analysis and other analysis of linde system is carried out by using various different gases with variable properties. Numerical computation is carried out to find out mutually dependency and effect of various properties on other properties and their involvement in exergydestruction. It was observed that inlet properties and every part performance put huge impact on overall out of system Inlet pressure ranging from 3 to 6 bar and inlet Temperature at 298 K while compressor pressure ranging from 300 to 400 bar is optimum values of performance parameters for linde system.

Nome culture

m_2 =mass of air compressed I compressor

m_5 =mass of liquefied in the separator

m_6 =mass of low pressure air passing through heat exchanger

h =Enthalpy

s =Entropy

X =Dryness fraction

T =temperature

P =Pressure

η_{comp} =Efficiency of compressor (approx. 80%)

$\eta_{2nd\ law}$ =Second law efficiency

ϵ =Effectiveness of heat exchanger (approx. 80%)

C =Specific heat capacity fluid or gas

W_t =Work of reversible isothermal compression

W_{comp} =Shaft work supplied to compressor per unit mass

R =Universal gas constant

1. Introduction

Cryogenics is a process producing very low

^{*} Corresponding Author,

E-mail address: devenderdahiya@in.com

All rights reserved: <http://www.ijari.org>

temperature (Below -150 or 123 K), But according to National Institute of Standard and Technology Boulder, Colorado the temperature of cryogenics is start below from -180 (93.15 K) .This Temperature consider as the dividing line because boiling point of permanent gases (helium, hydrogen, oxygen, nitrogen and air like gases).Various process are design and invent to achieve cryo temperature at different level of lower temperature Cryogenics is used in various important process at different level with different naming like cryobiology, cryonics, cryo-electronics, cryotrons, cryosurgery etc. The liquefy gases are store in special containers called Dewar flask. To transfer this liquid from carrier to tank the pump which used are called cryogenics transfer pumps. Cyogenic Process to liquefy air which is further extent to extract various particular gases like oxygen, nitrogen, feronetc. Today cryogenics industries are a billionaire industry and lots of research is going on to achieve best one improved process. Always various analyses is done to identify the loop hole of process and to rectify it to their upper level. Various research and different method are employed to increase efficiency of cryo system. Second law efficiency are very low in all system, it value ranging from 3% to 23 % for most of systems. Advance technology like different cryofluid includes nano one (nano fluid and nano lubricants) is also tried to reduces the losses.

Ceramic technology is also used in separator to increase the high output with less losses. Low increase in exergy efficiency is noticed in various different systems. Exergy efficiency are mainly depend upon the inlet condition of system and in most of cases the inlet conditions are NTP (normal temperature pressure) conditions that is 298 K temperature and one atmosphere pressure.

Except to increase the whole system efficiency stress are done on particular parts of system and research are done on that systems. Air separation unit and compressor, condenser and evaporator of cryo system are the center of research because most of exergy destruction takes place in these parts. This paper mainly dealt with thermodynamic (exergy and anergy) analysis of Linde system for determining the effect of every component of system with varying conditions for maximum second law efficiency.

2. Literature Review

In last several decades, exergy analysis has used for system optimization. Exergy analysis is power tool in thermal engineering which not only show the loop hole but give us the idea about how much a system is useful corresponding our input. Exergy and anergy are two terms mostly used get idea of feasibility of a process economically. Exergy is define as the availability of maximum useful work that can be obtained from a system in a given environment conditions. In exergy analysis exergy destruction of each component is noted and efforts are put to minimize them. Irreversibility is just the two face of a coin it also represent exergy destroyed, waste potential and represent energy that could not converted into work except wasted. So irreversibility which always should keep low as possible as an optimizer can do without effecting other properties. In the analyses of open cycle desiccant cooling systems, The analysis shows that an exergy analysis can provide some useful information with respect to the theoretical upper limit of the system performance, which cannot be obtained from an energy analysis alone. The analysis allows the determination of the sites with the losses of exergy, and therefore showing the direction for the minimization of exergy losses to approach the reversible COP [1].

Various research are done to examine the exergy losses in a process and It is found that the evaporating and condensing temperatures have strong effects on the exergy losses in the evaporator and condenser, and on the second law of efficiency and COP of the cycle but little effects on the exergy losses in the compressor and the expansion valve. The second law efficiency and the COP increases,

and the total exergy loss decreases with decreasing temperature difference between the evaporator and refrigerated space and between the condenser and outside air[2] and if advance technology like Nano fluid include it noiced that Nano fluid and Nano lubricant cause to reduce the exergy losses in the compressor indirectly [3].

Various components are taken under studied and ASU (air separation unit) using distillation columns are one of the main methods used for separating air components. Exergy analysis, inefficiencies were identified in the distillation system for an efficient cryogenic air separation plant producing large-tonnage quantities of nitrogen [4]. Exergy efficiency of a double diabatic column, with heat transfer all through the length of the column, is 23% higher than that of the conventional adiabatic double columns. In a simple adiabatic distillation column, most of the exergy losses occur in the column itself (57%) [5]. Now as advancement goes on technology switching toward more efficient method of separation; polymeric membrane and membrane on ceramic technology are used for separating oxygen [6].

Number of parameters for optimization are taken but still compressor are the main element which determining the energy parameters of low cryogenic technology. So, we have to first eliminate not only compressor part but use of all these type of machines which are not only efficient but also eco friendly too. In other word, the problem of making a transiting to new cooling principles is critical and for this one of the most promising alternatives may be electro caloric cooling [7]. Lindehampson cycle is one of the oldest and very prominent type of process which cryo technology used form last decades efficiently but its low mass producing inefficiency still a major drawback in advancement of Linde cycle. Linde cycle is suitable for large number of gases liquefaction. It is shown that more than half of the exergy loss takes place in the liquefaction unit and almost one-third in the air compression unit. Minor exergy losses are taking place in the distillation unit and the main heat exchanger. The major cause of exergy loss is the use of compressors and to a lesser extent the use of turbines [8].

3. Thermodynamic analysis of Linde system for liquefaction of gases

Compressor work

$$\eta_{\text{comp}} = \frac{W_t}{W_{\text{comp}}} \quad (1)$$

$$W_t = mRT \ln \frac{P_2}{P_1} \quad (2)$$

$$W_{\text{comp}} = h_2 - h_1 - T_1 (s_2 - s_1) \quad (3)$$

$$W_{\text{reversible}} = W_{\text{actual}} - T_0 s_{\text{gen}} \quad (4)$$

$$W_{\text{actual}} = \frac{W_{\text{comp}}}{x} \quad (5)$$

$$W_{\text{reversible}} = h_5 - h_1 - T_0 (s_5 - s_1) \quad (6)$$

Heat Exchanger

$$m_2 (h_2 - h_3) = m_6 (h_1 - h_6) \quad (7)$$

$$m_2 (h_2 - h_3) = (m_2 - m_5) (h_1 - h_6) \quad (8)$$

$$: m_6 = (m_2 - m_5) \quad (9)$$

$$= \frac{C_h (T_2 - T_3)}{C_{\min} (T_2 - T_6)} \quad (10)$$

Throttling process

$$h_3 = h_4 \quad (11)$$

Heat Balance of the separator

$$m_2 h_4 = m_5 h_5 + m_6 h_6 = m_5 h_5 + (m_2 - m_5) (h_6) \quad (12)$$

Second law analysis

$$\eta_{2\text{nd}} = \frac{W_{\text{rev}}}{W_{\text{actual}}} \quad (13)$$

COP (coefficient of performance)

$$\text{COP} = \frac{h_2 - h_1}{h_2 - h_1 - T_1 (s_2 - s_1)} \quad (14)$$

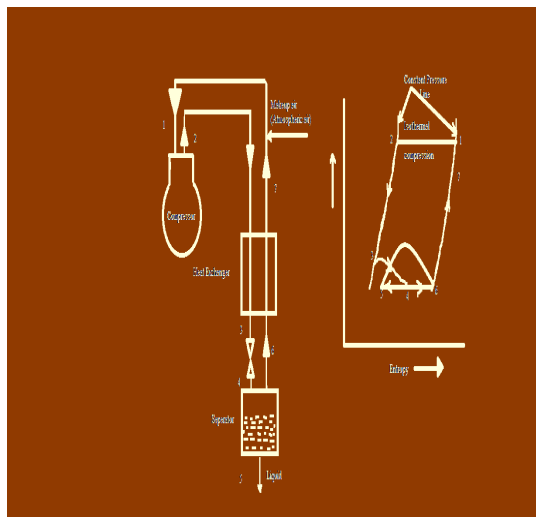


Fig: 1. (LindeHampson System)

An analysis of various parameters is measured for Lindehampspon cycle with the help of Engineer equation solver for various gases. Simplest cycles as shown in Fig. 1 are taken for analysis and measured the loop holes responsible for inefficiencies in various processes in cycle. In linde system fluid in gases form are fed into the system at atmospheric

condition, after that the air is isothermally compresses up to great pressure, then this pressurize and high temperature air is fed into the heat exchanger where it is cooled to a great extent after that the it is throttled where it become convert into partially liquid and partially gaseous form. A separator is provided to separate gaseous form to liquid form .Gaseous form is again fed to the compressor after passing through the same heat exchanger and after mixing with the makeup gaseous form.

Linde system is used to liquefy various forms of gases as per our convenience of our system efficiency of system for a particular gas. After reviewing literature it conclude that every part of system has its own and equal importance because ones effect on another whether it is small or big create a lot of difference in proper analysis of system. Ignoring one small system due less effect can put gap in complete research analysis of system that why it quite important take all parts of system as one and finding out the every part impact on another to calculate right equation for high output. Heat exchanger and expansion valve, expander and other addition parts should also properly analyze. Advanced technologies are used in very limited way and only on some part of system. From literature it noticed that exergy efficiency depend upon mainly upon the inlet condition of the system but which inlet condition best suit for a particular type of the system that is main work of research.

4. Results and Discussion

Fig. 2 shows the variation of liquefaction mass and compressor pressure and it is observed that compressor pressure increases liquefaction mass also increases but as seen above after compression pressure 350-400 the liquefaction mass start decreasing for most of gases and become stable for like methane. Fig. 3 COP is inversely proportional to the compressor pressure as it increases COP of system decreasing. In Fig. 4 the second law efficiency is best suited between 300-400 compressor pressure ranges.

In Fig. 5 show that there is increase in liquefaction mass of gas if the inlet pressure increases but as from graph this increase very low

COP is directly proportional to the inlet pressure as it increases COP increases significantly. Inlet pressure ranging from 4 to 6 bars in Fig. 6 show very good statics of COP.

Inlet pressures play a very important role in case of work input. In Fig. 7 it shows that as the pressure increases work input start decreasing. From 1 to 4

atmospheric there is significant drop of work input after that the drop is very marginal.

At NTP condition the liquefaction temperature of any gas is very low and keep that temperature in storage of Liquefy gas is very challenging task. In Fig. 8 the Inlet pressure increase also increases the liquefaction temperature of gas.

In Fig. 9 the graph show that there is increase in second law efficiency with increase in Inlet pressure but the increase is very less as shown in above graph. Liquefaction mass decreases as the inlet temperature increases, in Fig. 10 there is swift decrease in mass from 298 to 308 K but after that the decrease factor

slow down for further increase in inlet temperature. Fig. 11 show inlet temperature is directly proportional to the COP for fluorine and methane gas but for other gas it seems from graph trend that they become constant or very marginal increases in COP with increase in inlet temperature.

As the temperature increases work required increases but in case of methane the increase is very large as compare to other gas as show in Fig. 12.

There is decrease in second law efficiency corresponding to increase in inlet temperature. Methane gas show very large drop of efficiency compare to other gases as shown in Fig. 13 graph.

	Air	Methane	Oxygen	Nitrogen	Fluorine	Argon
Inlet Temp (K)	298	298	298	298	298	298
COP	0.07324	0.5161	0.4755	0.4954	0.4932	0.3454
inlet mass (kg)	1	1	1	1	1	1
liquefied mass (Kg)	0.0778	0.1991	0.1072	0.07564	0.07665	0.1154
□ 2nd (%)	12.64	27.8	16.77	12.3	12.67	17.61
Inlet pressure (Atmosp)	1.013	1.013	1.103	1.013	1.013	1.103
Compressor work (Wc) (kJ/kg gas)	450.8	772.6	401.9	468.2	341	322.2
Compressor outlet pressure	200	200	200	200	200	200
Dryness Fraction	0.9222	0.8009	0.8298	0.9244	0.9233	0.8846
liquefied Temp (K)	81.5	111.7	90.19	77.35	85.03	87.3

Table: 1.

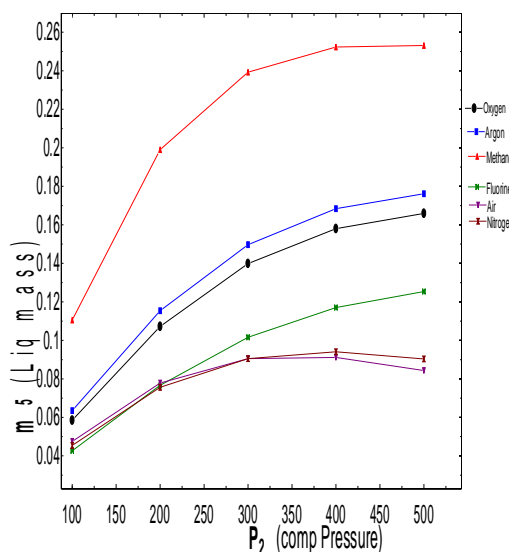


Fig. 2. Variation of liquefaction mass with compressor pressure

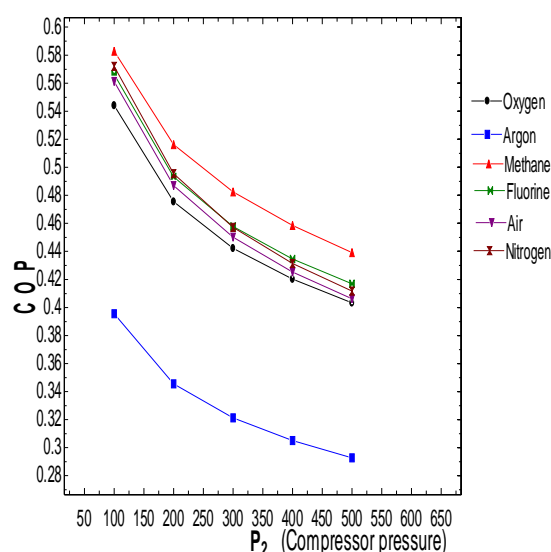


Fig. 3. Variation of COP with compressor pressure

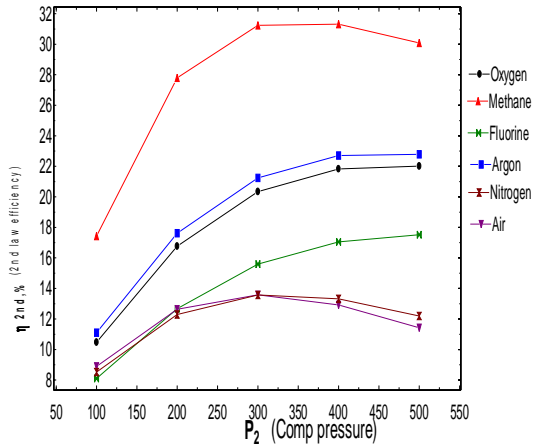


Fig. 4. Variation of Second law Efficiency with Compressor Pressure

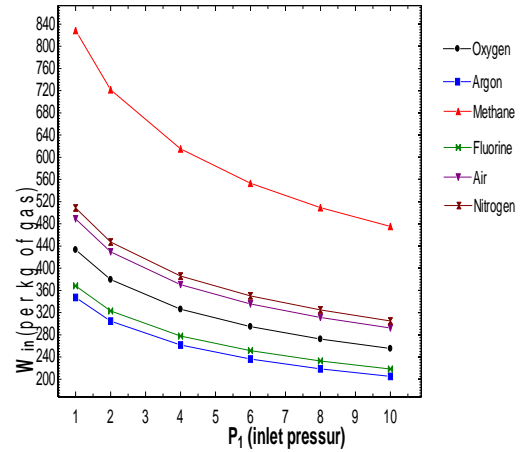


Fig. 7. Variation of W_{in} (Compressor work/kg gas) with inlet Pressure

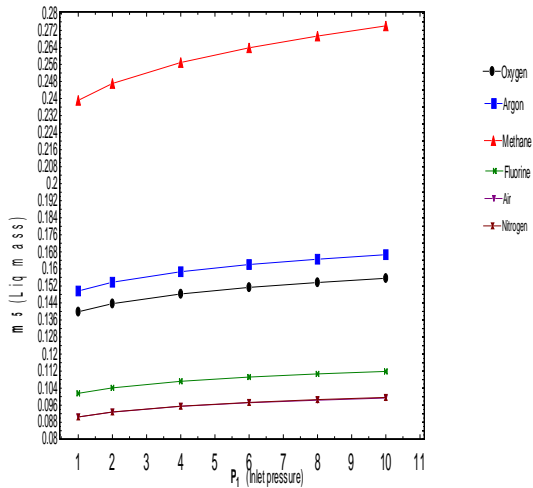


Fig. 5. Variation of liquefaction mass with inlet Pressure

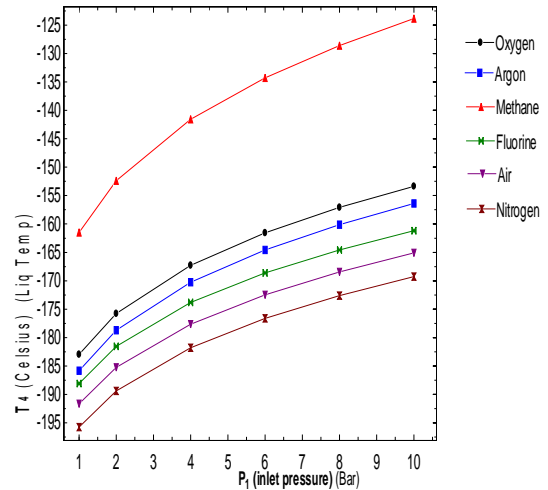


Fig. 8. Variation of liquefaction Temperature with inlet Pressure

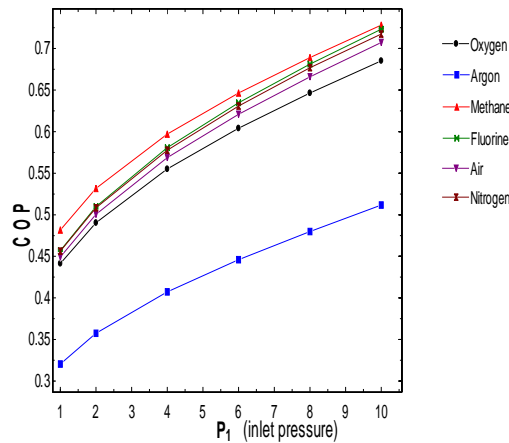


Fig. 6. Variation of COP with inlet Pressure

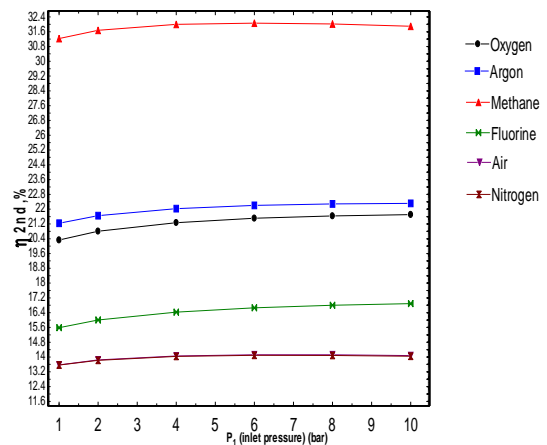


Fig. 9. Variation of Second law Efficiency with inlet Pressure

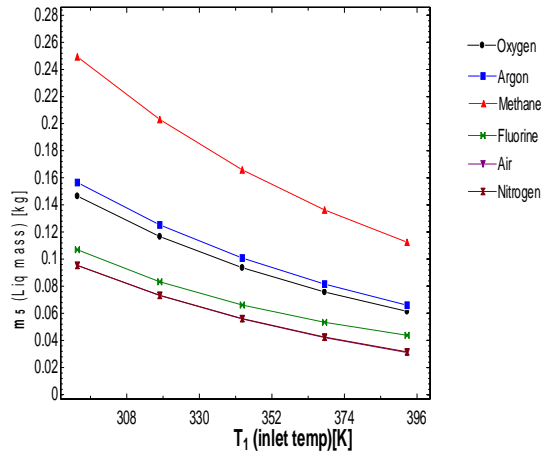


Fig: 10. Variation of liquefaction mass with inlet Temperature

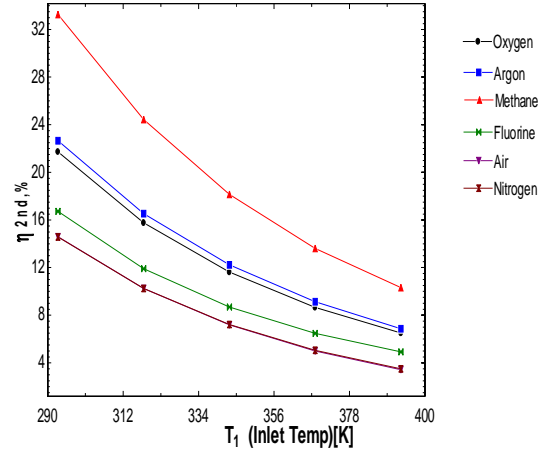


Fig: 13. Variation of Second law Efficiency with inlet Temperature

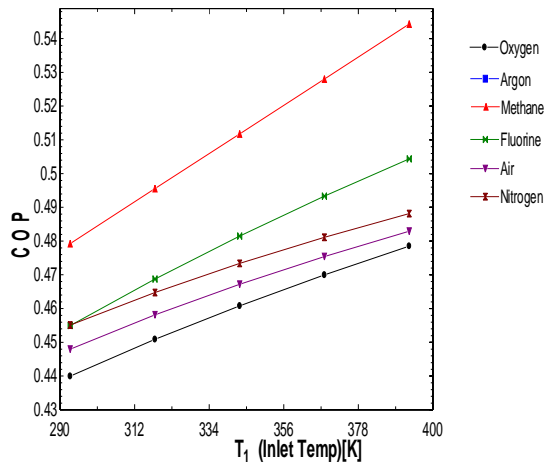


Fig: 11. Variation of COP with inlet Temperature

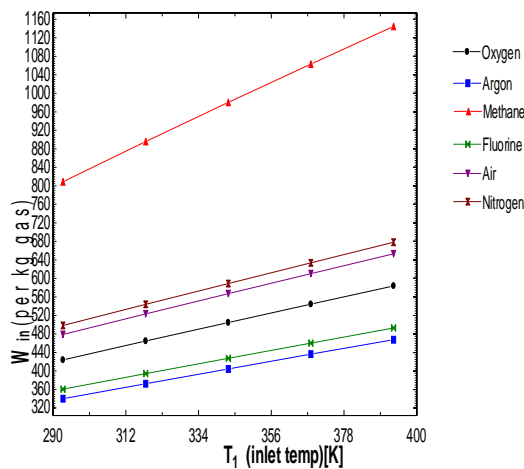


Fig: 12. Variation of W_{in} (Compressor work/kg gas) with inlet Temperature

5. Conclusion

- Compressor pressure ranging from 300 to 400 bar is very efficient for system
- From above analysis it noticed that inlet pressure of system should keep between 3 to 6 bar for good result.
- Second law efficiency for inlet temperature is high at NTP temperature.
- It is not significant to say that mainly inlet condition are responsible for system output, every part of system put their own effect on output condition.

References

- [1] Mehmet Kanoglu, MeldaOzdinc, Carpinlioglu and MurtazaYıldırım, "Energy and exergy analyses of an experimental open-cycle desiccant cooling system", *Applied Thermal Engineering* 24 (2004) 919–932
- [2] RecepYumrutaş, Mehmet Kunduz, Mehmet Kanoğlu, "Exergy analysis of vapor compression refrigeration systems", *Exergy, An International Journal*, 2 (4), 2002, Pages 266-272
- [3] J.U. Ahamed, R. Saidur, H. H. Masjuki, "A review on exergy analysis of vapor compression refrigeration system", *Renewable and Sustainable Energy Reviews*, 15 (3), April 2011, Pages 1593-1600
- [4] R. Agrawal, D.W. Woodward, "Efficient cryogenic nitrogen generators: An exergy analysis, *Gas Separation & Purification*", 5 (3), September 1991, Pages 139-150
- [5] J. Rizk, M. Nemer, D. Clodic, "A real column design exergy optimization of a cryogenic air separation unit", *Energy*, 37 (1), January 2012, Pages 417-429.
- [6] GaelleGosselin "Thermodynamic study of oxygen-enhanced combustion: analysis of different techniques of oxidant production" KTH industrial engineering and management, Master of Science Thesis EGI 2012: HT
- [7] Yu. V. Sinyavskii, "Electrocaloric refrigerators: A promising alternative to current low-temperature apparatus" *Chemical and Petroleum Engineering*, 31 (6), June 1995, pp 295-306
- [8] R.L. Cornelissen, G.G. Hirs, "Exergy analysis of cryogenic air separation", *Energy Conversion and Management*, 39 (16–18), November–December 1998, Pages 1821-1826.
- [9] R.S Khurmi and Gupta "Refrigeration and air conditioning"

VIBRATION INDUCED DUE TO ACOUSTIC EXCITATION IN DIFFUSE FIELD CONDITIONS

Naveen Garg^{1,2} and Sagar Maji²

¹ Apex Level Standards & Industrial Metrology Division, CSIR - National Physical Laboratory, New Delhi, India

² Department of Mechanical, Production & Industrial Engineering, Delhi Technological University, Delhi, India
ngarg@nplindia.org

The paper presents an experimental approach to quantify the vibrations induced due to acoustic excitation in diffuse field conditions. An empirical formulation correlating the varying sound field and vibration level generated in floors and walls in diffuse field conditions has been developed. A lower limiting frequency of 125 Hz for good diffusion is observed due to random wide band acoustic excitation in diffuse field conditions, below which lower vibration levels are registered due to discrete room modes.

INTRODUCTION

Structural vibrations results from both air-borne and ground-borne excitation. The induced vibration in buildings results from various external sources, for example, traffic, blasts, construction activities, sonic boom, low frequency noise from aircrafts flyover, impulsive impacts or human activities. The acoustic waves exert fluctuating forces over the building elements, causing them to vibrate which may be enhanced by resonances in case the frequency of sound waves interacting lie within the domains of natural frequency of structure. The acoustic-elastic coupling may be pronounced at lower frequencies, that is, at natural frequencies of a building, room, or wall vibration. Hubbard [1] correlated the measured accelerations for a number of different types of noise inputs on the basis of peak noise level and found that measured acceleration levels increase linearly as the input level increases. Walls, floors, ceilings and large windows respond mainly in the “oil canning” modes at frequencies below 100 Hz and their motions are controlled largely by the beam elements. The response of windows was observed to be 0.015 g/Pa, while the wall acceleration levels were observed to be 10 dB lower than the window levels. Hodgdon et al. [2] demonstrated a threshold of rattle to be 97 dB. The investigations revealed that the *A*-weighted sound levels correlate poorly with acceleration levels, while the unweighted Sound Exposure level L_E and the maximum sound pressure level correlate well. Santos Lopes et al. [3] worked on the determination of a noise level limit to be imposed on any music sound equipment operating inside the sensitive building in order to avoid damaging vibrations in the building facades. A sound level limit of 105 dB(A) was proposed corresponding to the maxima velocity value of 0.7 mm/s for the root mean square velocity measured in a direction normal to the wall, and 3.5 mm/s for peak normal velocity. A frequency limitation of 63 Hz corresponding to sound pressure of 80 dB(A) was also proposed as limit to be imposed by an electronic device, connected to a microphone.

The difference between a mechanical excitation and acoustic excitation of a given structure is actual coupling between

the structural modes and applied excitation. The coupling efficiency depends upon how well the sound waves interact with structural modes in case of acoustic excitation [4]. The problem of acoustic fatigue is also very critical for design of aircraft structures subjected to high acoustic loads due to which light weight structures are tested in reverberation chambers to simulate the launch conditions. Statistical Energy Analysis (SEA) has been widely employed by many researchers to predict vibroacoustic problems for interconnected mechanical systems [5,6]. Chang and Nicholas [7] used Green’s functions to study the frequency response of structural–acoustic systems. The sensitivity of the structure to diffuse acoustic field has been modelled explicitly by Cremer and Heckl [8] using the principle of acoustic reciprocity, wherein the sound power radiated by the structure is analyzed numerically when a mechanical force F acts upon the structure.

$$\frac{|v'|^2}{|p'|^2} = \frac{8\pi}{k^2 \rho^2 c^2} \frac{P_{rad}}{|F|^2} \quad (1)$$

where k is the wave number, ρ is the density of the medium and c is the speed of sound. $|v'|^2$ is the structural velocity response squared at a certain point A of the structure due to a diffuse acoustic sound field with a (spatially averaged) sound pressure level $|p'|^2$ (the sound incidence case), whereas P_{rad} is the acoustic sound power which is radiated by a force F acting on the same point A .

Rozen et al. [9] discussed a numerical procedure to predict the disturbances due to acoustic excitation of machinery. The sensitivity of a simple structure consisting of a cantilever beam and a base plate to diffuse acoustic field excitation typical for the sound fields in clean rooms was predicted and measured. It was observed that simulations agree reasonably well within the measurements in a reverberant room. A recent study by Løvholm et al. [10] reveals that low frequency sound interaction with the fundamental frequencies of the building components combined with air leaks in the building envelope are the main

factors that govern transmission of sound into the building. There are very few such studies that discuss the low-frequency coupling of the acoustic pressure field to the building dynamics using a 2D finite element model.

The present work aims in determining the amplitude of vibration levels induced due to sound fields in diffuse field to investigate the probability of damage in the buildings due to intense sound fields. An empirical formulation correlating the noise levels and vibration of walls and floors is developed. The magnitude of vibration levels generated is analyzed in frequency domain to understand the behaviour especially at low frequencies. However, the coupling efficiency gets accentuated in mid frequency region especially at coincidence zone. A source within the room will excite multiple resonances and thus the sound field is composed of the addition of the many standing waves that the room supports, whilst at the high frequencies, the wavelength is small compared to the room dimensions and also the acoustic energy levels are attenuated. Thus, in the high frequency region, sound waves are unable to excite the bending modes in the structure.

LABORATORY INVESTIGATIONS

An investigation was carried out in a diffuse field conditions in laboratory to measure the vibrations levels generated due to diffuse sound field excitation. The measurements were conducted in Reverberation chambers at the National Physical Laboratory, New Delhi. The dimensions of reverberation chamber are $6\text{ m} \times 6.5\text{ m} \times 7\text{ m}$. The reverberation chamber is a room within another room, both rooms being reinforced concrete [11]. The outer room has a floor slab 300 mm thick supported on folded RCC plates and wall and ceilings are 125 mm thick. The inner room is floated on a 150 mm thick bed of coarse dry sand washed free of mud and silt. The sand bed is initially covered with 50 mm thick fiberglass and 25 mm thick particle board. The walls of inner chamber are 125 mm thick RCC resting on the floated floor made of highly polished terrazzo concrete. Imparting high polish to the surfaces, the viscous drag and thereby energy loss is minimized. The measured value of reverberation time for empty room with random uncertainty less than $\pm 0.1\text{ s}$ is shown in Figure 1.

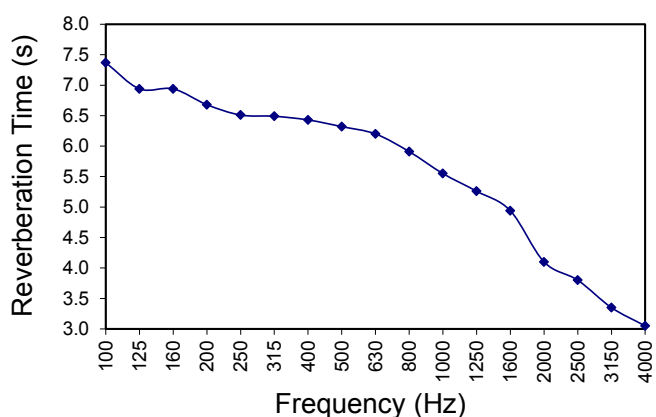


Figure 1. Reverberation time measurements for empty room

The walls, floor and ceiling are non parallel, the average inclination between the walls being 6° and between floor and ceiling 2° to 3° . To prevent the resonance modes, the 125 mm cavity between the inner and outer walls is partially filled with mineral wool blanket to cover 30% of the area. The ceiling of inner chamber is made of polished stone slabs 50 mm thick resting on steel girders and the plenum between the inner ceiling and outer room roof slab is partially filled with mineral wool to damp out resonance modes in this space. The double entry doors as shown in Figure 2 made of sandwich construction consisting of two sheets of 16 gauge mild steel on the outside and one sheet of 1.6 mm thick lead in the middle, with 25 mm air gap on the either side of lead sheet filled with fibre glass. The door panels fit into a rebated 14 gauge sheet steel frame filled with concrete after fixing in position, with rebates lined with soft rubber so as to give a good seal when door is tightly closed with wedged latch [11].

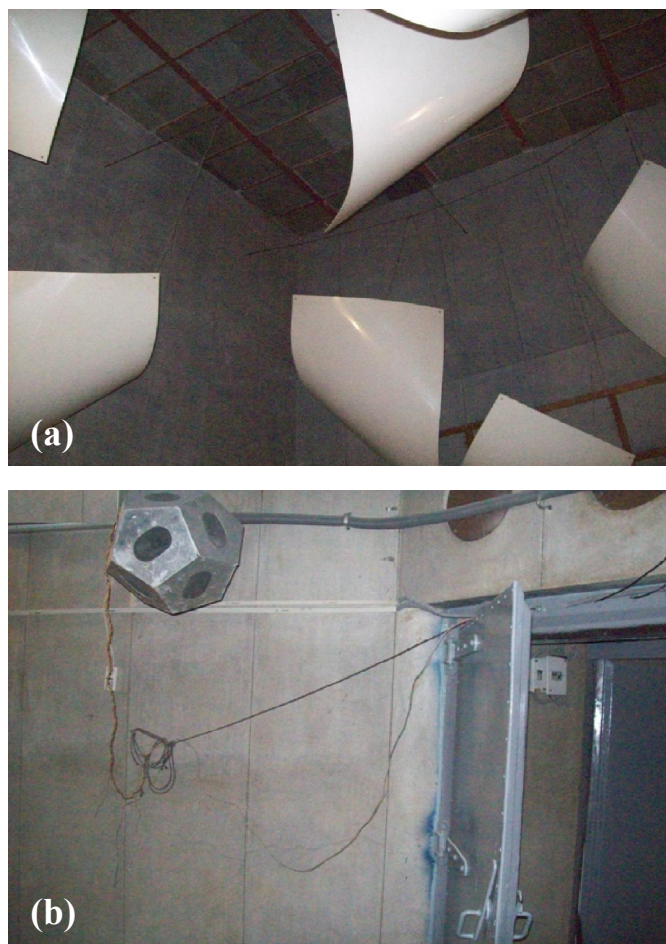


Figure 2. (a) Pictorial view of diffusers installed in reverberation chambers at NPL, (b) View of dodecahedral loudspeaker in reverberation chamber with double entry doors

The sound source installed in the room consists of twelve $100\text{ mm} \times 150\text{ mm}$ elliptical speaker units mounted in a dodecahedral enclosure fed through a power amplifier delivering up to 20 W (rms) output as shown in Figure 2. The omni-directional microphones measuring the sound

field are suspended from the ceiling at different heights and different locations so as to cover spatial zones in the chamber. A pink noise generated the acoustic excitation through a dodecahedral loudspeaker system coupled with an amplifier. Sound pressure levels inside the chamber were measured by a Norwegian Electronics 830 dual channel real time analyzer (RTA 830) in linear weighting. The vibration measurements were conducted using a seismic accelerometer B&K 8318 calibrated on primary vibration calibration system by a laser interferometer in frequency range 0.1 Hz to 1 kHz connected to a B&K measuring amplifier Type 2525 and the frequency spectrum of the induced vibration was obtained using an Agilent Audio Analyzer, Model U8903A. The sound field was generated in a varying range from 50 dB to 120 dB and the vibration levels (1 Hz to 1 kHz) on floor and walls of the chambers were measured as shown in the Figure 3 [12]. The magnitude of vibration level was measured at seven different points on the floor and walls of reverberation chamber. The standard deviation of magnitude was observed to be $\pm 2.88 \text{ mm/s}^2$ for walls and $\pm 3.67 \text{ mm/s}^2$ for floor vibration. The linear relationship of vibration levels induced due to acoustic excitation plotted in Figure 3 is consistent with Hubbard investigations [1] whereby the acceleration response increase generally as the sound pressure levels increase and follows a straight line relationship based on the assumption of linear behaviour of the structure.

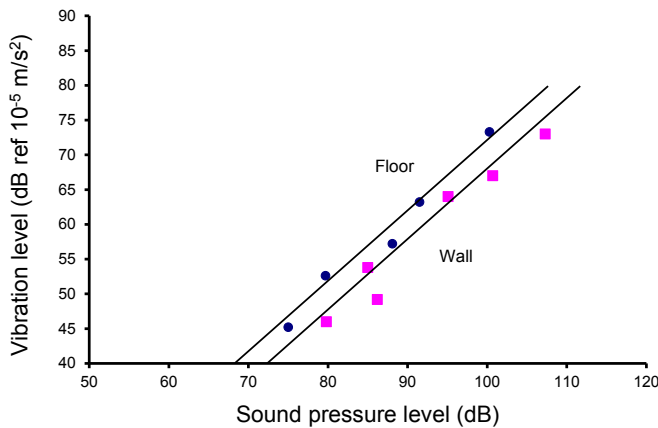


Figure 3. Induced floor and wall vibration due to wideband random acoustic excitation

The induced vibration of the floor ($L_{a(floor)rms}$) in the frequency domain shown in Figure 4 generated due to the random acoustic excitation is also correlated by a simple regression fit as

$$L_{a(floor)} = L_p - 10\log(f) - 10 \text{ (dB)} \quad f \geq LLF, r^2 = 0.74 \quad (2)$$

where $L_a = 20\log(a/a_{ref})$ and $a_{ref} = 10^{-5} \text{ m/s}^2$. Thus the above empirical relation can be used to predict the floor vibration induced to acoustic excitation in a diffuse field at different frequencies. The reverberation chamber has a lower limiting frequency (LLF) for good diffusion of 125 Hz. The relation

between random and the lower limiting frequency is observed to be

$$L_{a(floor)}(random) = L_{a(floor)}(LLF) + 3 \text{ (dB)} \quad (3)$$

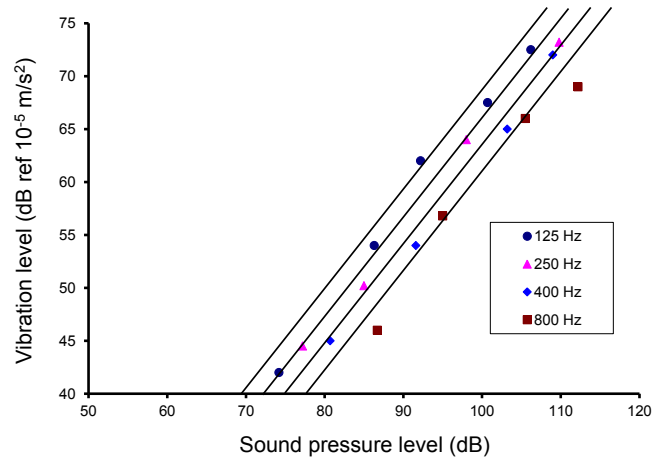


Figure 4. Induced floor vibration due to acoustic excitation of a filtered band at different centre frequencies

DISCUSSION

The enclosed space in the reverberation room can be considered as a complex resonator possessing many normal modes of vibrations excited by introducing a sound source into the room. The acoustic energy supplied by the source is considered as residing in the standing waves established in the enclosed space. The characteristic frequencies of vibration of the standing waves depend upon the room size and shape whereas the damping of these waves depends mainly on the boundary conditions. The extent of diffusion can be judged by uniformity of reverberation time within the volume of room, linearity of sound decay at different points in the room and uniformity of sound intensity distribution within the room. The experimental investigations carried out for measurement of reverberation time show that the decay curves at all positions in the room and at all frequencies have a smooth, linear drop of at least 40-45 dB from the initial sound cut-off. The distribution within the room of sound level of filtered band of white noise is within $\pm 0.5 \text{ dB}$ at high frequencies and within $\pm 1 \text{ dB}$ at low frequencies. Diffusing plates have also been additionally suspended from ceiling and oriented at random to enhance the state of diffusion in the room as shown in Figure 2(a). The standard deviation of correlation coefficient ($\sin kr / kr$) was measured to be within ± 0.06 [11,13] in the frequency range 100 Hz to 125 Hz.

The expression for modal density that applies approximately to rooms of any shape including cylindrical rooms is given by [14]

$$\frac{dN}{df} = \frac{4\pi f^2 V}{c^3} + \frac{\pi f S}{2c^2} + \frac{L}{8c} \quad (4)$$

where V is the volume, S is the total surface area and L is the

sum of length of all edges of the room. At higher frequencies, there is fairly even modal distribution and spacing between the characteristic frequencies is close, while at low frequencies, there are very few modes. So, the average sound energy density is not the same throughout the enclosed space and thus the sound field is not diffuse. A diffuse field can be established in a rectangular room if there is at least 20-30 modes in the measurement bandwidth [15], and there is at least one mode per Hz. In the present case, the number of modes has the value 21 for $f = 100$ Hz and $\Delta f = 13$ Hz (1/6 octave bandwidth). Since the room is not symmetrical, the eigen-tone frequencies cannot be calculated easily. However, if the room is assumed to be rectangular with dimensions corresponding to the average dimension, the eigen-tones between 110 Hz and 125 Hz would have been spaced 1 Hz apart. The lower limiting frequency for good diffusion is observed to be 125 Hz. Where diffuse conditions exist, Figure 3 shows that the acceleration level increases linearly with acoustic excitation (L_{in}). The diffuse field conditions are however difficult to achieve in a normal build up areas and thus there may exist deviations from the results predicted due to empirical formulation. This may be attributed due to the spatial distribution of sound field, inherent damping of the system and excitation of resonances in case the vibration frequency falls within bounds of natural frequency of structure. Hodgson observations [16] reveal that diffuse field theory can be applied in the case of an empty room with quasi-cubic dimensions, specularly reflecting surfaces and uniform surface absorption. However, it has been experimentally demonstrated that even in small rooms, the uniformity of the sound field can be significantly improved with diffusers [17, 18]. Schroeder [19,20] described a cross-over frequency that denotes approximately the boundary between reverberant room behaviour above and discrete room modes below for airborne sound in reverberant enclosures calculated empirically from equating the half-power bandwidth B ($B = 2.2/T_{60}$) of the resonances with three times the average asymptotic spacing Δf ($\Delta f = c^3 / 4\pi V f^2$) between resonance frequencies giving f_s as [20]

$$f_s = 2000 \sqrt{\frac{T_{60}}{V}} \quad (5)$$

where T_{60} is the reverberation time of the room in seconds and V is the volume of the room in m^3 and the factor 2000 (which contains the velocity of sound) guarantees that on average, at least three resonances fall within the half-power bandwidth of one resonance at frequencies above f . In the normal rooms, the frequency f of Eq. (2) becomes equivalent to f_s of Eq. (5).

The modified equation suggested by Néglise et al. [15] is given by

$$f_s \approx 3 \sqrt{\frac{\alpha c^3}{4\pi\eta V}} \quad (6)$$

where α is the model overlap, c is the speed of sound and η is the damping factor. For a damping of $\eta = 5 \times 10^{-3}$ [15] and model overlap $\alpha = 3$ as proposed by Schroeder, f_s is calculated to be 192 Hz in the present case.

Figure 5 shows the response of floor in g/Pa at different frequency. For sound pressure level of 1 Pa (or 94 dB), Eq. (2) reduces to

$$L_{a(floor)} = 84 - 10\log(f) \quad (dB) \quad (7)$$

The overall response of the floor is observed as 0.0002 g/Pa (20.4 mm/s²/Pa) and for the wall as 0.0015 g/Pa (13.2 mm/s²/Pa). It can be observed that the g/Pa value diminishes at higher frequencies and also strong coupling of sound waves with the structural modes in dominant in the frequency range from lower limiting frequency (LLF) up to 500 Hz.

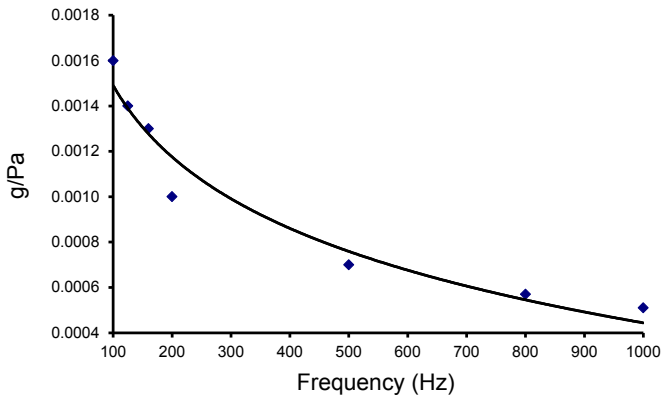


Figure 5. Response of floor to induced acoustic excitation in g/Pa

In most of the practical situations, the acoustic excitation in the free-field conditions and induced vibrations on the facades and low frequency response exhibit a complex behaviour with uncertainties arising from sound structure interaction. Some of the acoustic excitations like sonic boom, cracker bursting and open air detonation of charges can produce high acoustic stimulus of lower frequencies. Since their occurrence is hardly likely and is always confined to outdoors, this affect their coupling to the facade of a structure under free field condition and the induced vibrations never exceed the indoor diffuse criteria as described by Eq. (2). Air borne excitation is mainly low frequency sound waves interacting with building elements like windows, doors etc. causing them to vibrate, while ground borne vibration propagates through building foundation and floor supporting walls. The interaction of sound waves with structure in free-field conditions is quite cumbersome to model as various uncertainties are involved in acoustic-elastic coupling. Thus, a large database for vibration induced due to various noise sources like transportation, aircrafts flyover, blasts etc is required for analyzing the severity and perceived response by the community. For instance, a study conducted to ascertain the magnitude of maximum floor vibration level generated in a historical structure during ceremonial gun firing reveals a vibration level of 6×10^{-3} g (rms) for noise level of 125 dB(A). The floor modes of 25 Hz, 42 Hz, 69 Hz and 100 Hz get amplified during the excitation [21]. Another study conducted for monitoring the transient acceleration induced due to overflying aircrafts landing and take-off over ancient monument reveals a maximum acceleration observed as 3×10^{-3} g (rms) and major

resonant modes excited in structure lying in frequency range 10 Hz to 100 Hz [22]. Experience for blasting, explosions and for sonic booms suggest that damage to houses may occur at peak acceleration values between about 0.3 and 3.0 g in the frequency range of 10 to 100 Hz respectively [23]. The widely used German standard, DIN 4150 [24] provides limit values for different types of structures and for different sources of vibration in conjunction with assessment of building damage caused by short-term and long-term vibrations. The generally accepted code of degree of damage to structures is correlated with the ground motion peak velocity and frequency as the strain imposed on the building at foundation level is proportional to peak particle velocity. In present context, for the extreme condition of the random acoustic excitation in diffuse field, Eq. (2) can be considered for predicting the maximum acoustic excitation for structural integrity as prescribed by DIN 4150 and BS 7385 standards [25]. The present study also emphasizes the need for correlating the induced vibration levels with *C*-weighted sound pressure level or sound exposure levels as *A*-weighting devaluates the low frequency noise.

CONCLUSIONS

An empirical formulation correlating the vibration induced due to acoustic excitation in diffuse field conditions is developed. In practical situations, as the diffuse field conditions don't prevail, the interaction of sound waves with structural modes gets diminished resulting in weak coupling and thus lower vibration levels are registered. The transition frequency also called the Schroeder frequency thus governs the interaction of sound waves with structural modes in practical situations. It may be noted that the vibration of any structure is dependent upon the material properties and boundary conditions in addition to the external forcing function. The paper considers the forcing function (diffuse field conditions) only and can't be generally applied to other structures with a definite level of confidence. However, it quantifies the maximum vibration levels induced in a diffuse field set up for adjudging the severity of vibration levels induced due to high acoustic loads. Further investigations in this regard on vibration induced due to acoustic excitation in free field conditions and correlation of the induced vibration with weighted acoustic excitation (*A*-weighting, *C*-weighting, L_{max} and Sound Exposure Level) in free field conditions shall be helpful in better understanding of sound waves interaction with structural elements in practical situations. A comparison with diffuse field conditions is also to be investigated for characterizing the vibroacoustic behaviour of structures explicitly in different situations.

ACKNOWLEDGEMENTS

Authors would like to thank Archaeological Survey of India (*ASI*) for funding the project on investigations on induced vibrations due to acoustic excitation from Sound show at historic monuments, NPLI/CNP 090532 and CNP 090732. The author would also like to express his sincere gratitude to the Director of NPL for allowing the work to be published. Authors also thank retired colleague Mr Omkar Sharma for his support and help in experimental observations and analysis in this study.

REFERENCES

- [1] H.H. Hubbard, "Noise induced house vibrations and human perception", *Noise Control Engineering Journal* **19**, 49-55 (1982)
- [2] K.K. Hodgdon, A.A. Atchley and R.J. Bernhard, *Low frequency noise study*, Technical Report, The Partnership for Air Transportation Noise and Emissions Reduction, PARTNER-COE-2007-001, 2007 <http://web.mit.edu/aeroastro/partner/reports/proj1/lfnreport-2007-001.pdf> (last accessed 5 January 2014)
- [3] L. Santos Lopes, J. Patricio, Schiappa de Azevedo and F. Aristides Chaves, "Vibrations due to sound fields in a sensitive building. Damage criterion for the noise level", *Proceedings of Acústica 2008*, 20-22 October 2008, Coimbra, Portugal
- [4] D.C.G. Eaton, *An overview of structural acoustics and related high-frequency-vibration activities*, European Space Agency Bulletin No. 92, 1997 <http://www.esa.int/esapub/bulletin/bullet92/b92eaton.htm> (last accessed 5 January 2014)
- [5] K. Renji and M. Mahalakshmi, "High frequency vibration energy transfer in a system of three plates connected at discrete points using statistical energy analysis", *Journal of Sound and Vibration* **296**, 539-553 (2006)
- [6] A.J. Keane and W.G. Price, "Statistical energy analysis of strongly coupled systems", *Journal of Sound and Vibration* **117**, 363-386 (1987)
- [7] L. Chang and J. Nicholas, "Radiation of sound into a cylindrical enclosure from a point-driven end plate with general boundary conditions", *Journal of the Acoustical Society of America* **91**, 1504-1513 (1992)
- [8] L. Cremer, M. Heckl and B.A.T. Petersson, *Structure-borne sound*, 3rd edition, Springer, Berlin, 2005
- [9] N.B. Roozen and M.J. Vervoordeldonk, "Prediction and control of acoustically induced vibrations of high-precision equipment", *Proceedings of the 22nd American Society for Precision Engineering Annual Meeting*, Texas, USA, 14-19 October 2007
- [10] F. Løvholt, C. Madshus and K. Norén-Cosgriff, "Analysis of low frequency sound and sound induced vibration in a Norwegian wooden building", *Noise Control Engineering Journal* **59**, 383-396 (2011)
- [11] M. Pancholy, A.F. Chhapgar and O. Sharma, "Construction of a reverberation chamber at National Physical Laboratory of India", *Journal of the Acoustical Society of India* **V**, 27-33 (1977)
- [12] O. Sharma, M. Singh and N. Garg, *Investigations on induced vibrations due to acoustic excitation from sound and light show at Sri Brihadeeswarar temple*, Thanjavur, Tamil Nadu, NPL Technical Report No. AC.C.10-1.F, 2010
- [13] C.G. Balachandran, "Random sound field in reverberation chambers", *Journal of the Acoustical Society of America* **31**, 1319-1321 (1959)
- [14] D.A. Bies and C.H. Hansen, *Engineering noise control, Theory and practice*, 4th edition, Spon Press, 2009
- [15] H. Néglise and J. Nicolas, "Characterization of a diffuse field in a reverberant room", *Journal of the Acoustical Society of America* **101**, 3517-3524 (1997)
- [16] M. Hodgson, "When is diffuse-field theory applicable", *Applied Acoustics*, **49**, 197-207 (1996).
- [17] P. D'Antonio and J. Konnert, "The reflection phase grating diffusor: Design theory and application", *Journal of the Audio Engineering Society*, **32**, 228-238 (1984)
- [18] S.J. Loutridis, "Quantifying sound-field diffuseness in small rooms using multifractals", *Journal of the Acoustical Society of America* **125**, 1498-1505 (2009)
- [19] M.R. Schroeder, "Frequency-correlation functions of frequency responses in rooms", *Journal of the Acoustical Society of America* **34**, 1819-1823 (1962)

- [20] M.R. Schroeder, "The "Schroeder frequency" revisited", *Journal of the Acoustical Society of America* **99**, 3240-3241 (1996)
- [21] O. Sharma, V. Mohanan and M. Singh, "Damage criteria for induced vibration in buildings", *Journal of the Acoustical Society of India* **25**, III-3.1- 3.5 (1997)
- [22] V. Mohanan and O. Sharma, "Induced structural vibration on Khajuraho temples due to overflying aircrafts", *Journal of the Acoustical Society of India* **27**, 123-127 (1999)
- [23] H.R. Nicholls, C.F. Johnson and W.I. Duvall, *Blasting vibrations and their effects in structures*, US Bureau of Mines, Bulletin 656, Washington DC, 1971
- [24] DIN 4150-3:1999, *Structural vibration, Part 3: Effects of vibration on structures*
- [25] British Standard BS 7385-1:1990, *Evaluation and measurement for vibration in buildings*

ACOUSTICS AUSTRALIA REVIEW SURVEY 2013

In July 2013, the Council of the Australian Acoustical Society established a panel to review the current production of Acoustics Australia, the value of the journal to the membership of the Society and propose changes as necessary.

The editorial board, with reference to the review panel, developed a survey to assess the opinions of the membership regarding the journal itself and on plans for alternative distribution means. The questions in the survey were aimed to provide a balance between ranking type responses and free text comments.

Soon after the distribution of the August 2013 issue of the Acoustics Australia journal, the members of the Australian Acoustical Society (AAS) were asked by email to give their views on Acoustics Australia via an online survey. Of the approximately 500 members, 156 responded to the survey. A summary of the finding is given here and the full report an analysis is available on the webpage at

http://www.acoustics.asn.au/members/forms/Acoustics_Australia_Review_Survey-2013.pdf

This is in the members only area so you will need to log in to access.

While it is clear from the results is that there is a great diversity in the opinion of the journal, the bulk of those that responded do read and find the journal useful at least some of the time. The comments suggesting Acoustics Australia be more like the Acoustics Bulletin, (a non peer review journal) were offset by those saying Acoustics Australia should strive to achieve a higher impact factor. There were a number of comments suggesting preference for more Australian related articles and fewer theoretical papers from overseas. There also needs to be more clarity to the readership of the editorial process and the plans for future issues.

There was a mixed but strong feeling about editorial control for the letters to the editor with particular recommendations to clearly identify any background or vested interest of the letter writer and, where appropriate, to allow the right of reply in the same issue.

In regard to the format for distribution, the results indicate that it is time to go to a full electronic (pdf) distribution for the journal as the bulk of the respondents accepted a move to an electronic version. The distribution of responses to the question about preference for hard copy versus pdf if there was no change in membership fee is shown below. A move away from hard copy distribution will be a major cost saving for the journal production. For those few who are prepared to pay for a hard copy at a cost recovery price, a limited print run using a more cost effective process, could be made available.

Some commented that more articles may be submitted if the website is made clearer, the future planning of special issues is publicised and if members are invited to submit articles. This could be achieved with ad hoc emails from the General Secretary and specific prompts to individual members plus more information in the journal itself about the process and seeking submissions.

Marion Burgess